A.I. ALIKHANIAN NATIONAL SCIENCE LABORATORY

(YEREVAN PHYSICS INSTITUTE)

Hamid Arian Zad

Thermal Entanglement and Magnetic Properties of Metal-Containing Materials

Thesis for acquiring the degree of candidate of physical-mathematical sciences in division

01.04.02, Theoretical Physics

SUPERVISOR: PROF. NERSES ANANIKIAN

YEREVAN, 2021

Certificate

It is certified that the work contained in this thesis entitled "Thermal Entanglement and Magnetic Properties of Metal-Containing Materials" by "Hamid Arian Zad" has been carried out under my supervision and that it has not been submitted elsewhere for a degree.

Prof. Nerses Ananikian

Yerevan, 2021

Theoretical Physics Department

A.I. Alikhanian National Science Laboratory

Abstract

In this thesis we study the effects of Heisenberg exchange anisotropy and single-ion anisotropy on the ground-state phase spectra, magnetic, thermodynamic and quantum properties of various exactly solvable spin models. After an outline, we proceed to solve some modeled quantum spin systems by implementing different theoretical and computational methods such as exact diagonalization method, the transfer-matrix technique and the Quantum Monte-Carlo simulation (under open source ALPS package). Next, we investigate the influences of the anisotropies, interaction parameters together with the temperature and magnetic field on the physical behavior of solved spin systems. As a matter of fact, we demonstrate that the anisotropies dramatically change the quantum critically of the spin models at different parameter-planes.

Analytical and numerical procedures given in this thesis provide original evidences for exactly solving either finite-size or infinite-size Heisenberg spin systems such as small spin clusters, metal-containing compounds, coordination polymers, pure Heisenberg and Ising-Heisenberg spin lattices under arbitrary conditions. The results delivered from examination of mentioned systems corroborate that the magnetization, susceptibility, specific heat, and entropy remarkably change nearby the crirical points at which the first-order ground-state phase transition occurs. Moreover, we test the ability of cooling and heating of these spin models when anisotropies change. we observe that anisotropy variations can also influence the isothermal strategies such as magnetocaloric effect (MCE). During adiabatic demagnetization process, an enhanced MCE is seen in a proximity of the magnetization jumps accompanied with the first-order ground-state phase transitions. We conclude that anisotropies play essential role to determine the efficiency of MCE of the models under consideration.

We prove that, when a typical magnetic impurity is considered for one magnetic dimer of a Ising-Heisenberg heterotrimetallic coordination compound, the entanglement and the possibility of teleportation of information can be enhanced by tuning Heisenberg exchange anisotropy parameter. The same enhancement occurs in the tetranuclear spin-1/2 square complex. Furthermore, It is demonstrated that, the magnetization and specific heat of an octanuclear nickel phosphonate cage and a family of octanuclear heterometallic $3d/4f$ complexes, $Ni_4^{II}Ln_4^{III}$ (Ln = Tb, Dy, Ho, Er), undertake notable changes when an exchange anisotropy is considered for, respectively, Ni$\cdots$Ni and Ni$\cdots$Ln interactions. The ac susceptibility examinations of two

compounds $Ni_4^{II}Tb_4^{III}$ and $Ni_4^{II}Dy_4^{III}$ disclose that their out-of-phase susceptibility component illustrates a maximum in its curve. In addition, the considered anisotropy substantially suppresses Cole−Cole plot, denoting single median relaxation time becomes smaller. A striking entanglement is observed between interacted Ni atoms of $Ni_4^{II}Ln_4^{III}$ complexes depending on the exchange anisotropy of $Ni \cdots Ln$ interaction.

Acknowledgements

Contents

List of Figures

List of Tables

Abbreviations

ED	**E**xact **D**iagonalization
QMC	**Q**uantum **M**onte **C**arlo
MCE	**M**agneto**C**aloric **E**ffect
ECE	**E**lectro**C**aloric **E**ffect
SMM	**S**ingle **M**olecular **M**agnet
DMRG	**D**ensity **M**atrix **R**enormalization **G**roup
TIT	**T**riangles-**I**n-**T**riangles
ALPS	**A**lgorithms and **L**ibraries for **P**hysics **S**imulations
DM	**D**zyaloshinskii−Moriya

Symbols

H	Total Hamiltonian
$\mathcal{H}$	Unit-block Hamiltonian
H_z	Zeeman energy
B	Magnet field
T	Temperature
J	exchange coupling
D	Single-ion anisotropy
K	Cyclic four-spin Ising interaction
k_B	Boltzmann constant
M	Magnetization
M_s	Saturation magnetization
C	Specific heat
S	Entropy
Z	Partition function
Δ	Magnetic exchange anisotropy
ρ	reduced density matrix
$\mathbf{T}$	Transfer matrix
$\boldsymbol{w}$	Boltzmann factor
$\mathcal{C}$	Concurrence
$\mathcal{N}$	Negativity
$\mathcal{C}_{l_1}$	l_1-norm of coherence
$\mathcal{F}_A$	Average fidelity
Tr	Trace

I would like to dedicate this thesis to my wife and my parents.

Introduction

0.1 One-dimensional Ising-Heisenberg spin systems

The exactly solvable spin models provide significant cornerstones of the quantum magnetism and material science. Within this subject, 1-D Heisenberg spin chains and ladders have attracted a great deal of attention, since they naturally bear strong magnetic properties dominated by quantum effects and reveal several kinds of zero-temperature phase transitions between intriguing ground states, that properly coincide with the change in magnetization process [1, 2, 3, 4, 5, 6, 7, 8, 9, 10, 11, 12]. Many theoretical researches have been devoted to realize the physics of the 1-D pure Ising [13, 14] and Ising-Heisenberg spin models. Particular models from the later are Ising-Heisenberg spin chains [4, 9, 10, 11, 15, 16], sawtooth chains [17, 18, 19, 20], Ising-Heisenberg lattice stripes [21, 22, 23] and Ising-Heisenberg two-leg ladders [24, 25, 26, 27, 28] that have attracted a lot of attention. This is because of being fabricable and, as exactly solvable models, they exhibit rich magnetic behaviors such that they play an important role in statistical physics.

0.1.1 Solution with in the transfer-matrix technique

One of the most popular methods to solve a wide variety of 1-D spin models with nearest-neighbor and that of the next-nearest-neighbor interactions is the so called transfer-matrix method. Useful details about the solution of the spin-1/2 Ising-Heisenberg diamond chain within the transfer matrix technique can be found, for example, in Ref. [29] and references therein [30]. Analogously, O. Rojas *et al.* solved a mixed spin-(1/2, 1) Ising-Heisenberg double-tetrahedral chain in an external magnetic field using the classical transfer-matrix formalism and reported comprehensive results on the ground-state phase transition and the thermodynamics of such a model in their recent work [31]. The method is by far the prominent technique with wide general implementations in Ising-Heisenberg spin systems with infinite length [4, 9, 10, 11, 15, 17, 18, 19, 20, 21, 22, 24, 25]. The method is also east-to-use and can be pleasantly generalized to cover other models possessing mixed spin-(1/2, $S > 1/2$) Ising-Heisenberg systems [26, 27, 32], Potts spins [33, 34, 35] and lattice stripes [21, 22].

The Hamiltonian of a typical 1-D spin-1/2 Ising-Heisenberg chain in the presence of an external magnetic field with periodic boundary conditions can be written as

$$H = \sum_{i=1}^{N} \left[\mathcal{H}_i \right] + H_z, \tag{1}$$

where $\mathcal{H}_i$ reads the Hamiltonian of each sub-unit block that repeat through the chain, and H_z is the Zeeman part. N is the number of unit blocks that $N \longrightarrow \infty$. The pure Ising-type exchange coupling represents interaction between $(i, i+1)-$th nodal spins and Heisenberg
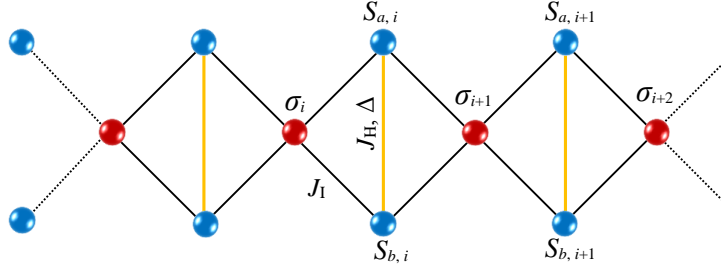
FIGURE 1: Schematic structure of a spin-1/2 diamond chain with Ising spins σ localized in the nodal sites, and Heisenberg dimer spins S localized in the interstitial sites.

(monomer, dimer, trimer) spins. The commutation relation between each of two different block Hamiltonians $[\mathcal{H}_i, \mathcal{H}_j] = 0$ enables us to calculate the partition function of the model from the following formula

$$Z = \text{Tr}\Big[\prod_{i=1}^{N} \exp\big[-\beta(\mathcal{H}_i + H_z) \big] \Big], \tag{2}$$

where $\beta = 1/k_B T$ with k_B the Boltzmann constant and T the temperature (for simplicity we set $k_B = 1$). Hence, we can write the 2×2 transfer matrix $\mathbf{T}$ as follows

$$\mathbf{T}_{\sigma_i, \sigma_{i+1}} = \langle \sigma_i | \mathbf{T} | \sigma_{i+1} \rangle = \sum_{k=1}^{n} \exp\big[-\beta \mathcal{E}_k(\sigma_i, \sigma_{i+1}) \big]. \tag{3}$$

$\mathbf{T}$ represents the transfer matrix of each unit block confined between two nodal spins σ_i and σ_{i+1}. n is the number of eigenvalues of the quantum Heisenberg part of the model, i.g., for spin-1/2 dimers $n = 4$ (Fig. 1). Moreover, $\mathcal{E}_k$ denote the eigenvalues of the Hamiltonian $\mathcal{H}_i + H^z$.

We then obtain the partition function of the model as

$$Z = \lambda_1^N + \lambda_2^N, \tag{4}$$

where λ_1 and λ_2 are two eigenvalues of the transfer matrix. Since we look for eigenvalues of the transfer matrix $\mathbf{T}$ in the thermodynamic limit $N \to \infty$, as usual the largest eigenvalue $\Lambda_{max} = \max\{\lambda_1, \lambda_2\}$ is the only one that plays the most important role to verify the thermodynamics of the model [36].

The transfer-matrix technique can be also applied for describing the thermodynamics of a 1-D Ising-Heisenberg diamond chains, for example, that shown in Fig. 1 in the presence of an external magnetic field with the corresponding unit-block Hamiltonian

$$\begin{aligned}
\mathcal{H}_i = &-J_{\text{H}}\big(S_{a,i}^x S_{b,i}^x + S_{a,i}^y S_{b,i}^y\big) - \Delta S_{a,i}^z S_{b,i}^z - J_{\text{I}}\big(S_{a,i}^z + S_{b,i}^z\big)\big(\sigma_i^z + \sigma_{i+1}^z\big) \\
&-B\big(S_{a,i}^z + S_{b,i}^z\big) - \tfrac{B}{2}(\sigma_i^z + \sigma_{i+1}^z),
\end{aligned} \tag{5}$$
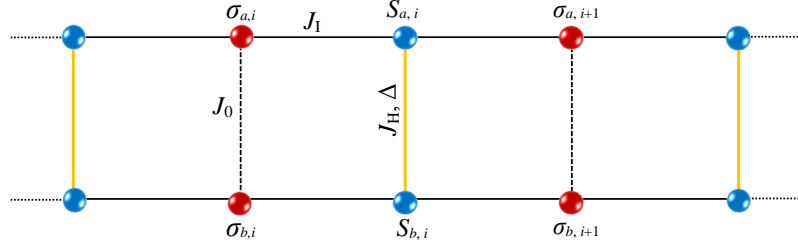
FIGURE 2: Schematic structure of a spin-1/2 two-leg ladder with Ising spins σ localized in the nodal sites, and Heisenberg spins S localized in the interstitial Heisenberg sites.

where $S_{\gamma,i}^{\alpha}(\alpha = \{x, y, z\}, \gamma = a, b)$ marks the Heisenberg spins and σ_i corresponds to the Ising spins. J_{I} represents the Ising-type interaction between nodal and interstitial sites, whereas J_{H} and Δ are the Heisenberg-type interaction between interstitial sites. The system is considered in the presence of an external magnetic field B along the $z-$axis.

Ising-Heisenberg two-leg ladders can be exactly solved within the transfer-matrix formalism. The general structure of these types of Ising-Heisenberg models are schematically illustrated in Fig. 2 by accounting the alternating Ising and Heisenberg inter-leg couplings in addition to the Ising intra-leg exchange coupling. Although, their unit block Hamiltonians are different from the Ising-Heisenberg diamond chains, they can be transformed to each other [24]. Following Hamiltonian can describe the Ising-Heisenberg two-leg ladder

$$
\begin{aligned}
\mathcal{H}_i = &-J_{\mathrm{H}}\big(S_{a,i}^x S_{b,i}^x + S_{a,i}^y S_{b,i}^y\big) - \Delta S_{a,i}^z S_{b,i}^z - J_{\mathrm{I}}\big[\big(\sigma_{a,i}^z + \sigma_{a,i+1}^z\big)S_{a,i}^z + \big(\sigma_{b,i}^z + \sigma_{b,i+1}^z\big)S_{b,i}^z\big] \\
&-J_0\big(\sigma_{a,i}^z \sigma_{b,i}^z + \sigma_{a,i+1}^z \sigma_{b,i+1}^z\big) - B\big(S_{a,i}^z + S_{b,i}^z\big) - \tfrac{B}{2}\big(\sigma_{a,i}^z + \sigma_{b,i}^z + \sigma_{a,i+1}^z + \sigma_{b,i+1}^z\big).
\end{aligned}
\tag{6}
$$

For these sets of spin systems, the following matrix representation for $\exp(-\beta H)$ in the two-qubit standard basis of the eigenstates of the composite spin operators $\{\sigma_{a,i}^z, \sigma_{a,i+1}^z, \sigma_{b,i}^z, \sigma_{b,i+1}^z\}$ corresponding to the two consecutive rungs of the square plaquette in $i-$th block is adopted, by which the partition function Z can be defined as

$$
Z = \mathrm{Tr}\big[\langle\sigma_{1,1}^z\sigma_{1,2}^z|\mathbf{T}|\sigma_{1,3}^z\sigma_{1,4}^{z\prime}\rangle\langle\sigma_{2,1}^z\sigma_{2,2}^z|\mathbf{T}|\sigma_{2,3}^z\sigma_{2,4}^z\rangle\cdots\langle\sigma_{N,1}^z\sigma_{N,2}^z|\mathbf{T}|\sigma_{N,3}^z\sigma_{N,4}^z\rangle\big],
\tag{7}
$$

where $\sigma_{i,j}^z = \pm\frac{1}{2}$ and

$$
\mathbf{T}(i) = \langle\sigma_{i,1}^z\sigma_{i,2}^z|\exp(-\beta\mathcal{H}_i)|\sigma_{i,3}^z\sigma_{i,4}^z\rangle = \sum_{k=1}^{4}\exp\big[-\beta\mathcal{E}_k(\sigma_{i,1}^z\sigma_{i,2}^z \mid \sigma_{i,3}^z\sigma_{i,4}^z)\big],
\tag{8}
$$

where the elements of the 4×4 transfer matrix $\mathbf{T}(i)$ are defined through eigenvalues $\mathcal{E}_k$.

0.2   Two-dimensional Ising-Heisenberg spin systems

Two-dimensional Heisenberg spin lattices as another family of exactly solvable models provide us particularly accessible routes to better understanding of such systems. As soon as Onsager launched the solution of 2-D Ising model [37], several attempts has been inspired to solve analogous models. For example, honeycomb lattice [38, 39, 40, 41], various kinds of triangular lattices whose exact solution with an external magnetic field were carried out [42, 43, 44, 45, 46, 47]. Besides, Kagomé lattice was also widely discussed in the literature [48, 49, 50] and references therein.

0.2.1   Solution by mapping Heisenberg lattice into Ising analogous

In order to solve $2-$D materials some applicable techniques have been introduced and widely developed [51, 52, 53, 54, 55]. Among useful techniques, one is the duality transformation which applies mainly to solve $2-$D cases. Ever since the first formulation of duality was described by Kramers and Wannier [56], the method has been used to predict the transition points of the Ising model on the square lattice [57], the Potts model on the square [58, 59], triangular, and hexagonal lattices [60]. Heretofore, J. Strečka *et al.* have utilized some maps such as mapping to hard-hexagon model, and mapping triangular Heisenberg bilayer lattice into Ising triangular lattice, to solve several triangles-in-triangles (TIT) lattices, decorated planar lattices, square lattices and etc. [42, 43, 44, 45, 46, 47]. Many interesting results obtained from the above methods for the physical behavior of the $2-$D lattices have been reported in the literature.

In Ref. [43] the spin-1/2 Ising-Heisenberg model on the geometrically related TIT lattices (Fig. 3) were exactly solved within the generalized star-triangle transformation with the aid of mapping the effective spin-1/2 Ising model on a triangular lattice.

The spin-1/2 Ising-Heisenberg model on a TIT lattice can be introduced by characterizing relevant Hamiltonian

$$H = -J_{\text{H}} \sum_{\langle i,j \rangle} \left[\Delta \left(S_i^x S_j^x + S_i^y S_j^y \right) + S_i^z S_j^z \right] - J_{\text{I}} \sum_{\langle k,l \rangle} S_k^z \sigma_l^z, \tag{9}$$

where S_i^α with $\alpha = x, y, z$ and σ_k^z are spatial components of the spin-1/2 operator of the Heisenberg and Ising spins, respectively. Parameter J_{H} and J_{I} stand for the XXZ Heisenberg and Ising interactions, respectively. The total Hamiltonian of the model can be rewritten as

$$H = \sum_{k=1}^{N} \mathcal{H}_k, \tag{10}$$
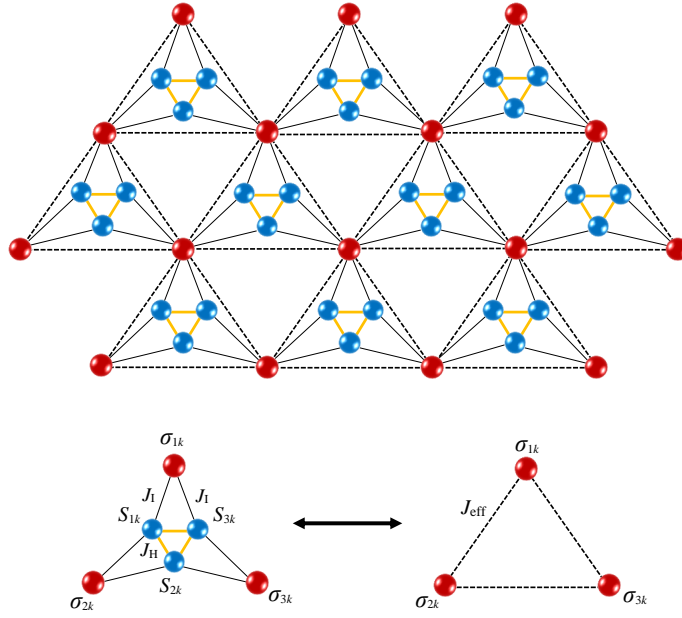
FIGURE 3: The spin-1/2 Ising-Heisenberg model on a TIT lattice and its rigorous mapping to the pure spin-1/2 Ising model on a triangular lattice (dashed triangles) with the relevant coupling constant J_{eff}. Blue cycles represent the Heisenberg spins interacted together via J_{H}, while red cycles indicate the Ising nodal spins interacted to Heisenberg counterparts through coupling constant J_{I} (Ref. [43]).

where cluster Hamiltonian $\mathcal{H}_k$ is given by

$$\mathcal{H}_k = -J_{\text{H}} \sum_{i=1}^{3} \left[\Delta\left(S_{k,i}^x S_{k,i+1}^x + S_{k,i}^y S_{k,i+1}^y\right) + S_{k,i}^z S_{k,i+1}^z \right] - J_{\text{I}} \sum_{i=1}^{3} \sigma_{k,i}^z \left(S_{k,i}^z + S_{k,i+1}^z\right), \qquad (11)$$

with periodic boundary conditions such that $S_{k,4}^\alpha = S_{k,1}^\alpha$. Owing to this fact, the partition function of the model can be written as

$$Z = \sum_{\{\sigma_i\}} \prod_{k=1}^{\gamma N} \text{Tr}_k \exp\left(-\beta\mathcal{H}_k\right) = \sum_{\{\sigma_i\}} \prod_{k=1}^{\gamma N} Z_k. \qquad (12)$$

Here, $\gamma = 1$ is the transformation coefficient. The partition function of unit blocks Z_k depends on the three nodal Ising spins σ_{k1}, σ_{k2} and σ_{k3} linked to the $k-$th Heisenberg trimer. Hence, the generalized star-triangle transformation will constitute to,

$$Z_k\left(\sigma_{k1}^z, \sigma_{k2}^z, \sigma_{k3}^z\right) = \text{Tr}_k \exp(-\beta\mathcal{H}_k) = A \exp\left[\beta J_{\text{eff}}\left(\sigma_{k1}^z \sigma_{k2}^z + \sigma_{k2}^z \sigma_{k3}^z + \sigma_{k3}^z \sigma_{k1}^z\right)\right]. \qquad (13)$$

In the absence of magnetic field, two independent equations is required to obtain A. First one is for two uniform configurations with the three equally aligned Ising spins, whereas second one is attributed to the six nonuniform spin structures possessing one Ising spin with opposite direction

compared to the other spins. Therefore, we have

$$
\begin{aligned}
V_1 &\equiv Z_k\big(\sigma^z_{k1}, \sigma^z_{k2}, \sigma^z_{k3}\big) = A\exp\big(\tfrac{3}{4}\beta J_{\mathrm{eff}}\big), \\
V_2 &\equiv Z_k\big(\pm\sigma^z_{k1}, \pm\sigma^z_{k2}, \mp\sigma^z_{k3}\big) = Z_k\big(\pm\sigma^z_{k1}, \mp\sigma^z_{k2}, \pm\sigma^z_{k3}\big) = \\
&\quad Z_k\big(\mp\sigma^z_{k1}, \pm\sigma^z_{k2}, \pm\sigma^z_{k3}\big) = A\exp\big(-\tfrac{1}{4}\beta J_{\mathrm{eff}}\big).
\end{aligned}
\tag{14}
$$

Consequently, mapping parameters A and J_{eff} are deduced by following equation

$$
A = \big(V_1 V_2^3\big)^{\frac{1}{4}}, \quad \beta J_{\mathrm{eff}} = \ln\left(\frac{V_1}{V_2}\right).
\tag{15}
$$

0.3   Small Spin Clusters: Metal containing complexes

In condensed matter physics, one of the most investigated subjects is magnetic properties of the single molecular magnets (SMMs) which has attracted considerable attention to explore magnetic behavior of small spin clusters [61, 62, 63, 64, 65, 66, 67, 68, 69, 70]. Over the past decade, a great deal of attention has been attracted by the heterometallic octa(deca)nuclear complexes composed of $3d/4f$ transition-metals. This attraction emanates from several points of view. From the view point of theoretical modeling, these compounds could be properly characterized by Heisenberg spin models. Second, they exhibit a wide variety of intriguing physical properties and quantum phase transitions, so they have been known as promising materials in various branches, such as material science and physical chemistry [71, 72, 73]. It has already become possible to synthesize a large variety of compounds including identical or mixed transition-metal ions with the geometry of butterfly-shaped subunit and S-shaped structures, which can be properly introduced in terms of Heisenberg models. The design of $3d/4f$ single molecular magnets (SMMs), different from the homometallic $3d$ ones, requires the use of lanthanide ions which present high anisotropy properties. The best candidates ions are: $\mathrm{Tb^{III}}$, $\mathrm{Dy^{III}}$, $\mathrm{Ho^{III}}$ and $\mathrm{Er^{III}}$ ions [74, 75]. SMMs are discrete metal compounds which behave like superparamagnets below a blocking temperature. They have already been the proposal of several technological applications including quantum information processing [76], spintronics [77], quantum dots [78] and preparing qubits for advanced quantum computing [79, 80, 81].

In the past few years, it has been corroborated that some exactly solvable spin models may capture basic magnetic features of a family of octanuclear complexes including lanthanide metal salts with the addition of nickel acetate $[\mathrm{Ni_4Ln_4}(\mu_2-\mathrm{OH})_2(\mu_3-\mathrm{OH})_4(\mu-\mathrm{OOCCH_3})_8(\mathrm{LH_2})_4]$. These products are new additions to the very small family of $\mathrm{Ni_2Ln_2}$ (Ln = Y, Tb, Gd, Dy, Ho, Er) clusters with planar butterfly (or rhombus) core and show the initial compounds prepared from the use of $\mathrm{pdH_2}$ in mixed transition-metal $3d/4f$ cluster chemistry. The magnetic properties of the mentioned polycrystalline samples with isotropic XXX interactions have been theoretically and experimentally investigated by P. Kalita *et al.* [73].

0.3.1 Solution by ED method and QMC simulation

Described small spin complexes and related groups of compounds in physical chemistry science [82, 83, 84, 85, 86] are of particular interests in resent years. To diagonalize the Hamiltonian of these finite-size systems, i.e., Eq. (16), some usual methods have been proponded so far.

$$H = \sum_{\langle i,j \rangle}^{N_v} \left[J\left(S_i^x S_j^x + S_i^y S_j^y\right) + \Delta S_i^z S_j^z \right] - B \sum_{i=1}^{N} S_i^z, \tag{16}$$

in which N_v denotes the number of edges and N accounts for the number of vertices (sites) in a favorite spin cluster system. Full exact diagonalization method (ED), density matrix renormalization group (DMRG) [87, 88, 89, 90, 91, 92] and Quantum Monte Carlo (QMC) simulations [93, 94, 95, 96, 97, 98] are popular methods to solve above Hamiltonian. To solve the problem of metal containing complexes, it is presumable to perfom two usual methods: full ED and QMC simulations by adopting the subroutine $dirloop - sse$ – a package from the Algorithms and Libraries for Physics Simulations (ALPS) project [99, 100]. The later is an open source and simple computational package to use for researchers [62, 63, 101].

0.4 Contents of this Thesis

In this thesis, we study the magnetic, thermodynamic and quantum properties of a variety of quantum spin models with anisotropy. For this purpose, we utilize various methods to solve these models and in some cases we compare our results with the experimental data. By employing the transfer-matrix technique, we solve several 1-D and 2-D Ising-Heisenberg spin models and by extracting the partition function, we try to reproduce the physical behavior of these spin systems. Next, we investigate the same properties but for some small spin clusters including metal containing complexes with anisotropy. We perform both of ED method and QMC simulations to diagonalize the Hamiltonian of these materials. According to our novel results, we think that this work is original and provides the first proposals possessing new outcomes for the ground-state phase transition, magnetic behavior and quantum properties of several kinds of spin models.

This thesis is continued by forthcoming chapters with the relevant partitioned contents.

In Chapter 1, we rigorously examine the magnetization process and thermodynamics of some types of 1-D Ising-Heisenberg spin models such as Ising-Heisenberg spin chain of a heterotrimetallic $Fe - Mn - Cu$ coordination polymer with magnetic impurity. The impurity effects on the bipartite quantum entanglement, quantum coherence, quantum Fisher information and the ability of teleportation of this spin system will be examined in detail.

In chapter 2, a spin $S=1/2$ Ising-Heisenberg double saw-tooth ladder and two geometrically different mixed spin-(1/2, 1) Ising-Heisenberg two-leg ladders are modeled as well. The ground-state phase transition of these models is investigated and a comparison is carried out between the ground-state phase diagram and their thermodynamics. Finally, the key results obtained for the anisotropies influences on the magnetization and cooling/heating ability of such systems are reported in this chapter.

In chapter 3, is proposed two different types of 2-D highly frustrated spin-1/2 Ising-Heisenberg model on TIT lattices. We then exactly solve these unconventional models through the generalized star-triangle transforming to an effective spin-1/2 Ising model on a triangular lattice. The main part of this chapter will be dedicated to study ordered-disordered ground states, spontaneous magnetizations and the specific heat of the spin-1/2 Ising-Heisenberg models defined on two different TIT lattices, that each of them geometrically reduces to a simple Ising triangular lattice.

In chapter 4, by taking advantage of the remarkable property of ED method and QMC simulations (implemented by ALPS-Package) we exactly solve some molecular cluster magnets such as lanthanide containing complexes such as two linked butterfly-shaped $Ni_2^{II}Ln_2^{III}$ (Ln = Tb, Dy, Ho, Er) subunits and an octanuclear nickel phosphonate cage with butterfly-shaped geometry. Further, a coupled tetranuclear Cu_4^{II} square complex is solved in parallel. Next, we study the magnetic properties and the specific heat anomalies of such materials with exchange anisotropy in the presence of an external magnetic field quite rigorously. We compare our results with the relevant experimental data and conclude that our numerical results are in a well agreement with the experimental data analysis. Ultimately, we verify the influences of the anisotropy on the magnetization and the specific heat of such materials. Further, we investigate the anisotropy effects on the dc and ac susceptibilities and qutrit-qutrit quantum correlations between nickel atoms of $Ni_4^{II}Ln_4^{III}$ complexes. Two spin-1/2 Heisenberg edge-shared tetrahedra and spin-1/2 Heisenberg octahedron with the corresponding Dzyaloshinskii-Moriya (DM) interaction have been solved as well, that the relevant outcomes have not been inscribed in this context.

Each chapter of this thesis will end up with several **concluding remarks**, manifesting the key results and future outlooks. The results and derivations of this thesis are published in Refs. [16, 22, 23, 26, 62, 63, 68, 69, 113, 114, 115].

Chapter 1

Heterotrimetallic $Fe - Mn - Cu$ coordination polymer

1.1   Preliminaries

With the motivation of heterotrimetallic coordination compound $[Cu^{II}Mn^{II}(L^1)][Fe^{III}(bpb)(CN)_2] \cdot ClO_4 \cdot H_2O$ [102], in Refs. [29, 30, 103] have investigated in detail the magnetization process and thermal entanglement of this polymeric complex owing to the characterizing an effective 1-D Ising-Heisenebrg spin model. Heretofore, the teleportation via a couple of quantum channel based on the Ising-Heisenberg spin structure of heterotrimetallic $Fe - Mn - Cu$ coordination polymer was studied [104]. Analogously, magnetization and quantum properties of the hetero-bimetalic coordination polymer $[(Tp)_2Fe_2(CN)_6(OAc)(bap)Cu_2(CH_3OH) \cdot 2CH_3OH \cdot H_2O]$ with different spin configuration were examined in Ref. [105].

In this chapter, we aim to investigate the thermal entanglement, quantum coherence, and the ability of quantum teleportation in an exactly solvable spin-1/2 Ising-Heisenberg model of the heterotrimetallic coordination compound $[Cu^{II}Mn^{II}(L^1)][Fe^{III}(bpb)(CN)_2] \cdot ClO_4 \cdot H_2O$, with simple notation $Fe - Mn - Cu$, including magnetic impurity (see Fig. 1.1). In our approach, we suppose that the magnetic impurity is located on a unit block of the chain whose variations can be an efficient way to control and modify the quantum correlations and the ability of the teleportation of information through the chain. Furthermore, investigating QFI and its first magnetic field derivative for the model with magnetic impurity is another goal of this chapter.

1.2   The model and method

The total Hamiltonian of the model including a typical magnetic impurity on a unit block is given by $H = \sum_{i=1}^{N} \mathcal{H}_i$ as we reported in Ref. [16], where the unit-block Hamiltonian $\mathcal{H}_i$ is
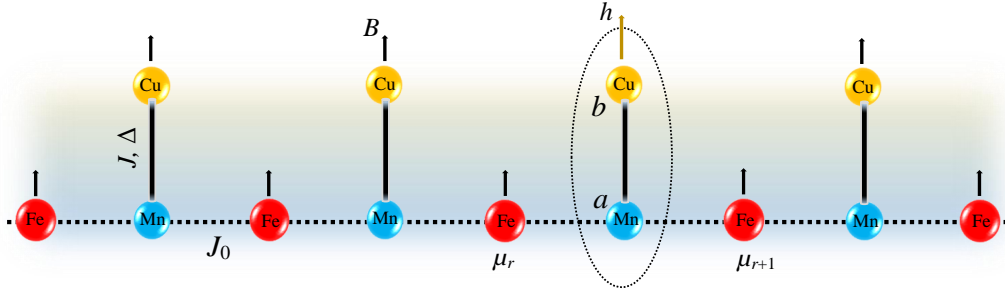
FIGURE 1.1: A representation of the spin-1/2 Ising-Heisenberg chain of $Fe - Mn - Cu$. The interaction between $Fe^{3+} - Mn^{2+}$ ions is assumed to be Ising-type interaction, while interaction $Mn^{2+} - Cu^{2+}$ to be an anisotropic Heisenberg exchange interaction. The magnetic impurity is indicated by elliptic dotted line.

$$\mathcal{H}_i = \mathcal{H}_i^{host} + \mathcal{H}_i^{imp}, \tag{1.1}$$

The host Hamiltonian reads

$$\mathcal{H}_i^{host} = J \left(\mathbf{S}_{a,i}, \mathbf{S}_{b,i} \right)_\Delta + J_0 S_{a,i}^z \left(\mu_i + \mu_{i+1} \right) - B_2 S_{a,i}^z - B_3 S_{b,i}^z - \frac{B_1}{2} \left(\mu_i + \mu_{i+1} \right),$$

for $i = 1, 2, \ldots, r - 1, r + 1, \ldots, N$.

As noted in previous chapter, $S_{a,i}^\alpha$ and $S_{b,i}^\alpha$ with $\alpha = \{x, y, z\}$ denote the Heisenberg spin$-\frac{1}{2}$ operators of, respectively, Mn^{2+} and Cu^{2+} ions. The quantum part $(\boldsymbol{S}_{a,i} \cdot \boldsymbol{S}_{b,i})_\Delta$ including exchange interactions J and Δ can be defined by

$$(\boldsymbol{S}_{a,i} \cdot \boldsymbol{S}_{b,i})_\Delta \equiv S_{a,i}^x S_{b,i}^x + S_{a,i}^y S_{b,i}^y + \Delta S_{a,i}^z S_{b,i}^z. \tag{1.2}$$

The theoretical and experimental results for the susceptibility of this compound unfold that the Weiss temperature is negative, denoting the antiferromagnetic nature of the predominant exchange coupling [103]. So, the antiferromagnetic coupling $J > 0$ is described for the spin-spin interactions between interstitial dimers $Mn^{2+} - Cu^{2+}$, while dimer-monomer interaction J_0 reflects the Ising-type interaction between nodal and interstitial magnetic ions $Fe^{3+} - Mn^{2+}$. $B_k = g_k \mu_0 B$ with $k = \{1, 2, 3\}$ is an external magnetic field along the z-axis (for simplicity we put $\mu_0 = 1$). μ_i and μ_{i+1}, taking values $(\frac{1}{2}, -\frac{1}{2})$, label the Ising nodal spins Fe^{3+}.

The impurity part of the Hamiltonian is given by

$$\mathcal{H}_i^{imp} = J \left(\mathbf{S}_{a,i}, \mathbf{S}_{b,i} \right)_\Delta + J_0 S_{a,i}^z \left(\mu_i + \mu_{i+1} \right) - h_2 S_{a,i}^z - h_3 S_{b,i}^z - \frac{B_1}{2} \left(\mu_i + \mu_{i+1} \right),$$

for $i = r$.

in which the induced impurity parameter γ can be seed into the magnetic impurity $h_k = g_k B (1 + \gamma)$ with $k = \{2, 3\}$.

Four eigenvalues of the Hamiltonian $\mathcal{H}_i^{host}$ are obtained by diagonalizing $i-$th XXZ dimer. So, we have

$$
\begin{aligned}
\varepsilon_{1,4} &= \tfrac{J\Delta}{4} \pm \tfrac{J_0}{2} (\mu_i + \mu_{i+1}) - \tfrac{B_1}{2} (\mu_i + \mu_{i+1}) \mp \tfrac{1}{2} (B_2 + B_3), \\
\varepsilon_{2,3} &= -\tfrac{J\Delta}{4} - \tfrac{B_1}{2} (\mu_i + \mu_{i+1}) \pm \sqrt{\Omega^2 + J^2},
\end{aligned}
\tag{1.3}
$$

where, $\Omega = J_0 (\mu_i + \mu_{i+1}) - (B_2 - B_3)$.

The corresponding eigenvectors in the standard dimer basis $\{|00\rangle, |01\rangle, |10\rangle, |11\rangle\}$ are given by

$$
\begin{aligned}
|\varphi_1\rangle &= |00\rangle, \\
|\varphi_2\rangle &= m_+ |01\rangle + n_+ |10\rangle, \\
|\varphi_3\rangle &= m_- |01\rangle + n_- |10\rangle, \\
|\varphi_4\rangle &= |11\rangle.
\end{aligned}
\tag{1.4}
$$

where following notations are adopted

$$
m_\pm = \frac{J}{\sqrt{2J^2 + 2\Omega^2 \mp 2\Omega\sqrt{\Omega^2 + J^2}}}, \quad n_\pm = \frac{\Omega \pm \sqrt{\Omega^2 + J^2}}{\sqrt{2J^2 + 2\Omega^2 \pm 2\Omega\sqrt{\Omega^2 + J^2}}}.
\tag{1.5}
$$

Analogously, eigenvalues of $\mathcal{H}_i^{imp}$ can be given by

$$
\begin{aligned}
\widetilde{\varepsilon}_{1,4} &= \tfrac{J\Delta}{4} \pm \tfrac{J_0}{2} (\mu_i + \mu_{i+1}) - \tfrac{B_1}{2} (\mu_i + \mu_{i+1}) \mp \tfrac{1}{2} (h_2 + h_3), \\
\widetilde{\varepsilon}_{2,3} &= -\tfrac{J\Delta}{4} - \tfrac{B_1}{2} (\mu_i + \mu_{i+1}) \pm \sqrt{\kappa^2 + J^2},
\end{aligned}
\tag{1.6}
$$

where $\kappa = J_0 (\mu_i + \mu_{i+1}) - (h_2 - h_3)$. The corresponding eigenstates are written as

$$
\begin{aligned}
|\widetilde{\varphi}_1\rangle &= |00\rangle, \\
|\widetilde{\varphi}_2\rangle &= \Sigma_+ |01\rangle + \Gamma_+ |10\rangle, \\
|\widetilde{\varphi}_3\rangle &= \Sigma_- |01\rangle + \Gamma_- |10\rangle, \\
|\widetilde{\varphi}_4\rangle &= |11\rangle.
\end{aligned}
\tag{1.7}
$$

where

$$
\Sigma_\pm = \frac{J}{\sqrt{2J^2 + 2\kappa^2 \mp 2\kappa\sqrt{\kappa^2 + J^2}}}, \quad \Gamma_\pm = \frac{-\kappa \pm \sqrt{\kappa^2 + J^2}}{\sqrt{2J^2 + 2\kappa^2 \mp 2\kappa\sqrt{\kappa^2 + J^2}}}.
\tag{1.8}
$$

The system state at thermal equilibrium is $\rho(T) = \frac{\exp(-\beta H)}{\text{Tr}[\exp(-\beta H)]}$.

1.2.1 The density operator and partition function

To find out the quantum properties of the $Mn^{2+} - Cu^{2+}$ ion dimers such as thermal pairwise entanglement, the quantum coherence, QFI and teleportation, partition function of the model is required at first step. Beforehand, the original model has been exactly solved in the thermodynamic limit within the transfer-matrix technique [103]. The transfer-matrix technique would help us to exactly solve such a model with a typical impurity dimer. Owing to this fact, the local density operator for Heisenberg dimer of site $i = r$ (site a and b labeled in Fig. 1.1) whose nodal Ising particles μ_i and μ_{i+1} blockade magnetic Mn^{2+}, is given by

$$\varrho(\mu_i,\ \mu_{i+1}) = \sum_{j=1}^{4} e^{-\beta \varepsilon_{i,j}(\mu_i,\ \mu_{i+1})} \mid \varphi_{i,j}\rangle\langle\varphi_{i,j} \mid \tag{1.9}$$

which, $\varepsilon_{i,j}(\mu_i,\ \mu_{i+1})$ are two-qubit operator eigenvalues (1.3). The partition function of the model can be obtained in terms of Boltzmann factor of the $i-$ block dimer as following

$$\boldsymbol{W}(\mu_i, \mu_{i+1}) = \text{Tr}_{ab}\left[\varrho(\mu_i, \mu_{i+1})\right] = \sum_{j=1}^{4} e^{-\beta \varepsilon_{i,j}(\mu_i,\ \mu_{i+1})}. \tag{1.10}$$

As our system includes a dimer impurity at site $i = r$, gaining the Boltzmann factor of the impurity is important to generate total partition function. On the other hand, the Boltzmann factor for an embedded impurity reads

$$\widetilde{\boldsymbol{w}}(\mu_i, \mu_{i+1}) = \sum_{j=1}^{4} e^{-\beta \widetilde{\mathcal{E}}_{ij}(\mu_i, \mu_{i+1})} \ .$$

Partition function can be thus written in terms of the multiplication of Boltzmann factors, i.e.,

$$Z = \sum_{\{\mu\}} \boldsymbol{W}(\mu_1, \mu_2)...\boldsymbol{W}(\mu_{r-1}, \mu_r)\widetilde{\boldsymbol{W}}(\mu_r, \mu_{r+1})\boldsymbol{W}(\mu_{r+1}, \mu_{r+2})...\boldsymbol{W}(\mu_N, \mu_1) \ . \tag{1.11}$$

Above equation can be straightforwardly defined by

$$Z = \text{Tr}\left(\widetilde{W}W^{N-1}\right),$$

in which the transfer-matrix $\widetilde{W}$ associated to the whole of spin chain except the impurity part. It is defined as

$$W = \begin{bmatrix} \boldsymbol{W}(\frac{1}{2},\frac{1}{2}) & \boldsymbol{W}(\frac{1}{2},-\frac{1}{2}) \\ \boldsymbol{W}(-\frac{1}{2},\frac{1}{2}) & \boldsymbol{W}(-\frac{1}{2},-\frac{1}{2}) \end{bmatrix} \ . \tag{1.12}$$

equivalently, the transfer-matrix $\widetilde{W}$ for the impurity is given by

$$\widetilde{W} = \left[\begin{array}{cc} \widetilde{\boldsymbol{w}}(\frac{1}{2}, \frac{1}{2}) & \widetilde{\boldsymbol{w}}(\frac{1}{2}, -\frac{1}{2}) \\ \widetilde{\boldsymbol{w}}(-\frac{1}{2}, \frac{1}{2}) & \widetilde{\boldsymbol{w}}(-\frac{1}{2}, -\frac{1}{2}) \end{array} \right] .$$

The transfer-matrix elements adopts following notations $\boldsymbol{w}_{++} \equiv \boldsymbol{w}(\frac{1}{2}, \frac{1}{2})$, $\boldsymbol{w}_{+-} \equiv \boldsymbol{w}(\frac{1}{2}, -\frac{1}{2})$, $\boldsymbol{w}_{-+} \equiv \boldsymbol{w}(-\frac{1}{2}, \frac{1}{2})$ and $\boldsymbol{w}_{--} \equiv \boldsymbol{w}(-\frac{1}{2}, -\frac{1}{2})$. Accordingly, the eigenvalues of the above transfer-matrix are given by,

$$\Lambda_{\pm} = \frac{\boldsymbol{w}_{++} + \boldsymbol{w}_{--} \pm Q}{2} , \tag{1.13}$$

assuming $Q = \sqrt{(\boldsymbol{w}_{++} - \boldsymbol{w}_{--})^2 + 4\boldsymbol{w}_{+-}^2}$. Therefore, under periodic boundary conditions, the total partition function for a finite-size spin chain modeled by heterotrimetallic $Fe - Mn - Cu$ is given by

$$Z = a\Lambda_{+}^{N-1} + d\Lambda_{-}^{N-1} , \tag{1.14}$$

where

$$a = \frac{4\boldsymbol{w}_{+-}\widetilde{\boldsymbol{w}}_{+-} + (\boldsymbol{w}_{++} - \boldsymbol{w}_{--})(\widetilde{\boldsymbol{w}}_{++} - \widetilde{\boldsymbol{w}}_{--}) + Q(\widetilde{\boldsymbol{w}}_{++} + \widetilde{\boldsymbol{w}}_{--})}{2Q},$$

$$d = \frac{-4\boldsymbol{w}_{+-}\widetilde{\boldsymbol{w}}_{+-} - (\boldsymbol{w}_{++} - \boldsymbol{w}_{--})(\widetilde{\boldsymbol{w}}_{++} - \widetilde{\boldsymbol{w}}_{--}) + Q(\widetilde{\boldsymbol{w}}_{++} + \widetilde{\boldsymbol{w}}_{--})}{2Q} .$$

In the thermodynamic limit $N \to \infty$, partition function is determined by the largest eigenvalue of the transfer matrix W as we labeled above Λ_{+}. Hence, we attain $Z_N = a\Lambda_{+}^{N-1}$. From now on, we are enabled to investigate the thermal quantum correlations, the concurrence, QFI and quantum teleportation after obtaining the reduced density operator $\widetilde{\rho}$ of the dimer impurity.

1.2.2   Two-qubit density operator in a matrix form

We employ the approach reported in Refs. [29, 30] in order to calculate the thermal average of the two-qubit operator corresponding to an impurity linked by Ising nodal ions μ_r and μ_{r+1}. This operator in the standard dimer basis becomes

$$\widetilde{\varrho}(\mu_r, \mu_{r+1}) = \left[\begin{array}{cccc} \widetilde{\varrho}_{1,1} & 0 & 0 & 0 \\ 0 & \widetilde{\varrho}_{2,2} & \widetilde{\varrho}_{2,3} & 0 \\ 0 & \widetilde{\varrho}_{3,2} & \widetilde{\varrho}_{3,3} & 0 \\ 0 & 0 & 0 & \widetilde{\varrho}_{4,4} \end{array} \right] , \tag{1.15}$$

with below expressions

$$
\begin{aligned}
\widetilde{\varrho}_{1,1}(\mu_r, \mu_{r+1}) &= \mathrm{e}^{-\beta\widetilde{\varepsilon}_{r1}}, \\
\widetilde{\varrho}_{2,2}(\mu_r, \mu_{r+1}) &= \mathrm{e}^{-\beta\widetilde{\varepsilon}_{r2}}\Sigma_+^2 + \mathrm{e}^{-\beta\widetilde{\varepsilon}_{r3}}\Sigma_-^2, \\
\widetilde{\varrho}_{2,3}(\mu_r, \mu_{r+1}) &= \widetilde{\varrho}_{3,2}(\mu_r, \mu_{r+1}) = \mathrm{e}^{-\beta\widetilde{\varepsilon}_{r2}}\Sigma_+\Gamma_+ + \mathrm{e}^{-\beta\widetilde{\varepsilon}_{r3}}\Sigma_-\Gamma_-, \\
\widetilde{\varrho}_{3,3}(\mu_r, \mu_{r+1}) &= \mathrm{e}^{-\beta\widetilde{\varepsilon}_{r2}}\Gamma_+^2 + \mathrm{e}^{-\beta\widetilde{\varepsilon}_{r3}}\Gamma_-^2, \\
\widetilde{\varrho}_{4,4}(\mu_r, \mu_{r+1}) &= \mathrm{e}^{-\beta\widetilde{\varepsilon}_{r4}}.
\end{aligned}
$$

Four coefficients $\Gamma_\pm$ and $\Sigma_\pm$ have already defined in Eq. (1.8).

1.2.3 The reduced density matrix of the impurity part

The reduced density matrix of the dimer impurity at thermal equilibrium can be expressed as

$$
\widetilde{\rho}(T) = \begin{bmatrix} \widetilde{\rho}_{11} & 0 & 0 & 0 \\ 0 & \widetilde{\rho}_{22} & \widetilde{\rho}_{23} & 0 \\ 0 & \widetilde{\rho}_{23} & \widetilde{\rho}_{33} & 0 \\ 0 & 0 & 0 & \widetilde{\rho}_{44} \end{bmatrix}, \tag{1.16}
$$

The components $\widetilde{\rho}_{k,l}$ can be identified by

$$
\widetilde{\rho}_{k,l} = \frac{1}{Z}\sum_{\{\mu\}} \boldsymbol{W}(\mu_1,\mu_2)...\boldsymbol{W}(\mu_{r-1},\mu_r)\widetilde{\varrho}_{k,l}(\mu_r,\mu_{r+1})\boldsymbol{W}(\mu_{r+1},\mu_{r+2})...\boldsymbol{W}(\mu_N,\mu_1). \tag{1.17}
$$

Performing the transfer-matrix technique results in deducing elements of $\widetilde{\rho}_{k,l}$ as

$$
\tilde{\rho}_{k,l} = \frac{1}{Z}\mathrm{Tr}\left(W^{r-1}\widetilde{P}_{k,l}W^{N-r}\right) = \frac{1}{Z}\mathrm{Tr}\left(\widetilde{P}_{k,l}W^{N-1}\right), \tag{1.18}
$$

where

$$
\widetilde{P}_{k,l} = \begin{bmatrix} \widetilde{\varrho}_{k,l}(\frac{1}{2},\frac{1}{2}) & \widetilde{\varrho}_{k,l}(\frac{1}{2},-\frac{1}{2}) \\ \widetilde{\varrho}_{k,l}(-\frac{1}{2},\frac{1}{2}) & \widetilde{\varrho}_{k,l}(-\frac{1}{2},-\frac{1}{2}) \end{bmatrix}, \tag{1.19}
$$

assuming $\widetilde{\varrho}_{k,l}(++) \equiv \widetilde{\varrho}_{k,l}(\frac{1}{2},\frac{1}{2})$, $\widetilde{\varrho}_{k,l}(+-) \equiv \widetilde{\varrho}_{k,l}(\frac{1}{2},-\frac{1}{2})$, $\widetilde{\varrho}_{k,l}(-+) \equiv \widetilde{\varrho}_{k,l}(-\frac{1}{2},\frac{1}{2})$, $\widetilde{\varrho}_{k,l}(--) \equiv \widetilde{\varrho}_{k,l}(-\frac{1}{2},-\frac{1}{2})$. Eventually, to derive the special components of the averaged reduced density matrix $\widetilde{\rho}_{k,l}$, we reproduce the unitary transformation operator U that diagonalizes the transfer matrix W. This operator is defined by

$$
U = \begin{bmatrix} \Lambda_+ - \boldsymbol{W}_{--} & \Lambda_- - \boldsymbol{W}_{--} \\ \boldsymbol{W}_{+-} & \boldsymbol{W}_{+-} \end{bmatrix}, \tag{1.20}
$$

where its inverse is written as

$$
U^{-1} = \begin{bmatrix} \frac{1}{Q} & -\frac{\Lambda_- - \boldsymbol{W}_{--}}{Q\boldsymbol{W}_{+-}} \\ -\frac{1}{Q} & \frac{\Lambda_+ - \boldsymbol{W}_{--}}{Q\boldsymbol{W}_{+-}} \end{bmatrix}. \tag{1.21}
$$

In result, the special components of the two-qubit density operator of the dimer impurity at site $i = r$ is given by

$$\widetilde{\rho}_{k,l} = \frac{\text{Tr}\left(U^{-1}\widetilde{P}_{k,l}U \begin{bmatrix} \Lambda_+^{N-1} & 0 \\ 0 & \Lambda_-^{N-1} \end{bmatrix}\right)}{Z} \ . \tag{1.22}$$

After calculating all elements $\widetilde{\rho}_{k,l}$, following relation will be achieved

$$\widetilde{\rho}_{k,l} = \frac{\mathcal{A}_{k,l} + \mathcal{B}_{k,l}}{\mathcal{M}} \ ,$$

where

$$\begin{aligned}
\mathcal{A}_{k,l} &= Q\left[\widetilde{\varrho}_{k,l}(++) + \widetilde{\varrho}_{k,l}(--)\right] + 4w_{+-}\widetilde{\varrho}_{k,l}(+-), \\
\mathcal{B}_{k,l} &= \left[\widetilde{\varrho}_{k,l}(++) - \widetilde{\varrho}_{k,l}(--)\right](w_{++} - w_{--}), \\
\mathcal{M} &= Q\left(\widetilde{w}_{++} + \widetilde{w}_{--}\right) + 4w_{+-}\widetilde{w}_{+-} + \\
&\quad + \left(\widetilde{w}_{++} - \widetilde{w}_{--}\right)(w_{++} - w_{--}) \ .
\end{aligned}$$

Quantum correlations, thermal entanglement, the l_1-norm of coherence $\mathcal{C}_{l_1}$, QFI and the average fidelity F_A for the impurity part of the model can be simply investigated using above achievements.

1.3 Quantum Correlations

In this part, we aim to discuss correlations between the magnetic ions of the dimer impurity $\text{Mn}^{2+}-\text{Cu}^{2+}$ as local bipartite quantum correlations. Due to commutation relation $[H, \sum_{i=1}^{N} S_i^z] = 0$ and the translation invariance, the two point spin-spin correlation functions corresponding to the $\{x, z\}$−axes can be characterized in terms of the reduced density operator elements [106].

1.3.1 Thermal entanglement

The reduced density matrix $\widetilde{\rho}_{k,l}$ provides all information about the bipartite entanglement. A good measure of the thermal entanglement of impurity part is provided by the concurrence $\mathcal{C}$ as [107]

$$\mathcal{C} = \max\{0, \lambda_1 - \lambda_2 - \lambda_3 - \lambda_4\}, \tag{1.23}$$

where λ_i $(i = 1, 2, 3, 4)$ are the square root of the eigenvalues of the matrix $R = \rho(\sigma^y \otimes \sigma^y)\rho^*$ $(\sigma^y \otimes \sigma^y)$ in descending order (σ^y is the Pauli matrix in the y−direction).

For the system in thermal equilibrium with density matrix in the X-form (1.16) the concurrence is given by

$$\mathcal{C}(\widetilde{\rho}) = 2\max\{|\widetilde{\rho}_{2,3}| - \sqrt{\widetilde{\rho}_{1,1}\widetilde{\rho}_{4,4}}, 0\} \ .$$
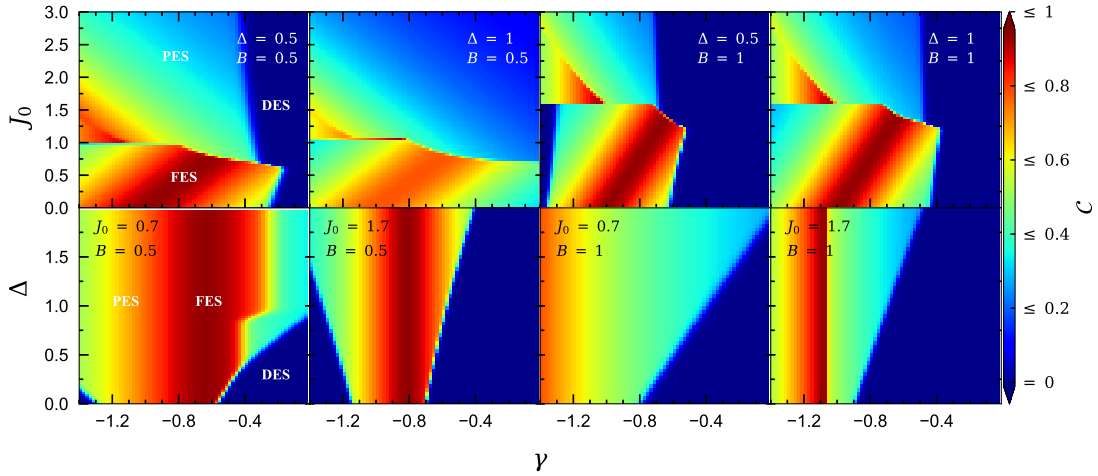
FIGURE 1.2: Panels of upper row illustrate the concurrence $\mathcal{C}$ in the $(\gamma - J_0)$ plane at low temperature $T = 0.02$, where for each of exchange anisotropy and magnetic field parameters two values $\Delta = \{0.5, 1\}$ and $B = \{0.5, 1\}$ are considered. Panels in lower row depict the concurrence in the $(\gamma - \Delta)$ plane such that $J_0 = \{0.7, 1.7\}$ and $B = \{0.5, 1\}$ are assumed.

Next, we examine the influences of the magnetic impurity embedded in the model under consideration on the thermal entanglement of the Heisenberg dimer at site $i = r$, on the quantum coherence, on the QFI, further on the quantum teleportation.

In plots correspond to the concurrence, l_1-norm of coherence and average fidelity, solid lines show information about the original model (without impurity), whereas dashed lines indicate information for the model consisting of a static dimer impurity with $\gamma = -0.8$. In all forthcoming figures, we consider the specific values of the gyromagnetic factors $g_1 = 1.2$, $g_2 = 5$, $g_3 = 1.1$ associated to the magnetic ions Fe^{3+}, Mn^{2+} and Cu^{2+}, respectively. Besides, in our numerical computations the Heisenberg coupling will be selected as the energy unit, i.e., $|J| = 1$.

In Fig. 1.2 (upper panels) we plot the concurrence $\mathcal{C}$ in the $(J_0 - \gamma)$ plane for two different values of B and Δ at finite low-temperature $T = 0.02$. In this figure, three different phases: disentangled state (DES), fully entangled state (FES) with an oblique band region, and partially entangled state (PES) are observable (see first panel). By tuning the both parameters B and Δ, phase boundaries undergo substantial changes. Similar to this, in lower row panels, we depict finite low-temperature Δ-dependence of the concurrence versus the impurity parameter γ for two different values of B and J_0. It could be understood that at a specific rage of γ there is a fully entangled state band which is independent of the anisotropy Δ. Increasing exchange coupling J_0 leads to strength the DES regime and to limit FES boundary.

To understand the anisotropy dependence of the threshold temperature at which the entanglement vanishes, we have plotted in Fig. 1.3 the density plot of the concurrence in the $\Delta - T$ plane such that the threshold temperature behavior versus Δ is engraved by dashed line in each panel. Plots in upper row present the concurrence for the original model ($\gamma = 0$), while lower
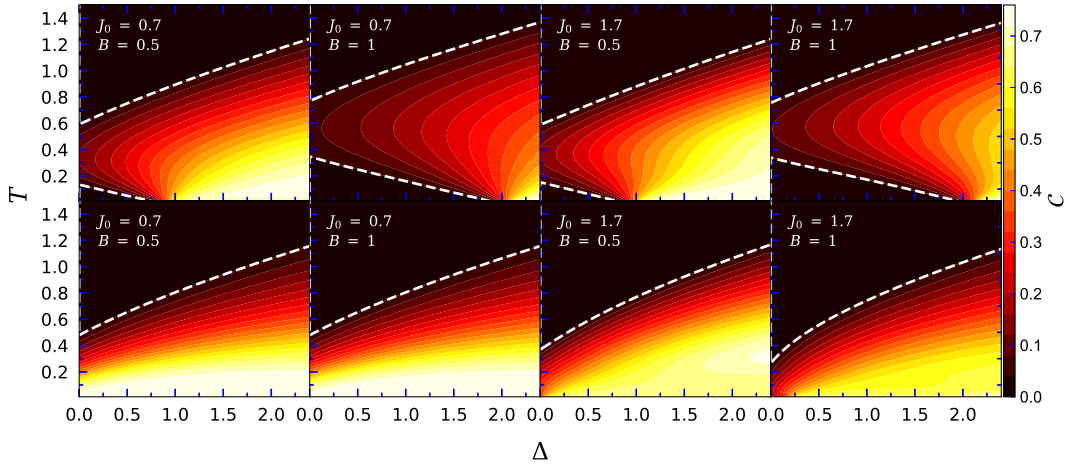
FIGURE 1.3: The density plot of the concurrence in the $(\Delta - T)$ plane, where exchange coupling J_0 and magnetic field B have been substitutionally taken up as $J_0 = \{0.7, 1.7\}$ and $B = \{0.5, 1\}$. Panels plotted in upper row represent the concurrence for the original model without impurity $(\gamma = 0)$, whereas plots in lower row show the concurrence for the model with magnetic impurity $(\gamma = -0.8)$ at site $i = r$. Dashed lines demonstrate the threshold temperature (at which the entanglement death occurs) against the anisotropy Δ.

row panels represent the same term but for the model with a magnetic impurity, supposing $\gamma = -0.8$. For the original mode, one sees there are two threshold temperature points which shifts toward higher temperatures upon increasing both of B and J_0. Besides, the entanglement death happens for higher anisotropies (see second and fourth panels). But on the other hand, for the case when the model involves with a magnetic impurity at site $i = r$ there is a single threshold temperature for each value of exchange anisotropy Δ, revealing the model with a magnetic impurity does not show re-entrant threshold temperature phenomenon. Regarding above findings, in Fig. 1.4 is shown the concurrence $\mathcal{C}$ as a function of magnetic field B for three different temperatures $T = 0.01$ (red lines), $T = 0.05$ (blue lines) and $T = 0.2$ (black lines), where J_0 and Δ have been considered to be tuneable terms. From left to right the figure shows the concurrence versus magnetic field when all parameters set to be fixed values except J_0. From up to down is considered all parameters as fixed values except Δ. As reported in previous work, at finite low temperature and low magnetic field the state of $Mn^{2+} - Cu^{2+}$ without magnetic impurity is partially entangled. With increase of the temperature the concurrence remarkably decreases. By embedding a magnetic impurity to the site r, we see a significant change in concurrence behavior. Surprisingly, the concurrence of the dimer impurity is alive for higher magnetic field while for the original model it vanishes. When the anisotropy Δ increases, the concurrence increases and reaches its maximum value $\mathcal{C} = 1$ at a special point on the magnetic field axis. With increase of the exchange coupling J_0, the concurrence increases for the both considered modes with and without magnetic impurity. But, the influence of J_0 on the impurity case is much more sensible than without impurity mode. Meanwhile, the sharp maximum of the concurrence curve changes to a dome-shaped maximum, revealing the fact that the entanglement
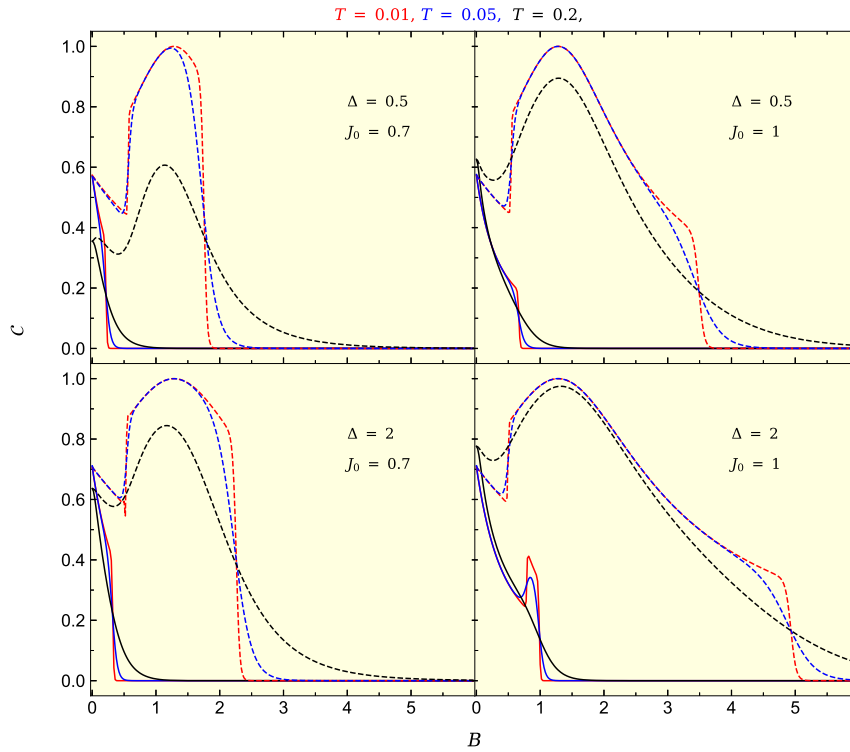
FIGURE 1.4: The concurrence $\mathcal{C}$ as a function of the magnetic field B, assuming three different temperatures $T = 0.01$ (red lines), $T = 0.05$ (blue lines) and $T = 0.2$ (black lines) and impurity parameter $\gamma = -0.8$. g-factors have been taken as $g_1 = 1.2$, $g_2 = 5$, $g_3 = 1.1$. Totally, we consider two different values of $\Delta = \{0.5, 2\}$, increasing from up to down panels, and $J_0 = \{0.7, 1\}$, increasing from left to right panels.

death occurs for the remarkably higher magnetic fields.

The most interesting finding from this special consideration is that, when the model is putted in an external uniform magnetic field (the system without the impurity), the state of the Heisenberg dimers does not reach maximum entanglement ($\mathcal{C} = 1$) even for low magnetic fields. When the model possesses an impurity the situation completely changes (dashed lines plotted in Fig. 1.4), namely, by increasing the magnetic field the concurrence in the magnetic dimer with an impurity $\gamma = -0.8$ goes to become maximally entangled. Surprisingly, the state of the model becomes maximally entangled at low temperature and critical magnetic field $B_{max} = 1.282$. With further increase of the magnetic field the concurrence decreases and the state of the model with impurity losses its maximum entanglement property. Another notable remark from this figure is that, for the case when the model does not encompass the impurity, the threshold magnetic field at which the concurrence vanishes, moves toward higher values as the both of parameters Δ and J_0 increase monotonically.

In Fig. 1.5 is illustrated the temperature dependence of concurrence $\mathcal{C}$ for several values of the magnetic field, where parameters Δ and J_0 are again assumed to be tuneable terms. In this case, we see that by inducing a magnetic impurity to the Ising-Heisenberg heterotrimetallic chain, the concurrence substantially increases at low temperatures. For the original model, the concurrence
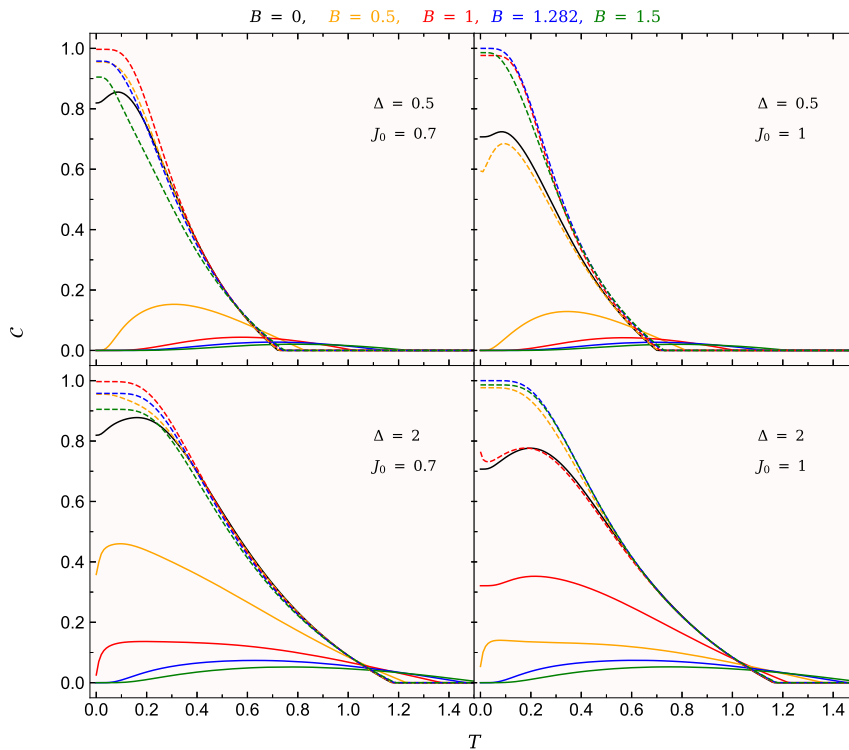
FIGURE 1.5: The concurrence $\mathcal{C}$ as a function of temperature T, for several fixed values of the magnetic field, assuming the same set of other parameters to Fig. 1.4.

does not reach maximally entangled state even for the low magnetic fields. It is quite clear that for the dimer impurity at low magnetic fields, the concurrence reaches its maximum $\mathcal{C} = 1$ as the temperature decreases. Increasing both parameters Δ and J_0 results in reaching maximum value of the concurrence at higher temperatures and higher magnetic fields (trace for example evolution of the dashed red lines and dashed blue lines in all panels). Another unconventional phenomenon that is visible from this figure is that, for the original model the threshold temperature at which the concurrence vanishes is strongly dependent on the magnetic field, while for the embedded impurity model the threshold temperature is almost a fixed constant when the magnetic field changes.

1.3.2 Quantum Coherence

To quantify the quantum coherence in a spin system a trace-distance measure of coherence is adopted. Naturally, we take up the l_1-norm of coherence that could be defined as

$$\mathcal{C}_{l_1}(\rho) = \sum_{i \neq j} |\langle i|\rho|j\rangle|.$$

Above equation means that the l_1-norm of coherence is given by the sum of absolute values of all off-diagonal elements in the density matrix ρ. We plot in Figs. 1.6 (a)-(d) l_1-norm $\mathcal{C}_{l_1}$ as a
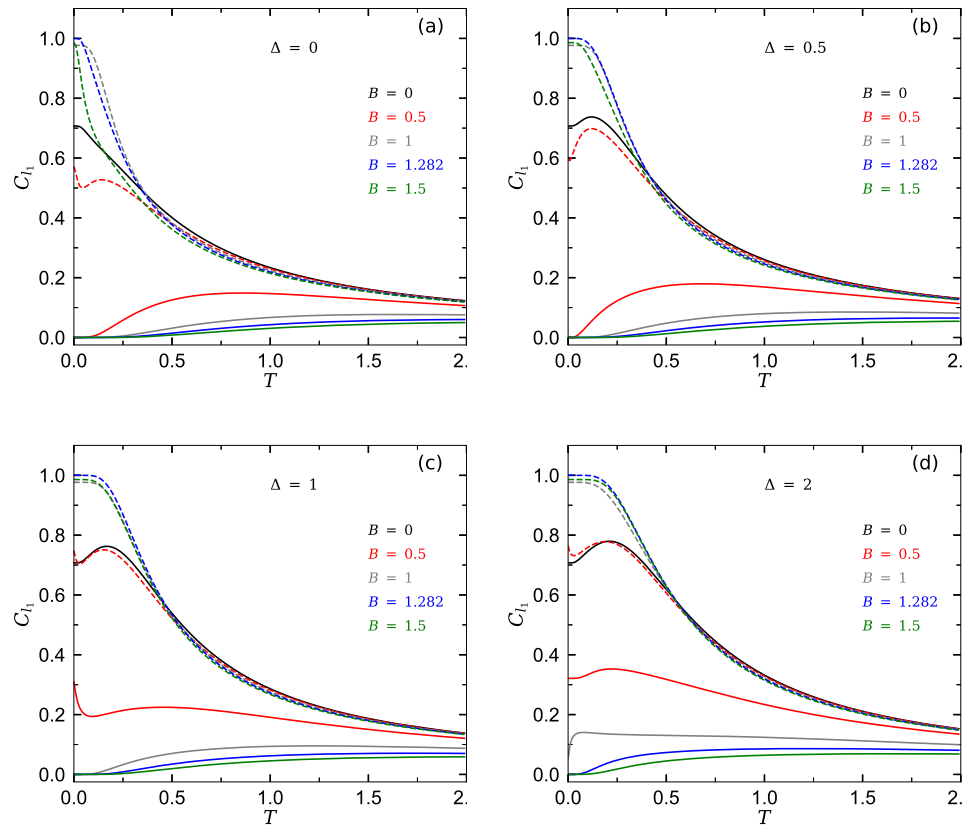
FIGURE 1.6: The quantum coherence $\mathcal{C}_{l_1}$ as a function of temperature T for several fixed values of the magnetic field and parameter set (a) $\Delta = 0$, (b) $\Delta = 0.5$, (c) $\Delta = 1$, (d) $\Delta = 2$, assuming fixed $J_0 = 1$ and the same set of other parameters to Fig. 1.4.

function of the temperature for the same fixed magnetic fields to Fig. 1.5, where $J_0 = 1$ has been optionally hypothesized. An interesting result obtained for the quantum property of the model is belong to our finding for the temperature dependence of $\mathcal{C}_{l_1}$. In Fig. 1.6 (a) is displayed the l_1-norm of coherence $\mathcal{C}_{l_1}$ versus temperature for the parameter set $\Delta = 0$ and $J_0 = 1$, where several fixed values of the magnetic field have been selected. At low-temperature region, l_1-norm behavior against the temperature T for the case when the model has a magnetic impurity is completely different from the original model. To clarify this point, under the cooling, norm $\mathcal{C}_{l_1}$ of the original model gradually decreases and eventually vanishes at a critical temperature (solid lines), demonstrating the system state becomes decoherence. While its curve intrinsically has a steep increase when an impurity induces to the model (see dashed lines). For the later, l_1-norm reaches its maximum $\mathcal{C}_{l_1} = 1$ at very low temperatures and threshold magnetic field $B = 1.282$ (blue dashed line). With increase of the anisotropy Δ, the low-temperature behavior of $\mathcal{C}_{l_1}$ undergoes substantial changes. For example, for the original model, when anisotropic XXZ interaction is considered for the dimers ($\Delta > 0$), the critical temperature at which $\mathcal{C}_{l_1}$ becomes zero shifts toward lower values (see panel Fig. 1.6 (b)). When the anisotropy increases further, under cooling the norm $\mathcal{C}_{l_1}$ not only does not decreases but also increases monotonically (see

Figs. 1.6 (c) and (d)). For the model with impurity, as Δ increases, quantum coherence $\mathcal{C}_{l_1}$ reaches its maximum value at higher temperatures (see blue dashed line plotted in Fig. 1.6 (d)).

1.3.3 Quantum Fisher Information (QFI)

Now, let us verify QFI (a useful tool for parameter estimation of quantum probability distributions) and its first magnetic field derivative for the Ising-Heisenberg spin chain of the heterotrimetallic coordination compound $Fe - Mn - Cu$ including magnetic impurity, and compare the QFI behavior with that of for the original model (without impurity). In general phase estimation scenarios, the evolution of a quantum state, given by the reduced two-spin density matrix $\tilde{\rho}$ in Eq. (1.16) with special components $\tilde{\rho}_{k,l}$, under a unitary transformation can be described as $\tilde{\rho}(\theta) = \exp[-i\mathcal{A}\theta]\tilde{\rho}\exp[i\mathcal{A}\theta]$, where θ is the phase shift and $\mathcal{A}$ is an operator. The estimation accuracy for θ is limited by the quantum Cramér-Rao inequality $\Delta\hat{\theta} \geq \frac{1}{\sqrt{\nu\mathcal{F}(\tilde{\rho}_\theta)}}$. where $\hat{\theta}$ expresses the unbiased estimator for θ, and ν is the number of times the measurement is repeated. Accordingly, the term $\mathcal{F}(\tilde{\rho}_\theta)$ characterizes the QFI, and is defined by [108, 109]

$$\mathcal{F}(\tilde{\rho}, \mathcal{A}) = 2 \sum_{i,j=1}^{4} \frac{(\tau_i - \tau_j)^2}{\tau_i + \tau_j} \mid \langle \chi_i \mid \mathcal{A} \mid \chi_j \rangle \mid^2, \tag{1.24}$$

where $|\chi_i\rangle$ and τ_i are, respectively, the eigenvectors and their corresponding eigenvalues of the density matrix $\tilde{\rho}$, and are utilized as the gauge states of estimation parameter θ. Since, we are going to examine the QFI for a typical Heisenberg dimer $Mn^{2+} - Cu^{2+}$, along side of the density matrix $\tilde{\rho}$, we have to apply arbitrary complete sets of local orthonormal observables $\{\mathcal{A}_\eta\}$ and $\{\mathcal{B}_\eta\}$ associated to the both of subsystems Mn^{2+} and Cu^{2+}, respectively. Correspondingly, the QFI for a general bipartite spin-1/2 system reads [110]

$$\mathcal{F} = \sum_{\eta} \mathcal{F}(\tilde{\rho}, \mathcal{A}_\eta \otimes I + I \otimes \mathcal{B}_\eta). \tag{1.25}$$

In above, the local orthonormal observables $\{\mathcal{A}_\eta\}$ and $\{\mathcal{B}_\eta\}$ can be written as

$$\{\mathcal{A}_\eta\} = \{\mathcal{B}_\eta\} = \sqrt{2}\{I, \; S^x, \; S^y, \; S^z\}, \tag{1.26}$$

which I is identity 2×2 matrix. Putting this equation in Eq. (1.24), QFI $\mathcal{F}$ can be eventually evaluated.

Figures 1.7(a) and 1.7(b) illustrate the QFI of the original model ($\gamma = 0$) for various fixed values of Δ and two selected values of exchange interaction $J_0 = 0.7$ and $J_0 = 1$, respectively. It is observable that $\mathcal{F}$ increases monotonically upon increase of the magnetic field, then reaches an intermediate minimum. The magnetic position of this minimum depends on the exchange anisotropy Δ. In other words, by increasing Δ, the mentioned minimum appears at higher magnetic fields. For all of considered Δ there is a steep increase of the QFI in a special magnetic
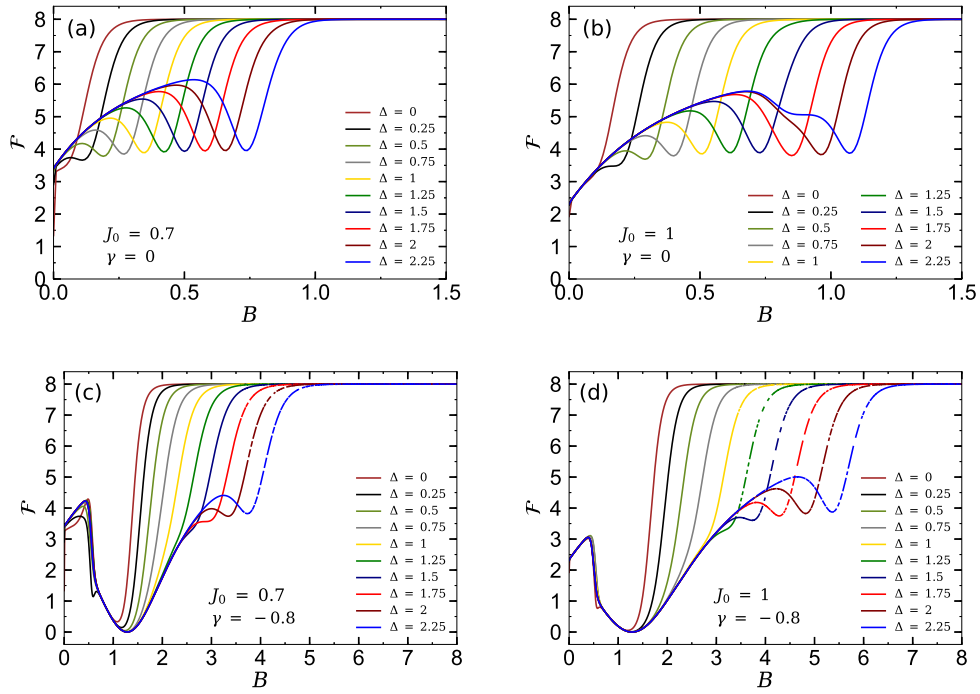
FIGURE 1.7: The QFI as a function of magnetic field B for several fixed values of the anisotropic parameter Δ. (a) and (b) correspond to the original model in the absence of impurity ($\gamma = 0$), assuming $J_0 = 0.7$ and $J_0 = 1$, respectively. (c) and (d) show QFI of the model with magnetic impurity, $\gamma = -0.8$, assuming $J_0 = 0.7$ and $J_0 = 1$, respectively. In all panels we considered low temperature $T = 0.05$. We fixed other parameters as in Fig. 1.4. We note that here and in the next figure, the discontinuity in lines related to the high exchange anisotropy $\Delta > 1$ and high magnetic fields happens for the sake of we calculated the QFI numerically and does not result in losing the accuracy of the subject.

field interval. This function ultimately reaches its maximum value at sufficiently high magnetic fields. By inspecting Fig. 1.7(b) one sees that as the Ising coupling constant J_0 increases, the magnetic position of the produced minimum shifts towards higher magnetic fields. Moreover, for high values of the Δ there are two intermediate minima (see blue line).

One of the most interesting and novel results for the Ising-Heisenberg spin chain of the heterotrimetallic coordination compound $Fe - Mn - Cu$ with magnetic impurity is crystal clear in Figs. 1.7(c) and 1.7(d). We see that the QFI behavior is significantly different from the original case. In fact, by inducing a magnetic impurity into the model, the QFI increases with increase of the magnetic field till reaches a typical maximum at very low magnetic fields. Then sharply drops down at critical magnetic field $B_c \approx 0.5$. Surprisingly, the QFI reaches its minimum value $\mathcal{F} = 0$ at the critical magnetic field $B_c = 1.282$. We remind that at this critical magnetic field the concurrence becomes maximum (review Fig. 1.4). With further increase of the magnetic field, QFI shows a steep increase, reaching its maximum value for the exchange anisotropy range $\Delta \lesssim 1$. For the range $\Delta > 1$, the QFI makes an intermediate minimum at high magnetic fields afterwards reaches its maximum. Comparing panel 1.7(b) with 1.7(a) corroborates that increase
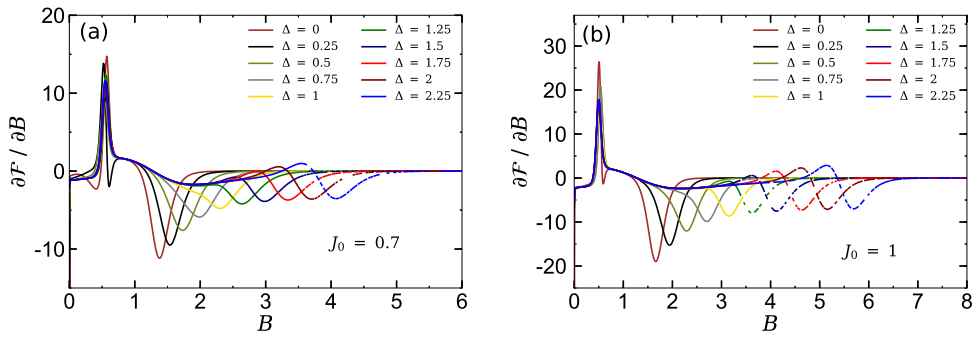
FIGURE 1.8:   The first magnetic field derivative of the QFI of the model with impurity ($\gamma = -0.8$) against the magnetic field for several fixed values of Δ. (a) $J_0 = 0.7$ and (b) $J_0 = 1$. In both panels we supposed low temperature $T = 0.05$ for the model. Other parameters have been taken as in Fig. 1.4.

of the Ising nodal exchange interaction J_0 entails the QFI reaches its maximum at remarkably higher magnetic fields.

The first magnetic field derivative of the QFI of the model with impurity as a function of the magnetic field has been displayed in Figs. 1.8(a) and 1.8(b), assuming fixed $J_0 = 0.7$ and $J_0 = 1$, respectively. The QFI shows a sharp pick at critical magnetic field $B_c \approx 0.5$. According to the expressions in Ref. [111], one can observe that regardless of the value J_0 a quantum phase transition happens at $B_c \approx 0.5$.

1.4   Quantum teleportation

In this section, we study the quantum teleportation by means of an entangled mixed state as resource. We remind that a mixed entangled state is a state of a bi- or multi-partite system consisting of two or more subsystems which can be decomposed into (a convex combination of) other states, but cannot be produced by local operations and classical communication. Particularly, an entangled mixed state is always a mixed state, but a mixed state may be an entangled mixed state, a separable mixed state, or even a mixed state of a system that does not consist of several subsystems, so that the terms "separable" and "entangled" don't even make sense for that system. The standard teleportation can be regarded as a general depolarizing channel [112] and we investigate the influence of the magnetic impurity of the Ising-Heisenberg spin chain of the heterotrimetallic coordination compound $Fe - Mn - Cu$ on the teleportation. We suppose the input state that would be teleported has the form

$$|\psi_{in}\rangle = \cos\left(\frac{\theta}{2}\right)|10\rangle + e^{i\phi}\sin\left(\frac{\theta}{2}\right)|01\rangle \,, \tag{1.27}$$

where $0 \leq \theta \leq \pi$ and $0 \leq \phi \leq 2\pi$. Here θ describe all states with different amplitudes and ϕ are phase of these states, and in the density operator formalism, the state input is $\rho_{in} = |\psi_{in}\rangle\langle\psi_{in}|$.

The concurrence $\mathcal{C}_{in}$ of the input state can be written as

$$\mathcal{C}_{in} = 2 \left| e^{i\phi} \sin\left(\frac{\theta}{2}\right) \cos\left(\frac{\theta}{2}\right) \right| = |\sin(\theta)|. \tag{1.28}$$

When a two-qubit state ρ_{in} (as depicted in Fig. 1.9) is teleported via the mixed channel $\widetilde{\rho}_{ch}$ of the two independent Ising-Heisenberg spin chain of the heterotrimetallic coordination compound $Fe - Mn - Cu$, the output state $\widetilde{\rho}_{out}$ is given by

$$\widetilde{\rho}_{out} = \sum_{i,j=\{0,1,2,3\}} p_i p_j \left(\sigma_i \otimes \sigma_j\right) \rho_{in} \left(\sigma_i \otimes \sigma_j\right) ,$$

where $\sigma^0 = I$, $\sigma^1 = \sigma^x$, $\sigma^2 = \sigma^y$ and $\sigma^3 = \sigma^z$ are Pauli matrices. $p_i = tr\left[E^i \widetilde{\rho}_{ch}\right]$, $E^0 = |\Psi^-\rangle\langle\Psi^-|$, $E^1 = |\Phi^-\rangle\langle\Phi^-|$, $E^2 = |\Phi^+\rangle\langle\Phi^+|$, $E^3 = |\Psi^+\rangle\langle\Psi^+|$, for which $\{|\Psi^\pm\rangle, |\Phi^\pm\rangle\}$ denote the Bell states. Here, we consider the density operator channel as $\widetilde{\rho}_{out} \equiv \widetilde{\rho}(T)$.

Therefore, we can write the output state as

$$\widetilde{\rho}_{out} = \begin{bmatrix} c & 0 & 0 & 0 \\ 0 & f & \kappa & 0 \\ 0 & \kappa & g & 0 \\ 0 & 0 & 0 & c \end{bmatrix} , \tag{1.29}$$

where

$$
\begin{aligned}
c &= \left(\widetilde{\rho}_{2,2} + \widetilde{\rho}_{3,3}\right)\left(\widetilde{\rho}_{1,1} + \widetilde{\rho}_{4,4}\right), \\
f &= \left(\widetilde{\rho}_{1,1} + \widetilde{\rho}_{4,4}\right)^2 \cos^2\left(\tfrac{\theta}{2}\right) + \left(\widetilde{\rho}_{2,2} + \widetilde{\rho}_{3,3}\right)^2 \sin^2\left(\tfrac{\theta}{2}\right), \\
g &= \left(\widetilde{\rho}_{2,2} + \widetilde{\rho}_{3,3}\right)^2 \cos^2\left(\tfrac{\theta}{2}\right) + \left(\widetilde{\rho}_{1,1} + \widetilde{\rho}_{4,4}\right)^2 \sin^2\left(\tfrac{\theta}{2}\right), \\
\kappa &= 2 e^{i\phi} \widetilde{\rho}_{2,3}^2 \sin\theta.
\end{aligned}
$$

To get a better understanding of the quantum teleportation and average fidelity, let us first describe the thermal entanglement of the output state $\mathcal{C}_{out}$. Using Eq. (1.29) in the definition of concurrence (1.23), we obtain the output concurrence $\mathcal{C}_{out}$ defined by

$$\mathcal{C}_{out} = 2 \max\left\{ 2\widetilde{\rho}_{2,3}^2 \mathcal{C}_{in} - |\widetilde{\rho}_{2,2} + \widetilde{\rho}_{3,3}||\widetilde{\rho}_{1,1} + \widetilde{\rho}_{4,4}|, 0 \right\}.$$

In the following subsection, we analyze the quality of the process of the teleportation.
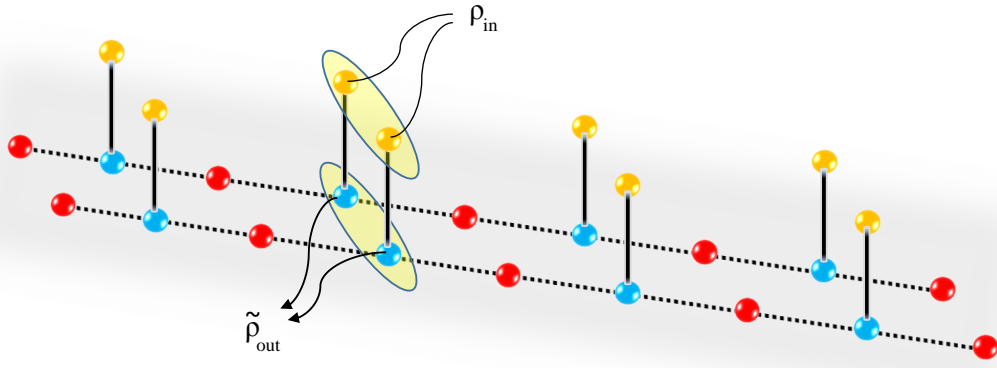
FIGURE 1.9: The schematic representation for the teleportation of the input state ρ_{in} through a couple of independent quantum channels (ρ_{ch}). The teleported output state is denoted by $\widetilde{\rho}_{out}$.

1.4.1 Average fidelity of teleportation

In this section, we turn our attention to the quality of the process of teleportation. The fidelity between ρ_{in} and ρ_{out} characterizes the quality of the teleported state. The fidelity is defined by

$$F = \langle \psi_{in}|\rho_{out}|\psi_{in} \rangle .$$

After some straightforward algebra, the fidelity can be described as

$$F = \frac{\sin^2 \theta}{2} \left[(\widetilde{\rho}_{1,1} + \widetilde{\rho}_{4,4})^2 + 4\widetilde{\rho}_{2,3}^2 - (\widetilde{\rho}_{2,2} + \widetilde{\rho}_{3,3})^2 \right] + (\widetilde{\rho}_{2,2} + \widetilde{\rho}_{3,3})^2 . \tag{1.30}$$

When the input state is a pure state, the efficiency of quantum communication is characterized by average fidelity. We can calculate the average fidelity as

$$F_A = \frac{1}{4\pi} \int\limits_0^{2\pi} d\phi \int\limits_0^{\pi} F \sin\theta d\theta .$$

For the model described here, the average fidelity F_A can be given by

$$F_A = \frac{1}{3} \left[(\widetilde{\rho}_{1,1} + \widetilde{\rho}_{4,4})^2 + 4\widetilde{\rho}_{2,3}^2 - (\widetilde{\rho}_{2,2} + \widetilde{\rho}_{3,3})^2 \right] + (\widetilde{\rho}_{2,2} + \widetilde{\rho}_{3,3})^2 . \tag{1.31}$$

To transmit the input state better than any classical communication protocol, F_A must be greater than $\frac{2}{3}$ which is the best fidelity in the classical world. In Fig. 1.10(a) we show the behavior of average fidelity F_A in terms of temperature T for several fixed values of the magnetic field, assuming $J_0 = 1$ and $\Delta = 0.5$ and impurity parameter $\gamma = -0.8$. The horizontal dashed lines at $F_A = 2/3$ denote the limit of quantum fidelities. In Fig. 1.10(a), we can see that for this choice of parameters the only possibility of teleportation of information happens for null
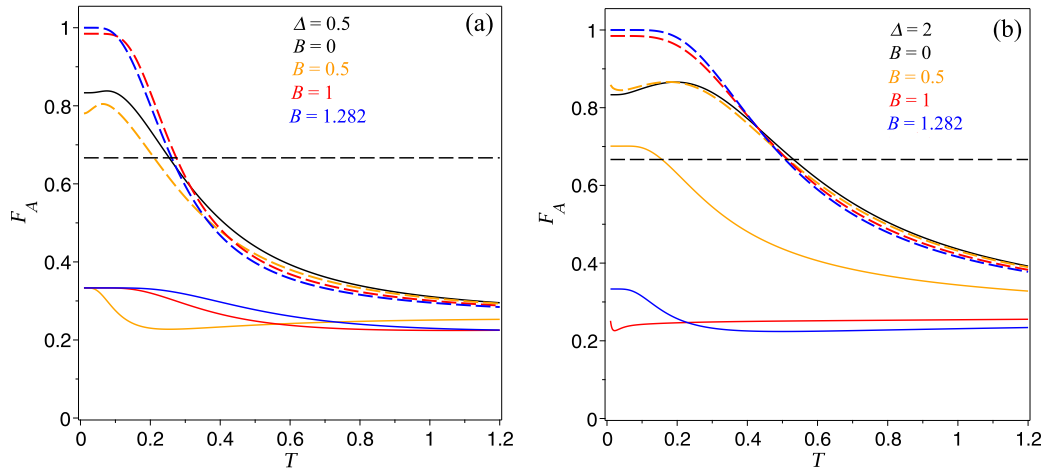
FIGURE 1.10: The average fidelity F_A as a function of temperature T for several fixed values of the magnetic field and parameter set (a) $\Delta = 0.5$, (b) $\Delta = 1$, assuming fixed $J_0 = 1$ and impurity parameter $\gamma = -0.8$.

magnetic field in the original model. Meanwhile, when we insert magnetic impurity, we have a considerable improvement in quantum teleportation. It is quite noteworthy that for the critical point $B_{max} = 1.282$ the average fidelity becomes maximal at sufficiently low temperatures. It can be seen that average fidelity is above 2/3 for our model with magnetic impurity in contrast to the original model where it is not possible to teleport information.

In Fig. 1.10(b) is depicted the temperature dependence of the average fidelity for $\Delta = 2$. For this choice of anisotropy parameter, the original model allows teleportation for weak magnetic fields and lower temperatures. For example, for $B = 0.5$ (see orange solid curve), as soon as the temperature increases, the average fidelity falls down below 2/3, signaling the impossibility of teleportation. On the other hand, the fidelity behavior is significantly different for the case when a magnetic impurity is embedded. Our results show major improvement in the average fidelity that can be achieved by tuning the strength of the magnetic impurity. In conclusion, we can take up the way of inducing magnetic impurities as a creative technique to manipulate and to enhance the teleportation processing.

Finally, in Fig. 1.11, the average fidelity F_A is plotted as a function of magnetic field B for three selected temperatures $T = 0.1$, $T = 0.6$ and $T = 1$ and $\gamma = -0.8$. In panels of this figure, solid lines describe the average fidelity of the original model recently investigated by Y. -D. Zheng *et al.* [104]. In Fig. 1.11(a), we fixed $J_0 = 4$, and $\Delta = 0.5$. As can be seen, the average fidelity remains above 2/3 for weak magnetic fields in the original model. When the impurity is induced in the model, in contrast to the original case, the behavior of the average fidelity becomes more robust, enabling teleportation of information in the regions of very strong magnetic fields.

Analogously, Fig. 1.11(b) illustrates the average fidelity F_A for the case $J_0 = 2$, and $\Delta = 1$. Under this condition, one can immediately have two stimulating observations when the original model is considered. First, the average fidelity sharply decreases upon increasing the magnetic
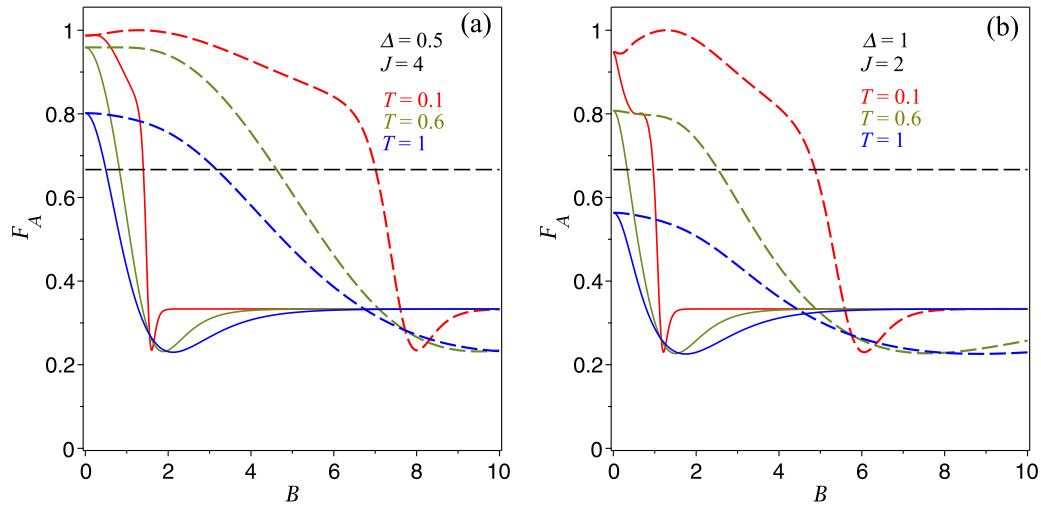
FIGURE 1.11: The average fidelity F_A as a function of magnetic field B for several fixed values of the temperature and parameter set (a) $J_0 = 4$, $\Delta = 0.5$, and (b) $J_0 = 2$, $\Delta = 1$, assuming impurity parameter $\gamma = -0.8$.

field. Secondly, the teleportation of information is only possible for weak magnetic fields. However, by assuming the inclusion of the magnetic impurity (dashed curves), we have a dramatic enhancement of the average fidelity F_A. In particular, for the low-temperature regime (i.e., $T = 0.1$), the inclusion of magnetic impurity generates an increase in the average fidelity until reaching maximum fidelity ($F_A = 1$). Then, this function decreases monotonically as the magnetic field increases further. However, for the higher temperature ($T = 1$), the average fidelity remains below 2/3, making it impossible the existence of the quantum teleportation of information. All of these findings show again that a considerable enhancement of the teleportation of information can be achieved by tuning the strength of the magnetic impurity for the Ising-Heisenberg spin chain of the heterotrimetallic coordination compound $Fe - Mn - Cu$.

1.5   Conclusions

In this chapter we have studied the influences of a typical magnetic impurity on the quantum properties of the Ising-Heisenberg spin-1/2 chain of the heterotrimetallic coordination compound $Fe - Mn - Cu$. The magnetic impurity has been considered on a local Heisenberg dimer of the chain. Next, we have exactly solved the model within the transfer-matrix formalism and paid our attention to the study the thermal pairwise entanglement and l_1-norm of the coherence as measures of the quantum correlation of the impurity dimer. One of our notable results is that the thermal pairwise entanglement can be controlled and tuned by imposing a magnetic impurity into the model.

By verifying the QFI of the model we understood that the inclusion of the magnetic impurity substantially affects on the behavior of this function. Furthermore, QFI presented anomalous

behavior nearby the critical magnetic fields $B_c \approx 0.5$ and $B_c = 1.282$. Based on the investigations carried out in this chapter, we proved that QFI can be considered as a useful quantum tool for estimating the quantum phase transition of the Ising-Heisenberg spin-1/2 chain of the heterotrimetallic coordination compound $Fe - Mn - Cu$.

The teleportation scenario for the two-qubits in a typical quantum state has been also discussed through a couple of quantum channel including a Heisenberg dimer with magnetic impurity. Each of channels has been assumed to be constructed by an infinite Ising-Heisenberg spin-1/2 chain of heterotrimetallic coordination compound $Fe - Mn - Cu$. We have demonstrated that at low-temperature regime, the inclusion of magnetic impurity leads to remarkable enhancement in the average fidelity until reaching maximum value. Based on our findings regarding the model with magnetic impurity, we claimed that the average fidelity becomes more robust compared with the original model, enabling teleportation of information in the regions of very strong magnetic fields.

Chapter 2

Ising-Heisenberg ladders

2.1 Preliminaries

The both spin-1/2 and mixed-spin (1/2,1) double saw-tooth Ising-Heisenberg ladders have been considered in Refs. [113, 114, 115]. These ladders can be constructed from the two parallel so-called saw-tooth chains (or delta chains) or by the decorating the square two-leg ladder (See Fig. 2.1). The Ising-Heisenberg variant of the saw-tooth chain has been considered earlier in Ref. [17, 18, 20], however, there the quantum cluster was the two-spin bond along each second tooth of the chain. In the double saw-tooth ladder the quantum spin clusters are the bond, connecting each tip of the teeth. In Refs. [113, 114, 115] the exact solution of the model within the modified classical transfer-matrix technique have been obtained. The ground state phase diagrams, magnetization curves and the quantum entanglement properties have been also considered for the spin-1/2 double saw-tooth Ising-Heisenberg ladder.

MCE can be defined as the temperature variation of magnetic materials upon changing the external magnetic field. In many-body problem, MCE has attracted much attention because of having a strong potential of cooling applications in material science and technology [116, 117, 118, 119]. An important application of the MCE is the study of phase transitions by using the magnetocaloric anomalies at the magnetic phase transitions [120, 121]. To demonstrate MCE the standard quantity, the so-called Grüneisen parameter Γ_B (named after Eduard Grüneisen), is coming out which can be counted as one of applicable tools for detecting quantum critical points [122]. The Grüneisen parameter of magnetic systems under adiabatic conditions can be identified by

$$\Gamma_B = \frac{1}{T}\left(\frac{\partial T}{\partial B}\right)_S = -\frac{T}{C_B}\left(\frac{\partial S}{\partial B}\right)_T = -\frac{1}{C_B}\left(\frac{\partial M}{\partial T}\right)_B, \tag{2.1}$$

where C_B is the heat capacity at the constant magnetic field, T is the temperature (for simplicity we consider $k_B = 1$) and B is the applied magnetic field. In the recent decades a series of theoretical and computational researches have been conducted on the magnetic properties and MCE

in low-dimensional quantum and Ising spin models [67, 123, 124, 125, 126, 127, 128, 129, 131, 132, 133, 134, 135, 136, 137, 138, 139, 140, 141, 142, 143]. The exact results obtained within the low-dimensional quantum and mixed classical-quantum interacting spin models figure out many important features of the MCE nearby the quantum critical points, particularly the enhancing role of frustration and residual entropy, the possibility of magnetic cooling and magnetic heating during the adiabatic demagnetization, deep connection of the MCE and the ground-state phase transitions, etc. Besides, by examining the behavior of adiabatic cooling rate, important information about the MCE can be obtained from the plots of the isentropes in the temperature-magnetic field plane. During the current decade, a number of exact results on the MCE in the Ising-Heisenberg one-dimensional spin models have been obtained [133, 134, 135, 136, 137, 138].

The four-spin Ising interaction can be identified as the Ising limit of the cyclic permutation of the quantum spins localized on the vertices of a plaquette. It was demonstrated that this particular term is important to realize the magnetic properties of the solid He^3 [144], as well as in some cuprates Ref. [145]. The Ising-Heisenberg spin models with additional four-spin Ising interaction have been also examined in several papers as an Ising limit of the four-spin cyclic permutation [128, 146, 147, 148, 149, 150, 151].

In this chapter we focus on the MCE, and particularly, on the effects of anisotropies and four-spin Ising interaction on the magnetic and thermodynamic behaviors of double saw-tooth Ising-Heisenberg models and a mixed spin-(1/2, 1) Ising-Heisenberg two-leg ladder.

2.2 spin-1/2 double saw-tooth Ising-Heisenberg model

2.2.1 Model and method

At first, we consider a uniform spin-1/2 double saw-tooth Ising-Heisenberg spin ladder (or decorated two-leg ladder [113]) with four-spin Ising interaction (Fig. 2.1). The Hamiltonian of the model is given by

$$H = \sum_{j=1}^{N} \Big[(\boldsymbol{S}_{1,j} \cdot \boldsymbol{S}_{2,j})_{\eta,\Delta} + \sum_{a=1,2} \big(J_{\parallel} \sigma_{a,j}\sigma_{a,j+1} + J S_{a,j}^z (\sigma_{a,j} + \sigma_{a,j+1}) \big) \\ + J_{\perp}\sigma_{1,j}\sigma_{2,j} + K\sigma_{1,j}\sigma_{1,j+1}\sigma_{2,j}\sigma_{2,j+1} - B \sum_{a=1,2} \Big(S_{a,j}^z + \sigma_{a,j} \Big) \Big]. \tag{2.2}$$

Here N is the number of rungs. We assume that each pair of quantum $S = 1/2$ spins, $\boldsymbol{S}_{1,j}$ and $\boldsymbol{S}_{2,j}$ interact with the XXZ exchange interaction:

$$(\boldsymbol{S}_{1,j} \cdot \boldsymbol{S}_{2,j})_{\eta,\Delta} = \big[\eta \big(S_{1,j}^x S_{2,j}^x + S_{1,j}^y S_{2,j}^y \big) + \Delta S_{1,j}^z S_{2,j}^z \big], \tag{2.3}$$

with $S_i^\alpha (\alpha = x, y, z)$ being the spin-1/2 operators. $J_{\perp}$ and $J_{\parallel}$ are the Ising-type couplings on the rungs and along the legs, and K is the coupling constant of four-spin Ising term for each
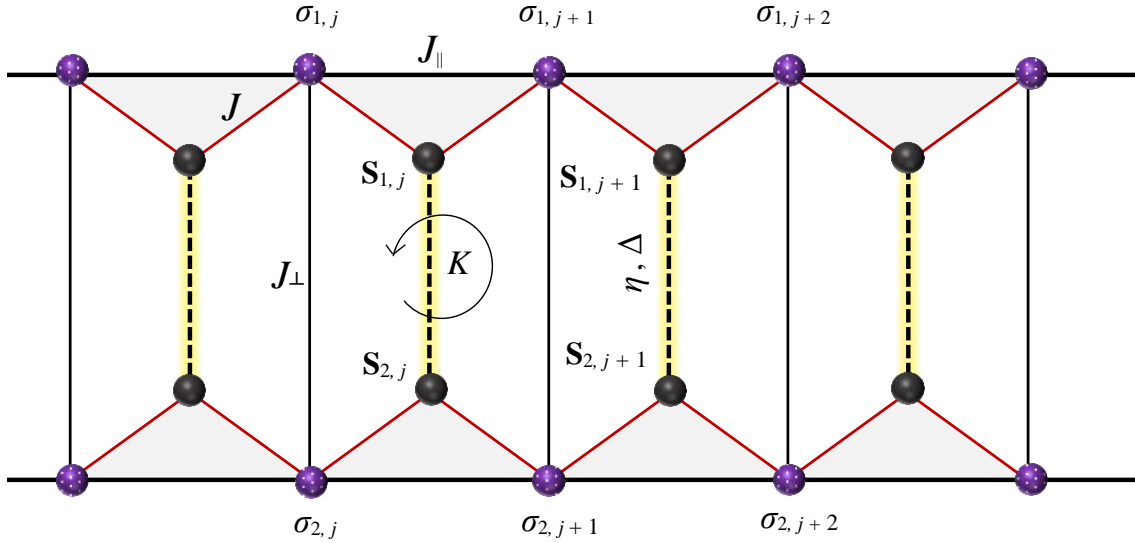
FIGURE 2.1: Schematic structure of the spin-1/2 Ising-XXZ double saw-tooth ladder. The balls denote spin-1/2 particles, where dark balls represent Heisenberg dimers and the other show Ising spins.

square plaquette of the ladder. J is the Ising coupling between the spins on the legs and two quantum spins of the interstitial Heisenberg dimer. These coupling is supposed to include only z-component of the quantum spins. $\sigma_{a,j}$ are Ising spin variables, taking values $(1, -1)$. B is the external homogeneous magnetic field applied in the z-direction. Let us mention that all parameters here are supposed to be dimensionless by assuming J being the energy unit.

2.2.2 The exact solution in terms of the generalized classical transfer-matrix method

Let us present the method of the calculation of the partition function of the model within the generalized classical transfer matrix technique. First, we proceed to the H model.

$$Z = \sum_{\{\sigma_1\}} \sum_{\{\sigma_2\}} \mathrm{Tr}_{\{\sigma_1,\sigma_2\}} e^{-\beta H} = \prod_{j=1}^{N} \mathbf{T}\left(\sigma_{1,j}, \sigma_{2,j} | \sigma_{1,j+1}, \sigma_{2,j+1}\right) = \mathrm{Tr}\, \mathbf{T}^N, \tag{2.4}$$

where 4×4 transfer matrix is given by

$$\mathbf{T}\left(\sigma_{1,j}, \sigma_{2,j} | \sigma_{1,j+1}, \sigma_{2,j+1}\right) \tag{2.5}$$
$$= \exp\left\{-\beta H^{cl}\left(\sigma_{1,j}, \sigma_{2,j} | \sigma_{1,j+1}, \sigma_{2,j+1}\right)\right\} \mathcal{W}_{\left(\sigma_{1,j}, \sigma_{2,j} | \sigma_{1,j+1}, \sigma_{2,j+1}\right)}$$

where

$$\mathcal{W}_{\left(\sigma_{1,j}, \sigma_{2,j} | \sigma_{1,j+1}, \sigma_{2,j+1}\right)} = \sum_{l=1}^{4} e^{-\beta \varepsilon_n \left(\sigma_{1,j}, \sigma_{2,j} | \sigma_{1,j+1}, \sigma_{2,j+1}\right)}, \tag{2.6}$$

$\varepsilon_n \left(\sigma_{1,j}, \sigma_{2,j}|\sigma_{1,j+1}, \sigma_{2,j+1}\right), \quad n = 1, ..., 4$ are the eigenvalues of the quantum part of the Hamiltonian:

$$H^q = \left(\boldsymbol{S}_{1,j} \cdot \boldsymbol{S}_{2,j}\right)_{\eta,\Delta} - \sum_{a=1,2} \left[B - J(\sigma_{a,j} + \sigma_{a,j+1})\right] S_{a,j}^z. \tag{2.7}$$

and the classical part of the system Hamiltonian reads

$$H^{cl} \left(\sigma_{1,j}, \sigma_{2,j}|\sigma_{1,j+1}, \sigma_{2,j+1}\right) = J_{\parallel} \sum_{a=1,2} \sigma_{a,j}\sigma_{a,j+1} + J_{\perp}\sigma_{1,j}\sigma_{2,j}$$
$$+K\sigma_{1,j}\sigma_{1,j+1}\sigma_{2,j}\sigma_{2,j+1} - B \sum_{a=1,2} \sigma_{a,j}. \tag{2.8}$$

The eigenstates of the quantum Hamiltonian are explicitly depended on the values of four classical spin variables, interacting with the quantum spin dimer. They can be easily found by the straightforward diagonalization of the quantum Hamiltonian in the standard Isign basis, $(|\uparrow\uparrow\rangle, |\uparrow\downarrow\rangle, |\downarrow\uparrow\rangle, |\downarrow\downarrow\rangle)$. The eigenvalues are

$$\varepsilon_{1,2} = -\Delta \pm \sqrt{J^2 \left(\sigma_{1,j} - \sigma_{2,j} + \sigma_{1,j+1} - \sigma_{2,j+1}\right)^2 + \eta^2}, \tag{2.9}$$
$$\varepsilon_{3,4} = \Delta \pm \left(2B - J(\sigma_{1,j} + \sigma_{2,j} + \sigma_{1,j+1} + \sigma_{2,j+1})\right).$$

the corresponding eigenvectors are given by

$$|\varphi_{1,2}\rangle = \frac{1}{\sqrt{1 + A_{\pm}^2}} \left(|\uparrow\downarrow\rangle + A_{\pm}|\downarrow\uparrow\rangle\right), \tag{2.10}$$
$$|\varphi_3\rangle = |\downarrow\downarrow\rangle,$$
$$|\varphi_4\rangle = |\uparrow\uparrow\rangle,$$

where

$$A_{\pm} = \frac{J \left(\sigma_{2,j} - \sigma_{1,j} + \sigma_{2,j+1} - \sigma_{1,j+1}\right) \pm \sqrt{J^2 \left(\sigma_{2,j} - \sigma_{1,j} + \sigma_{2,j+1} - \sigma_{1,j+1}\right)^2 + \eta^2}}{\eta} \tag{2.11}$$

Thus, we see here that for the whole chain, the eigenvectors of the quantum spin dimer are dependent on the four values of the classical spin variables they are interacting with. The explicit form of the 4×4 classical transfer-matrix is

$$\begin{pmatrix} z_1^{-1}z_2^{-1}\lambda^{-1}\mu^2(\chi_0 + \psi_2) & z_2^{-1}\lambda\mu^2(\chi_1 + \psi_1) & z_2^{-1}\lambda\mu^2(\chi_1 + \psi_1) & z_1z_2^{-1}\lambda^{-1}\mu^2(\chi_0 + \psi_0) \\ z_2\lambda(\chi_1 + \psi_1) & z_1z_2^{-1}\lambda(\chi_2 + \psi_0) & z_1z_2\lambda^{-1}(\chi_0 + \psi_0) & z_2\lambda(\chi_1 + \psi_{-1}) \\ z_2\lambda(\chi_1 + \psi_1) & z_1z_2\lambda^{-1}(\chi_0 + \psi_0) & z_1^{-1}z_2\lambda^{-1}(\chi_2 + \psi_0) & z_2\lambda(\chi_1 + \psi_{-1}) \\ z_1z_2^{-1}\lambda^{-1}\mu^{-2}(\chi_0 + \psi_0) & z_2^{-1}\lambda^{-1}\mu^{-2}(\chi_1 + \psi_{-1}) & z_2^{-1}\lambda^{-1}\mu^{-2}(\chi_1 + \psi_{-1}) & z_1^{-1}z_2^{-1}\lambda^{-1}\mu^{-2}(\chi_0 + \psi_{-2}) \end{pmatrix} \tag{2.12}$$
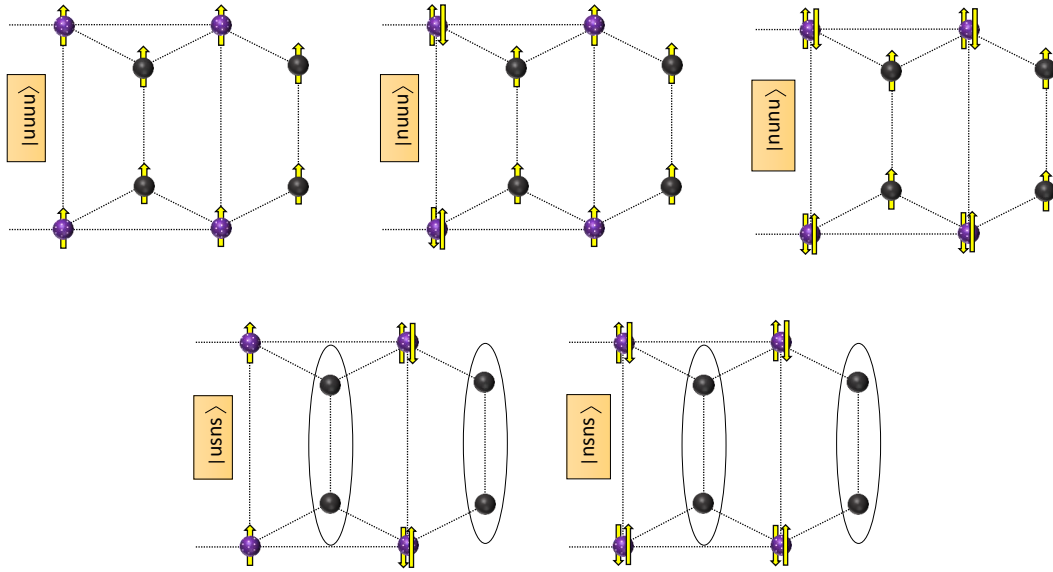
FIGURE 2.2: The possible spin configurations of the spin-1/2 double saw-tooth ladder associated to the ground-state phases.

where the following notations are adopted:

$$z_1 = e^{2\beta J_\parallel}, \ z_2 = e^{\beta J_\perp}, \ \lambda = e^{\beta K}, \ \mu = e^{\beta B}, \tag{2.13}$$

$$\chi_n = 2e^{\beta\Delta}\cosh\frac{\beta}{2}\sqrt{(2nJ)^2 + \eta^2}, \ \ n = 0, 1, 2.$$

$$\psi_n = 2e^{-\beta\Delta}\cosh\left(\beta\left(B - nJ\right)\right), \ \ n = -2, -1, 0, 1, 2.$$

2.2.3 Ground-State Phase Transition

The system under consideration possesses large number of possible zero-temperature ground states, depending on the value of its microscopic parameters, η; Δ; $J_\perp$; J; $J_\parallel$; K/J and the magnetic field B/J. As the main goal of our study is to clarify the role of the Ising-type four spin interaction in the enhancement of the MCE, we focus here on a particular range of the parameters values which admit the special points on the ground state phase diagram with maximal degeneracy. The MCE is particularly stronger around triple points and moreover around points of confluence of more phases [127]. We are going to examine the role of the four-spin Ising interaction K/J in behaviour of the cooling rate. We found that for our purposes the following special spin configuration presented in Fig. 2.2 are interesting. All these sates feature the doubling of the unit cell, which is the manifestation of the antiferromagnetic coupling along the legs. These ground states with the corresponding values of the magnetization per unit block are given by the following expressions
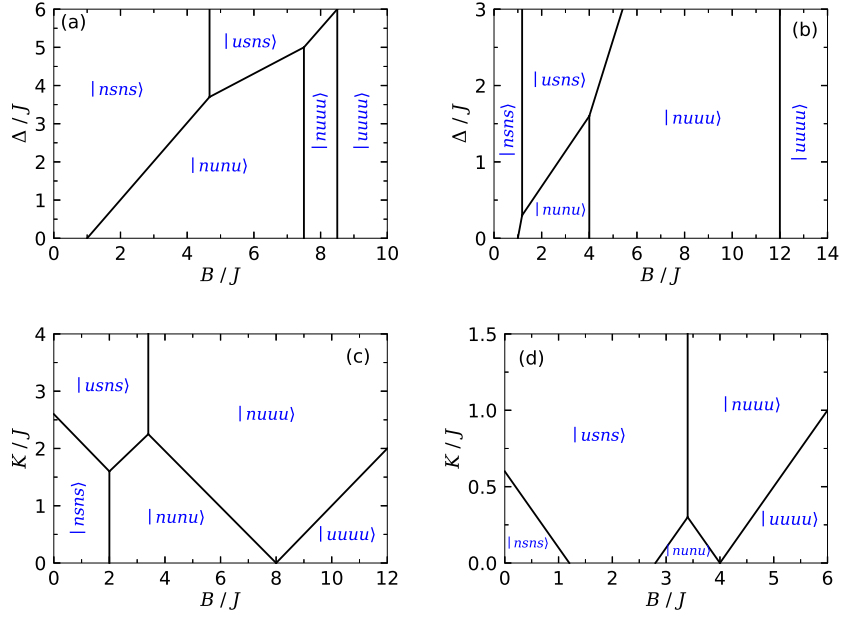
FIGURE 2.3: Ground-state phase diagram of the double saw-tooth ladder. (a) In the $(B/J - \Delta/J)$ plane for fixed $K/J = 0.25$, and (b) in the $(B/J - \Delta/J)$ plane for fixed $K/J = 2$. (c) In the $(B/J - K/J)$ plane for $\Delta/J = 1$. Other parameters of the Hamiltonian have been taken such that the system is in its maximum degeneracy, i.e., $\eta/J = 1$, $J_\perp/J = J_\parallel/J = 2$. (d) In the $(B/J - K/J)$ plane for fixed $\Delta/J = 1$, $\eta/J = 1$, $J_\perp/J = 1$ and $J_\parallel/J = 0.5$ in such a way the maximum degeneracy is destroyed.

$$
\begin{aligned}
|uuuu\rangle &= \prod_{i=1}^{N/2} |\uparrow\uparrow\rangle_{2i-1} \otimes |\varphi_4\rangle_{2i-1} \otimes |\uparrow\uparrow\rangle_{2i} \otimes |\varphi_4\rangle_{2i}, \\
E_{uuuu} &= 2\Delta - 8B + 8 + 4J_\parallel + 2J_\perp + 2K, \quad M/M_s = 1, \\
|nuuu\rangle &= \prod_{i=1}^{N/2} |\downarrow\uparrow\rangle_{2i-1} \otimes |\varphi_4\rangle_{2i-1} \otimes |\uparrow\uparrow\rangle_{2i} \otimes |\varphi_4\rangle_{2i}, \\
E_{nuuu} &= 2\Delta - 6B + 4 - 2K, \quad M/M_s = \quad M/M_s = \tfrac{3}{4}, \\
|nunu\rangle &= \prod_{i=1}^{N/2} |\uparrow\downarrow\rangle_{2i-1} \otimes |\varphi_4\rangle_{2i-1} \otimes |\downarrow\uparrow\rangle_{2i} \otimes |\varphi_4\rangle_{2i}, \\
E_{nunu} &= 2\Delta - 4B - 4J_\parallel - 2J_\perp + 2K, \quad M/M_s = \tfrac{1}{2}, \\
|usns\rangle &= \prod_{i=1}^{N/2} |\uparrow\uparrow\rangle_{2i-1} \otimes |\varphi_2\rangle_{2i-1} \otimes |\uparrow\downarrow\rangle_{2i} \otimes |\varphi_2\rangle_{2i}, \\
E_{usns} &= -2B - 2\Delta - 2K - 4\sqrt{2}, \quad M/M_s = \tfrac{1}{4}, \\
|nsns\rangle &= \prod_{i=1}^{N/2} |\uparrow\downarrow\rangle_{2i-1} \otimes |\varphi_2\rangle_{2i-1} \otimes |\downarrow\uparrow\rangle_{2i} \otimes |\varphi_2\rangle_{2i}, \\
E_{nsns} &= 2K - 2\Delta - 4J_\parallel - 2J_\perp - 4, \quad M/M_s = 0,
\end{aligned}
\tag{2.14}
$$

We restricted ourselves to investigate quantum phase transition between the most popular ground-states characterized in Eq. (2.14), revealing the magnetization plateaux with respect

to the saturation value.

Here the following principles in notations are adopted. The unit cell in the configurations with period doubling contains four pairs of spins, each pair is coupled by rung of the ladder. Thus, for the two spins pointing up(down) we use "u"("d"), for the pair of spins pointing in opposite directions we use "n", and finally for the quantum quasi-singlet state φ_{2i} we use "s" (solid elliptic line in Fig. 2.2). The ground-state phase diagrams in the $(K/J - B/J)$ plane containing configurations from Eq. (2.14) are presented in Fig. 2.3 for various fixed values of the anisotropic exchange interaction Δ and for particular values of other interaction parameters, $J_\perp/J = J_\parallel/J = 2$ and $\eta/J = 1$. The main feature of the phase diagrams is a triple point, the point with specific particular values of K/J and B/J where three ground states become degenerate. Important role of the Ising four-spin interaction, K/J, is clearly seen, as for the line $K/J = 0$ we found that the phase boundary between ground states $|nunu\rangle$ and $|nuuu\rangle$ disappears. Actually, at $B/J = 8$ (see Fig. 2.3(c)) we have triple degeneracy between $|nunu\rangle$, $|nuuu\rangle$ and $|uuuu\rangle$, where for region $B/J < 8$ the state $|nunu\rangle$ is the ground state, while for the region $B/J > 8$, $|uuuu\rangle$ is the ground state.

One can realize from Figs. 2.3(a) and 2.3(b) that increase of the K/J leads to substantially restriction of the $|nsns\rangle$ phase, and to widen the phase $|nuuu\rangle$. The phase boundaries are remarkably affected by the change of the anisotropy Δ/J accompanied with the magnetization jumps and plateaux. Surprisingly, when the maximum degeneracy is lifted (see Fig. 2.3(d)), alteration of the both parameters K/J and Δ/J also results in the notable changes of the ground-state phase transitions. For example, the boundary between $|nsns\rangle$ and $|nunu\rangle$ disappears by assuming interaction parameter set $J_\perp/J = 1, J_\parallel/J = 0.5$ and $\eta/J = 1$.

2.2.4   Adiabatic (de)magnetization process of the spin-1/2 double saw-tooth Ising-Heisenberg ladder

Recently, many authors have widely reported that various kinds of quantum spin systems exhibit enhanced magnetocaloric effects (MCE) during the adiabatic demagnetization process leading to study the low-temperature magnetic refrigeration. Hence, let us also investigate the adiabatic demagnetization process of the spin-1/2 Ising-XXZ Heisenberg double saw-tooth ladder under the particular adiabatic circumstances. We here study the isentropes (entropy levels) in the $(B/J - T/J)$ plane, besides the Grüneisen parameter times the temperature $T\Gamma_B$ as a function of magnetic field. The effects of the cyclic four-spin Ising interaction K/J on the entropy levels and cooling rate are investigated in detail.

Figure 2.4 shows our results for the entropy of spin-1/2 double saw-tooth ladder in the $(B/J - T/J)$ plane, having set parameter values to $J_\parallel/J = J_\perp/J = 2$ and $\eta/J = 1$ (highly degenerate mode for the system). Comparing Fig. 2.4 (a) with the ground-state phase diagram depicted in Fig. 2.3(c) reveals that the MCE in the finite low entropy S/N (low-temperature regimes)
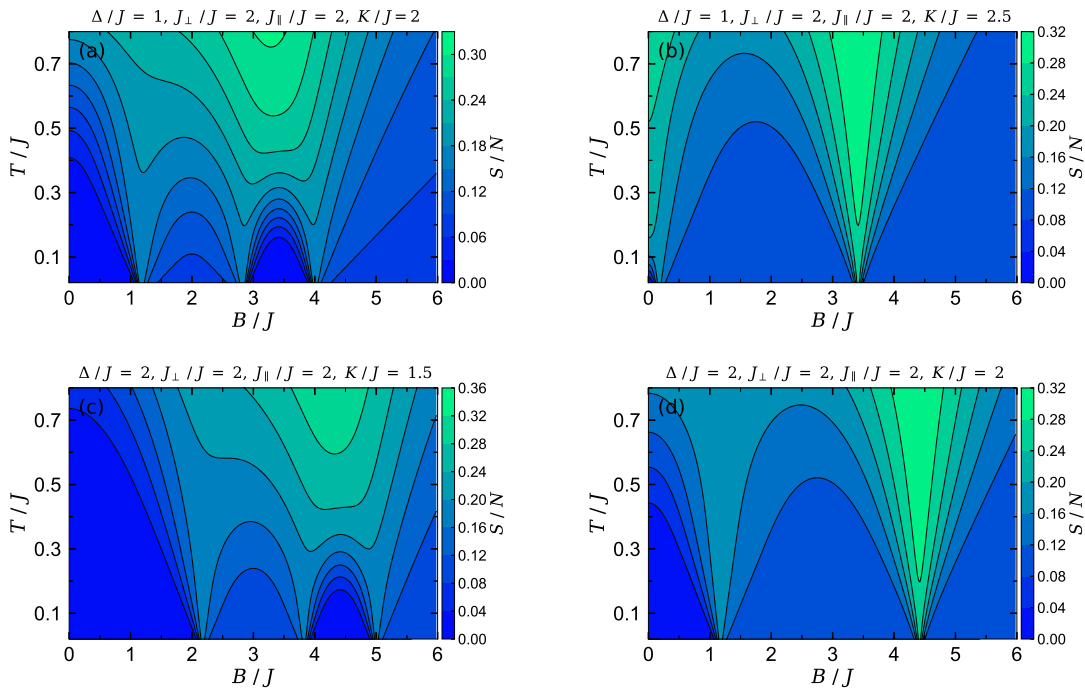
FIGURE 2.4: Contour plots of the isentropic dependence T/J against magnetic field B/J of the spin-1/2 double saw-tooth ladder for fixed values of $J_{\parallel}/J = J_{\perp}/J = 2$ and $\eta/J = 1$. Regarding to Fig. 2.3 the corresponding coordinates in the $(K/J - B/J)$ plane nearby the cross-section of triple points are taken as (a) $\Delta/J = 1$ and $K/J = 2$, (b) $\Delta/J = 1$ and $K/J = 2.5$. Also, (c) $\Delta/J = 2$ and $K/J = 1.5$, (d) $\Delta/J = 2$ and $K/J = 2$. By inspecting Fig. 2.3, each temperature dropping (MCE) occurs nearby the phase boundary of a pair of typical ground states.

perfectly reproduces the ground state phase transition boundaries. By inspecting this figure, it can be understood that if the magnetic field decreases adiabatically from $B/J = 3.5$ to $B/J = 3$ the temperature dramatically falls down. When B/J decreases isothermally from $B/J = 3$ to $B/J = 2$, the entropy noticeably decreases (e.g., approximately from $S/4N = 0.2$ to $S/4N = 0.1$ at $T/J \approx 0.025$), indicting the model loss heat ($S(B/J = 3) - S(B/J = 2) < 0$).

By decreasing cyclic four-spin Ising term K/J and in turn increasing the exchange anisotropy Δ/J the critical magnetic point at which the temperature falls down shifts toward stronger magnetic fields (see Fig. 2.4 (c)), this phenomenon is accompanied by the triple points coordination in the $(K/J, \Delta/J, B/J)$ plane. Totally, we observe three enhanced regions of MCE accompanied by a relatively fast cooling of the model at two selected coordinates $(K/J, \Delta/J)$ associated to the intersection points. First region is due to field-induced ground-state phase transition from $|nsns\rangle$ to $|nsus\rangle$, second one appears nearby the transition from $|usns\rangle$ to $|nunu\rangle$, and the third is accompanied with the transition from $|nunu\rangle$ to $|nuuu\rangle$. Analogously, we observe that altering parameters Δ/J and K/J result in changing the magnetic position of critical points at which the MCE occurs (see Figs. 2.4 (b) and (d)).

Now, let us discuss the effects of the cyclic four-spin Ising interaction K/J on the Grüneisen
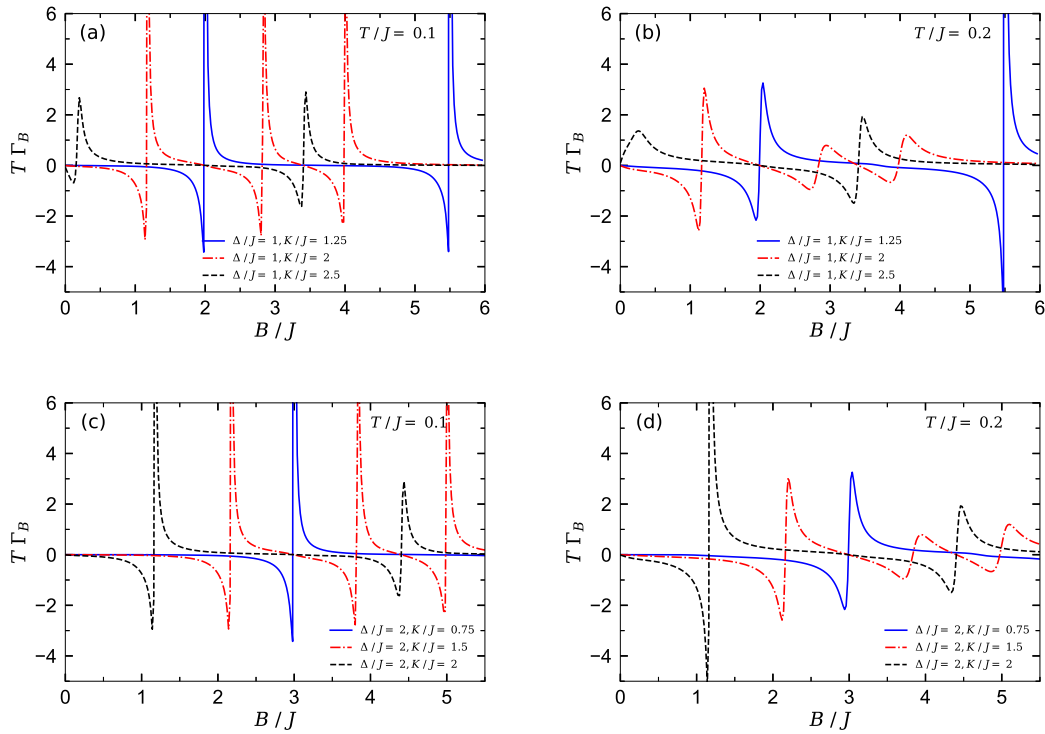
FIGURE 2.5: The magnetic Grüneisen parameter multiplied by the temperature $T\,\Gamma_B$ as a function of magnetic field B/J where three different modes have been considered for coordinates $(K/J,\ \Delta/J)$ in each panel. Panels (a) and (c) indicate Grüneisen parameter at low temperature $T/J = 0.1$, and panels (b) and (d) show the same parameter at moderate temperature $T/J = 0.2$. The same set of other parameters have been considered as Fig. 2.4.

parameter. To this end, we plot the the magnetic Grüneisen parameter $T\Gamma_B$ against the applied magnetic field at two different temperatures: the relatively low temperature $T/J = 0.1$ and moderate temperature $T/J = 0.2$. Three modes have been assumed for the coordinates $(K/J,\ \Delta/J)$. The same fixed values of the coupling constants $J_\parallel/J = J_\perp/J = 2$ and $\eta/J = 1$ have been supposed. Figure 2.5(a) illustrates the sign of the parameter $T\Gamma_B$ changes close to the critical magnetic fields $B_c/J \approx 0.1$ and $B_c/J \approx 3$ denoting a rapid accumulation of the entropy due to the phase intersection between aforementioned ground-states. The magnetic behavior of Grüneisen parameter corroborates that by tuning the coordinates $(K/J,\ \Delta/J)$ the magnetic position of the critical magnetic fields at which the enhanced MCE occurs during the adiabatic demagnetization process, will remarkably change.

Another notable result gained from our examinations is the particular response of the Grüneisen parameter to the temperature variations. The most sagely question to ask is that what happens for the magnetic dependencies of the Grüneisen parameter when the temperature changes. To achieve the authentic answer we display in panels 2.5(b) and 2.5(d) this parameter as a function of the magnetic field at different temperature for the same fixed values of other parameters to the panels 2.5(a) and (c). Obviously, large enhanced MCE occurred at low magnetic fields gradually diminishes when the temperature increases. One another interesting point to declare
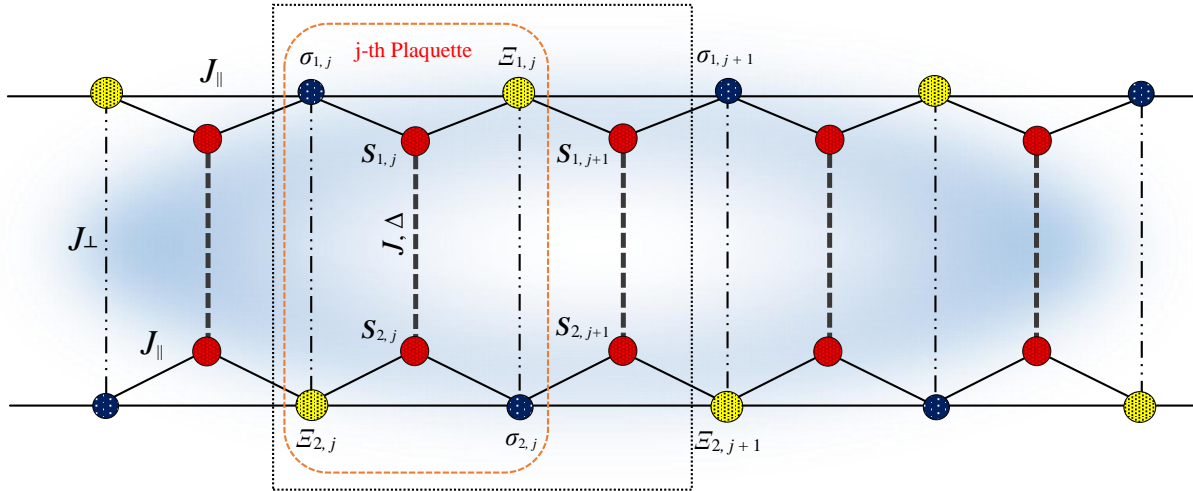
FIGURE 2.6: The mixed spin-$(1/2, 1)$ Ising-Heisenberg double saw-tooth ladder schematically structured by all considered magnetic exchange pathways. Yellow balls present spin-1 particles, while dark-blue balls denote spin-1/2 Ising nodal particles, and red balls show the spin-1/2 interstitial Heisenberg dimers. Region restricted by dotted rectangle displays $j - th$ unit block, while red dashed line limits a single plaquette. Dashed lines indicate the quantum Heisenberg interaction between dimers, and solid lines represent classical Ising-type interaction. Dotted-dotted dashed lines denote the alternating weak-rung Ising interaction between nodal spins, supposing fixed value $J_\perp/J_\parallel = 0.1$ in the forthcoming diagrams.

is that, upon the variations of exchange anisotropy and cyclic four-spin Ising interaction, the observed MCE at lower magnetic field show a restriction against the temperature increment. As a matted of fact, when the exchange anisotropy Δ/J increases, by tuning cyclic four-spin Ising interaction K/J the enhanced MCE is observable even for higher temperatures.

2.3 Mixed spin-(1/2, 1) Ising-Heisenberg double saw-tooth ladders

The present section deals with the study of mixed spin-$(1/2, 1)$ Ising-Heisenberg double saw-tooth ladder as a decorated two-leg ladder. Obtained results for the magnetic and thermodynamic properties of this model have been reported in Ref. [26]. The most general Hamiltonian of the model can be thus obtained by the sum of all unit blocks rounded by dotted rectangle in Fig. 2.6. Therefor, the Hamiltonian of the ladder reads

$$H = \sum_{j=1}^{N} \mathcal{H}_j, \tag{2.15}$$

The operator $\mathcal{H}_j$ defines Hamiltonian of the $j-$th unit block. Thus, it can be written as

$$
\begin{aligned}
\mathcal{H}_j = &\Big\{ (\boldsymbol{S}_{1,j} \cdot \boldsymbol{S}_{2,j})_\Delta - \sum_{r=0,1} \sum_{l=1,2} S_{l,j}^z \big(g_1 B - J_\| [\sigma_{l,j+rj'} + \Xi_{l,j+rj''}] \big) \Big\}_q \\
&+ \Big\{ \tfrac{J_\perp}{2} \big[\Xi_{1,j}\, \sigma_{2,j} + \sigma_{1,j+1}\, \Xi_{2,j+1} \big] + \tfrac{D}{2} \big(\Xi_{1,j}^2 + \Xi_{2,j}^2 \big) \\
&+ J_\| \big(\sigma_{1,j}\Xi_{1,j} + \sigma_{2,j}\Xi_{2,j} + \Xi_{1,j}\sigma_{1,j+1} + \sigma_{2,j}\Xi_{2,j+1} \big) \\
&- \tfrac{B}{2} \big[g_1(\sigma_{2,j} + \sigma_{1,j+1}) + g_2(\Xi_{1,j} + \Xi_{2,j+1}) \big] \Big\}_c,
\end{aligned}
\tag{2.16}
$$

where $S_{l,j}^\alpha (\alpha \in \{x,y,z\})$ indicate spatial components of the standard spin-1/2 operator to the leg l and rung j under periodic boundary conditions. In addition, we supposed $j' = -\frac{(-1)^l - 1}{2}$ and $j'' = \frac{(-1)^l + 1}{2}$. Here, N is the number of rungs and must be even. Also, we assume that each pair of $S = 1/2$ quantum spins $\boldsymbol{S}_{1,j}$ and $\boldsymbol{S}_{2,j}$, interact through a typical XXZ exchange coupling:

$$
(\boldsymbol{S}_{1,j} \cdot \boldsymbol{S}_{2,j})_{J,\Delta} = \big[J \big(S_{1,j}^x S_{2,j}^x + S_{1,j}^y S_{2,j}^y \big) + \Delta S_{1,j}^z S_{2,j}^z \big],
\tag{2.17}
$$

with $S_i^\alpha (\alpha = x,y,z)$ being the special quantum spin operators. $J_\perp$ and $J_\|$ are the Ising-type couplings on the rungs and along the legs. These couplings are supposed to include only z-component of the quantum spins. J represents the isotropic interaction between the interstitial Heisenberg dimers, and Δ stands for the exchange anisotropy between them. It is noteworthy that in the remaining parts of this article we consider just two species of Ising-Heisenberg spin ladders, i.e., mixed spin-(1/2, 1) Ising-XX double saw-tooth ladder by supposing $\Delta = 0$, and mixed spin-(1/2, 1) Ising-XXX double saw-tooth ladder by supposing $\Delta = 1$ with respect to the coupling constant $J_\|$. $\sigma_{a,j}$ and $\Xi_{a,j}$ are the $S = 1/2$ and $S = 1$ Ising spin variables, taking values $(1/2, -1/2)$ and $(1, 0, -1)$, respectively. B is the external homogeneous magnetic field applied in the z-direction. D represents the single-ion anisotropy parameter, and g_1 and g_2 are Landé g-factors associated to, respectively, spins-1/2 and spins-1. Although Eq. (4.4) seems to be a long complicated formula for the total Hamiltonian of the system, we try to show in detail all parts of the Hamiltonian with different symbols that may help readers to deep understand of the model, as well as, to follow our analytical and numerical calculations easily.

2.3.1 The exact solution within the classical transfer-matrix formalism

We perform transfer-matrix technique to obtain the partition function of the model. Consequently, the partition function of the mixed-spin Ising-Heisenberg double saw-tooth ladder can be written in the form

$$
Z_N = \text{Tr} \left[\mathbf{T}^N \right],
\tag{2.18}
$$

The average spin value of the $j-$th plaquette in our favorite one-dimensional Ising-Heisenberg model when the system reaches thermodynamic equilibrium is the same for all values of j. Although, each two adjacent plaquettes are geometrically different (because of localizing different Ising spins on the vertices), they are mathematically the same since all Heisenberg dimers are

identical. Actually, the Hamiltonians of each adjacent plaquettes follow the commutation relation $[\mathcal{H}_j^P, \mathcal{H}_{j+1}^P] = 0$. This property enables us to deduce the partition function of the model through the transfer-matrix of $j-$th plaquette. Accordingly, 6×6 transfer-matrix $\mathbf{T}$ of the $j-$th plaquette has typical form

$$\mathbf{T} = \boldsymbol{w}(\sigma_{1,j}, \, \Xi_{2,j} | \Xi_{1,j}, \, \sigma_{2,j}). \tag{2.19}$$

The fully symmetric matrix $\boldsymbol{w}$ is a Boltzmann factor for the associated plaquette bounded by red-dashed rectangle in Fig. 4.5.

The eigenvalues of the quantum part of the Hamiltonian block explicitly depend on the values of four nodal spins, interacting with the quantum spin dimer. Rely on this fact, the eigenvalues of the Hamiltonian of the $j-$th plaquette can be easily found by its diagonalization in the standard basis $(|\uparrow\uparrow\rangle, |\uparrow\downarrow\rangle, |\downarrow\uparrow\rangle, |\downarrow\downarrow\rangle)$. Therefore, the eigenvalues are

$$\begin{aligned}
\varepsilon_{1,2} &= \\
&-\tfrac{\Delta}{4} \pm \tfrac{1}{2}\sqrt{J_\parallel^2 \left(\sigma_{1,2j-1} - \Xi_{2,2j-1} + \Xi_{1,2j} - \sigma_{2,2j}\right)^2 + J^2}, \\
\varepsilon_{3,4} &= \\
&\tfrac{\Delta}{4} \pm \tfrac{1}{2}\left(2g_1 B - J_\parallel(\sigma_{1,2j-1} - \Xi_{2,2j-1} + \Xi_{1,2j} - \sigma_{2,2j})\right),
\end{aligned} \tag{2.20}$$

with the corresponding eigenvectors

$$\begin{aligned}
|\Psi_{1,2}\rangle &= \tfrac{1}{\sqrt{1+A_\pm^2}} \left(|\uparrow\downarrow\rangle + A_\pm|\downarrow\uparrow\rangle\right), \\
|\Psi_3\rangle &= |\downarrow\downarrow\rangle, \\
|\Psi_4\rangle &= |\uparrow\uparrow\rangle,
\end{aligned} \tag{2.21}$$

where

$$\begin{aligned}
A_\pm &= \\
&\tfrac{1}{J}\Big[J_\parallel\left(\Xi_{2,2j-1} - \sigma_{1,2j-1} + \sigma_{2,2j} - \Xi_{1,2j}\right) \\
&\pm\sqrt{J_\parallel^2\left(\Xi_{2,2j-1} - \sigma_{1,2j-1} + \sigma_{2,2j} - \Xi_{1,2j}\right)^2 + J^2}\Big].
\end{aligned} \tag{2.22}$$

The transfer-matrix $\mathbf{T}$ has the symmetric form

$$\mathbf{T} = \begin{pmatrix}
\mathcal{A} & \mathcal{G} & \alpha & \alpha & \mathcal{K} & \mathcal{U} \\
\mathcal{G} & \mathcal{B} & \Omega & \mathcal{Q} & \mathcal{R} & \mathcal{S} \\
\alpha & \Omega & \mathcal{C} & \mathcal{V} & \mathcal{W} & \gamma \\
\alpha & \mathcal{Q} & \mathcal{V} & \mathcal{C} & \mathcal{X} & \gamma \\
\mathcal{K} & \mathcal{R} & \mathcal{W} & \mathcal{X} & \mathcal{D} & \mathcal{J} \\
\mathcal{U} & \mathcal{S} & \gamma & \gamma & \mathcal{J} & \mathcal{E}
\end{pmatrix}, \tag{2.23}$$

where by considering

$$z_1 = e^{\beta J_\perp}, \; z_2 = e^{\beta J_\parallel}, \; \lambda = e^{\beta D}, \; \mu = e^{\beta B}, \; \delta = e^{\beta \Delta},$$

the following notations are adopted for the all components of the transfer-matrix:

$$
\begin{aligned}
&\mathcal{A} = 4(z_1^{-1}z_2^{-2}\lambda^{-2}\mu^2)(\varphi_4 + \psi_2^0), \ \mathcal{G} = 4(z_1^{-\frac{1}{2}}z_2^{-1}\mu^{\frac{3}{2}})(\varphi_3 + \psi_2^1), \\
&\mathcal{K} = 4(z_1^{\frac{1}{2}}z_2^{-1}\mu^{-\frac{1}{2}})(\varphi_1 + \psi_2^3), \ \mathcal{U} = 4(z_1 z_2^{-2}\lambda^{-2})(\varphi_0 + \psi_2^4), \\
&\mathcal{B} = 4(\mu)(\varphi_2 + \psi_2^0), \ \mathcal{Q} = 4(z_1^{-\frac{1}{2}}z_2\mu^{\frac{1}{2}})(\varphi_1 + \psi_2^1), \\
&\mathcal{R} = 4(\varphi_0 + \psi_2^2), \ \mathcal{S} = 4(z_1^{\frac{1}{2}}z_2^{-1}\mu^{-\frac{1}{2}})(\varphi_1 + \psi_2^3), \\
&\mathcal{C} = 4(z_1 z_2^2\lambda^{-2})(\varphi_0 + \psi_2^0), \ \mathcal{V} = 4(z_1^{-1}z_2^2\lambda^{-2})(\varphi_0 + \psi_2^0), \\
&\mathcal{W} = 4(z_1^{-\frac{1}{2}}z_2\lambda^{-1}\mu^{-\frac{1}{2}})(\varphi_{-1} + \psi_2^1), \ \mathcal{X} = 4(z_1^{\frac{1}{2}}z_2\mu^{-\frac{1}{2}})(\varphi_{-1} + \psi_2^1), \\
&\mathcal{D} = 4(\mu^{-1})(\varphi_{-2} + \psi_2^0), \ \mathcal{J} = 4(z_1^{-\frac{1}{2}}z_2^{-1}\lambda^{-1}\mu^{-\frac{3}{2}})(\varphi_{-3} + \psi_2^1), \\
&\mathcal{E} = 4(z_1^{-1}z_2^{-2}\lambda^{-2}\mu^{-2})(\varphi_{-4} + \psi_2^0), \\
&\alpha = 4(\lambda^{-2}\mu)(\varphi_2 + \psi_2^2), \ \gamma = 4(\lambda^{-1}\mu^{-2})(\varphi_{-2} + \psi_2^2), \\
&\Omega = 4(z_1^{\frac{1}{2}}z_2^1\lambda^{-1}\mu^{-\frac{3}{2}})(\varphi_1 + \psi_2^1), \quad\quad\quad\quad\quad\quad\quad\quad (2.24)
\end{aligned}
$$

for which functions φ and ψ are defined as

$$
\begin{aligned}
\varphi_n &= 2\delta^{-1}\cosh(\beta[2B - nJ]), \\
\psi_m^{m'} &= 2\delta\cosh(\beta\sqrt{(m\eta)^2 + (m'J)^2}).
\end{aligned}
$$

2.3.2 Free energy

To derive exact expressions for all thermodynamic parameters of the mixed spin-(1/2, 1) Ising-Heisenberg double saw-tooth ladder, the partition function should be calculated by using above analytical procedure. In the thermodynamic limit, the free energy per unit plaquette can be expressed as

$$
f = -\tfrac{1}{\beta}\ln\Lambda_{max}, \quad\quad\quad\quad (2.25)
$$

where, Λ_{max} is the largest eigenvalue of the transfer matrix. Now, one can investigate the thermodynamic parameters of the model under consideration quantitatively.

2.3.3 Magnetization

At the beginning, let us discuss possible magnetic ground states reproduced by magnetization curve. In Figs. 2.7 (a) and 2.7 (d), we display the low-temperature magnetization in the $(B/J_\parallel - J/J_\parallel)$ plane for $\Delta/J_\parallel = 0$ and $\Delta/J_\parallel = 1$, respectively. The single-ion anisotropy assumed to be $D/J_\parallel = 1$. We note that in all of forthcoming figures we optionally assume different fixed values $g_1 = 1$ and $g_2 = 2$ for the Heisenberg dimers and spin-1 Ising nodal sites, and alternating weak-rung interaction coupling $J_\perp/J_\parallel = 0.1$ between nodal spins. The magnetization exhibits
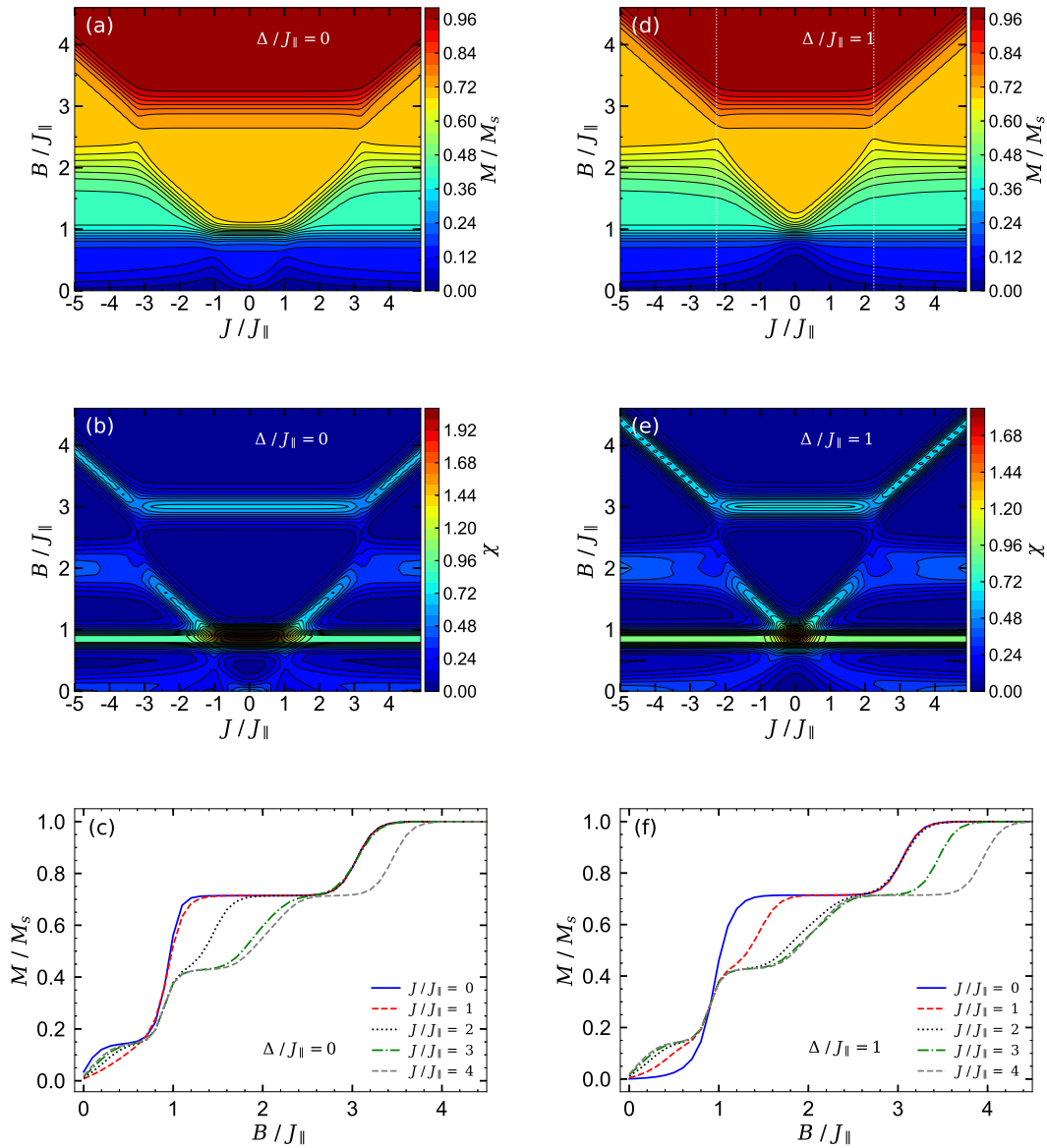
FIGURE 2.7: (a) and (d) Contour plot of the magnetization per saturation of the mixed spin Ising-Heisenberg double saw-tooth ladder, in the $(B/J_\parallel - J/J_\parallel)$ plane for fixed values of $\Delta/J_\parallel = 0$ (mixed spin Ising-XX double saw-tooth ladder) and $\Delta/J_\parallel = 1$ (mixed spin Ising-XXX double saw-tooth ladder), respectively. (b) and (e) show the corresponding magnetic susceptibility to panels (a) and (d) respectively. (c) and (f) 2-D plot of the magnetization for some selected exchange coupling ratio $J/J_\parallel$. In all panels are assumed fixed parameters $g_1 = 1$, $g_2 = 2$, $J_\perp/J_\parallel = 0.1$, $D/J_\parallel = 1$ and $T/J_\parallel = 0.1$. Dotted lines show the special point $|J/J_\parallel| = 2.25$ which would be our interest to consider in numerical process.

at sufficiently low temperatures abrupt but continuous changes in a vicinity of each critical field being reminiscent of zero-temperature magnetization jumps.

Figure 2.7(a) illustrates the magnetization curve of the mixed spin-(1/2, 1) Ising-XX double saw-tooth ladder in the $(B/J_\parallel - J/J_\parallel)$ plane for the case when Heisenberg XX interaction is considered for the dimers, namely $\Delta/J_\parallel = 0$, assuming other parameters of the Hamiltonian as fixed values

$g_1 = 1$, $g_2 = 2$, $J_\perp/J_\parallel = 0.1$, $D/J_\parallel = 1$. It is clear from this panel that the magnetization at $J/J_\parallel = 0$ (see blue solid line plotted in panel 2.7(c)) shows intermediate plateaux at $M/M_s = 1/7$ and widely at $M/M_s = 5/7$, M_s means saturation magnetization. As the exchange coupling $J/J_\parallel$ increases another intermediate plateau appears at $M/M_s = 3/7$, such that the plateau at $M/M_s = 5/7$ becomes narrower. By considering isotropic case XXX Heisenberg interaction for the dimers (panel 2.7(d)) we witness that the magnetic phase boundaries accompanying with the magnetization jumps are considerably limited. Furthermore, the magnetization becomes zero at low magnetic fields and weak interaction $J/J_\parallel$. This phenomenon tell us that an unconventional plateau at $M/M_s = 0$ arises in the magnetization curve (see panel 2.7(f)) which gradually disappears upon increasing $J/J_\parallel$. The magnetization plateau at $M/M_s = 3/7$ is created at lower exchange coupling $J/J_\parallel$ for the mixed spin Ising-XXX model, see for example, red dashed line plotted in panels 2.7(c) and 2.7(f). In Figs. 2.7(b) and 2.7(e) are depicted the magnetic susceptibility in the same conditions to panels 2.7(a) and 2.7(d), respectively. One can see that the magnetic susceptibility has a sharp peak nearby the critical magnetic fields at which first-order magnetic phase transition occurs.

2.3.4 Entropy and magnetic Grüneisen parameter

The contour plot of the entropy per block is displayed in Fig. 2.8 in the $(B/J_\parallel - T/J_\parallel)$ plane for arbitrary anisotropic parameters set $\Delta/J_\parallel = \{0, 1\}$ and $D/J_\parallel = \{1, 2\}$, assuming fixed $J/J_\parallel = 2.25$. Contour plot showed in Fig. 2.8(a) implies that the entropy variation can be qualitatively a good evidence of the first-order phase transition between magnetic ground states of mixed spin Ising-XX ladder with the magnetization values $M/M_s = \{1/7, 3/7, 5/7\}$ whose boundaries are confined by magnetization jumps. The reason is that the isentropy lines are significantly accumulated close to the critical magnetic fields $B/J_\parallel \approx \{0, 1, 1.6, 3.2\}$, where at each point an enhanced MCE exists. It can be concluded from Fig. 2.8(b) that the entropy per plaquette of the mixed spin Ising-XXX ladder in terms of ratios $B/J_\parallel$ and $T/J_\parallel$ can particularly show the discontinuous magnetic phase transition corresponding to the magnetization jump from an intermediate plateau appeared in Fig. 2.7(f) to one another. Evidently, the feature and magnetic position of the magnetization jumps is different from the case mixed-spin Ising-XX ladder (or when $\Delta/J_\parallel = 0$).

The adiabatic demagnetization process of the both cases, mixed-spin Ising XX double saw-tooth ladder and mixed spin Ising-XXX double saw-tooth ladder, strongly depends on the single-ion anisotropy parameter $D/J_\parallel$. To prove our claim, we have plotted in Figs. 2.8(c) and 2.8(d) the isothermal dependences of entropy S/N of, respectively, the mixed spin Ising-XX ladder and that of mixed-spin Ising-XXX ladder, in the temperature-field plane for $D/J_\parallel = 2$. The adiabatic demagnetization curves (solid lines of the contour plots) are illustrated in these panels, as well. We see that by tuning the single-ion anisotropy parameter the shape of entropy undergoes significant alterations, and the isentropy lines suddenly accumulate. Moreover, it results
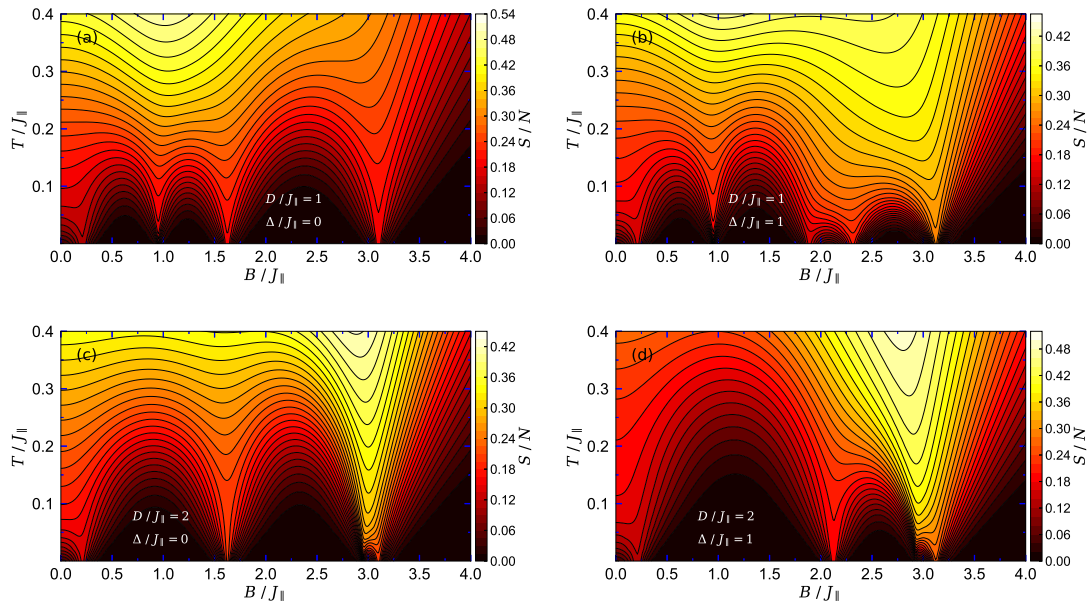
FIGURE 2.8: Contour plot of the entropy as a function of the temperature and the magnetic field of the mixed spin-(1/2, 1) Ising-Heisenberg double saw-tooth ladder for fixed values of $J/J_\parallel = 2.25$ and $J_\perp/J_\parallel = 0.1$. (a) $\Delta/J_\parallel = 0$ and $D/J_\parallel = 1$, (b) $\Delta/J_\parallel = 0$ and $D/J_\parallel = 2$, (c) $\Delta/J_\parallel = 1$ and $D/J_\parallel = 1$, (d) $\Delta/J_\parallel = 1$ and $D/J_\parallel = 2$. The entropy changes from its minimum value $S/N = 0$ (dark regions) up to $S/N \approx 0.5$ (bright regions).

in disappearing some accumulations and appearing new ones at different magnetic positions, revealing the MCE enhances at different magnetic field values. This is true for both models.

Now, let us discuss the effects of single-ion anisotropy $D/J_\parallel$ on the magnetic Grüneisen parameter times magnetic field to realize the cooling/heating property of the models under consideration at low temperature. For this purpose, we plot in Fig. 2.9 the cooling rate as function of ratios $B/J_\parallel$ and $T/J_\parallel$, keeping other parameters of the Hamiltonian as in Fig. 2.8. In accordance with general expectations, we witness sharp fall-and-rise containing positive and negative values in vicinity of the critical magnetic fields. When the temperature increases, the magnitude of these peaks rapidly decreases. This behavior is directly connected to the anomalous zero-temperature entropy of the models under consideration at critical points.

Figure 2.9(a) displays the cooling rate of the mixed spin Ising-XX double saw-tooth ladder as a function of the magnetic field for three selected temperatures $T/J_\parallel = 0.04$, $T/J_\parallel = 0.06$, and $T/J_\parallel = 0.1$ by assuming fixed $\Delta/J_\parallel = 0$ and $D/J_\parallel = 1$. The blue curve starts at zero magnetic field and crosses the first transition at $B_c/J_\parallel \approx 0.2$ that recalls the magnetization jump from zero to intermediate 1/7-plateau of saturation magnetization. Further increase of the magnetic field results in arising second fall-and-rise at proximately $B_c/J_\parallel \approx 1$ which cuts two ground states with magnetization value $M/M_s = 1/7$ and $M/M_s = 3/7$. Third peak arises at $B_c/J_\parallel \approx 1.5$, where the the magnetization jump occurs from 3/7-plateau to 5/7 plateau with respect to saturation value. Compared with aforementioned enhanced MCEs, there is a giant
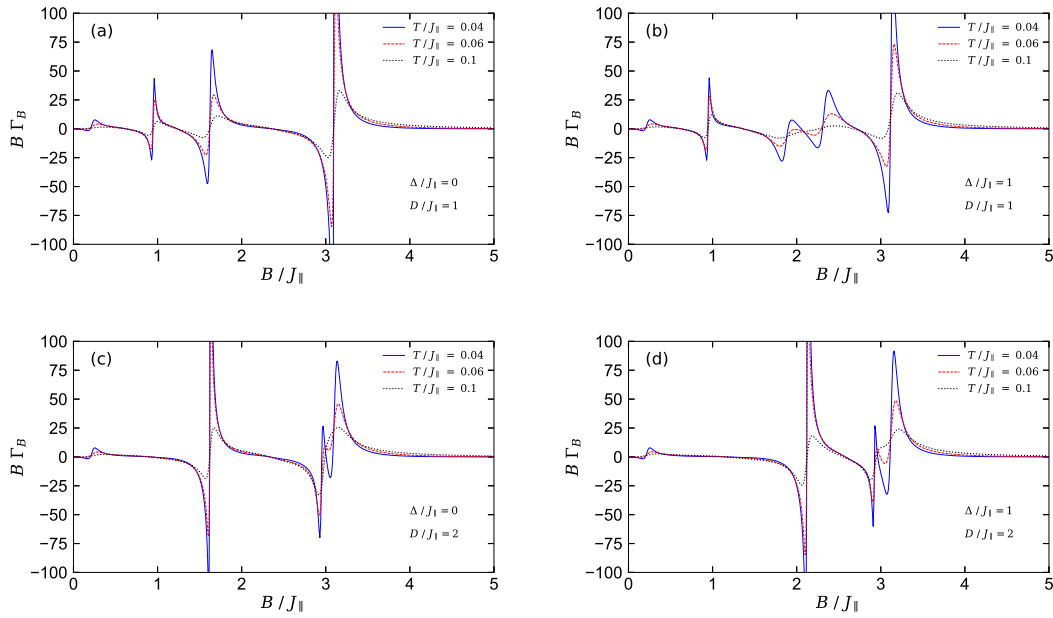
FIGURE 2.9: Grüneisen parameter multiplied by the magnetic field $B\Gamma_B$ as a function of the magnetic field for three temperatures $T/J_\parallel = 0.04$, $T/J_\parallel = 0.06$, and $T/J_\parallel = 0.1$ at fixed exchange coupling $J/J_\parallel = 2.25$. (a) $\Delta/J_\parallel = 0$ and $D/J_\parallel = 1$. (b) $\Delta/J_\parallel = 1$ and $D/J_\parallel = 1$. (c) $\Delta/J_\parallel = 0$ and $D/J_\parallel = 2$. (d) $\Delta/J_\parallel = 1$ and $D/J_\parallel = 2$. Other parameters have been taken as in Fig. 2.8.

MCE nearby the critical field $B_c/J_\parallel \approx 3.1$ accompanied with the magnetization jump from 5/7-plateau to saturation magnetization. By considering the second model, i.e., mixed spin Ising-XXX double saw-tooth ladder (look at Fig. 2.9(b)), the shape and height of the peaks will notably change. This phenomenon is in accordance with the change in magnetization steps and jumps as illustrated in Fig. 2.7(f).

To get an overall insight into the influence of ratio $D/J_\parallel$ on the cooling process, we display in Figs. 2.9(c) and 2.9(d) the field dependence of the magnetic Grüneisen parameter multiplied by the magnetic field , $B\Gamma_B$ for both models at three different temperatures $T/J_\parallel = 0.04$, $T/J_\parallel = 0.06$, $T/J_\parallel = 0.1$ and fixed $J/J_\parallel = 2.25$, assuming $D/J_\parallel = 2$. Evidently, different critical magnetic fields are observed nearby which the MCE could become enhanced. In result, the single-ion anisotropy considerably affects on the cooling/heating property of the both models. Besides, we observe that the parameter $D/J_\parallel$ has substantial influences on the temperature dependence of the residual entropy in analogous to the mixed spin Ising-XX ladder.

2.4   Mixed spin-(1/2, 1) Ising-Heisenberg two-leg ladder

Various Heisenberg spin models defined on the two-leg ladders have attracted a great deal of attention in theoretical condensed matter due to reveal extremely rich behaviors, dominated by

quantum effects [152, 153, 154, 155, 156]. Two-leg ladders with antiferromagnetic exchange along their rungs [157, 158], as well as, both of antiferromagnetic and ferromagnetic exchanges along legs have been investigated in previous studies [159, 160, 161, 162]. From this perspective, M. T. Batchelor *et al.* [163] have comprehensively investigated the magnetic properties, ground-state phase transition and thermodynamics of various versions of exactly solvable two-leg ladders, both pure spin-1/2 models and mixed spin (1/2, 1) ones, and discussed their implementation in the physics of strong-rung interaction ladder compounds.

Although, there is a great interest on the magnetic and thermodynamic properties of the Spin-1/2 two-leg ladder systems, mixed spin-(1/2, S) Ising-Heisenberg ladders have been much less studied. They exhibit many interesting aspects that would definitely attract a numerous attentions in theoretical condensed matter and magnetic material science. From the experimental point of view, various magnetic materials with obvious quantum nature have been detected whose structures can be characterized in terms of the mixed spin ladders. With this regard, a widespread of organic mixed spin ladders with strong rung coupling have been synthesised [163, 164, 165]. In a resent report [166], H. Lu *et al.* experimentally studied the synthesis, structure, and magnetic properties of a novel diamond chain $Cu_2FePO_4F_4(H_2O)_4$ composed of mixed spins $S_{Cu^{2+}} = 1/2$ and $S_{Fe^{3+}} = 5/2$. The model possesses a noncollinear spin order with successive ground-state phase transitions. In the current section, we introduce a mixed spin-(1/2,1) Ising-XYZ two-leg ladder whose nodal Ising spins play the decoration role. One of applications of this model is that, it can effectively reproduce the mixed spin diamond chain compound $Cu_2FePO_4F_4(H_2O)_4$ by rigorously mapping to equivalence with the introduced mixed-(1/2,1) Ising-Heisenberg two-leg ladder. We prove that the generalized mixed spin-(1/2, 1) Ising-Heisenberg model on a decorated two-leg ladder can be exactly solved through the classical transfer matrix technique and discloses many interesting magnetic properties.

The current progress contributes to manufacture low-dimensional magnetic materials with desired parameters, particularly, when the system involves with the alternating dimer-rung exchange. Moreover, the selected model properly creates the possibility of understanding an Ising-Heisenberg ladder system with the four-spin Ising interaction and leg-rung exchange modulations. The main discoveries form our investigations of this model have been noted in Ref. [27].

2.4.1 Model and its exact solution

The most general Hamiltonian of the two-leg ladder could be then obtained by the sum of all unit blocks represented by dashed rectangle in Fig. 2.10. Due to better characterizing the Hamiltonian, we split all unit blocks to two sub-unit blocks as

$$H = \sum_{j=1}^{N} \left(\mathcal{H}_{\Box}^{j,1} + \mathcal{H}_{\Box}^{j,2} \right), \tag{2.26}$$
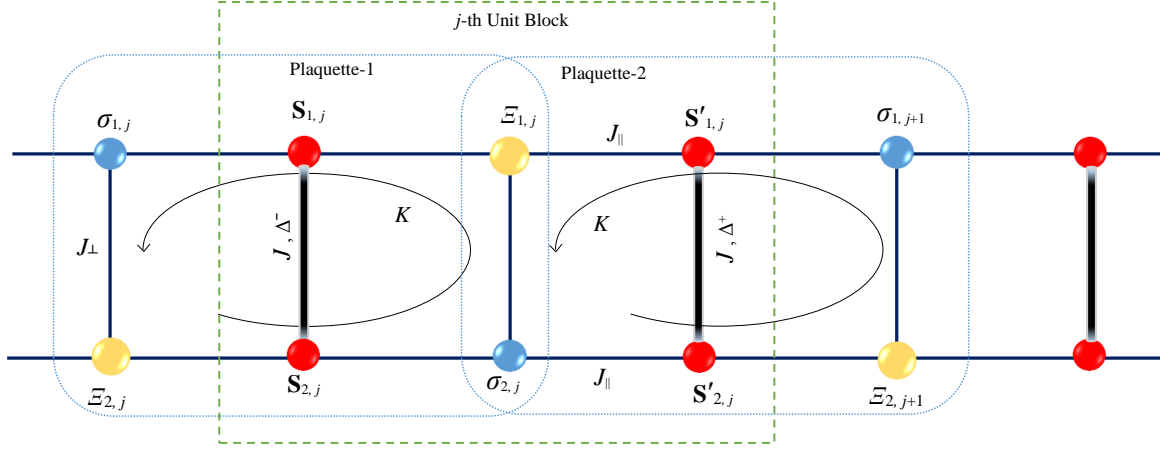
FIGURE 2.10: Sketch of the mixed spin-(1/2,1) Ising-Heisenberg two-leg model on a decorated ladder. Gold balls present effective spin-1 particles, while blue balls denote effective spin-1/2 particles. They interact with their nearest-neighbor sites through Ising-type coupling constant $J_\parallel$ along the legs and through $J_\perp$ along the rungs. Red balls linked together with tick lines show the spin-1/2 interstitial Heisenberg dimers. The region indicated by dashed rectangle displays a unit block (including two plaquettes) that repeats throughout the ladder.

The operators $\mathcal{H}_\square^{j,1}$ and $\mathcal{H}_\square^{j,2}$ define Hamiltonians of two sub-unit blocks so-called square Plaquette-1 ($\mathcal{P}_1$) and Plaquette-2 ($\mathcal{P}_2$), respectively. Hamiltonians of the two square plaquettes can be written as below abbreviated forms

$$
\begin{aligned}
\mathcal{H}_\square^{j,1} = &\Big\{ -J\left(\boldsymbol{S}_{1,j} \cdot \boldsymbol{S}_{2,j}\right)_{\Delta^-} - \sum_{\kappa=1,2} S_{\kappa,j}^z\big(g_1 B + \alpha J_\parallel\big[\sigma_{\kappa,j} + \Xi_{\kappa,j}\big]\big)\Big\}_q + \\
& \Big\{ -\frac{J_\perp}{2}\big[\sigma_{1,j}\,\Xi_{2,j} + \Xi_{1,j}\,\sigma_{2,j}\big] + K\left(\sigma_{1,j}\,\Xi_{2,j}\,\sigma_{2,j}\,\Xi_{1,j}\right) \\
& -\frac{B}{2}\big[g_2(\sigma_{1,j} + \sigma_{2,j}) + g_3(\Xi_{1,j} + \Xi_{2,j})\big]\Big\}_c, \\
\\
\mathcal{H}_\square^{j,2} = &\Big\{ -J\left(\boldsymbol{S}'_{1,j} \cdot \boldsymbol{S}'_{2,j}\right)_{\Delta^+} - \sum_{\kappa=1,2} S_{\kappa,j}^{\prime z}\big(g_1 B + \alpha J_\parallel\big[\sigma_{\kappa,j+j'} + \Xi_{\kappa,j+j''}\big]\big)\Big\}_q + \\
& \Big\{ -\frac{J_\perp}{2}\big[\Xi_{1,j}\,\sigma_{2,j} + \sigma_{1,j+1}\,\Xi_{2,j+1}\big] + K\left(\Xi_{1,j}\,\sigma_{1,j+1}\,\Xi_{2,j+1}\,\sigma_{2,j}\right) \\
& -\frac{B}{2}\big[g_2(\sigma_{2,j} + \sigma_{1,j+1}) + g_3(\Xi_{1,j} + \Xi_{2,j+1})\big]\Big\}_c,
\end{aligned}
\tag{2.27}
$$

where $\boldsymbol{S}_{\kappa,j}^a(\boldsymbol{S}_{\kappa,j}^{\prime a})$ indicates spatial components of being the Pauli operators to the leg κ and j-th ($j+1$-th) rung under periodic boundary conditions. $a = \{x, y, z\}$ denotes the direction of the Pauli matrices in the $x-$, $y-$ and $z-$axis, respectively. Subscripts q and c represent, respectively, the quantum and classical parts of the Hamiltonians. Here, N is the number of unit blocks which is supposed to be even, and we assume that each pair of quantum spins $\boldsymbol{S}_{1,j}$ ($\boldsymbol{S}'_{1,j}$) and $\boldsymbol{S}_{2,j}$ ($\boldsymbol{S}'_{2,j}$), interact through the fully anisotropic XYZ exchange coupling

$$
\begin{aligned}
J\left(\boldsymbol{S}_{1,j} \cdot \boldsymbol{S}_{2,j}\right)_{\Delta^-} &= J\big[\big((1+\gamma)S_{1,j}^x S_{2,j}^x + (1-\gamma)S_{1,j}^y S_{2,j}^y\big) + \Delta^-\, S_{1,j}^z S_{2,j}^z\big], \\
J\left(\boldsymbol{S}_{1,j}^{\prime z} \cdot \boldsymbol{S}_{2,j}^{\prime z}\right)_{\Delta^+} &= J\big[\big((1+\gamma)S_{1,j}^x S_{2,j}^x + (1-\gamma)S_{1,j}^y S_{2,j}^y\big) + \Delta^+\, S_{1,j}^z S_{2,j}^z\big],
\end{aligned}
\tag{2.28}
$$

where, J represents the ferromagnetic exchange interaction between the interstitial Heisenberg dimers, while γ is the XY-anisotropy. Subscripts $\Delta^- = (1 - \Delta)/2$ and $\Delta^+ = (1 + \Delta)/2$ denote alternative rung-exchange anisotropy in the interstitial dimers respectively, $\mathcal{P}_1$-dimer and $\mathcal{P}_2$-dimer, where Δ $(-1 \leq \Delta \leq 1)$ stands for the exchange anisotropy. In addition we supposed $j' = -\frac{(-1)^\kappa - 1}{2}$ and $j'' = \frac{(-1)^\kappa + 1}{2}$. $J_\perp$ and $J_\parallel$ are the Ising-type couplings on the rungs and along the legs, respectively. Tunable coefficient α typically represents the strength of $J_\parallel$ with respect to other parameters. To invoke the strong ferromagnetic Ising-rung interaction condition $J_\perp \gg 0$, in the current research we consider $0 < \alpha < 1$. K manifests four-spin Ising interaction between four nodal sites of each plaquette. These couplings are supposed to include only z-component of the quantum spins. $\sigma_{\kappa,j}$ and $\Xi_{\kappa,j}$ are the $S = 1/2$ and $S = 1$ Ising spin variables, taking values $(1, -1)$ and $(1, 0, -1)$, respectively. B is the external homogeneous magnetic field applied in the z-direction. Motivated by assuming mixed spin parties in the ladder, we here optionally consider three different static Landé g-factors g_1, g_2 and g_3, denoting three different particles in the spin model. Multiplicity of the parameters in the Hamiltonian makes enable us to introduce a more flexible and eligible model for both of the theoretical investigations and experimental analysis specially for mixed-spin two-leg ladders and metal ions doped spin ladders [167, 168, 169].

2.4.2 The exact solution within the classical transfer-matrix formalism

We perform the generalized classical transfer-matrix technique to obtain the partition function of the model. To study the thermodynamics of the mixed spin-(1/2,1) Ising-Heisenberg two-leg ladder, we realize that Hamiltonians of each pair of unit block commute with each other. Consequently, the partition function of the model could be expressed as the product of Boltzmann factors corresponding to the unit blocks possessing the same transfer matrix $\mathbf{T}$, namely

$$Z = \text{Tr}\,[\mathbf{T}^N] = \text{Tr}\left(\prod_{j=1}^{N} e^{\left[-\beta\left(\mathcal{H}_\square^{j,1} + \mathcal{H}_\square^{j,2}\right)\right]}\right). \tag{2.29}$$

To obtain above partition function, one can apply the transfer-matrix approach using the product of Boltzmann factors for the sub-unit blocks with Hamiltonians $\mathcal{H}_\square^{j,1}$ and $\mathcal{H}_\square^{j,2}$. Hence, the 6×6 transfer-matrix of a unit block can be written as

$$\mathbf{T} = \boldsymbol{\mathcal{W}}(\sigma_{1,j},\ \Xi_{2,j} | \Xi_{1,j},\ \sigma_{2,j}) \overline{\boldsymbol{\mathcal{W}}}(\Xi_{1,j},\ \sigma_{2,j} | \sigma_{1,j+1},\ \Xi_{2,j+1}). \tag{2.30}$$

6×6 fully symmetric matrices $\boldsymbol{\mathcal{W}}$ and $\overline{\boldsymbol{\mathcal{W}}}$ are Boltzmann factors for the sub-unit blocks with Hamiltonians $\mathcal{H}_\square^{j,1}$ and $\mathcal{H}_\square^{j,2}$, respectively.

The procedure of deducing eigenvalues of the Hamiltonians of 4-sites plaquettes and their corresponding transfer-matrix coefficients is given below.

Consider the mixed spin-(1/2,1) Ising-Heisenberg two-leg model on a decorated ladder. The corresponding 6×6 transfer-matrix per block is given by Eq. (2.30). For simplicity, we divide the Boltzmann factors $\boldsymbol{w}$ and $\overline{\boldsymbol{w}}$ into classical and quantum parts such that

$$\boldsymbol{w}\left(\sigma_{1,j},\ \Xi_{2,j}|\Xi_{1,j},\ \sigma_{2,j}\right) = e^{-\beta\mathcal{H}_c^{1,j}(\sigma_{1,j},\,\Xi_{2,j}|\Xi_{1,j},\,\sigma_{2,j})} \cdot \boldsymbol{w}_q\left(\sigma_{1,j},\ \Xi_{2,j}|\Xi_{1,j},\ \sigma_{2,j}\right),$$

$$\overline{\boldsymbol{w}}\left(\Xi_{1,j},\ \sigma_{2,j}|\sigma_{1,j+1},\ \Xi_{2,j+1}\right) = e^{-\beta\mathcal{H}_c^{2,j}(\Xi_{1,j},\,\sigma_{2,j}|\sigma_{1,j+1},\,\Xi_{2,j+1})} \cdot \overline{\boldsymbol{w}}_q\left(\Xi_{1,j},\ \sigma_{2,j}|\sigma_{1,j+1},\ \Xi_{2,j+1}\right). \tag{2.31}$$

On above, we have the Boltezmann's weight for the quantum parts of the Hamiltonians (2.27)

$$\boldsymbol{w}_q\left(\sigma_{1,j},\ \Xi_{2,j}|\Xi_{1,j},\ \sigma_{2,j}\right) = \sum_{n=1}^{4} e^{-\beta\varepsilon_n(\sigma_{1,j},\,\Xi_{2,j}|\Xi_{1,j},\,\sigma_{2,j})},$$

$$\overline{\boldsymbol{w}}_q\left(\Xi_{1,j},\ \sigma_{2,j}|\sigma_{1,j+1},\ \Xi_{2,j+1}\right) = \sum_{n=1}^{4} e^{-\beta\overline{\varepsilon}_n(\Xi_{1,j},\,\sigma_{2,j}|\sigma_{1,j+1},\,\Xi_{2,j+1})}, \tag{2.32}$$

for which ε_n and $\overline{\varepsilon}_n$ ($n = 1, ..., 4$) denote the eigenvalues of the quantum parts of the Hamiltonians (2.27).

The eigenvalues ε_n and $\overline{\varepsilon}_n$ explicitly depend on the values of four classical spin variables of the unit-cells in each block, interacting with the quantum Heisenberg spin dimers $\mathcal{P}_1$-dimer and $\mathcal{P}_2$-dimer. They can be easily found by the straightforward diagonalization of the quantum parts of the Hamiltonians in the standard Ising basis $(|\uparrow\uparrow\rangle, |\uparrow\downarrow\rangle, |\downarrow\uparrow\rangle, |\downarrow\downarrow\rangle)$. Thus eigenvalues ε_n are

$$\frac{\varepsilon_{1,4}}{J_\parallel} = \frac{J}{J_\parallel}(1 - \Delta) \mp \left[\frac{2g_1 B}{J_\parallel} \pm \left(\sigma_{1,j} + \Xi_{2,j} + \sigma_{2,j} + \Xi_{1,j}\right)\right]$$

$$\frac{\varepsilon_{2,3}}{J_\parallel} = \frac{J}{J_\parallel}(\Delta - 1) \pm \sqrt{\left(\sigma_{1,j} - \Xi_{2,j} - \sigma_{2,j} + \Xi_{1,j}\right)^2 + 16\left(\frac{J}{J_\parallel}\right)^2}, \tag{2.33}$$

and for $\overline{\varepsilon}_n$ we have analogously

$$\frac{\overline{\varepsilon}_{1,4}}{J_\parallel} = \frac{J}{J_\parallel}(1 + \Delta) \mp \left[\frac{2g_1 B}{J_\parallel} \pm \left(\Xi_{1,j} + \sigma_{2,j} + \Xi_{1,j+1} + \sigma_{2,j+1}\right)\right]$$

$$\frac{\overline{\varepsilon}_{2,3}}{J_\parallel} = \frac{J}{J_\parallel}(-1 - \Delta) \pm \sqrt{\left(\Xi_{1,j} - \sigma_{2,j} - \Xi_{2,j+1} + \sigma_{1,j+1}\right)^2 + 16\left(\frac{J}{J_\parallel}\right)^2}. \tag{2.34}$$

The transfer matrix of the $\mathcal{P}_1$ has the symmetric form

$$\mathcal{T} = \begin{pmatrix} \mathcal{A} & \mathcal{G} & \tau & \tau & \mathcal{K} & \mathcal{U} \\ \mathcal{G} & \mathcal{B} & \Omega & \mathcal{Q} & \mathcal{R} & \mathcal{S} \\ \tau & \Omega & \mathcal{C} & \mathcal{V} & \mathcal{W} & \gamma \\ \tau & \mathcal{Q} & \mathcal{V} & \mathcal{C} & \mathcal{X} & \gamma \\ \mathcal{K} & \mathcal{R} & \mathcal{W} & \mathcal{X} & \mathcal{D} & \mathcal{J} \\ \mathcal{U} & \mathcal{S} & \gamma & \gamma & \mathcal{J} & \mathcal{E} \end{pmatrix}, \tag{2.35}$$

where by considering

$$z_1 = e^{\beta J_\perp}, \ \lambda = e^{\beta K}, \ \mu_1 = e^{\beta g_1 B}, \ \mu_2 = e^{\beta g_2 B}, \ \mu_3 = e^{\beta g_3 B}, \ \delta = e^{\beta \Delta^- J},$$

the following notations are adopted for the all components of the transfer-matrix:

$$
\begin{aligned}
\mathcal{A} &= 4(z_1^{-1}\lambda^{-1}\mu_2^2\mu_3^2)(\varphi_4 + \psi_2^0), \ \mathcal{G} = 4(z_1^{-\frac{1}{2}}\mu_2^2\mu_3)(\varphi_3 + \psi_2^1), \\
\mathcal{K} &= 4(z_1^{-\frac{1}{2}}\mu_3)(\varphi_1 + \psi_2^1), \ \mathcal{U} = 4(z_1^{-1}\lambda^{-1})(\varphi_0 + \psi_2^0), \\
\mathcal{B} &= 4(\mu_2^2)(\varphi_2 + \psi_2^0), \ \mathcal{Q} = 4(z_1^{-\frac{1}{2}}\mu_3)(\varphi_1 + \psi_2^3), \\
\mathcal{R} &= 4(\varphi_0 + \psi_2^2), \ \mathcal{S} = 4(z_1^{-\frac{1}{2}}\mu_3^{-1})(\varphi_1 + \psi_2^1), \\
\mathcal{C} &= 4(z_1\lambda^{-1})(\varphi_0 + \psi_2^0), \ \mathcal{V} = 4(z_1^1\lambda^{-1})(\varphi_0 + \psi_2^4), \\
\mathcal{W} &= 4(z_1^{\frac{1}{2}}\mu_3^{-1})(\varphi_{-1} + \psi_2^3), \ \mathcal{X} = 4(z_1^{\frac{1}{2}}\mu_2^{-2}\mu_3)(\varphi_{-1} + \psi_2^1), \\
\mathcal{D} &= 4(\mu_2^{-2})(\varphi_{-2} + \psi_2^0), \ \mathcal{J} = 4(z_1^{-\frac{1}{2}}\mu_2^{-2}\mu_3^{-1})(\varphi_{-3} + \psi_2^1), \\
\mathcal{E} &= 4(z_1^{-1}\lambda^{-1}\mu_2^{-2}\mu_3^{-2})(\varphi_{-4} + \psi_2^0), \\
\tau &= 4(\lambda\mu_2^2)(\varphi_2 + \psi_2^2), \ \gamma = 4(\lambda\mu_3^{-2})(\varphi_{-2} + \psi_2^2), \\
\Omega &= 4(z_1^{\frac{1}{2}}\mu_2^2\mu_3^{-1})(\varphi_1 + \psi_2^1),
\end{aligned}
\tag{2.36}
$$

for which functions φ and ψ are defined as

$$
\begin{aligned}
\varphi_n &= 2\delta^{-1}\cosh(\beta[2g_1 B - nJ]), \\
\psi_m^{m'} &= 2\delta\cosh(\beta\sqrt{(mJ)^2 + (m'J_\parallel)^2}).
\end{aligned}
$$

Analogously, the Boltzmann factors for the $\mathcal{P}_2$-dimer are expressed in a similar way to the $\mathcal{P}_1$-dimer. The transfer matrix of the $\mathcal{P}_2$ can be easily obtained in an analogous procedure to the $\mathcal{P}_1$, but by substituting parameter Δ^- with Δ^+. Eventually, the transfer matrix of the unit blocks can be given by $\mathbf{T} = \mathcal{T}\mathcal{T}'$, for which $\mathcal{T}'$ is the transfer matrix of the Plaquette-2. Due to abbreviate analytical expressions we leave writing this matrix.

2.4.3 Gibbs free energy and thermodynamic parameters

To derive forthright expressions for all thermodynamic parameters of the mixed spin-(1/2,1) Ising-Heisenberg two-leg ladder, the partition function should be calculated by considering unit block Hamiltonians of the model written in Eq. (2.27). In the thermodynamic limit, the free energy per block can be expressed as

$$f = -\frac{1}{\beta}\ln \Lambda_{max}, \tag{2.37}$$

where, Λ_{max} is the largest eigenvalue of the transfer matrix **T**. Magnetization, entropy and specific heat of the model can be obtained using the Gibbs free energy as follows

$$M = -\Big(\frac{\partial f}{\partial B}\Big)_T, \quad S = -\Big(\frac{\partial f}{\partial T}\Big)_B, \quad C = -T\Big(\frac{\partial^2 f}{\partial T^2}\Big)_B. \tag{2.38}$$

One can exactly obtain Λ_{max} and in turn the thermodynamic parameters of the model under consideration using numerical procedure that we have expressed in our publication [62].

2.4.4 Magnetization process and discontinuous ground-state phase transition

We begin by exploring the low-temperature magnetization process of the mixed spin-(1/2, 1) Ising-XYZ two-leg ladder. The 3-D magnetization curves in the $(B/\alpha J - J/\alpha J_\parallel)$ plane are plotted in Fig. 4.6 for three different fixed values of the special parameter $K/\alpha J_\parallel$. In all figures, two distinguished sets of Landé g-factors g_1, g_2 and g_3 have been optionally assumed. In fact, we formally consider two different versions of spin localization in the body of ladder. First version is assembled, for example, by set $\{g_1 = 1,\ g_2 = 1,\ g_3 = 2\}$, revealing nodal spin-1/2 particles (dark-blue balls in Fig. 2.10) and Heisenberg dimers (red balls in Fig. 2.10) have identical nature. Second version is modulated by set $\{g_1 = 1,\ g_2 = 4,\ g_3 = 2\}$, motivating by consideration all particles in the ladder have different nature. Nevertheless, we enable readers to select a wide range of Landé g-factors to investigate the model by following our technical procedure.

Panels 4.6(a), 4.6(c), 4.6(e) display the normalized magnetization M with respect to its saturation value M_s for the set $\{g_1 = 1,\ g_2 = 1,\ g_3 = 2\}$, denoting spin-1/2 particles localized on the legs and on the rungs have identical g-factors. Panels 4.6(b), 4.6(d), 4.6(f) illustrate the magnetization for different set of g-factors, i.g., $\{g_1 = 1,\ g_2 = 4,\ g_3 = 2\}$ revealing all particles interacted together have different g-factors. Meanwhile, three different values of the cyclic four-spin Ising interaction $K/\alpha J_\parallel$ have been considered. Panels 4.6(a) , 4.6(b) represent 3-D magnetization curve of the model for two different sets of Landé g-factors such that $K/\alpha J_\parallel = 0$. In panels 4.6(c) , 4.6(d) we consider fixed value $K/\alpha J_\parallel = 1$, and in panels 4.6(e) , 4.6(f) we have assumed $K/\alpha J_\parallel = 2$.

Generally speaking, as it is illustrated in Fig. 4.6, the alterations of cyclic four-spin Ising interaction has substantial influences on the magnetization behavior in $(B/\alpha J_\parallel - J/\alpha J_\parallel)$ plane. We discuss this stimulating medium in Fig. 2.12. Possible magnetic ground states of the mixed spin-(1/2,1) Ising-Heisenberg two-leg ladder can be found by changing in magnetization behavior, depending on the mutual interplay between the model parameters Δ^-, Δ^+, $J_\perp/\alpha J_\parallel$ and $K/\alpha J_\parallel$. It is argued in Figs. 2.12 and 2.13, the ground-state phase diagram in the $(B/\alpha J_\parallel - J/\alpha J_\parallel)$ plane and $(B/\alpha J_\parallel - K/\alpha J_\parallel)$ plane, respectively. In this study, we focus on the interplay between the ratio $K/\alpha J_\parallel$ and zero-temperature phase spectra of the model.
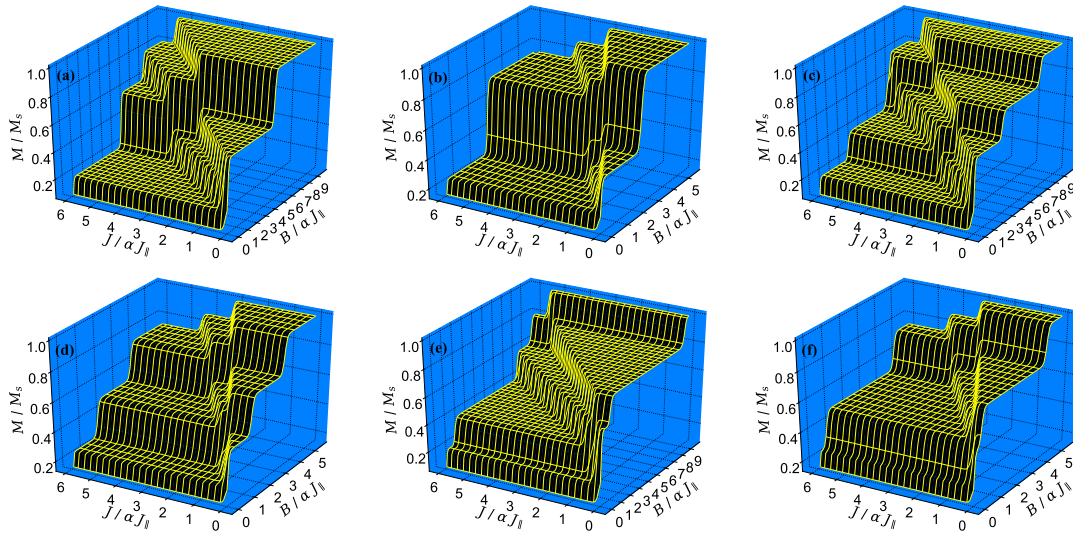
FIGURE 2.11: 3-D plots of the low-temperature magnetization per its saturation value as a function of the magnetic field $B/\alpha J_\parallel$ and the interaction ratio $J/\alpha J_\parallel$ where fixed values, $\alpha = 0.5$, $\Delta = 0.5$, $\gamma = 0.5$, and $J_\perp/\alpha J_\parallel = 5$ are assumed. In this plot and next plots we generally consider two different sets for the Landé g-factors g_1, g_2 and g_3. (a), (c), (e) $\{g_1 = 1,\ g_2 = 1,\ g_3 = 2\}$; (b), (d), (f) $\{g_1 = 1,\ g_2 = 4,\ g_3 = 2\}$. Also, three different values of the four-spin Ising term $K/\alpha J_\parallel$ have been evaluated. (a) , (b) $K/\alpha J_\parallel = 0$; (c) , (d) $K/\alpha J_\parallel = 1$; (e) , (f) $K/\alpha J_\parallel = 2$. We here consider $T/\alpha J_\parallel = 0.12$.

Figure 2.12 (a) illustrates the zero-temperature phase diagram of the ladder in $(B/\alpha J_\parallel - J/\alpha J_\parallel)$ plane for $K/\alpha J_\parallel = 0$ and g-factors set $\{g_1 = 1,\ g_2 = 1,\ g_3 = 2\}$. Other parameters have been assumed to be $\alpha = 0.5$, $\Delta = 0.5$, $\gamma = 0.5$, and $J_\perp/\alpha J_\parallel = 5$. The later assumption denotes the interaction between spin-1/2 and spin-1 particles localized on the Ising rungs of the ladder to be strong-rung ferromagnetic interaction. A notable remark from Fig. 2.12 is that level-crossing magnetic field shown by red and blue lines in all panels has identical gradients with a linear dependence on the exchange interaction $J/\alpha J_\parallel$. The model, independent of the quantity $K/\alpha J_\parallel$, presents in the low-temperature magnetization curve an instant magnetization jump from zero to an intermediate plateau normalized with respect to the saturation magnetization.

It can be seen from Fig. 2.12 (a) that for the case $K/\alpha J_\parallel = 0$ when the set of g-factors $\{g_1 = 1,\ g_2 = 1,\ g_3 = 2\}$ is considered, the model may also exhibits several intermediate plateaux such as $(1/5)-$plateau, $(2/5)-$plateau, $(3/5)-$plateau and $(4/5)-$plateau of the saturation value M_s. On the other hand, as illustrated in Fig. 2.12 (b), when the set $\{g_1 = 1,\ g_2 = 4,\ g_3 = 2\}$ is assumed, the model reproduces magnetic ground-state phase spectra corresponding to the magnetization $(1/4)-$plateau, $(3/8)-$plateau, $(1/2)-$plateau, $(3/4)-$plateau and $(7/8)-$plateau of the saturation value (the same fixed values of all parameters to Fig. 4.6(b) are supposed). Filled-plus marks in both panels 2.12 (a) and 2.12 (b) demonstrate the co-ordinates of critical exchange interactions $J/\alpha J_\parallel = 4$ and $J/\alpha J_\parallel = 2$ at which four ground-states become degenerate. Although, each point of the both blue and red lines is fascinating to count in our investigations, on an optional basis we choose two introduced quadruple points such that they play the most
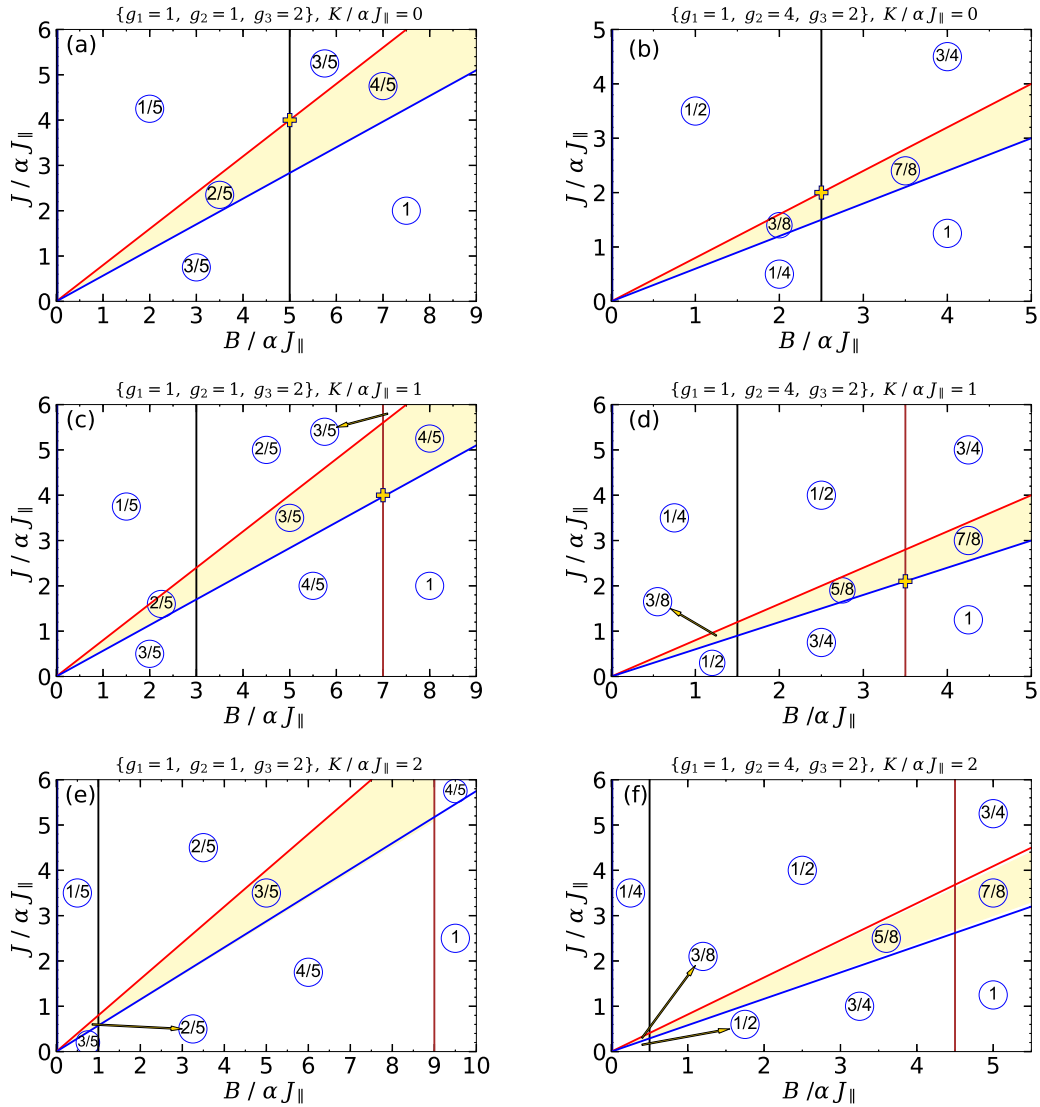
FIGURE 2.12: The ground-state phase diagram of the mixed-spin Ising-XYZ two-leg ladder within the $(B/\alpha J_\parallel - J/\alpha J_\parallel)$ plane for three different values of the ratio $K/\alpha J_\parallel$. Solid lines with different colors label discontinuous phase transitions. Shaded area in all figures are the same. Fractional numbers rounded by circles indicate the corresponding magnetization plateau to a given ground-state in units of saturated magnetization M_s. For example, 1/5 denotes intermediate one-fifth plateau, whereas 1/2 represents magnetization one-half plateau, and so on. (a) $\{g_1 = 1, g_2 = 1, g_3 = 2\}$ and $K/\alpha J_\parallel = 0$, (b) $\{g_1 = 1, g_2 = 4, g_3 = 2\}$ and $K/\alpha J_\parallel = 0$. (c) $\{g_1 = 1, g_2 = 1, g_3 = 2\}$ and $K/\alpha J_\parallel = 1$, (d) $\{g_1 = 1, g_2 = 4, g_3 = 2\}$ and $K/\alpha J_\parallel = 1$. (e) $\{g_1 = 1, g_2 = 1, g_3 = 2\}$ and $K/\alpha J_\parallel = 2$, (f) $\{g_1 = 1, g_2 = 4, g_3 = 2\}$ and $K/\alpha J_\parallel = 2$. The same set of other parameters to Fig. 4.6 have been conceived.

important role to continue our studies on the quantum correlation and the thermodynamics of the model.

A deep insight into the nature of different phase boundaries can be obtained by considering the typical cyclic four-spin Ising interaction in the magnetization process. With this in mind, we have plotted in Figs. 2.12 (c)-2.12 (f) the ground-state phase diagram when the system involves
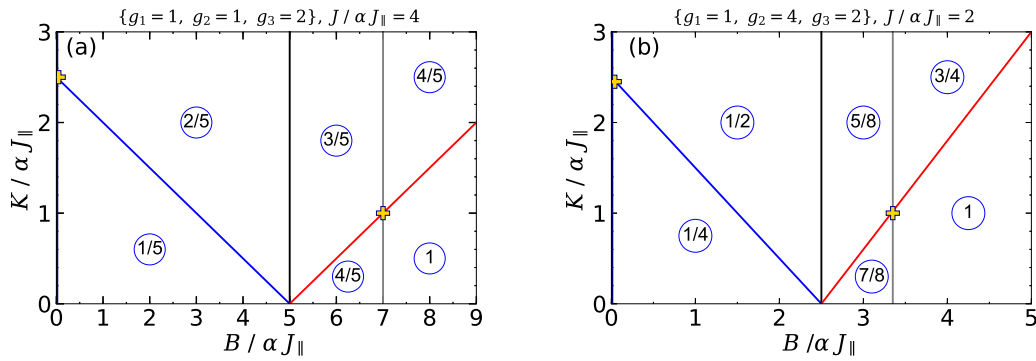
FIGURE 2.13: First-order zero-temperature phase transition of the model within the $(B/\alpha J_\parallel - K/\alpha J_\parallel)$ plane. (a) $\{g_1 = 1, g_2 = 1, g_3 = 2\}$ and $J/\alpha J_\parallel = 4$, (b) $\{g_1 = 1, g_2 = 4, g_3 = 2\}$ and $J/\alpha J_\parallel = 2$. Other parameters of the Hamiltonian have been taken as for Fig. 4.6. Filled pluses display the intersection of multiple ground states, where the degeneracy between them occurs.

an additional Ising term $K/\alpha J_\parallel \neq 0$. Surprisingly, the phase boundaries undergo substantial changes. For instance, when $K/\alpha J_\parallel > 0$ for the set $\{g_1 = 1, g_2 = 4, g_3 = 2\}$ an intermediate $(5/8)$−plateau is visible in the magnetization curve (Fig. 2.12 (d)).

To bring an insight into how the cyclic four-spin Ising term play its rule to confine magnetic ground-state phase boundaries, we plot in Fig. 2.13 the possible ground-state phase diagram in the $(B/\alpha J_\parallel - K/\alpha J_\parallel)$ plane, where the co-ordinates of two aforementioned quadruple points have been optionally taken as fixed exchange interactions. To verify this point, in Fig. 2.13(a), is plotted the ground-state phase diagram when the set of Landé g-factors $\{g_1 = 1, g_2 = 1, g_3 = 2\}$ and fixed $J/\alpha J_\parallel = 4$ are assumed. Figure 2.13(b) demonstrates the same theme but for the set of $\{g_1 = 1, g_2 = 4, g_3 = 2\}$ and fixed $J/\alpha J_\parallel = 2$.

As a result, one perceives from both panels of Fig. 2.13 that there are three critical points at which the boundaries of two or more ground states cut each other off, revealing that they become degenerate. The co-ordinates of these fancy points are as $\{B/\alpha J_\parallel = 0, K/\alpha J_\parallel = 2.5\}$, $\{B/\alpha J_\parallel = 5, K/\alpha J_\parallel = 0\}$ and $\{B/\alpha J_\parallel = 7, K/\alpha J_\parallel = 1\}$ (see panel 2.13(a)). In a different fashion, as shown in panel 2.13(b), we find the same critical points for the cyclic four-spin Ising term at the special co-ordinates $\{B/\alpha J_\parallel = 0, K/\alpha J_\parallel = 2.5\}$, $\{B/\alpha J_\parallel \approx 3.4, K/\alpha J_\parallel = 1\}$. In what follows, we will also focus on the special critical point $K/\alpha J_\parallel = 1$ as a quadruple point to investigate the thermodynamics of the model in different situations.

2.4.5 Specific heat

Let us continue our discussion with the all dependencies of the specific heat of the mixed-spin Ising-XYZ ladder in the $(B/\alpha J_\parallel - T/\alpha J_\parallel)$ plane by considering the co-ordinates of the above-described critical points as fixed values for interaction parameters $J/\alpha J_\parallel$ and $K/\alpha J_\parallel$. To this end, we display in Figs. 2.14 (a) and 2.14 (d) contour plot of the specific heat as a function of

the temperature and the magnetic field with $K/\alpha J_\parallel = 0$ by supposing two conditions $\{g_1 = 1, g_2 = 1, g_3 = 2\}$, $J/\alpha J_\parallel = 4$, and $\{g_1 = 1, g_2 = 4, g_3 = 2\}$, $J/\alpha J_\parallel = 2$, respectively. By inspecting Fig. 2.14 (b) one can realize that there is an anomalous Schottky maximum arisen at high temperatures $(T/\alpha J_\parallel > 1)$ and moderate magnetic fields $(1 < B/\alpha J_\parallel < 3)$. With increase of the magnetic field is demonstrated a smaller peak at relatively low temperatures. The transition temperature could be fixed in the temperature intervals in which the specific heat curve has a steep increase and changes much, as we illustrated by upside down arrows. Under the situation $\{g_1 = 1, g_2 = 4, g_3 = 2\}$, $J/\alpha J_\parallel = 2$ (Fig. 2.14 (e)), the typical Schottky maximum appears at lower magnetic fields.

Another interesting phenomenon observed at sufficiently low temperatures is that, the contour lines of the specific heat are remarkably accumulated nearby the critical magnetic fields at which magnetization jump occurs. It is quite noteworthy that we witness a huge accumulation of contour lines close to the co-ordinates of quadruple point (filled-plus marks in Fig. 2.12) rather than other critical points. For more clarity, we plot in Figs. 2.14 (c) and 2.14 (f) the specific heat as a function of the magnetic field for several fixed values of the temperature where other parameters have been set as panels 2.14 (a) and 2.14 (d), respectively. One can find that the specific heat becomes minimum for a wide range of the temperature at the critical magnetic fields, for example $B_c/\alpha J_\parallel = \{0, 5, 7\}$ when the situation $\{g_1 = 1, g_2 = 1, g_3 = 2\}$, $J/\alpha J_\parallel = 4$, $K/\alpha J_\parallel = 0$ is considered. Under different condition $\{g_1 = 1, g_2 = 4, g_3 = 2\}$, $J/\alpha J_\parallel = 2$, $K/\alpha J_\parallel = 0$, the specific heat minima occur at the critical points $B_c/\alpha J_\parallel = \{0, 2.5, 3.5\}$.

To uncover the effect of cyclic four-spin Ising term $K/\alpha J_\parallel$ on the specific heat behavior, in Fig. 2.15, is shown the specific heat in the $(B/\alpha J_\parallel - T/\alpha J_\parallel)$ plane by assuming fixed value $K/\alpha J_\parallel = 1$ where other parameters have been taken as Figs. 2.14(a)− 2.14(f). In panels 2.15(a) and 2.15(d), we observe significant evolution in the specific heat curve as we consider non-zero cyclic four-spin Ising term $K/\alpha J_\parallel \neq 0$. More importantly, the term $K/\alpha J_\parallel$ results in changing the field-temperature position of the Schottky peak (compare Figs. 2.14(b) and 2.14(e) with Figs. 2.15(b) and 2.15(e)). Analogously, the density of contour lines of the specific heat remarkably increases close to the critical magnetic fields $B_c/\alpha J_\parallel = \{0, 3, 5, 7\}$ (Fig. 2.15(a)) and $B_c/\alpha J_\parallel = \{0, 1.5, 2.5, 3.5\}$ (Fig. 2.15(d)), at which a magnetization jump occurs between two ground states. The specific heat becomes minimum at these special critical magnetic fields (see panels 2.15(c) and 2.15(f)).

2.4.6 Magnetocaloric effect

In this part, let us examine MCE properties of the mixed-spin (1/2, 1) Ising-XYZ two-leg ladder and present the most interesting results obtained for the isentropy lines together with magnetic Grüneisen parameter multiplied by the magnetic field $B\Gamma_B$ for two arbitrary sets of Landé g-factors in the limit of quadruple points co-ordinates depicted in Figs. 2.12 and 2.13. We
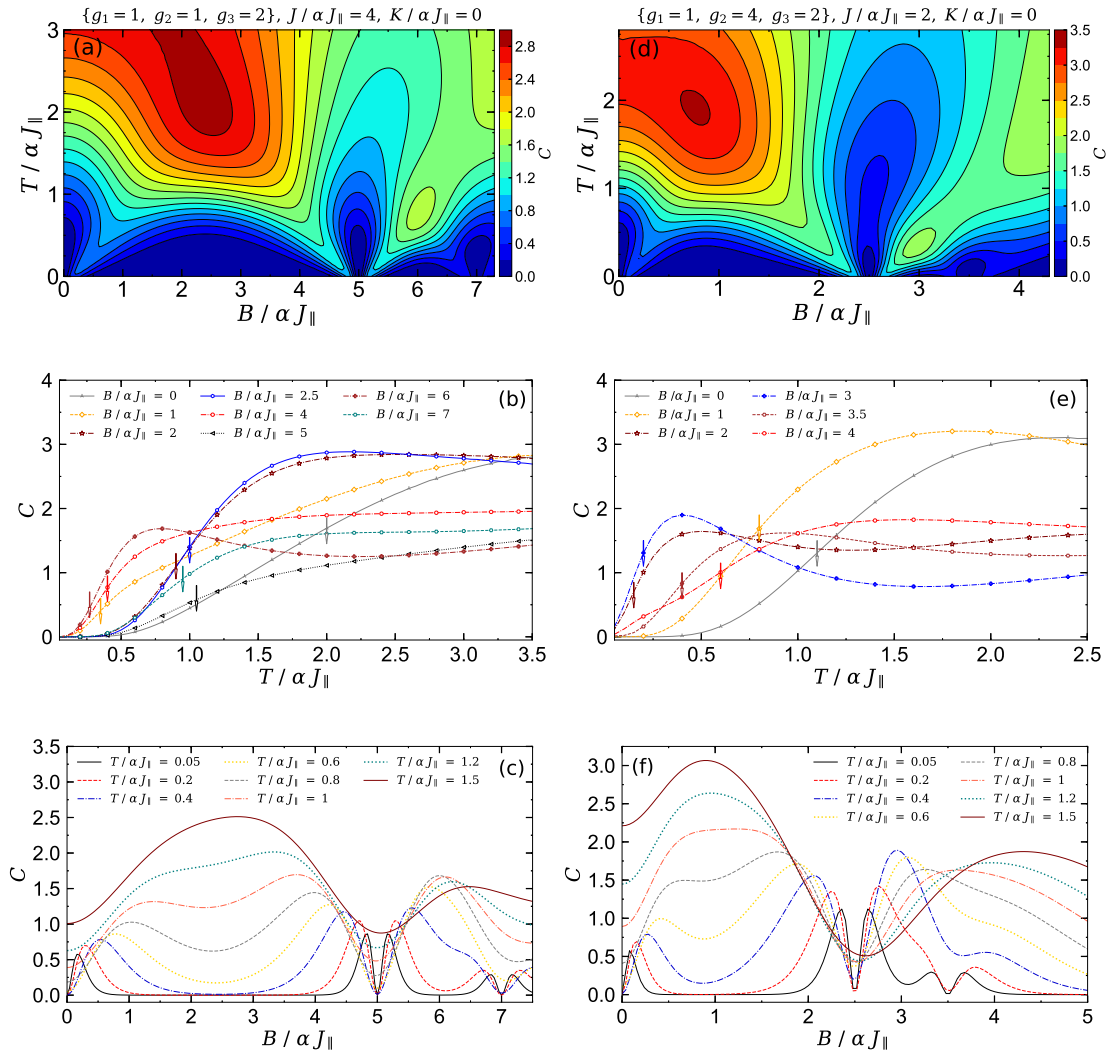
FIGURE 2.14: (a) Contour plot of the specific heat in the $(B/\alpha J_\parallel - T/\alpha J_\parallel)$ plane for the set $\{g_1 = 1, g_2 = 1, g_3 = 2\}$ and fixed value $J/\alpha J_\parallel = 4$. (b) The temperature dependence of the specific heat for several fixed magnetic fields when the condition $\{g_1 = 1, g_2 = 1, g_3 = 2\}$ and $J/\alpha J_\parallel = 4$ is assumed. Arrows illustrate the transition temperature at which the specific heat has a steep increasing to make a maximum. (c) The specific heat as a function of the magnetic field for a number of selected temperatures under the condition $\{g_1 = 1, g_2 = 1, g_3 = 2\}$ and $J/\alpha J_\parallel = 4$. (d) Contour plot of the specific heat for the arbitrary set $\{g_1 = 1, g_2 = 4, g_3 = 2\}$ and fixed value $J/\alpha J_\parallel = 2$. (e) The specific heat curve versus temperature for various fixed values of the magnetic field when the condition $\{g_1 = 1, g_2 = 4, g_3 = 2\}$ and fixed $J/\alpha J_\parallel = 2$ are hypothesized. (f) The specific heat as a function of the magnetic field for a number of selected temperatures, visualizing the set $\{g_1 = 1, g_2 = 4, g_3 = 2\}$ and fixed value $J/\alpha J_\parallel = 2$. In all panels is assumed the zero value for the cyclic four-spin Ising term, i.e., $K/\alpha J_\parallel = 0$, and other parameters have been taken as Fig. 4.6.

would note that one of the most important results obtained from our numerical calculations and simulations is uncovering the fact that the adiabatic demagnetization process strongly depends on the cyclic four-spin Ising interaction parameter $K/\alpha J_\parallel$. In what follows, we try to pave a way to understand this fact through plotting intelligible figures in different perspectives.

Figure 2.16(a) shows the isothermal dependence of entropy $S/8N$ in the field-temperature plane
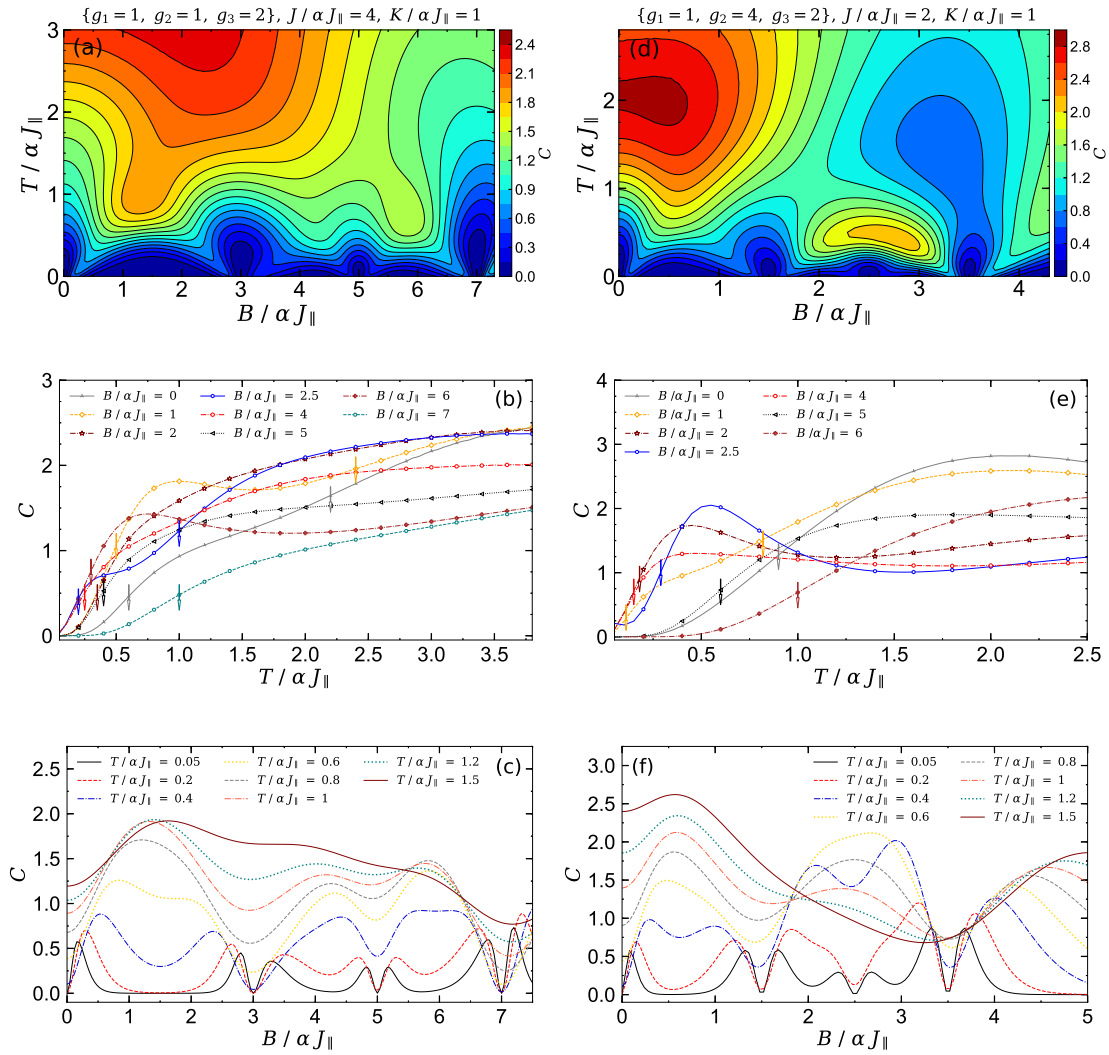
FIGURE 2.15: (a) The temperature and magnetic field dependencies of the specific heat of the model under the same situation to Fig. 2.14 but for non-zero value of the cyclic four-Ising interaction $K/\alpha J_\parallel = 1$. (a), (b), (c) display the specific heat for the set $\{g_1 = 1, g_2 = 1, g_3 = 2\}$, $J/\alpha J_\parallel = 4$, and (d), (e), (f) correspond to the set $\{g_1 = 1, g_2 = 4, g_3 = 2\}$ and fixed value $J/\alpha J_\parallel = 2$, fitting with co-ordinates of the quadruple point marked in Fig. 2.13 (b). Arrows imply the same definition to Figs. 2.14 (b) and 2.14 (e).

including adiabatic demagnetization curves (solid contour lines) for the case when we consider the situation $\{g_1 = 1, g_2 = 1, g_3 = 2\}$ and fixed value $J/\alpha J_\parallel = 4$. It is quite evident that the isentropy lines are suddenly accumulated nearby the critical magnetic fields $B_c/\alpha J_\parallel = \{0, 5, 7\}$. The density of the isentropy lines close to the field-position of quadruple point with the corresponding co-ordinates $(B/\alpha J_\parallel, J/\alpha J_\parallel, K/\alpha J_\parallel) \equiv (5, 4, 0)$ is much more than other places.

In Fig. 2.16(d), we display the isentropic changes of temperature $T/\alpha J_\parallel$ as a function of the external magnetic field $B/\alpha J_\parallel$ for the set $\{g_1 = 1, g_2 = 4, g_3 = 2\}$, assuming fixed values of $J/\alpha J_\parallel = 2$ and $K/\alpha J_\parallel = 0$. It can be seen enhanced regions of MCE at critical points $B_c/\alpha J_\parallel = \{0, 2.5, 3.5\}$ due to the ground-state phase transition and/or magnetization jump
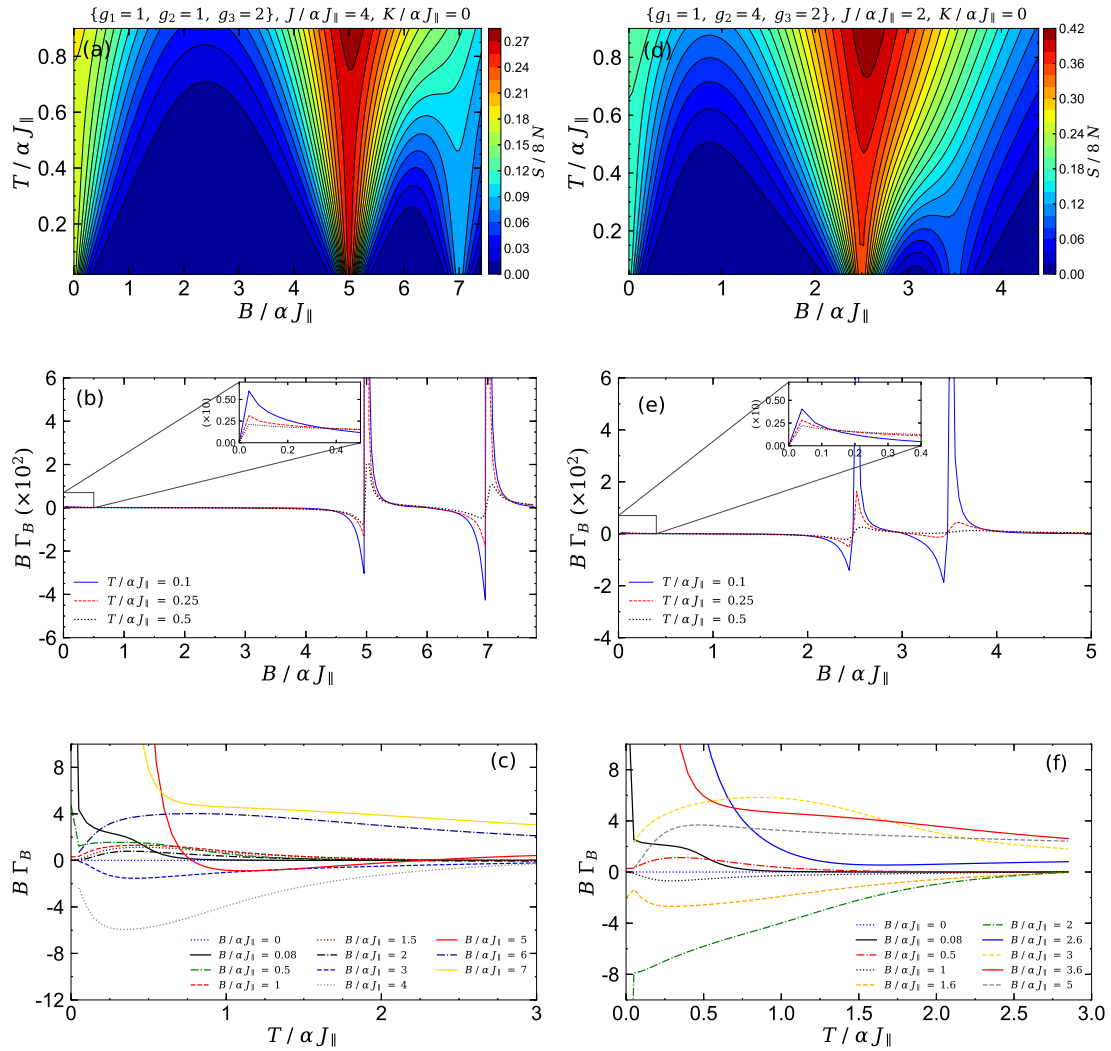
FIGURE 2.16: Entropy of the mixed-spin (1,1/2) Ising-XYZ two-leg ladder and the corresponding magnetic Grüneisen parameter times the magnetic field $B\Gamma_B$ as a functions of the temperature and the magnetic field for the zero cyclic four-Ising interaction $K/\alpha J_\parallel = 0$. (a) The entropy in the field-temperature plane for the case when the set $\{g_1 = 1, g_2 = 1, g_3 = 2\}$ and fixed $J/\alpha J_\parallel = 4$ are assumed. (b) The magnetic field dependencies of the dimensionless parameter $B\Gamma_B$ for three selected temperatures $T/\alpha J_\parallel = 0.1$, $T/\alpha J_\parallel = 0.25$ and $T/\alpha J_\parallel = 0.5$. (c) The temperature dependencies of the parameter $B\Gamma_B$ for several selected values of ratio $B/\alpha J_\parallel$ and the same set of other parameters to panel (a). (d) Isentropic curve in the field-temperature plane such that the set $\{g_1 = 1, g_2 = 4, g_3 = 2\}$ and fixed $J/\alpha J_\parallel = 2$ are considered. (e) The corresponding Grüneisen parameter as function of the magnetic field under the circumstance $\{g_1 = 1, g_2 = 4, g_3 = 2\}$, where fixed $J/\alpha J_\parallel = 2$ is supposed. (f) Grüneisen parameter as function of the temperature under the same circumstances to panel (d) such that various fixed values of the magnetic field are supposed. Remaining parameters have been taken as Fig. 4.6.

from one plateau to another one. In this case, the maximum value of entropy is $S_{\max}/8N \approx 2.07$, where $T > 0$.

To identify the cooling rate of the model in the vicinity of particular field-induced phase transitions, in Fig. 2.16(b), is depicted the quantitative fingerprint of magnetic Grüneisen parameter multiplied by the applied field with respect to the original magnetic field when the set $\{g_1 = 1, g_2 = 1, g_3 = 2\}$ and fixed interaction ratios $J/\alpha J_\parallel = 4$ and $K/\alpha J_\parallel = 0$ are used. In accordance with general expectations, we witness very sharp peaks containing positive and negative values close to the critical magnetic fields at which a ground-state phase transition occurs. When the temperature increases, the magnitude of these peaks rapidly changes. This behavior is directly connected to the anomalous zero-temperature entropy of the model under consideration at critical points.

Accordingly, a similar scenario is presented in Fig. 2.16(e) but for the case $\{g_1 = 1, g_2 = 4, g_3 = 2\}$ and fixed interaction ratio $J/\alpha J_\parallel = 2$, assuming the same set of other parameters as used in Fig. 2.16(d). This imagination reveals an identical enhanced MCE at respective ground-state phase transitions, namely, at critical points $B_c/\alpha J_\parallel = \{0, 2.5, 3.5\}$. In both plots Fig. 2.16(b) and Fig. 2.16(e), is seen a steep decreasing of the cooling rate in the vicinity of zero magnetic field point $B_c/\alpha J_\parallel \approx 0$ (zoomed insets), reminiscing a quick magnetization jump from $M/M_s = 0$ to the magnetization intermediate $(1/5)-$plateau of saturation value.

The temperature dependence of the parameter $B\Gamma_B$ for various fixed values of the magnetic field is presented in Figs. 2.16(c) and 2.16(f) under the same circumstances to, respectively, Fig. 2.16(a) and Fig. 2.16(d). One sees that by cooling the system, close to the critical magnetic field at which ground-state phase transition occurs, parameter $B\Gamma_B$ goes to infinity (solid lines), while for other values of the magnetic field, by ultra-cooling the system ($T/\alpha J_\parallel \ll 1$), $B\Gamma_B$ tends to zero.

Figure 2.17(a) shows the isentropy lines in the field-temperature plane under the same circumstances to Fig. 2.16(a) but for non-zero value $K/\alpha J_\parallel = 1$. By inspecting this figure, one can see that by imposing a non-zero value of cyclic four-spin Ising interaction, an enhanced MCE will appear nearby one another critical magnetic field $B/\alpha J_\parallel = 3$, denoting phase transition from the ground-state with magnetization $M/M_s = 1/5$ to that of with magnetization $M/M_s = 2/5$ (see Fig. 2.12(c)). In Fig. 2.17(d), we plot contour plot of the entropy and a number of isentropy lines for the case $\{g_1 = 1, g_2 = 4, g_3 = 2\}$ and fixed $J/\alpha J_\parallel = 2$ and $K/\alpha J_\parallel = 1$. Again, we observe an extensive variation in the entropy of the model specifically close to the point $B/\alpha J_\parallel = 1.5$, where the magnetization jump happens from $(1/4)-$plateau to $(1/2)-$plateau normalized with the saturation magnetization (see Fig. 2.12(d)). In result, the four-spin Ising interaction $K/\alpha J_\parallel$ has a great influence on the entropy behavior regardless of what values we choose for Landé g-factors.
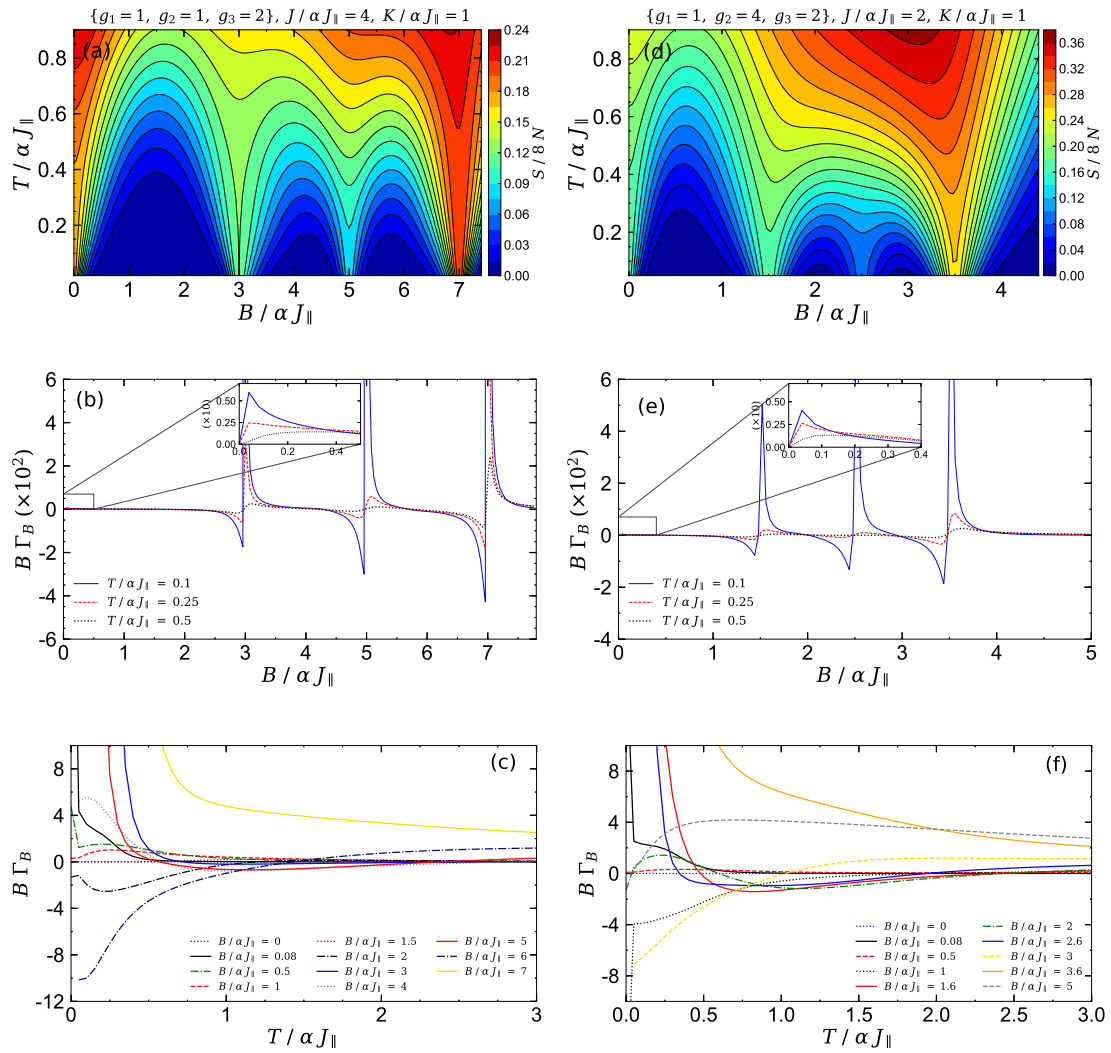
FIGURE 2.17: The entropy and Grüneisen parameter as functions of the temperature and the magnetic field for the non-zero cyclic four-spin Ising interaction $K/\alpha J_\parallel = 1$. (a) The contour plot of the entropy together with a number of isentropy lines for the case $\{g_1 = 1, g_2 = 1, g_3 = 2\}$ and fixed $J/\alpha J_\parallel = 4$. (b) The corresponding magnetic Grüneisen parameter $B\Gamma_B$ versus ratio $B/\alpha J_\parallel$ for three selected temperatures $T/\alpha J_\parallel = 0.1$, $T/\alpha J_\parallel = 0.25$ and $T/\alpha J_\parallel = 0.5$. (c) Dimensionless parameter $B\Gamma_B$ as a function of the ratio $T/\alpha J_\parallel$ for the same parameters set to panel (a), while several fixed magnetic fields are assumed. (d) Isentropy lines for the set $\{g_1 = 1, g_2 = 4, g_3 = 2\}$ and fixed $J/\alpha J_\parallel = 2$. (e) The corresponding magnetic Grüneisen parameter as a function of magnetic field at three different temperatures $T/\alpha J_\parallel = 0.1$, $T/\alpha J_\parallel = 0.25$ and $T/\alpha J_\parallel = 0.5$ under the same condition to panel (d), i.e., $\{g_1 = 1, g_2 = 4, g_3 = 2\}$ and fixed $J/\alpha J_\parallel = 2$. (f) The Grüneisen parameter multiplied by the magnetic field as a function of the temperature for the same parameter set to panel (d), where different fixed values of the magnetic field are selected. Remaining parameters such as α, γ, Δ and $J_\perp/\alpha J_\parallel$ have been assumed as Fig. 4.6.

Last but not least, let us discuss the effects of parameter $K/\alpha J_\parallel$ on the cooling rate. For this purpose, we plot in Figs. 2.17(b) and 2.17(e), the magnetic Grüneisen parameter times the field against ratio $B/\alpha J_\parallel$ at three different temperatures $T/\alpha J_\parallel = \{0.1, 0.25, 0.5\}$, by keeping other parameters of the Hamiltonian as in panels 2.17(a) and 2.17(d), respectively. The blue solid curve in Fig. 2.17(b) starts at almost zero magnetic field with a steep slope (see zoomed

inset) and crosses the first transition at $B/\alpha J_{\parallel} = 3$, and cuts two ground states with the corresponding magnetization values $M/M_s = 1/5$ and $M/M_s = 2/5$ numbered in Fig. 2.12(c). Third peak arises at $B/\alpha J_{\parallel} = 5$, where the boundary between ground states with magnetization $M/M_s = 2/5$ and $M/M_s = 3/5$ exists. Final peak arises at $B/\alpha J_{\parallel} = 7$ which is the magnetic field-position of the quadruple point marked in Fig. 2.12(c). By assuming the set $\{g_1 = 1, g_2 = 4, g_3 = 2\}$ and utilizing fixed value of $J/\alpha J_{\parallel} = 2$ (Fig. 2.17(e)), the magnetic-position of the Grüneisen peaks will change. This phenomenon is in accordance with the change in magnetization steps and jumps as shown in Figs. 4.6(d) and 2.12(d).

The temperature dependence of the parameter $B\Gamma_B$ for several fixed values of the magnetic field is depicted in Figs. 2.17(c) and 2.17(f), where the other parameters have been taken as Fig. 2.17(a) and Fig. 2.17(d), respectively. Nearby the critical magnetic fields, we observe that the behavior of $B\Gamma_B$ against the temperature is similar to the case when $K/\alpha J_{\parallel} = 0$ is assumed. Nonetheless, it is understandable that by considering $K/\alpha J_{\parallel} > 0$, during ultra-cooling process ($T/\alpha J_{\parallel} \ll 1$), parameter $B\Gamma_B$ changes remarkably unlike the case when $K/\alpha J_{\parallel} = 0$. One can optionally allocate different values to the g-factors and creates another g-factor sets and repeat the same procedure. Hence, different outcomes may be achieved.

It could be expected from ground-state phase diagram plotted in Fig. 2.12(e) that by considering higher values of the interaction parameter $K/\alpha J_{\parallel}$ (for instance, $K/\alpha J_{\parallel} = 2$ and fixed $J/\alpha J_{\parallel} = 4$) the magnetic Grüneisen curve would has an extra peak at critical magnetic field $B/\alpha J_{\parallel} = 1$ when the g-factors are set as $\{g_1 = 1, g_2 = 1, g_3 = 2\}$. By inspecting Fig. 2.12(f), one immediately finds that an enhanced MCE will occur at the critical field $B/\alpha J_{\parallel} = 0.5$, as long as, the g-factors are set as $\{g_1 = 1, g_2 = 4, g_3 = 2\}$ and fixed value $J/\alpha J_{\parallel} = 2$ is assumed.

2.4.7 Correlation function

General expression of the nearest neighbor correlation function between Heisenberg dimers of each plaquette relies on the exchange interaction derivative of the Gibbs free energy (Eq. (2.37)). Since we have assumed all interaction parameters between Heisenberg dimers are identical, namely, $J_{j-1} = J_j = J_{j+1} = \cdots = J_{2N} = J$, to get an overall introduction of the first derivative of free energy f, and evoke the pair correlation function $\mathcal{G}_j^{xx}$ of the j-th Heisenberg dimer-rung, we need to consider

$$\mathcal{G}_j^{xx} = \langle \sigma_{1,j}^x \sigma_{2,j}^x \rangle = \langle \sigma_{1,j}'^x \sigma_{2,j}'^x \rangle = -\frac{1}{2\gamma}\frac{\partial f}{\partial J}. \tag{2.39}$$

We plot in Fig. 2.18 the correlation function (2.39) against the interaction ratio $J/\alpha J_{\parallel}$ for a few selected temperatures under particular conditions assumed in previous plots. In order to compare the correlation function of the Heisenberg dimer-rungs $\mathcal{G}_j^{xx}$ with the investigated thermodynamic parameters in previous parts, we first consider the set $\{g_1 = 1, g_2 = 1, g_3 = 2\}$ and a zero value for the cyclic four-spin Ising interaction (Fig. 2.18(a)). The magnetic field has been taken as
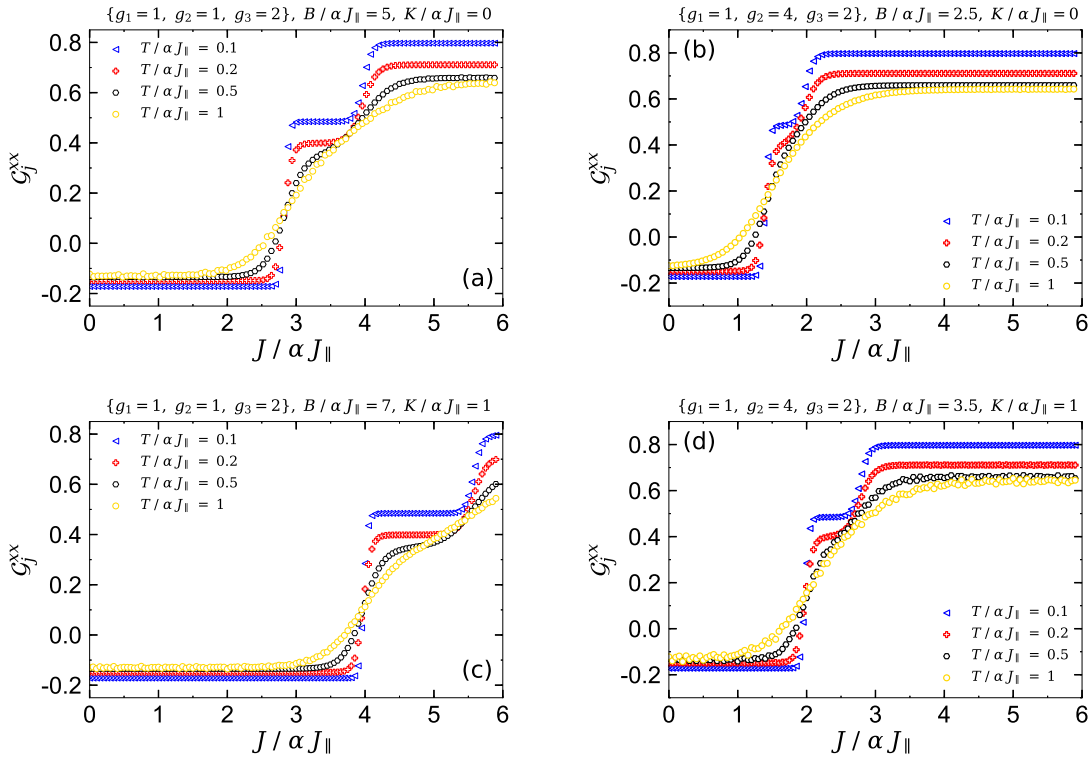
FIGURE 2.18: Pair correlation function for the Heisenberg dimers under different conditions. (a) $\mathcal{G}_j^{xx}$ with respect to the exchange interaction ratio $J/\alpha J_\parallel$ for the set $\{g_1 = 1, g_2 = 1, g_3 = 2\}$ and zero value of the parameter $K/\alpha J_\parallel$. The critical magnetic field $B/\alpha J_\parallel = 5$ has been considered, where other parameters have been assumed as for Fig. 4.6(a), i.e., $\alpha = 0.5$, $\Delta = 0.5$, $\gamma = 0.5$, and $J_\perp/\alpha J_\parallel = 5$. (b) $\mathcal{G}_j^{xx}$ for the set $\{g_1 = 1, g_2 = 4, g_3 = 2\}$ and $K/\alpha J_\parallel = 0$, assuming critical magnetic field $B/\alpha J_\parallel = 2.5$. (c) $\mathcal{G}_j^{xx}$ for the set $\{g_1 = 1, g_2 = 1, g_3 = 2\}$ and non-zero value $K/\alpha J_\parallel = 1$ and fixed $B/\alpha J_\parallel = 7$. (d) $\mathcal{G}_j^{xx}$ for the set $\{g_1 = 1, g_2 = 4, g_3 = 2\}$ and fixed values $K/\alpha J_\parallel = 1$ and $B/\alpha J_\parallel = 3.5$.

fixed value $B/\alpha J_\parallel = 5$ as well, which conveys the field-position of quadruple point marked in Fig. 2.12(a). It is quite surprising that at low temperature ($T/\alpha J_\parallel = 0.1$) there are some plateaux and jumps in the pair correlation function curve. By comparing this figure with Fig. 2.12(a), one instantly finds out that the correlation function jumps occur in the vicinity of quadruple points. As mentioned before, these intriguing points are intersection of four separated ground states. Another elegant remark to pronounce is that when the temperature increases monotonically, the correlation function plateaux gradually disappear until the correlation function curve becomes smooth at high temperatures. In different situation $\{g_1 = 1, g_2 = 4, g_3 = 2\}$, by assuming the fixed field $B/\alpha J_\parallel = 2.5$ the correlation function jumps occur at lower amounts of interaction ratio $J/\alpha J_\parallel$ (Fig. 2.18(b)).

Now, the main question that may involve our mind is that whether the cyclic four-spin Ising term $K/\alpha J_\parallel$ affects the correlation function $\mathcal{G}_j^{xx}$ or not? To answer this question we illustrate in Fig. 2.12(c), the pair correlation function versus the interaction parameter $J/\alpha J_\parallel$ for the set $\{g_1 = 1, g_2 = 1, g_3 = 2\}$ and fixed $K/\alpha J_\parallel = 1$. The field-position of triple point (shown

by filled-plus mark in Fig. 2.12(c)) is optionally considered. The mentioned triple point is the intersection of three ground states with the magnetization values $M/M_s = 3/5$, $M/M_s = 4/5$ and $M/M_s = 1$. Amazingly, imposing a non-zero cyclic four-spin Ising interaction in each plaquette leads to widen the correlation function plateaux. The correlation function jumps occur at higher interaction ratio $J/\alpha J_\parallel$.

Furthermore, we observe that the plateaux appeared in the correlation function curve stay alive at higher temperatures (compare black curve marked with honeycombs plotted in both Figs. 2.18(a) and 2.18(c)). Lower right panel 2.18(d) depicts $\mathcal{G}_j^{xx}$ with respect to the interaction parameter $J/\alpha J_\parallel$, assuming the set $\{g_1 = 1, g_2 = 4, g_3 = 2\}$ and fixed magnetic field $B/\alpha J_\parallel = 3.5$ and $K/\alpha J_\parallel = 1$. By comparing Figs. 2.18(b) and 2.18(d) with each other, we realize that the correlation function intermediate plateau is broadened by applying a non-zero value of the ratio $K/\alpha J_\parallel$. The width of the intermediate plateau appeared in the correlation function curve is in a good agreement with the width of shaded region between red and blue lines plotted in Fig. 2.12.

2.5 Conclusions

The present chapter deals with the magnetic and thermodynamic properties, as well as, MCE of Ising-Heisenberg double saw-tooth ladders and an Ising-Heisenberg mixed spin-(1/2,1) model on a decorated two-leg ladder, which are exactly solvable within the transfer-matrix technique. We performed an extra term so-called cyclic four-spin Ising interaction in the Hamiltonian of the model, which is important to take in to account when the purpose is investigating the physical properties of spin ladders. We have also considered anisotropy property for the Heisenberg dimers in the $z-$direction.

The isentropy lines of models are rapidly accumulated nearby the critical points/lines, which denotes both cooling and heating properties under the same condition at low temperature. The most interesting finding for these selected models is that, alteration of the magnetic anisotropy and single-ion anisotropy considered for the integer spins slightly above (below) the critical points results in cooling/heating during the adiabatic demagnetization process, where the temperature rapidly falls down. So, the anisotropies play an important role to understand cooling process together with discontinuous zero-temperature phase transitions of such spin ladders.

We have also realized that there are some particular points in the field-induced ground-state phase diagram of the model which makes the intersection of several different ground states. Assuming the cyclic four-spin Ising term affects the co-ordinates of these special points. It has been demonstrated that at low temperatures, the specific heat curve anomalously behaves nearby the critical magnetic fields at which a magnetization jump occurs. An anomalous magnetocaloric

effect has been observed close to respective magnetization jumps of the Ising-Heisenberg two-leg ladder. More importantly, toning the magnetic field, four-spin Ising interaction, and the exchange coupling parameter slightly above (below) the critical points result in cooling/heating during the adiabatic demagnetization process, where the temperature rapidly falls down and reaches close to the first-order zero-temperature phase transition.

It is quite surprising that we found an enhanced magnetocaloric effect in the vicinity of discontinuous phase transition points. A notable result is that, for the Ising-Heisenberg two-leg ladder, under ultra-cooling the magnetic Grüneisen parameter goes to infinity nearby the critical magnetic field at which first-order zero-temperature phase transition occurs. We evidenced that by tuning cyclic four-spin Ising term, magnetization plateaux undergoes a substantial changes. Further, the change in correlation function behavior is in an excellent coincidence with the magnetization variations.

Chapter 3

Spin-1/2 Ising-Heisenberg model on 2-D TIT lattices

3.1 Preliminaries

The spin-1/2 Ising-Heisenberg model on geometrically frustrated planar lattices attracts a great deal of research interest as it may exhibit both spontaneous long-range order as well as peculiar spin-liquid phases [170]. Recently $Cu_9X_2(cpa)_6$ (cpa=carboxypentonic acid; X =F, Cl, Br) was discovered to form a particular topological structure, a triangles-in-triangles Kagomé structure [171]. For such group of 2-D Ising-Heisenberg models, the magnetic moments come from Heisenberg trimers with antiferromagnetic interaction. Hence, they can be exactly solved by the transfer-matrix formalism like their 1-D counterparts [22, 26]. Theoretical studies for the spin-1/2 Ising-Heisenberg model on the similar sets of 2-D triangular lattices also exist in the literature [42, 43, 44, 45].

In this chapter, we shed light on the ground-state phase diagram, magnetization and specific heat of the spin-1/2 Ising-Heisenberg model on two modes of new triangle-hexagon lattices including Heisenberg exchange anisotropy in the presence of magnetic field.

3.2 Model and its exact solution

Let us proceed the definition of the spin-1/2 Ising-Heisenberg model on the TIT lattice, which resembles the magnetic data of polymeric coordination compounds $Cu_9X_2(cpa)_6$ on the basis of the spin topology depicted in Fig. 3.1 which leads to the Hamiltonian

$$H = -J_{\mathrm{H}} \sum_{\triangle}^{N} \left[\Delta \left(S_i^x S_j^x + S_i^y S_j^y \right) + S_i^z S_j^z \right] - J_{\mathrm{I}} \sum_{i}^{3N} S_i^z \sigma_i^z, \qquad (3.1)$$
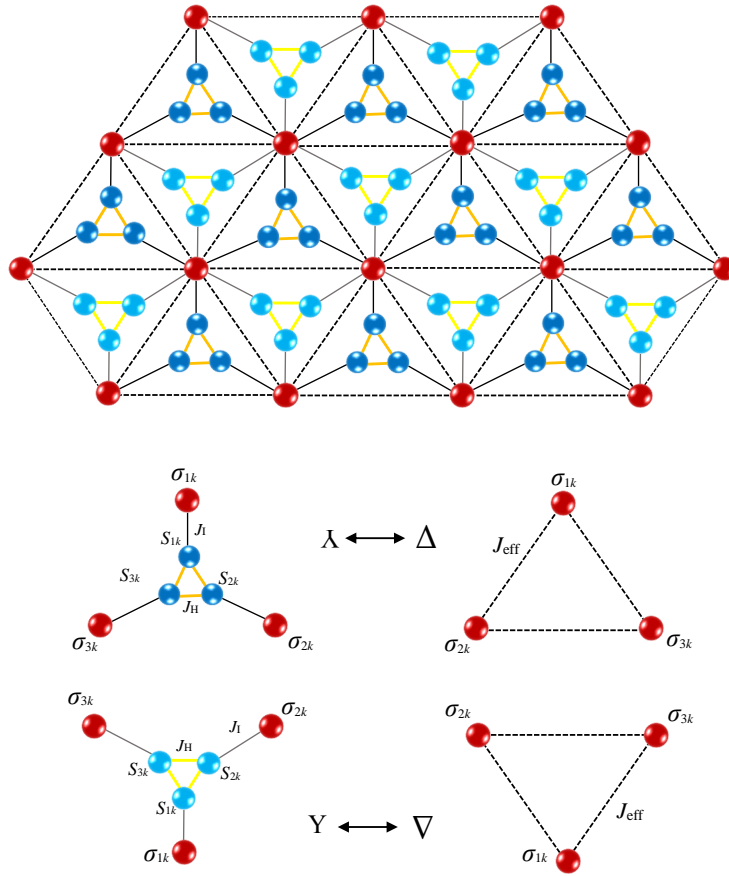
FIGURE 3.1: Schematic drawing of spin-1/2 Ising-Heisenberg model on a 2-D TIT lattices manifested by solid bold lines and balls. And its rigorous mapping to the spin-1/2 Ising model on a simple triangular lattice represented by dashed lines. For mapping process, once we consider just solid bold lines and balls (marking $\gamma = 1$), once we artificially fill the empty part of model with pale lines and balls (marking $\gamma = 2$). Red balls denote the Ising nodal spins, while, all blue balls are Heisenberg trimers.

where S_i^α with $\alpha = x, y, z$ and σ_i^z are spatial components of the spin-1/2 operator of the Heisenberg and Ising spins, respectively. Parameters J_H and J_I stand for the XXZ Heisenberg and Ising interactions, respectively. The total Hamiltonian of the model can be rewritten as

$$H = \sum_{k=1}^{N} \mathcal{H}_k, \tag{3.2}$$

where cluster Hamiltonian $\mathcal{H}_k$ is given by

$$\mathcal{H}_k = -J_\mathrm{H} \sum_{i=1}^{3} \left[\Delta\left(S_{k,i}^x S_{k,i+1}^x + S_{k,i}^y S_{k,i+1}^y\right) + S_{k,i}^z S_{k,i+1}^z \right] - J_\mathrm{I} \sum_{i=1}^{3} \sigma_{k,i}^z S_{k,i}^z, \tag{3.3}$$

with periodic boundary conditions. We suppose $h_1 = J_I\sigma_{k,1}^z$, $h_2 = J_I\sigma_{k,2}^z$, $h_3 = J_I\sigma_{k,3}^z$. The eigenvalues of the uniform case $h_1 = h_2 = h_3 = \pm\frac{J_I}{2}$ are given by

$$
\begin{aligned}
E_{1,2} &= -\frac{3J_H}{4} \mp \frac{3J_I}{4}, & E_{3,4} &= \frac{J_H}{4}(1+2\Delta) + \frac{J_I}{4}, \\
E_{5,6} &= \frac{J_H}{4}(1+2\Delta) - \frac{J_I}{4}, & E_{7,8} &= \frac{J_H}{4}(1-4\Delta) \mp \frac{J_I}{4}.
\end{aligned}
\tag{3.4}
$$

For the non-uniform case $h_1 = h_2 = -h_3 = \pm\frac{J_I}{2}$ (or any other permutation) we have

$$
\begin{aligned}
E_{1,2} &= -\frac{3J_H}{4} \mp \frac{J_I}{4}, & E_{3,4} &= \frac{J_H}{4}(2\Delta+1) \mp \frac{J_I}{4}, \\
E_{5,6} &= \frac{J_H(1-\Delta) - J_I}{4} \mp \frac{1}{2}\sqrt{\left(\frac{J_H\Delta}{2} - J_I\right)^2 + 2(J_H\Delta)^2}, \\
E_{7,8} &= \frac{J_H(1-\Delta) + J_I}{4} \mp \frac{1}{2}\sqrt{\left(\frac{J_H\Delta}{2} + J_I\right)^2 + 2(J_H\Delta)^2}.
\end{aligned}
\tag{3.5}
$$

The partition function of the model can be defined by

$$
Z = \sum_{\{\sigma_i\}} \prod_{k=1} \mathrm{Tr}_k \exp\left(-\beta\mathcal{H}_k\right) = \sum_{\{\sigma_i\}} \prod_{k=1} Z_k.
\tag{3.6}
$$

After tracing out the spin degrees of freedom of the $k-$th Heisenberg trimeric cluster, the partition function of each unit block Z_k through the generalized star-triangle transformation can be formulated as

$$
Z_k\left(\sigma_{k1}^z, \sigma_{k2}^z, \sigma_{k3}^z\right) = \mathrm{Tr}_k \exp(-\beta\mathcal{H}_k) = A \exp\left[\beta J_{\mathrm{eff}}\left(\sigma_{k1}^z\sigma_{k2}^z + \sigma_{k2}^z\sigma_{k3}^z + \sigma_{k3}^z\sigma_{k1}^z\right)\right].
\tag{3.7}
$$

In the absence of any external magnetic field, one reaches just two independent equations; once for the uniform configurations with the three equally aligned Ising spins $h_1 = h_2 = h_3 = \pm\frac{J_I}{2}$,

$$
\begin{aligned}
V_1 &\equiv Z_k\left(\mp\sigma_{k1}^z, \mp\sigma_{k2}^z, \mp\sigma_{k3}^z\right) = 2e^{\frac{3}{4}\beta J_I}\cosh\left(\frac{3}{4}\beta J_I\right) + 4e^{-\frac{\beta J_H}{4}(1+2\Delta)}\cosh\left(\frac{\beta J_I}{4}\right) \\
&\quad + 2e^{-\frac{\beta J_H}{4}(1-4\Delta)}\cosh\left(\frac{\beta J_I}{4}\right) = A\exp\left(\frac{3}{4}\beta J_{\mathrm{eff}}\right),
\end{aligned}
\tag{3.8}
$$

and once for six nonuniform spin arrangements with one Ising spin pointing in opposite direction of other two

$$
\begin{aligned}
V_2 &\equiv Z_k\left(\pm\sigma_{k1}^z, \pm\sigma_{k2}^z, \mp\sigma_{k3}^z\right) = Z_k\left(\pm\sigma_{k1}^z, \mp\sigma_{k2}^z, \pm\sigma_{k3}^z\right) = Z_k\left(\mp\sigma_{k1}^z, \pm\sigma_{k2}^z, \pm\sigma_{k3}^z\right) = \\
&\quad 2e^{\frac{3}{4}\beta J_H}\cosh\left(\frac{1}{4}\beta J_H\right) + 2e^{-\frac{\beta J_H}{4}(1+2\Delta)}\cosh\left(\frac{\beta J_I}{4}\right) + 2e^{-\frac{\beta}{4}\left[J_H(1-\Delta) - J_I\right]}\cosh\left(\frac{\beta}{2}Q_-\right) \\
&\quad + 2e^{-\frac{\beta}{4}\left[J_H(1-\Delta) + J_I\right]}\cosh\left(\frac{\beta}{2}Q_+\right) \\
&= A\exp\left(-\frac{1}{4}\beta J_{\mathrm{eff}}\right),
\end{aligned}
\tag{3.9}
$$

for which $Q^{\pm} = \sqrt{\left(\frac{1}{2}J_{\mathrm{H}}\Delta \pm J_{\mathrm{I}}\right)^2 + 2\left(J_{\mathrm{H}}\Delta\right)^2}$. Mapping parameters A and J_{eff} can be determined by

$$A = \left(V_1 V_2^3\right)^{\frac{1}{4}}, \quad \beta J_{\mathrm{eff}} = \ln\left(\frac{V_1}{V_2}\right). \tag{3.10}$$

Hence, the partition function of the spin-1/2 Ising-Heisenberg model on the TIT lattice can be obtained by rigorous mapping to the spin-1/2 Ising model on a simple triangular lattice (dashed lines in Fig. 3.1), i.e., $Z = A^{\gamma N} Z_{\mathrm{IM}}^{\triangle}\left(\beta, J_{\mathrm{eff}}\right)$.

the internal energy U of the 2-D Ising-Heisenberg model on the TIT lattice can be linked to the internal energy U_{IM} of the spin-1/2 pure Ising model on the triangular lattice via following equation

$$U/N = -\frac{\gamma}{4}\left(\frac{W_1}{V_1} + \frac{3W_2}{V_2}\right) + \frac{U_{\mathrm{IM}}/N}{J_{\mathrm{eff}}}\left(\frac{W_1}{V_1} - \frac{W_2}{V_2}\right), \tag{3.11}$$

where, new functions $W_1 = \partial V_1/\partial\beta$ and $W_2 = \partial V_2/\partial\beta$ can be calculated from Eqs. (3.8) and (3.9). The straightforward form of internal energy U_{IM} can be, for example, found in Refs. [51, 52]. Hence, we can acquire the specific heat of the model from formula $C = \partial U/\partial T$.

The spontaneous magnetization of the Ising spins m_{I} in the spin-1/2 Ising-Heisenberg model on the TIT lattice can be deduced from the single-site magnetization m_{IM} of the spin-1/2 Ising model on the triangular lattice [172] as following

$$m_{\mathrm{I}} = \frac{1}{2}\left[1 - \frac{16 V_1^{\gamma} V_2^{3\gamma}}{\left(V_1^{\gamma} + 3V_2^{\gamma}\right)\left(V_1^{\gamma} - V_2^{\gamma}\right)^3}\right]^{\frac{1}{8}}, \tag{3.12}$$

in which $\gamma = 1$ is for the TIT lattice shown in Fig. 3.1 without pale parts, whereas $\gamma = 2$ is for the TIT lattice including pale parts. On the other hand, the spontaneous magnetization of the Heisenberg spins m_{H} can be written in terms of the single-site magnetization m_{IM} of the Ising spins such that

$$m_{\mathrm{H}} = \frac{m_{\mathrm{IM}}}{2}\left(\frac{Q_1}{V_1} + \frac{Q_2}{V_2}\right) + \frac{2t_{\mathrm{IM}}}{3}\left(\frac{Q_1}{V_1} - 3\frac{Q_2}{V_2}\right), \tag{3.13}$$

where triplet correlation $t_{\mathrm{IM}} = \langle\sigma_{k1}^z\sigma_{k2}^z\sigma_{k3}^z\rangle_{\mathrm{IM}}$ between three Ising spins from the k-th cluster Hamiltonian reads

$$t_{\mathrm{IM}} = \frac{m_{\mathrm{IM}}}{4}\left[1 + 2\frac{V_1^{2\gamma} - 2V_2^{2\gamma} + V_1^{\gamma}V_2^{\gamma} - V_1^{\gamma}\sqrt{\left(V_1^{\gamma} + 3V_2^{\gamma}\right)\left(V_1^{\gamma} - V_2^{\gamma}\right)}}{\left(V_1^{\gamma} - V_2^{\gamma}\right)^2}\right]. \tag{3.14}$$
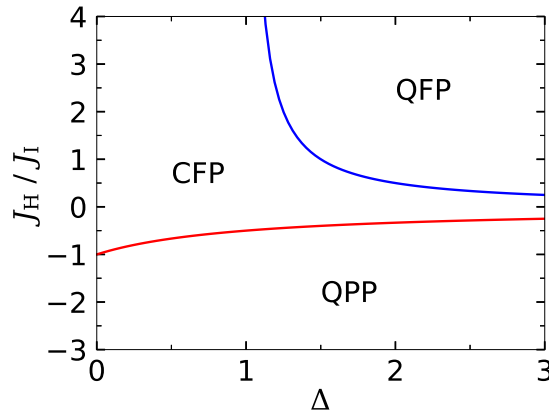
FIGURE 3.2: The ground state phase diagram for our new TIT model for $\gamma = 1$.

3.3 Results and discussion

The critical condition in the vicinity of critical temperature β_c of the spin-1/2 Ising-Heisenberg model on the TIT lattices can be demonstrated from following expression

$$\gamma \beta_c J_{\text{eff}} = \ln \left(\frac{V_1^\gamma}{V_2^\gamma} \right) = \ln 3 \implies V_1^\gamma = 3 V_2^\gamma. \tag{3.15}$$

We have plotted in Fig. 3.2 the ground-state phase diagram of the introduced TIT lattice with $\gamma = 1$ in the $\Delta - J_{\text{H}}/J_{\text{I}}$ plane. This model displays in its ground-state phase diagram one disordered ground state, disordered quantum paramagnetic phase (QPP), and a couple of spontaneously long-range-ordered states called as the classical ferromagnetic phase (CFP), and the quantum ferromagnetic phase (QFP). Boundaries between these phases are manifested by two lines

$$\begin{aligned} \text{QFP} &\Longleftrightarrow \text{CFP} \ : J_{\text{H}}/J_{\text{I}} = \frac{1}{2(\Delta - 1)}, \\ \text{CFP} &\Longleftrightarrow \text{QPP} \ : J_{\text{H}}/J_{\text{I}} = -\frac{1}{\Delta + 2}. \end{aligned} \tag{3.16}$$

The effective exchange interaction $\gamma \beta_c J_{\text{eff}}$ versus the temperature is depicted in Figs. 3.3 and 3.4 for the corresponding TIT lattices, where two different values of the exchange anisotropy $\Delta = 1$ and $\Delta = 2$ are assumed. One sees that the effective coupling of the case $\gamma = 1$ (see Fig. 3.3(a)) in the Ising isotropic $\Delta = 1$ either tends towards zero for $J_{\text{H}}/J_{\text{I}} = 0$ when the temperature goes to zero or diverges for $J_{\text{H}}/J_{\text{I}} < 0$. By considering $\Delta = 2$ (Fig. 3.3(b)) we observe that the effective coupling diverges at lower temperatures when $J_{\text{H}}/J_{\text{I}} < 0$. For the TIT lattice $\gamma = 2$ (see Fig. 3.4), the effective coupling tends to zero with a steep decrease from higher value and it diverges at higher temperatures with respect to the case $\gamma = 1$. Evidently, according to the critical condition (3.15), TIT lattice is spontaneously long-range ordered whenever $\gamma \beta J_{\text{eff}} > \ln(3)$, namely the
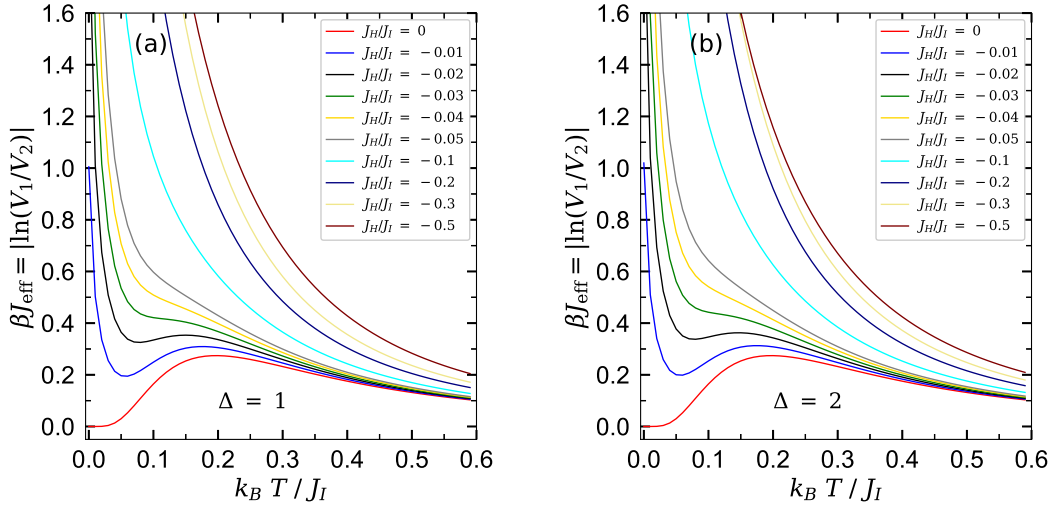
FIGURE 3.3: The critical temperature of the spin-1/2 Ising-Heisenberg model on the TIT lattice when $\gamma = 1$ as a function of the temperature for several values of the exchange interaction J_H/J_I and exchange anisotropies (a) $\Delta = 1$ and (b) $\Delta = 2$.
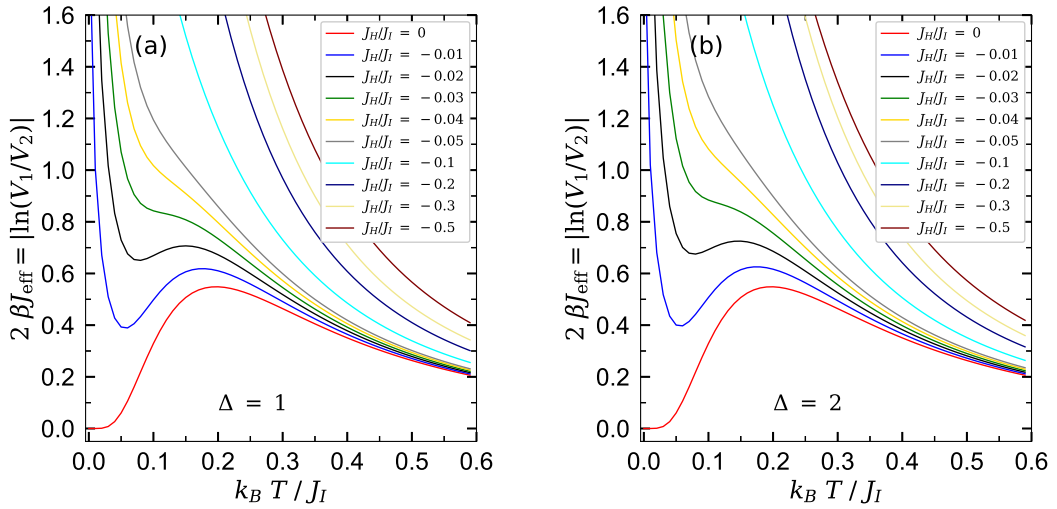
FIGURE 3.4: The critical temperature of the spin-1/2 Ising-Heisenberg model on the TIT lattice when $\gamma = 2$ as a function of the temperature for several values of the exchange interaction J_H/J_I and exchange anisotropies (a) $\Delta = 1$ and (b) $\Delta = 2$.
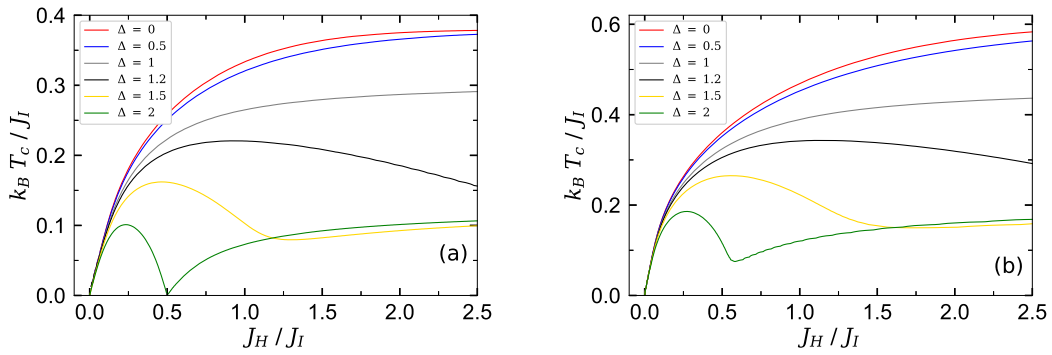
FIGURE 3.5: The results obtained for the critical temperature of the spin-1/2 Ising-Heisenberg model on the TIT lattices as a function of the exchange interaction J_H/J_I for several values of the exchange anisotropy. (a) $\gamma = 1$, (b) $\gamma = 2$ (see Fig. 2 of Ref. [42]).

effective coupling constant is greater than the critical value, otherwise it becomes disordered, i.e., for $\gamma \beta J_{\text{eff}} < \ln(3)$.

Let us now discuss the dependence of the critical temperature on the effective coupling J_H/J_I between the Heisenberg and Ising interactions. It is evident in Fig. 3.5(a) that, for particular case of the easy-axis exchange anisotropy $\Delta \leq 1$, the critical temperature is a monotonically decreasing function of the effective coupling until it completely vanishes at the ground-state boundary between phases CFP and QFP. When the critical behavior of the second TIT lattice (Fig. 3.5(b)) is under consideration, the critical temperature is shifted towards higher values because of the higher connectivity of the Ising spins in the TIT lattice with $\gamma = 2$.

In Fig. 3.6 are illustrated the magnetization curves of the TIT lattices for several fixed values of the exchange coupling ratio J_H/J_I and fixed $\Delta = 1$. It is quite clear from Fig. 3.6(a) that the spontaneous magnetizations of the Heisenberg and Ising spins for the TIT lattice $\gamma = 1$ start from their saturation magnetization 0.5, denoting the ground-state CFP. Moreover, the magnetization of the Heisenberg spins exhibits a greater temperature-induced than the spontaneous magnetization of the Ising spins even though both sublattice magnetizations tend towards zero with the same critical exponent from the standard universality class of the two-dimensional Ising model [43]. A similar behavior can be observed in the temperature dependencies of the spontaneous magnetizations of the TIT lattice with $\gamma = 2$. But in this case, the critical temperature at which magnetizations suddenly vanish moves towards higher temperatures.

By inspecting Fig. 3.7(a) the spontaneous magnetization of the Heisenberg spins in the TIT model with $\gamma = 1$ for anisotropic case $\Delta = 2$ starts from nonzero but remarkably less than saturation value, i.e., $m_H = 0.1667$ for the exhcange coupling region $J_H/J_I > 0.5$, which bears evidence of the phase QFP being ground-state. In Fig. 3.7(b) we prove that the spontaneous magnetizations of the Heisenberg and Ising spins in the model with $\gamma = 2$ show similar behavior to the previous case, but with higher critical temperatures at which they vanish.
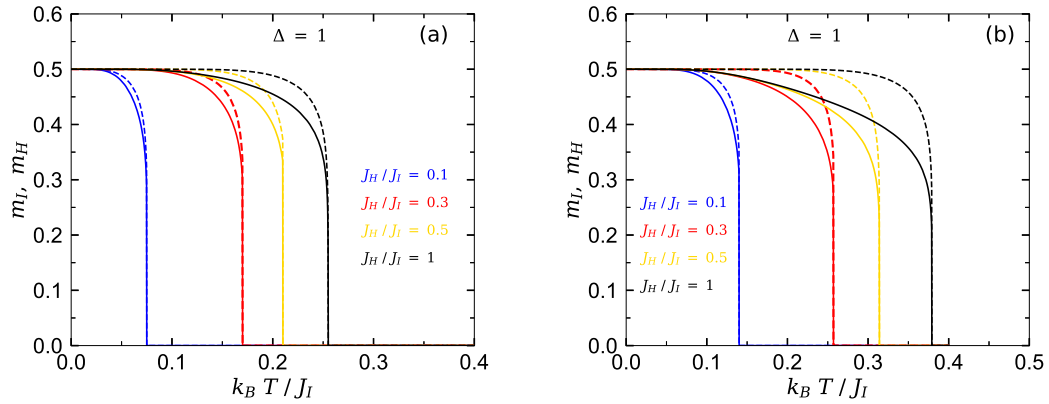
FIGURE 3.6: Temperature dependencies of the spontaneous magnetization m_I of the Ising spins (broken lines) and the spontaneous magnetization m_H of the Heisenberg spins (solid lines) for the fixed $\Delta = 1$ and several values of the interaction ratio J_H/J_I. (a) $\gamma = 1$, (b) $\gamma = 2$.
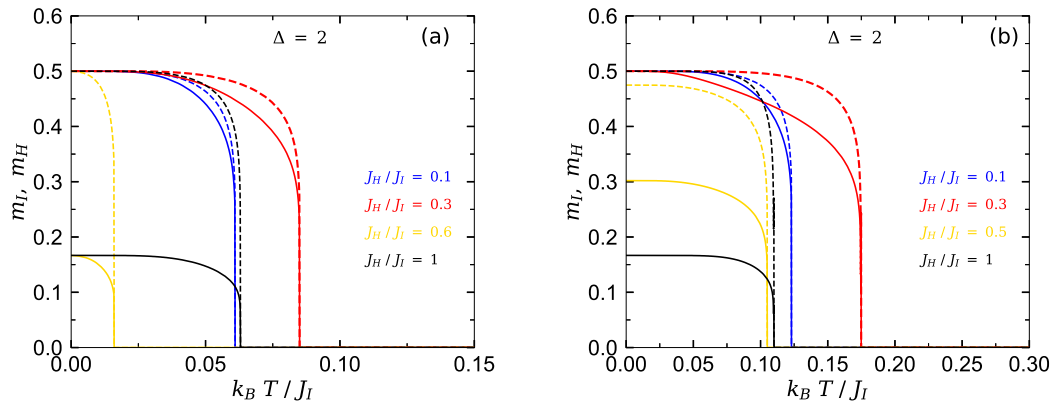
FIGURE 3.7: The spontaneous magnetization m_I of the Ising spins (broken lines) and the spontaneous magnetization m_H of the Heisenberg spins (solid lines) for the fixed $\Delta = 2$ and the same set of other parameters to Fig. 3.6.
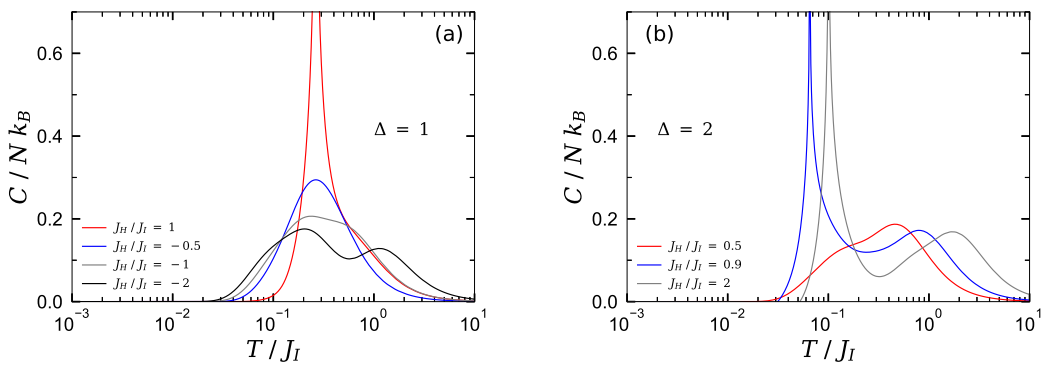
FIGURE 3.8: The temperature dependence of specific heat of the spin-1/2 Ising-Heisenberg model on the TIT lattice with $\gamma = 1$ for several values of J_H/J_I. (a) $\Delta = 1$ and (b) $\Delta = 2$.
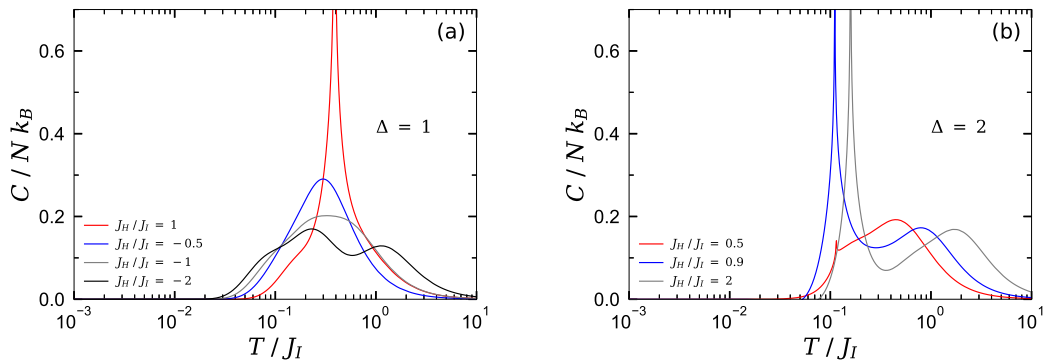
FIGURE 3.9: The temperature dependence of specific heat of the spin-1/2 Ising-Heisenberg model on the TIT lattice with $\gamma = 2$ for several values of J_H/J_I. (a) $\Delta = 1$ and (b) $\Delta = 2$.

Finally, let us turn to a detailed analysis of the temperature dependencies of the specific heat. In Fig. 3.8 is shown the zero-field specific heat for TIT lattice with $\gamma = 1$ in a semilogarithmic scale by taking two different exchange anisotropies for various fixed values of the exchange interaction ratio J_H/J_I. Thermal variations of the specific heat for the isotropic Heisenberg trimers are typically illustrated in Fig. 3.8(a). As one can see in this figure, the specific heat of Ising-Heisenberg model on this TIT lattice exhibits a logarithmic singularity from the standard Ising universality class when considering the ferromagnetic Heisenberg interaction $J_H/J_I > 0$ and $\Delta = 1$, where the system's ground state is CFP. With transition from CFP to QPP (see Fig. 4.13) we observe that the singularity changes to an anomalous Schottky-type maximum. With further decrease of J_H/J_I a double-peak appears in the specific heat curve.

Figure Fig.3.8(b) represents the specific heat as a function of temperature for the particular case of the ferromagnetic Heisenberg interaction with the easy-axis exchange anisotropy $\Delta = 2$. Interestingly, we witness a singularity for the interaction region nearby the phase boundary between CFP and QFP (in this case $J_H/J_I > 0.5$). When the model is in CFP state a double-peak is evident.

When the specific heat of the second TIT lattice with $\gamma = 2$ is concerned, we see somewhat similar thermal behavior for $\Delta = 1$ (Fig. 3.9(a)) but the singularity happens at higher temperature. On the other hand, one can see that for the case $\Delta = 2$ (Fig. 3.9(b)) when the ground state of the system is QFP the specific heat shows a large strict singularity. Nearby the ground-state phase transition between phases QFP and CFP the singularity gradually weakens.

3.4   Conclusions

In this chapter, at first, we exactly solved two 2-D spin-1/2 Ising-Heisenberg model on the TIT lattices through the generalized star-triangle transformation by establishing a rigorous mapping

to a simple spin-1/2 Ising model on a triangular lattice. Then, their ground-state and finite-temperature phase diagrams have been constructed. We uncovered that the Ising-Heisenberg model on two TIT lattices exhibits a rich magnetic behavior with several unconventional quantum phases and boundaries. Besides, we have investigated the spontaneous magnetizations of the Heisenberg and Ising spins of the spin-1/2 Ising-Heisenberg model on two different but geometrically related TIT lattices. We witnessed that a quantum reduction of the spontaneous magnetizations of the Heisenberg and Ising spins is the result of quantum fluctuations and strongly depends on the anisotropy.

Ultimately, it has been demonstrated that the specific heat of Ising-Heisenberg model on the TIT lattices exhibits a logarithmic singularity from the standard Ising universality class for the isotropic ferromagnetic Heisenberg interaction, where the model is in the ground state CFP. Within the phase boundary QPP this singularity changes to a single Schottky maximum, where for $J_H/J_I < -1$ we observed double-(triple-) peaks. When an anisotropic interaction were considered, a singularity was observed in the specific heat curve for the interaction region within the phase boundary QFP.

Chapter 4

Molecular cluster magnets

4.1 Preliminaries

In the past few years, it has been verified that some exactly solved Heisenberg spin models may capture basic magnetic features of a family of octanuclear nickel containing complexes. In this chapter, we present our results gained for the low-temperature magnetization process and the specific heat of the octanuclear nickel phosphonate cage $\left[\text{Ni}_8(\mu_3-\text{OH})_4(\text{OMe})_2(\text{O}_3\text{PR}_1)_2(\text{O}_2\text{CtBu})_6(\text{HO}_2\text{CtBu})_8\right]$ in the presence of an external magnetic field by assuming aditional anisotropic terms: Heisenberg exchange anisotropies Δ_1 and Δ_2, also single-ion anisotropy D.

Moreover, another family of octanuclear complexes including lanthanide metal salts with the addition of nickel acetate $[\text{Ni}_4\text{Ln}_4(\mu_2-\text{OH})_2(\mu_3-\text{OH})_4(\mu-\text{OOCCH}_3)_8(\text{LH}_2)_4]$ have attracted much attention due to reveal rich ground-state phase diagram and great magnetic properties. These products are new additions to the very small family of Ni_2Ln_2 (Ln = Tb (**a**); Dy (**b**); Ho (**c**); Er (**d**)) clusters with planar butterfly (or rhombus) cores and show the initial compounds prepared by using of 2-methoxy-6-[2-(2 hydroxyethylamino)ethylimino-methyl] phenol (LH$_3$) ligand to modulate mixed metal $3d/4f$ cluster chemistry. Studies of the magnetization, dc and ac susceptibilities and magnetocaloric effect have been performed on polycrystalline samples **a** − **d** by P. Kalita *et al.* [73]. They realized a ferromagnetic interaction between the lanthanide and the nickel centres, with estimated strength $J_{\text{Ni}\cdots\text{Ln}} = +0.86$ cm^{-1}. They also noted that none of the complexes are SMMs because of the existence of very weak Ni $\cdots$ Ln and Ln $\cdots$ Ln magnetic interactions. In an earlier study [173], S. Biswas *et al.* considered similar compounds called octanuclear heterobimetallic assemblies ($[\text{Ln}_4\text{Ni}_4(\text{H}_3\text{L})_4(\mu_3-\text{OH})_4(\mu_2-\text{OH})_4]_4\text{Cl}\cdot x\text{H}_2\text{O}\cdot y\text{CHCl}_3$), and examined their magnetization together with the dc and ac susceptibilities.

In this chapter, we consider a series of $\text{Ni}_4^{\text{II}}\text{Ln}_4^{\text{III}}$ complexes, then exactly examine their low-temperature magnetization process, magnetic relaxation studies using Cole-Cole formalism [174,

175, 176], and specific heat. These complexes are composed of two butterfly-shaped heterometal-lic $Ni_2^{II}Ln_2^{III}O_4$ distorted cubes connected to each other by acetate and hydroxide bridging ligands. Herein, we consider a typical exchange anisotropy for the Ni$\cdots$Ln interactions, next focus on realizing how this anisotropy influences the magnetization process, the specific heat and Cole−Cole plot of ac susceptibility (for compounds **a** and **b**). The entanglement between ions of small clusters with prominent of ferromagnetic interaction have been considered much less in the literature. The entanglement between pair spins of mixed $3d/4f$ metal complexes has not considered in a broadcast medium so far. Hence, we study the entanglement negativity between Ni$\cdots$Ni of the complexes **a**−**d**.

To investigate the low-temperature magnetization behavior, thermodynamics, as well as, quantum properties of the considered nickel complex discused above, we utilize ED method to diagonalize their Hamiltonians. To ensure the correctness and completeness, we compare our exact results of magnetization process with those obtained through QMC method.

In the final section of this chapter, a tetranuclear square complex on a spin-1/2 chain is considered, and the exact solution of this model via ED method is presented. Next, we discuss the possible ground-state phase diagram and the magnetization of the model. The effects of anisotropy, exchange interaction, and external magnetic field on the local quantum uncertainty and quantum coherence are discussed in detail. By using the standard teleportation protocol, the output state of the two-qubit entangled state is investigated as well.

4.2 Octanuclear nickel phosphonate-based cage

4.2.1 Model

Hamiltonian of the octanuclear nickel phosphonate-based cage $\big[Ni_8(\mu_3 - OH)_4(OMe)_2(O_3P$ $R_1)_2(O_2C^tBu)_6(HO_2C^tBu)_8\big]$ shown in Fig. 4.12 can be expressed as

$$
\begin{aligned}
H = -J_1 & \big[\boldsymbol{S}_1 \cdot \boldsymbol{S}_2 + \boldsymbol{S}_3 \cdot \boldsymbol{S}_4 + \boldsymbol{S}_5 \cdot \boldsymbol{S}_6 + \boldsymbol{S}_7 \cdot \boldsymbol{S}_8 \big] \\
-J_2 & \big[\boldsymbol{S}_1 \cdot \boldsymbol{S}_3 + \boldsymbol{S}_2 \cdot \boldsymbol{S}_3 + \boldsymbol{S}_4 \cdot \boldsymbol{S}_5 + \boldsymbol{S}_4 \cdot \boldsymbol{S}_6 + \\
& \boldsymbol{S}_5 \cdot \boldsymbol{S}_7 + \boldsymbol{S}_6 \cdot \boldsymbol{S}_7 + \boldsymbol{S}_1 \cdot \boldsymbol{S}_8 + \boldsymbol{S}_2 \cdot \boldsymbol{S}_8 \big] \\
-g\mu_B B & \sum_{j=1}^{8} S_j^z + D \sum_{j=1}^{8} \big(S_j^z\big)^2,
\end{aligned}
\tag{4.1}
$$

First and second parts in equation (4.1) correspond to the anisotropic Heisenberg couplings between each pair spins interacted together, which is explicitly given by

$$
(\boldsymbol{S}_i \cdot \boldsymbol{S}_j)_{J,\Delta} = J\big(S_i^x S_j^x + S_i^y S_j^y\big) + \Delta S_i^z S_j^z,
\tag{4.2}
$$
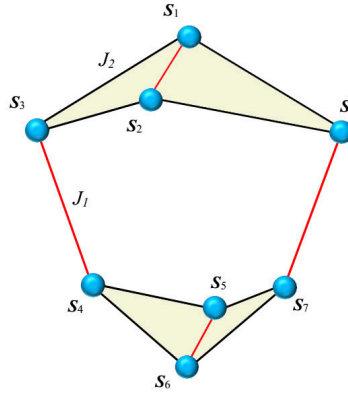
FIGURE 4.1: Schematic structure of the Heisenberg octanuclear nickel phosphonate cage. The balls denote Ni atoms that are connected together via Body-Body (BB) interadimer interaction J_1 and the corresponding Wing-Body (WB) interdimer interaction J_2.
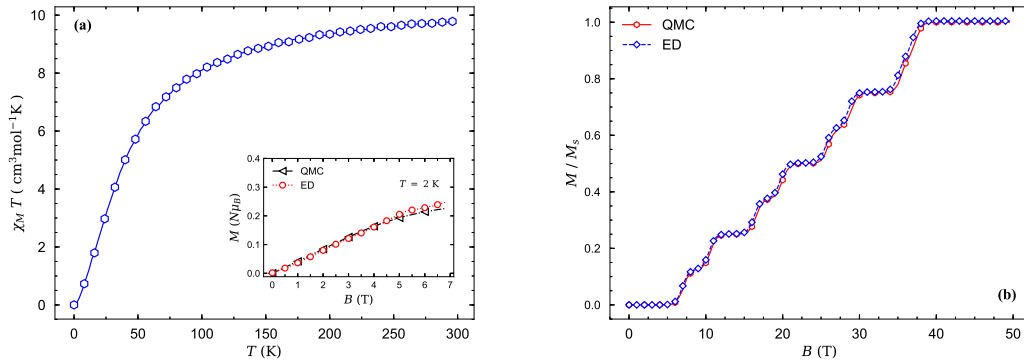
FIGURE 4.2: (a) QMC results obtained for the temperature dependence of the product of magnetic susceptibility times the temperature $\chi_M T$ for the Heisenberg octanuclear nickel phosphonate-based cage in the absence of the magnetic field ($B = 0.1$T), assuming fixed values of $J_1 = 7.6$ cm^{-1} and $J_2 = -22.4$ cm^{-1}. The inset shows deduced magnetization per saturation M/M_s by QMC simulation and ED method as a function of the external magnetic field B, assuming fixed values of $J_1 = 7.6$ cm^{-1}, $J_2 = -22.4$ cm^{-1} at moderate temperature $T = 2$ K. Due to compare with the experimental data in Ref. [177], other parameters have been taken as $\Delta 1 = J_1$, $\Delta 2 = J_2$ and $D = 0$. (b) The ED and QMC results for the magnetization per saturation value of the model versus magnetic field at low temperature $T = 1$K for the same fixed values of other parameters as panel (a) divided by k_B, namely, $J_1/k_B = 7.6$ K and $J_2/k_B = -22.4$ K.

where $J = \{J_1, J_2\}$ denotes isotropic coupling constants, and $\Delta = \{\Delta_1, \Delta_2\}$ corresponds to the anisotropy exchange interactions. S^α for which $\alpha = \{x, y, z\}$ are spin-1 operators (with $\hbar = 1$). B is the applied homogeneous magnetic field in the z-direction. The gyromagnetic ratio would be taken as $g = 2.42$ [177] in the plots drawn in this section. The characterization of the partition function of the model under consideration can be defined as $Z = Tr\big[\exp(-\beta H)\big]$. The Gibbs free energy can be obtained from the partition function of the system as $f = -k_B T \ln Z$.

4.2.2 Results and Discussion

This part demonstrates the most interesting results obtained from the study of the magnetization process, magnetic susceptibility, and specific heat of the butterfly-shaped octanuclear cluster $\left[\mathrm{Ni}_8(\mu_3-\mathrm{OH})_4(\mathrm{OMe})_2(\mathrm{O}_3\mathrm{PR}_1)_2(\mathrm{O}_2\mathrm{C}^t\mathrm{Bu})_6(\mathrm{HO}_2\mathrm{C}^t\mathrm{Bu})_8\right]$ by utilizing the thermodynamic relations as following

$$M = -\left(\tfrac{\partial f}{\partial B}\right)_T, \quad \chi = \left(\tfrac{\partial M}{\partial B}\right)_T, \quad C = -T\left(\tfrac{\partial^2 f}{\partial T^2}\right)_B. \tag{4.3}$$

The most stimulating results obtained for this magnetic material have been mentioned in Ref. [63].

Figure 4.2(a) illustrates the QMC results of the temperature dependencies of the product of zero-field magnetic susceptibility times the temperature $\chi_M T$ of the model calculated by ALPS project. By comparing our numerical results and the experimental data expressed in Refs. [177, 178, 179], we find that our results are in an excellent agreement with their experimental measurements. The room temperature $\chi_M T$ value for the model under consideration is 10.0 cm^{3}mol^{-1}K for the set of other parameters as $J_1 = 7.6$ cm^{-1}, $J_2 = -22.4$ cm^{-1} and $g = 2.4$, which is close to the expected value 9.96 cm^{3}mol^{-1}K for eight isolated Ni$^{\mathrm{II}}$ ions. We note that in this step, we consider the model as a pure Heisenberg spin-1 cluster system isolated from any anisotropy dependencies. The inset of Fig. 4.2(a) displays the ED and QMC results for the magnetization versus magnetic field at moderate temperature $T = 2$ K and the same set of coupling constants considered for examining $\chi_M T$. One can see from the inset that, not only ED and QMC results are in accordance with each other, but also they are in a good agreement with the experimental results reported in Ref. [177].

Figure 4.2(b) shows deduced magnetization per saturation value M/M_s from the ED and QMC methods as a function of the magnetic field at low temperature $T = 1$K for fixed values of $J_1/k_B = 7.6$ K, $J_2/k_B = -22.4$ K and $g = 2.4$. We mention that in order to reduce the complexity of our numerical calculations, we change the units of exchange couplings into the temperature unit (Kelvin). The system has a complex magnetization scenario due to multiplicity of intermediate magnetization plateaus. It is quite obvious that the magnetization curve shows intermediate plateaus at 0, $\frac{1}{8}$, $\frac{1}{4}$, $\frac{2}{5}$, $\frac{1}{2}$, $\frac{2}{3}$, and $\frac{3}{4}$ of the saturation magnetization. The large number of magnetization plateaus is due to existence of a strong interdimer antiferromagnetic interaction $J_2/k_B = -22.4$ K. This figure also manifests a plausible coincidence between results of the both ED and QMC procedures.

Now, let us investigate the magnetization process and the specific heat of the model when it involves with the Heisenberg exchange anisotropies Δ_1 and Δ_2, as well as, single-ion anisotropy property D. Typical dependencies of the magnetization per saturation value are plotted in Fig. 4.6(a) against magnetic field B for different selected values of the single-ion anisotropy
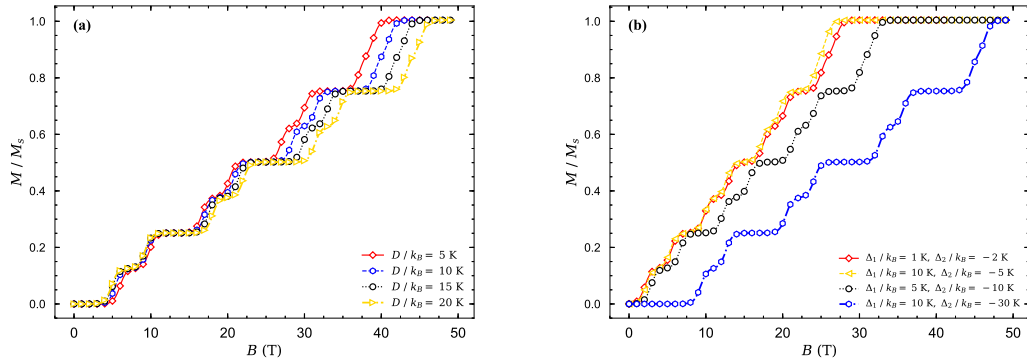
FIGURE 4.3: (a) ED results for the magnetization per saturation value M/M_s of the isotropic octanuclear nickel phosphonate-based cage as a function of the magnetic field B at low temperature $T = 1$K for several fixed values of the single-ion anisotropy parameter D, by assuming fixed values of $J_1/k_B = \Delta_1/k_B = 7.6$ K, and $J_2/k_B = \Delta_2/k_B = -22.4$ K. (b) Magnetization per saturation value M/M_s as a function of the magnetic field at low temperature $T = 1$K for different fixed values of exchange anisotropies Δ_1 and Δ_2, by assuming an optional value $D/k_B = 10$ K.

parameter D/k_B, when the isotropic XXX Heisenberg case is considered for the model, namely, $\Delta_1/k_B = J_1/k_B = 7.6$ K and $\Delta_2/k_B = J_2/k_B = -22.4$ K. Interestingly, the single-ion anisotropy variations have no remarkable influence on the magnetic dependence of magnetization in the magnetic field interval $B \lesssim 20$ T, where a magnetization jump occurs between $\frac{2}{5}$−plateau and $\frac{1}{2}$−plateau (accompanying with the ground-state phase transition between plateaus $\frac{2}{5}$ and $\frac{1}{2}$ of the saturation magnetization). As a matter of fact, for the magnetic field range $B > 20$ T, intermediate magnetization plateaus at $M/M_s \geq \frac{1}{2}$ ($\frac{1}{2}$, $\frac{2}{3}$, and $\frac{3}{4}$ of the saturation magnetization) become wider and shift toward stronger magnetic fields. Generally, there is a delay in the magnetization behavior to reach its saturation when the single-ion anisotropy increases.

To understand the spin exchange anisotropy effects on the magnetization process of the octanuclear nickel phosphonate cage, we plot in Fig. 4.6(b) the magnetization per saturation value M/M_s with respect to the magnetic field for various fixed values of the both exchange anisotropies Δ_1 and Δ_2, and optional value $D/k_B = 10$ K at low temperature $T = 1$K. Coupling constants J_1 and J_2 have been taken as panel 4.6(a). As could be expected, the width and magnetic position of all plateaus undergo significant changes upon altering anisotropies. To clarify this point, the magnetization scenario for relatively small anisotropies $\Delta_1 \ll J_1$ and $|\Delta_2| \ll |J_2|$ is illustrated in Fig. 4.6(b) on a particular example with $\Delta_1/k_B = 1$ K and $\Delta_2/k_B = -2$ K (red solid line marked with diamonds). One can see that, the width of all plateaus becomes narrower and their magnetic positions shift toward lower magnetic fields. Consequently, the magnetization reaches its saturation value in lower magnetic fields (in this case $B_s \approx 28$ T). The similar behavior can be seen for the magnetization under condition $\Delta_1 > J_1$ and $|\Delta_2| \ll |J_2|$ (orange curve marked with triangles). For the case $\Delta_1 < J_1$ and $|\Delta_2| < |J_2|$ (black dotted line with
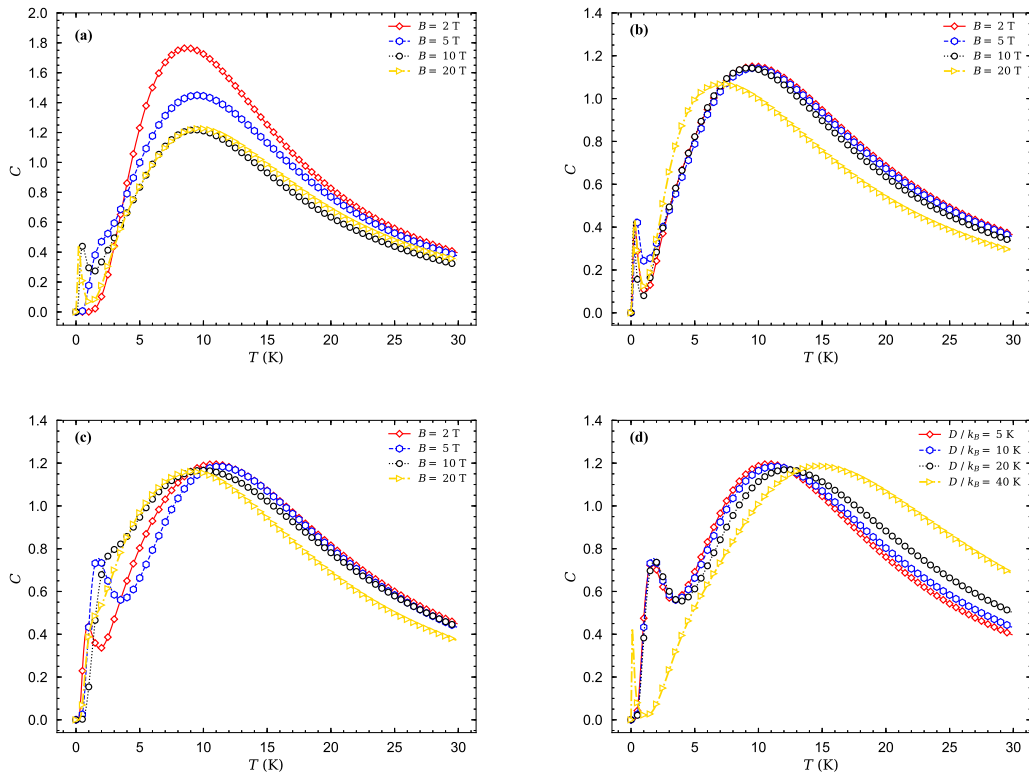
FIGURE 4.4: (a) Specific heat of the isotropic Heisenberg octanuclear nickel cage as a function of the temperature for various fixed values of the magnetic field $B = 2$ T, 5 T, 10 T, and 20 T, where other parameters are taken as $J_1/k_B = 7.6$ K and $J_2/k_B = -22.4$ K, $\Delta_1 = J_1$, $\Delta_2 = J_2$, $D = 0$ and $g = 2.4$. (b) The temperature dependence of specific heat of the anisotropic octanuclear nickel cage model for the same set of fixed magnetic fields as panel (a) and fixed anisotropies $\Delta_1/k_B = 10$ K, $\Delta_2/k_B = -5$ K and arbitrary single-ion anisotropy $D/k_B = 10$ K. (c) The temperature dependence of the specific heat for the same fixed values of magnetic fields and single-ion anisotropy ($D/k_B = 10$ K) as panel (b), but for different selected values of spin exchange anisotropies, i.e., $\Delta_1/k_B = 5$ K, $\Delta_2/k_B = -10$ K. (d) The specific heat of the model versus temperature for the same fixed values of the exchange anisotropies as panel (c), where several selected values of the single-ion anisotropy are taken as $D/k_B = 2$ K, 5 K, 20 K, 40 K in the presence of a weak magnetic field $B = 5$ T.

circular marks) wider magnetization plateaus are presented by magnetization curve, whose magnetic positions are in the stronger magnetic fields. When we consider high amounts of exchange anisotropies for the model such that $\Delta_1 > J_1$ and $|\Delta_2| > |J_2|$, the width of all magnetization plateaus considerably increase and their magnetic positions move to stronger magnetic fields, so the magnetization reaches its saturation value in the stronger magnetic fields (for this case $B_s \approx 45$ T).

Next, let us discuss the effects of exchange anisotropies Δ_1 and Δ_2, as well as, single-ion anisotropy D on the specific heat of the model versus the temperature T for the same set of coupling constants J_1 and J_2 as before. To this end, we display in Fig. 4.10 the temperature dependence of the specific heat of the octanuclear nickel phosphonate-based cage under different circumstances. Figure 4.10(a) demonstrates the specific heat C versus temperature T for several

fixed values of the magnetic field when the system is assumed as a pure isotropic Heisenberg model, namely, $\Delta_1 = J_1$, $\Delta_2 = J_2$, and $D = 0$. When the temperature arises from zero, the specific heat manifests a steep increase in the temperature interval $2 \text{ K} < T < 9 \text{ K}$ in the presence of weak magnetic fields (red solid curve), and reaches its maximum at temperature $T \approx 9\text{K}$. As a result, there is a Schottky-type maximum in the specific heat curve at $T \approx 9\text{K}$ and weak magnetic fields ($B < 5$ T). With increase of the magnetic field, the Schottky peak's height gradually decreases until a second peak appears at finite low temperature $T \approx 0.2$ K. By inspecting Figs. 4.10(a) and 4.2(b), one can realize that converting the Schottky peak into a double-peak coincides the magnetization jump from zero plateau to first intermediate $\frac{1}{8}$−plateau.

We illustrate in Fig. 4.10(b) the temperature dependence of the specific heat for a particular anisotropic case $\Delta_1/k_B = 10$ K, $\Delta_2/k_B = -5$ K and $D/k_B = 10$ K, and several fixed values of the magnetic field B. In this situation, we see a stable double-peak temperature dependence. There is no outstanding alteration in the specific heat behavior for the weak magnetic field variations ($B = 2$ T, 5 T, 10 T). When the the magnetic field increases further than $B = 10$ T, the height and the position of larger peak change. Actually, its height decreases and its temperature position moves toward lower temperatures.

When different anisotropies are considered for the model (Fig. 4.10(c)), we see that the double-peak gradually changes to the Schottky peak at lower temperatures upon increasing the magnetic field. This scenario indicates that the system goes to the ground-state phase corresponding to the magnetization $\frac{1}{2}$−plateau. Finally, our exact results for the effects of single-ion anisotropy on the temperature dependence of the specific heat are plotted in Fig. 4.10(d), where other parameters have been taken as $\Delta_1/k_B = 5$ K, $\Delta_2/k_B = -10$ K and $B = 5$ T. Interestingly, increase of the single-ion anisotropy results in varying the shape and the temperature position of the larger peak of the double-peak appeared in the specific heat curve. Strong single-ion anisotropy property has fundamental influence on the height and temperature position of the both peaks. Generally, both peaks move away from each other on the temperature axis. Indeed, by increasing the single-ion anisotropy, the specific heat practically tries to make a single Schottky maximum at higher temperatures, while there is still a cusp reminiscent the smaller peak at sufficiently low temperatures. These changes in specific heat behavior are in a good coincidence with the magnetization response to the single-ion anisotropy variations (see Fig. 4.6(a)).

4.3 Heterometallic octanuclear $Ni_4^{II}Ln_4^{III}$ (Ln = Tb, Dy, Ho, Er) Complexes

Our motivation to study the complexes $\mathbf{a} - \mathbf{d}$ is based on recent works such as theoretical investigations and experimental analysis of the mixed $Ni_4^{II}Ln_4^{III}$ complexes [73]. We assume two linked butterflied-shape structure of the heterometallic $Ni_2^{II}Ln_2^{III}O_4$ distorted cubes together as
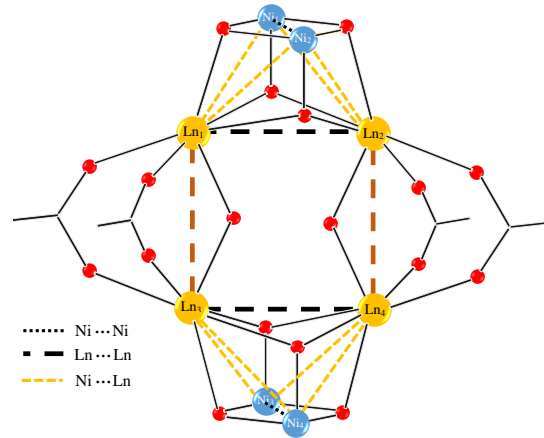
FIGURE 4.5: Butterfly-shaped molecular core of complexes **a** − **d**. Orange balls present lanthanides, blue balls denote nickel atoms. All magnetic coupling constants are illustrated in this figure.

labeled on the links between atoms (Fig. 4.5). The total Hamiltonian of the complex systems $Ni_4^{II}Ln_4^{III}$ can be modeled as

$$
\begin{aligned}
H = {} & -J_{nn}\big[\boldsymbol{S}_{Ni_1}\cdot\boldsymbol{S}_{Ni_2} + \boldsymbol{S}_{Ni_3}\cdot\boldsymbol{S}_{Ni_4}\big] - J_{ll}\big[\boldsymbol{S}_{Ln_1}\cdot\boldsymbol{S}_{Ln_2} + \boldsymbol{S}_{Ln_3}\cdot\boldsymbol{S}_{Ln_4}\big] \\
& -J_{nl}\Big[\sum_{\{a,b\}=1,2}\boldsymbol{S}_{Ni_a}\cdot\boldsymbol{S}_{Ln_b} + \sum_{\{c,d\}=3,4}\boldsymbol{S}_{Ni_c}\cdot\boldsymbol{S}_{Ln_d}\Big] + D_n\sum_{j=1}^{4}\big(S_{Ni_j}^z\big)^2 \\
& +D_l\sum_{j=1}^{4}\big(S_{Ln_j}^z\big)^2 - zJ_{nl}\langle S_{Ln}^z\rangle S_{Ln}^z - \mu_B B\sum_{a=1}^{4}\big(g_n S_{Ni_a}^z + g_l S_{Ln_a}^z\big),
\end{aligned}
\tag{4.4}
$$

where $\boldsymbol{S}$ indicate spatial effective components of the standard spin operators of the metal centre(s) Ni^{II} and Ln^{III}. Although, in lanthanide ions the spin usually is not a good quantum number, reproducing an effective spin model can be useful to account for spin moment and orbital contributions. Here, J_{nn}, J_{ll} and J_{nl} are the exchange interactions between each ion(s) pair, namely $Ni\cdots Ni$, $Ln\cdots Ln$ and $Ni\cdots Ln$, respectively. The presence of low-lying excited states has been disclosed in such complexes [73] that is in agreement with the existence of weak $Ni\cdots Ln$ magnetic interactions. zJ_{nl} accounts for the intercubane exchange interactions between Ln^{III} using the molecular field approach. As expressed in Ref. [73], this interaction is very weak, so we ignore its effects on the magnetization process and other quantities investigated in this context. B denotes the external magnetic field along the $z-$direction. it should be noted that, as concluded in Ref. [73], the single-ion anisotropy property of Ni^{II} and Ln^{III} ions naturally depend on their geometry in the complexs, such that Ln^{III} in a low-coordination behavior is mainly expected to constitute a prominent single-ion anisotropy compared with its counterpart for Ni^{II} ions. Hence, we impose in the Hamiltonian both of single-ion anisotropies D_n and D_l associated to, respectively, Ni^{II} and Ln^{III} ions. For anisotropic case, we assume each pair of

quantum spins $\boldsymbol{S}_{\text{Ni}}$ and $\boldsymbol{S}_{\text{Ln}}$ linked together through XXZ exchange interaction such that

$$J_{\text{nl}}\big(\boldsymbol{S}_{\text{Ni}} \cdot \boldsymbol{S}_{\text{Ln}}\big) = J_{\text{nl}}\big(S_{\text{Ni}}^x S_{\text{Ln}}^x + S_{\text{Ni}}^y S_{\text{Ln}}^y\big) + \Delta_{\text{nl}} S_{\text{Ni}}^z S_{\text{Ln}}^z, \tag{4.5}$$

where, Δ_{nl} is an arbitrary Heisenberg exchange anisotropy for each Ni$\cdots$Ln interaction. For simplicity, we keep other interactions Ni$\cdots$Ni and Ln$\cdots$Ln remain XXX-type.

The Hamiltonian of Ni$_4^{\text{II}}$Ln$_4^{\text{III}}$ complexes can be subsequently put into a diagonal form (4.6) as long as we introduce the total spin operator of the whole system as S_{t} and its z-component to be conserved quantities with well defined quantum spin numbers $S_{\text{t}} = 0, 1, 2, \cdots, 4(S_{\text{L}} + S_{\text{N}})$, and $S_{\text{t}}^z = -S_{\text{t}}, -S_{\text{t}} + 1, \cdots, S_{\text{t}} - 1, S_{\text{t}}$.

$$\begin{aligned}
H = &-\frac{J_{\text{nl}}}{2}\boldsymbol{S}_{\text{t}}^2 - (J_{\text{nn}} - 3J_{\text{nl}})\boldsymbol{S}_{\text{t}_{\text{NN}}}^2 - (J_{\text{ll}} - 3J_{\text{nl}})\boldsymbol{S}_{\text{t}_{\text{LL}}}^2 - 2(J_{\text{nn}} - 5J_{\text{nl}})S_{\text{N}}^2 - 2(J_{\text{ll}} - 5J_{\text{nl}})S_{\text{L}}^2 \\
&-4(\Delta_{\text{nl}} - J_{\text{nl}})(S_{\text{t}_{\text{NL}}}^{z2} + S_{\text{L}}^{z2} + S_{\text{N}}^{z2}) + 4D_{\text{n}}S_{\text{N}}^{z2} + 4D_{\text{l}}S_{\text{L}}^{z2} - 4\mu_B B\big(g_{\text{n}}S_{\text{t}}^z + g_{\text{l}}S_{\text{L}}^z\big).
\end{aligned} \tag{4.6}$$

So, the eigenenergies can be then expressed in terms of composite quantum spin numbers $\{S_{\text{t}}, S_{\text{t}_{\text{NN}}}, S_{\text{t}_{\text{NL}}}, S_{\text{t}_{\text{NL}}}^z, S_{\text{L}}^z, S_{\text{t}_{\text{NN}}}^z, S_{\text{N}}^z\}$ such that

$$\begin{aligned}
E_\Lambda = &-\frac{J_{\text{nl}}}{2}[S_{\text{t}}(S_{\text{t}} + 1)] - (J_{\text{nn}} - 3J_{\text{nl}})[S_{\text{t}_{\text{NN}}}(S_{\text{t}_{\text{NN}}} + 1)] - (J_{\text{ll}} - 3J_{\text{nl}})[S_{\text{t}_{\text{NL}}}(S_{\text{t}_{\text{NL}}} + 1)] \\
&-2(J_{\text{nn}} - 5J_{\text{nl}})[S_{\text{t}_{\text{N}}}(S_{\text{t}_{\text{N}}} + 1)] - 2(J_{\text{ll}} - 5J_{\text{nl}})[S_{\text{t}_{\text{L}}}(S_{\text{t}_{\text{L}}} + 1)] \\
&-4(\Delta_{\text{nl}} - J_{\text{nl}})(S_{\text{t}_{\text{NL}}}^{z2} + S_{\text{L}}^{z2} + S_{\text{N}}^{z2}) + 4D_{\text{n}}S_{\text{N}}^{z2} + 4D_{\text{l}}S_{\text{L}}^{z2} - 4\mu_B B\big(g_{\text{n}}S_{\text{N}}^z + g_{\text{l}}S_{\text{L}}^z\big),
\end{aligned} \tag{4.7}$$

which principally entails the values $S_{\text{t}_{\text{NN}}} = 0, 1, 2$; $S_{\text{t}_{\text{NL}}} = |S_{\text{L}} - 1|, \cdots, S_{\text{L}} + 1$; $S_{\text{t}_{\text{NL}}}^z = -S_{\text{t}_{\text{NL}}}, \cdots, S_{\text{t}_{\text{NL}}}$ and so on. Here $g_{\text{n}} = 2$ and g_{l} is gyromagnetic factor of lanthanides and μ_B is the Bohr magneton. The local g_{l}-tensors are assumed to be isotropic with the g_{l} principal values.

One can straightforwardly obtain the partition function of the compounds using Eq. 4.7, and in turn investigates the magnetic and thermodynamic properties of them. We will perform exact numerical solution to achieve partition function and the thermal reduced density matrix of the bipartite Ni$\cdots$Ni interaction.

In the next subsections we discuss the most stimulating results for the mixed Ni$_4^{\text{II}}$Ln$_4^{\text{III}}$ complexes, assuming the particular case with the intracubane ferromagnetic interaction for the Ni$\cdots$Ni ($J_{\text{nn}} > 0$) and Ni$\cdots$Ln ($J_{\text{nl}} > 0$) junctions, and respectively weak antiferromagnetic exchange interaction for Ln$\cdots$Ln ($J_{\text{ll}} \lesssim 0$) within each butterfly-shaped cage Ni$_2^{\text{II}}$Ln$_2^{\text{III}}$.

4.3.1 Magnetic properties

In what follow, we examine in detail the low-temperature magnetization, dc and ac susceptibilities together with the Cole-Cole plots of the complexes introduced by Eq. (4.4) consisting of the special tunable exchange anisotropy Δ_{nl} in the presence of the external uniform magnetic field B.

TABLE 4.1: Main magnetic data and ED results of data fitting parameters for the isotropic samples **a−d**, assuming $\Delta_{nl} = J_{nl}$ and the same coupling constant value of Ni$\cdots$Ni to that of obtained in Ref. [73], i.e., $J_{nn} = +5.2$ cm^{-1}.

Sample	J_{nl} (cm^{-1})	J_{ll} (cm^{-1})	D_n (cm^{-1})	D_l (cm^{-1})	ED for $\chi_M T_{300 \text{ K}}$ cm^3 K mol^{-1}	Exp. data $\chi_M T_{300 \text{ K}}$ cm^3 K mol^{-1} [73]
Ni$_4^{II}$Tb$_4^{III}$	2.5	-1.5	0.25	2.6	($\approx$) 52	52.5
Ni$_4^{II}$Dy$_4^{III}$	1.75	-1.25	0.5	2.6	($\approx$) 59	61.4
Ni$_4^{II}$Ho$_4^{III}$	0.01	-0.75	1	4.75	($\approx$) 60	61.6
Ni$_4^{II}$Er$_4^{III}$	0.9	-1.1	0.5	2.2	($\approx$) 52	51.6

4.3.1.1 Magnetization process

To gain insight into how the spin ground states of the Ni$_4^{II}$Ln$_4^{III}$ complexes are manifested at finite temperatures, we plot in Fig. 4.6 the magnetization as a function of the magnetic field B. At first glace, we compare our deduced results of the magnetization at temperature $T = 2$ K with the experimental data reported in Ref. [73] (curves marked with black cycles), assuming isotropic XXX interaction $\Delta_{nl} = J_{nl}$. We consider exchange coupling Ni$\cdots$Ni as fixed value $J_{nn} = 5.2$ cm^{-1} in all forthcoming simulations, while remaining exchange interactions J_{nl} and J_{ll}, as well as, single-ion anisotropies D_n and D_l are selected such that the best fit with the experimental data of magnetization and dc susceptibility (Fig. 4.7) is achieved.

Based on the ED method and QMC simulations, the best fit of the magnetic data with the Hamiltonian (4.4) led to the magnetic parameters of table 4.1. As unfolded in Ref. [73], low-lying excited states play determinative role in being weak Ni$\cdots$Ln magnetic exchange interactions in all samples **a−d**. A steep increase in the magnetization curve at $B \lesssim 1$T supports the interaction Ni$\cdots$Ln is ferromagnetic. For magnetic range $B > 1$T, slow increase without reaching saturation at $B = 5$ T could be mainly due to the presence of striking magnetic anisotropy for lanthanides. The slope of the magnetization curve against B below 1 T is higher for **a** than for **b**, indicating a stronger magnetic coupling Ni$\cdots$Ln for the former. Analogously, a weaker magnetic exchange interaction is deduced for complexes **c** and **d** than in their counterparts **a** and **b**. ED results of data fitting parameters for the isotropic case of compounds shown in table 4.1 confirm these presumptions.

It is evident from Fig. 4.6 that for all compounds, our results obtained from ED method and from QMC simulation are in a good agreement with the experimental data of the magnetization process. According to the compatibility between ED results and QMC simulations, hereafter, we perform ED method to realize the low-temperature magnetic properties and the behavior of other variables investigated in this work.

The magnetization curve exhibits at low temperatures abrupt in vicinity of each critical field, addressing the zero-temperature magnetization jumps. It is clear from Fig. 4.6 that four possible
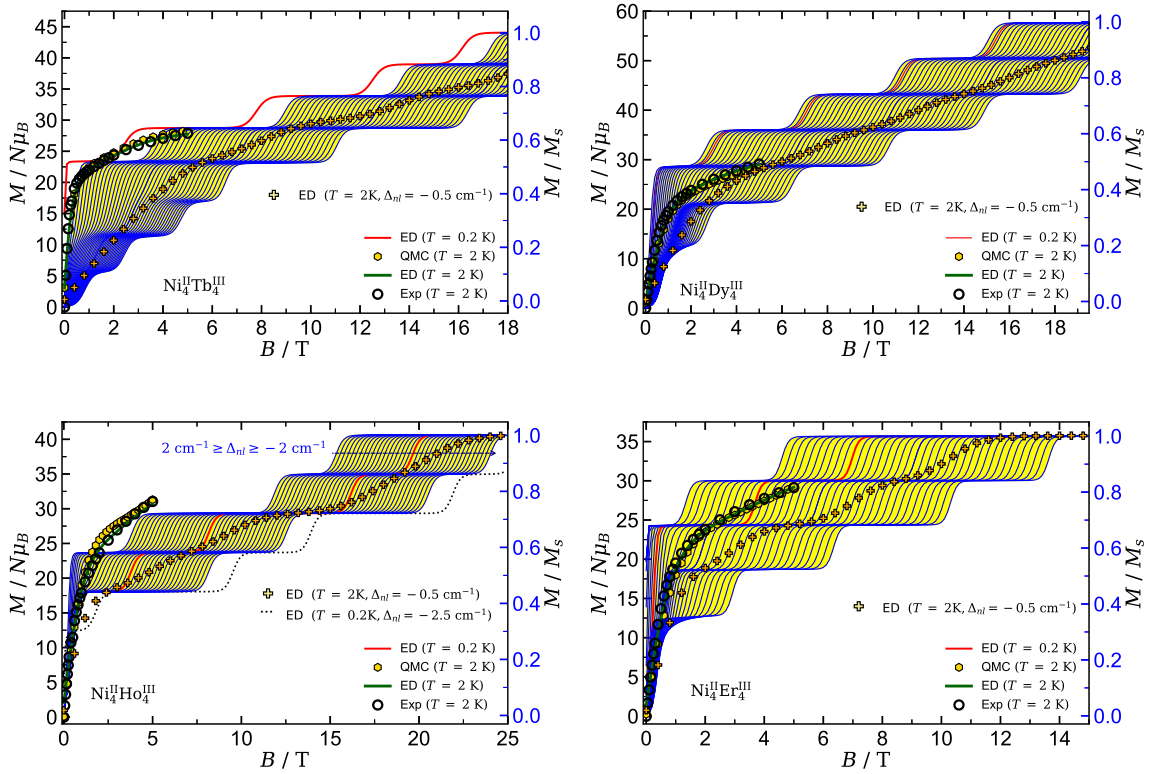
FIGURE 4.6: Numerical results of the magnetization of the complexes **a**−**d** as a function of the transverse magnetic field B at low temperature $T = 0.2K$ (red solid lines) and at $T = 2K$, obtained form QMC-ALPS algorithms (hexagons) and from ED method (green solid lines) where we have considered exchange couplings as $J_{nn} = 5.2$ cm^{-1}, and other data parameters selected from table 4.1 to achieve the best fit with the experimental data analysis reported in Ref. [73] (black cycles). Blue solid curves demonstrate the low temperature ($T = 0.2K$) magnetization process of compounds for various fixed values of the exchange anisotropy Δ_{nl} ($2 \geq \Delta_{nl} \geq -2$ with a numerical step 0.1). Pluses show the ED results of the magnetization at higher temperature $T = 2K$, assuming fixed value $\Delta_{nl} = -0.5$ cm^{-1}. Right hand axes indicate the magnetization per saturation of compounds.

sequences of the intermediate magnetization plateaux can be generally detected at low temperature $T = 0.2$ K for **a**−**c** (red solid lines), and two plateaus for complex **d**. Depending on the strength of exchange anisotropy parameter Δ_{nl}, the magnetization jump occur at different critical magnetic field. As the anisotropy decreases in all compounds, the magnetic position of the critical points moves toward higher magnetic fields. Upon further decrease of Δ_{nl}, one sees that new narrower plateaux appear at respective lower fractional values of saturation magnetization. We figured out a considerable influence of assumed exchange anisotropy Δ_{nl} on the magnetization of the complexes at higher temperature. We display in Fig. 4.6 how the magnetization curve deviates at $T = 2$ K when fixed $\Delta_{nl} = -0.5$ cm^{-1} is hypothesized. Consequently, at low temperature region, by tracing the magnetization jumps and steps the possible discontinuous ground-state phase transitions of the complexes can be pleasantly demonstrated.

Figure 4.7 displays our ED results obtained for the $\chi_M T$ product for isotropic complexes **a**−**d** when $\Delta_{nl} = J_{nl}$ in the $2-300$ K temperature range in the presence of an applied magnetic field
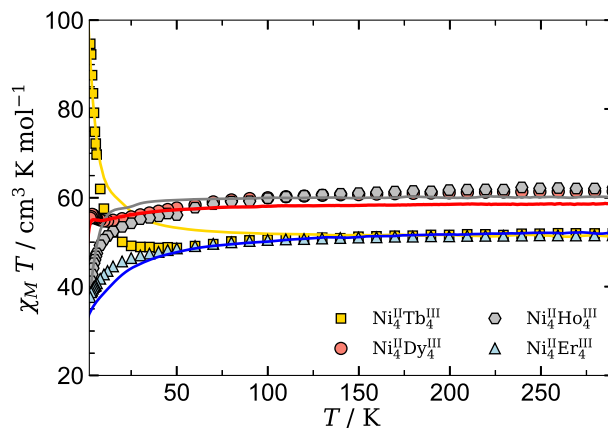
FIGURE 4.7: Experimental data of the $\chi_M T$ product together with the corresponding ED results (solid lines) versus the temperature for isotropic complexes **a**−**d** in the $2-300$ K range with an applied magnetic field $B = 0.1$ T.

$B = 0.1$ T. This figure manifests all necessary information about the magnetic interactions of the compounds under consideration. As elucidated in Ref. [73], due to a ferromagnetic interaction between Ni^{II} and Ln^{III} we observe an increase of function $\chi_M T$ under cooling for complexes **a** and **b**. With further decrease of the temperature ($T < 5$K), $\chi_M T$ decreases for **b**, denoting the magnetic anisotropy of the Ni^{II} ions. For complexes **c** and **d**, it is evident that the $\chi_M T$ product increases steadily upon decreasing the temperature then more sharply down to $T < 5$K. The depopulation of the magnetic sub-level energies m_J of the Ln^{III} ions leads to this behavior. Along side this, the Ln^{III} anisotropies may overcome the $Ni^{II} - Ln^{III}$ ferromagnetic interactions at sufficiently low temperatures.

4.3.1.2 AC susceptibility

For a paramagnetic system in thermal equilibrium, a dc magnetic field can play as the anisotropy role in the Hamiltonian and lifts the degeneracy. Dynamic susceptibility χ_{ac} is defined as the response of the magnetization of a substance to a small change in the magnetic field, namely, as the dc applied magnetic field is changed different susceptibility is given. Assume a material in the presence of an external magnetic field $B(t) = B_0 + b\cos(\omega t)$, alternating with the angular frequency $\omega = 2\pi\nu$ of the ac field, where b corresponds to the amplitude of the driving field.

In thermal equilibrium, it is expected that the temperature of the spin system and the lattice temperature are equal. The temperature of the spin system will change upon the magnetic field variations that contributes to the spin-lattice relaxation. Therefore, the entropy of the spin system undergoes changes [180, 181]. From this, one can deduce analytical expression for the complex susceptibility χ_{ac} as

$$\chi_{ac}(\omega) = \chi_S + \frac{(\chi_T - \chi_S)}{1 + i\omega\tau}, \tag{4.8}$$

where quantity χ_T is the isothermal susceptibility in the limit of the low frequency and is associated to the spin-lattice relaxation, while χ_S denotes the adiabatic susceptibility in the limit of the high frequency which is related to spin-spin relaxation. $\omega = 2\pi\nu$ (ν reads frequency), and τ is called relaxation time after which the magnetization of the system reaches a new equilibrium state. Real and imaginary parts of Eq. (4.8) can be written as

$$\chi'(\omega) = \chi_S + \frac{(\chi_T - \chi_S)}{1 + \omega^2\tau^2}, \quad \chi''(\omega) = \frac{(\chi_T - \chi_S)\,\omega\tau}{1 + \omega^2\tau^2}. \tag{4.9}$$

The Argand plot is a semicircle when one relaxation time (the Debye process) exists, whereas for the distribution of relaxation times the plot is an arc. Here, the strategy that might apply is a spread of relaxation times into the complexes **a**−**d**. The generalized Debye model can be thus formulated as

$$\chi_{\mathrm{ac}}(\omega) = \chi_S + \frac{(\chi_T - \chi_S)}{1 + (i\omega\tau)^{1-\alpha}}, \tag{4.10}$$

where $0 \leq \alpha \leq 1$. For the Debye model $\alpha = 0$, while for spin glasses value $\alpha = 0.9$ can be achieved. For the complexes under study we attain $\alpha \neq 0$, because $\chi''_{\max}/\chi'_{\max} < 1$.

The relaxation time of superparamagnets with respect to the temperature may be described by the Arrhenius law $\tau(t) = \tau_0 \exp(\Delta E/k_B T)$, in which ΔE is the energy barrier. In all complexes **a** − **d**, existence of weak magnetic interactions Ni$\cdots$Ln and Ln$\cdots$Ln result in a small energy barrier for the flipping of the magnetization, further lead to a favor quantum tunneling of magnetization by mixing of low-lying excited states in the ground state. Characteristic time τ_0 is considered as temperature independent and varies from $\tau_0 \approx 10^{-9}$ s for nonmetallic to $\tau_0 \approx 10^{-13}$ s for metallic systems.

Experimental analysis enlightened that only compounds **a** and **b** show out-of-phase component of the susceptibility χ'' for the temperature region below 4 K [73]. Besides, none of these complexes exhibit any maximum in the χ'' curve above 2 K at frequencies upto 1.4 kHz, even in the presence of a small dc field ($B = 0.1$ T) to fully or partly suppress the possible quantum tunneling relaxation.

In this section let us study the effect of the dc field on the ac susceptibility measurements of the complexes **a** and **b**, propounding either isotropic or anisotropic case at lower temperature region below 2 K. Figure 4.8 illustrates χ' and χ'' simulations for **a** and **b**. We consider the both XXX and XXZ ($\Delta_{\mathrm{nl}} = -0.5$ cm^{-1}) interactions for theses compounds. The behavior of these functions versus temperature and their responses to the dc magnetic field are in agreement with the experimental analysis pronounced in supporting information of Ref. [73]. Surprisingly, we find a maximum in the χ'' curve in the temperature region 1.5 K $< T <$ 2.5 K at frequencies reaching 1.4 kHz, showing blocking temperature at $T_{\mathrm{B}} \approx 2$K. The anisotropy Δ_{nl} considerably reduces the height of this maximum approximately to fifty percent, whereas does not change the blocking temperature.
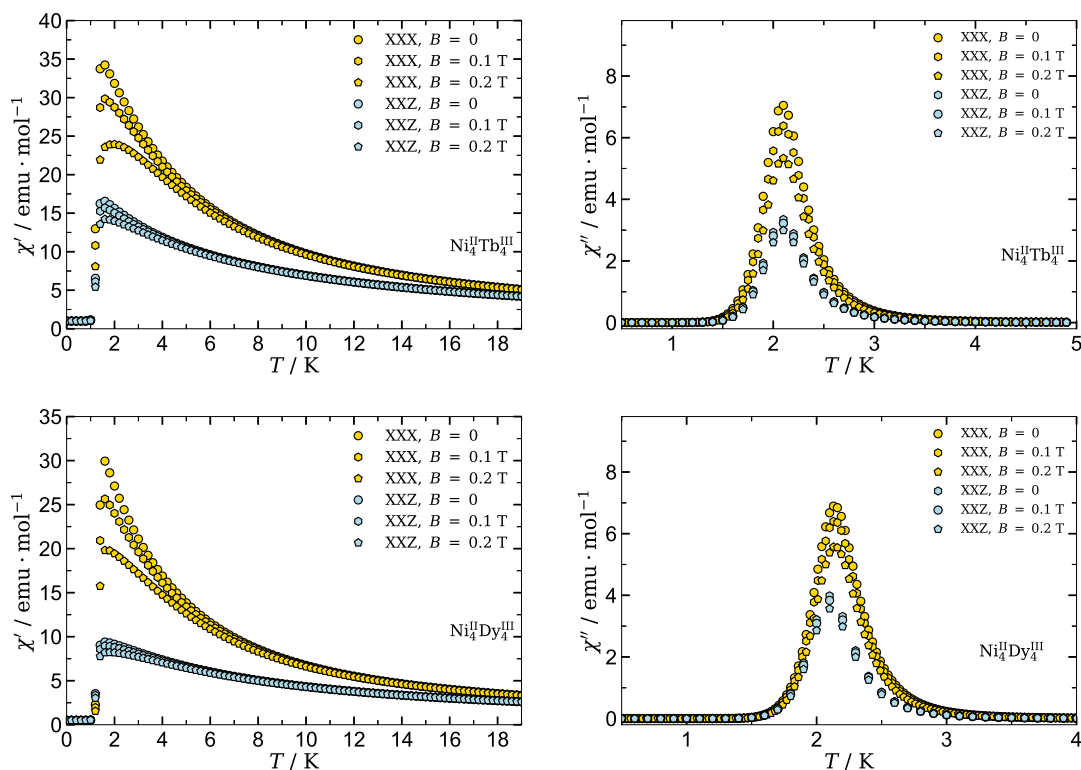
FIGURE 4.8: Numerical results for the temperature dependence of components χ' and χ'' of complexes **a** (upper panels) and **b** (lower panels), assuming three different values of the applied dc magnetic field $B = 0$, 0.1 T, 0.2 T. In all panels, both of XXX and XXZ (with the special easy-axis $\Delta_{nl} = -0.5$ cm^{-1}) models have been considered.
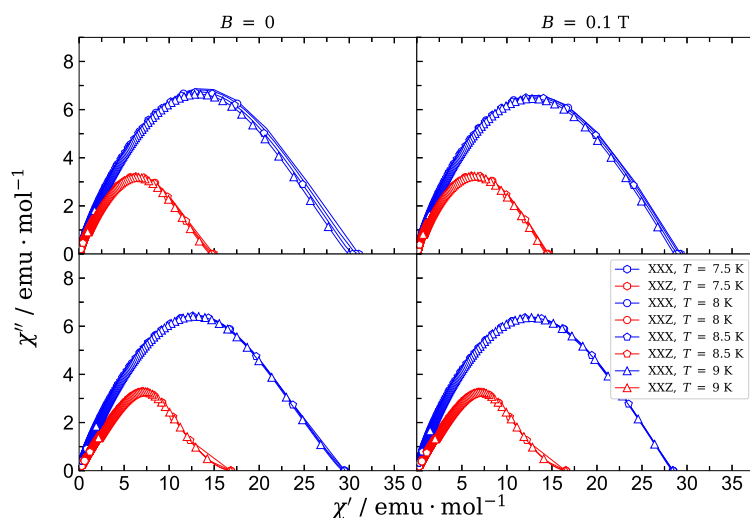
FIGURE 4.9: Argand (cole−cole) plots of **a** and **b** for the parameter sets to χ' and χ'' for $\nu = 1$ Hz − 1400 Hz. In all panels, both of XXX and XXZ (with the special case $\Delta_{nl} = -0.5$ cm^{-1}) models have been considered.

Figure 4.9 shows the Cole-Cole plot of **a** and **b** that is asymmetric and pertains to a distribution of relaxation times. This result is a fingerprint of the SMM-like behavior of these compounds. The relaxation time decreases with increase of the magnetic field and considering anisotropy $\Delta_{\mathrm{nl}} < J_{\mathrm{nl}}$.

4.3.1.3 Specific heat

Next, let us proceed to argument of the results for the specific heat of all complexes derived within the framework of the full ED method. The temperature dependence of the specific heat of complexes is plotted in Fig. 4.10 for several fixed values of the magnetic field. It can be realized from this figure that our results provide a well description of the thermodynamics of complexes under consideration, whenever the applied magnetic field changes from zero upto 2T. We conclude that, the specific heat of **a** exhibits a double-peak temperature dependence at low magnetic field (see for example pluses). By increasing the magnetic field, maxima of the double-peak merge together and make a hill-shaped single Schottky maximum at higher temperatures. As well as, considering anisotropyic XXZ model, taking $\Delta_{\mathrm{nl}} = -0.5$ cm^{-1}, the double-peak exists for higher magnetic fields.

For other compounds we see a relatively similar behavior. The specific heat depicts a steep increase at low temperature region and reaches its maximum under heating. It is easy to find a field-dependence double-peak in low magnetic fields. The anisotropy parameter substantially affects the temperature dependence of the specific heat in the presence of each selected magnetic field. The change in shape of the double-peak appeared in the specific heat of complexes likely remind us the first-order ground state phase transition accompanied with the magnetization jumps and plateaux.

4.3.2 Thermal entanglement

Final stimulating topic that reserves its own right to notify in this context is the measure of quantum entanglement between the Ni$\cdots$Ni spin pairs of the studied complexes. The quantity that we consider as a measure of bipartite entanglement is thermal negativity that can be identified through the qutrit-qutrit reduced density matrix ρ, and reads

$$\mathcal{N}(\rho) = \frac{\parallel \rho^{\mathrm{T_A}} \parallel -1}{2}, \tag{4.11}$$

which corresponds to the absolute value of the sum of negative eigenvalues of the partial transposed density matrix $\rho^{\mathrm{T_A}}$ with respect to the first sub-system (A). The trace norm of matrix $\rho^{\mathrm{T_A}}$ is identified by $\parallel \rho^{\mathrm{T_A}} \parallel = \sqrt{\mathrm{Tr}[(\rho^{\mathrm{T_A}})^\dagger \rho^{\mathrm{T_A}}]}$.
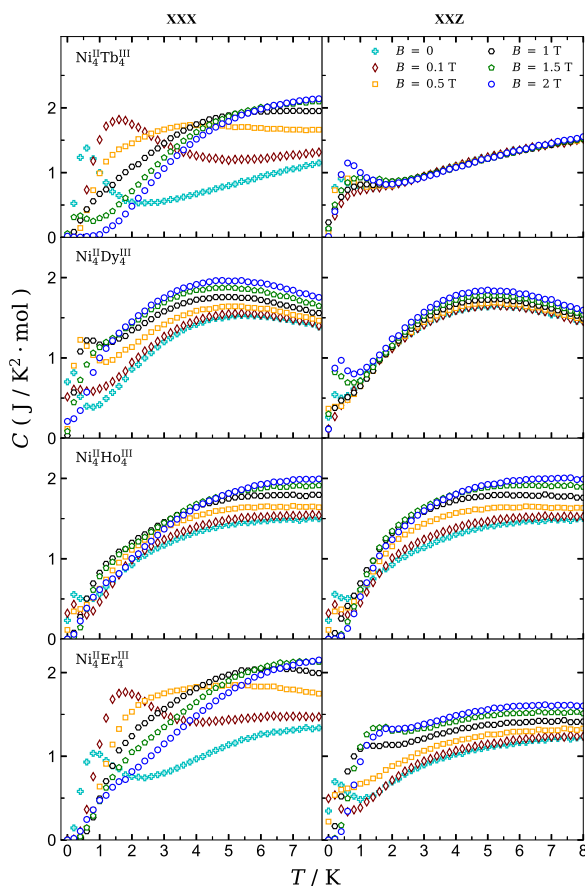
FIGURE 4.10: ED results for the specific heat of complexes **a−d** as a function of the temperature at several fixed values of the magnetic field B. Both of XXX (left column) and XXZ (right column) models are presented. In the panels of right column we assume $\Delta_{nl} = -0.5$ cm^{-1}.

In Fig. 4.11 is plotted the negativity $\mathcal{N}(\rho)$ as a measure of bipartite entanglement between spin-1 pairs Ni$\cdots$Ni of the complexes **a−d** with respect to the temperature for several fixed values of the magnetic field. In this figure one can see that the behavior of negativity is generally different for each compound. Particularly, when an external magnetic field is applied, this function behaves anomalously. To clarify this point, in the absence of the magnetic field, for **a**, there is a very small entanglement between pairs of Ni atoms that rapidly increases with increase of the temperature, then monotonically tends to a constant value $\mathcal{N} \approx 0.06$. With increase of the magnetic field, one observes that by heating, the negativity reaches a relative minimum within the interval 1 K $< T_c <$ 3 K, then increases upto $\mathcal{N} \approx 0.06$.

The temperature dependence of the thermal negativity for Ni$\cdots$Ni of the complexes **b−d** are unlike **a** in the absence of magnetic field (see black dashed lines). The entanglement of pair spin Ni$\cdots$Ni strengthens upon cooling the complexes, where a notable entanglement is demonstrated at sufficiently low temperatures and low magnetic fields. Applying a stronger magnetic field substantially alters the temperature dependence of the negativity. For instance, upon cooling
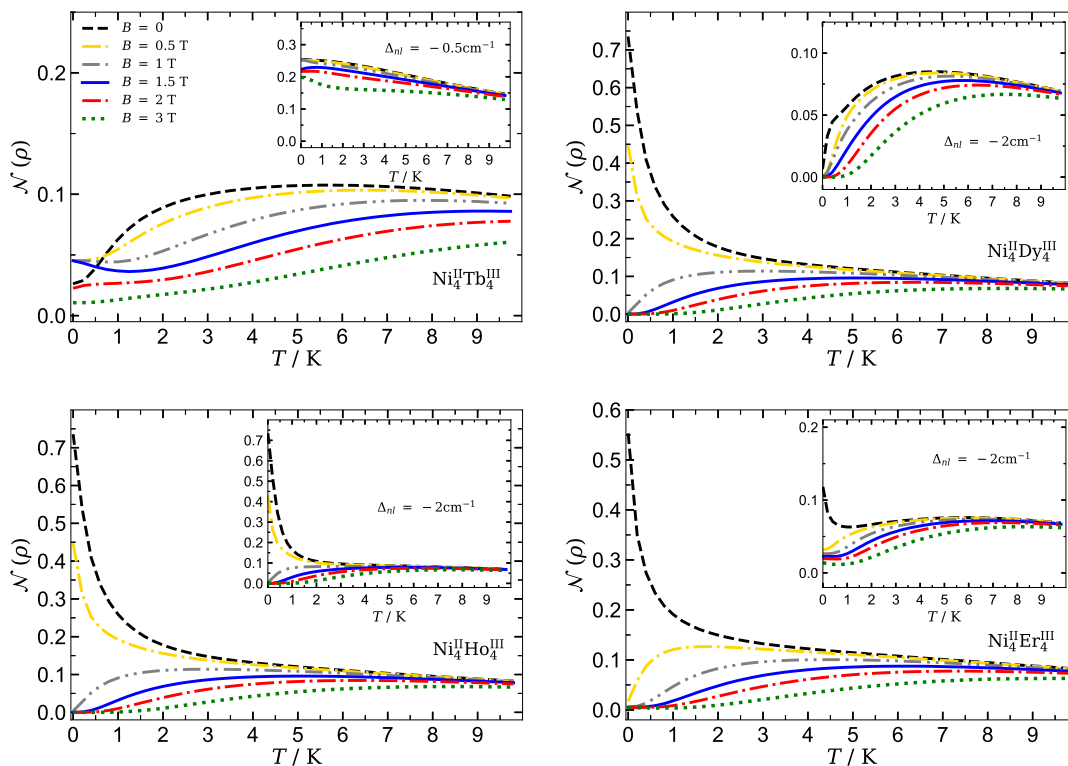
FIGURE 4.11: Thermal negativity as a function of temperature T for various fixed values of the magnetic field, supposing XXX model of compounds **a**−**d**. Insets illustrate the temperature dependence of the negativity where XXZ model of the corresponding complexes were examined for easy-axis anisotropy $\Delta_{\mathrm{nl}} = -2$ cm^{-1}.

the negativity reaches a relative maximum and then sharply decreases where an entanglement death happens in these complexes at low temperatures.

Insets assigned in the panels of Fig. 4.11 depict relevant entanglement negativity versus temperature when the anisotropic XXZ models are hypothesized for the complexes such that $\Delta_{\mathrm{nl}} = -2$ cm^{-1}. The interesting point to observe from insets is that, when a typical easy-axis anisotropy $\Delta_{\mathrm{nl}} = -2$ cm^{-1} is assumed, the entanglement is restricted for a wide rage of magnetic field.

4.4 Coupled tetranuclear $\mathrm{Cu}_4^{\mathrm{II}}$ square complexes

4.4.1 The model

In this section, let us consider the Hamiltonian of the tetranuclear copper(II) compounds abbreviated by simple notation $\mathrm{Cu}_4^{\mathrm{II}}$ (see Fig. 4.12) as a magnetic system which is under the influence of an external magnetic field. The Hamiltonian of the model can be expressed as follows
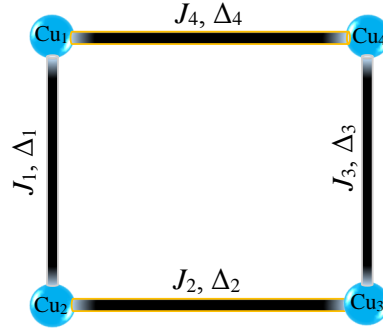
FIGURE 4.12: schematic structure of the four spin-1/2 Cu_4^{II} complexes on the XXZ Heisenberg model with the corresponding magnetic exchange interactions.

$$
\begin{aligned}
H = & [-J_1(S_1^x S_2^x + S_1^y S_2^y) + \Delta_1 S_1^z S_2^z] + \\
& [-J_2(S_2^x S_3^x + S_2^y S_3^y) + \Delta_2 S_2^z S_3^z] + \\
& [-J_3(S_3^x S_4^x + S_3^y S_4^y) + \Delta_3 S_3^z S_4^z] + \\
& [-J_4(S_4^x S_1^x + S_4^y S_1^y) + \Delta_4 S_4^z S_1^z] - \\
& \mu_B g B(S_1^z + S_2^z + S_3^z + S_4^z).
\end{aligned}
\tag{4.12}
$$

The coupling J_i with $i = \{1, 2, 3, 4\}$ describes the strength of the spin interaction, being ferromagnetic when $J_i > 0$. B is the external magnetic field which is only applied to the z-direction, while Δ is the exchange anisotropy parameter. g is the Landé g-factor with the assumption $g = 2$, and S_i^α ($\alpha = x, y, z$) are the spin-1/2 operators. For simplicity, we set $\hbar = 1$, and Bohr magneton μ_B was absorbed into a definition of the magnetic field term. We notify that for simplicity, in the forthcoming analytical expressions and simulations, we consider $J_2 = J_3 = J_4 = J$ and uniform anisotropy $\Delta_1 = \Delta_2 = \Delta_3 = \Delta_4 = \Delta$, assuming $J_1 = 1$ as energy unit for all other parameters with $\{B, J, \Delta, T\}$ being dimensionless parameters. In the next sections, we will assume both pure ferromagnetic interactions ($J > 0$) and mixed ferromagnetic-antiferromagnetic interactions between nearest-neighbor spins by adopting $J < 0$ that means $J_2, J_3, J_4 < 0$ but $J_1 = 1 > 0$.

4.4.2 Ground-state phase transition

The spin-1/2 tetranuclear square complex with the Hamiltonian (4.12) exhibits four different ground states in the presence of a transverse magnetic field. The ground-state phase diagram of the model involves two localized one-magnon phases, $|\text{LOM}\rangle_1$ and $|\text{LOM}\rangle_2$, the localized two-magnon phase $|\text{LTM}\rangle$ and the fully polarized phase $|\text{FPS}\rangle$ given by the eigenvectors

$$
\begin{aligned}
|\text{LOM}\rangle_1 &= |\psi_{11}\rangle \quad \text{with} \quad M/M_s = \frac{1}{2}, \\
|\text{LOM}\rangle_2 &= |\psi_2\rangle \quad \text{with} \quad M/M_s = \frac{1}{2}, \\
|\text{LTM}\rangle &= |\psi_{16}\rangle \quad \text{with} \quad M/M_s = 0, \\
|\text{FPS}\rangle &= |\psi_9\rangle \quad \text{with} \quad M/M_s = 1.
\end{aligned}
\tag{4.13}
$$
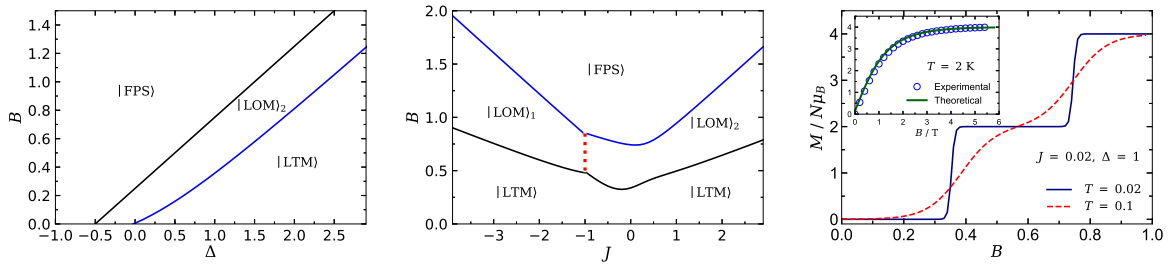
FIGURE 4.13: (Left panel) Ground-state phase diagram in the $(B - \Delta)$-plane by assuming fixed $J = 0.02$. (Middle panel) Ground-state phase diagram in the $B - J$ plane by assuming fixed $\Delta = 1$. (Right panel) The total magnetization with respect to the transverse magnetic field B for fixed values $J = 0.02$ and $\Delta = 1$ at two different temperatures $T = 0.02$ and $T = 0.1$. The inset displays the experimental data (blue cycles) and our numerical data fitting (green solid line) for the field dependence of the magnetization of Cu^{II} square complex at high temperature $T = 2$ K when the same set of exchange couplings to those reported in Ref. [182], i.e., $J_1 = -|\Delta_1| = +5.81$ cm^{-1}, $J_2 = -|\Delta_2| = +2.36$ cm^{-1}, $J_3 = -|\Delta_3| = +1.73$ cm^{-1} and $J_4 = -|\Delta_4| = +2.37$ cm^{-1} is considered.

M is the total magnetization and M_s denotes the saturation magnetization.

In Fig. 4.13 (left panel), we illustrate the zero-temperature phase diagram in the $(B - \Delta)$-plane where weak coupling constant $J = 0.02$ is assumed. In this situation, one detects three different ground states $|\,\text{LOM}\rangle_2$, $|\,\text{LTM}\rangle$ and $|\,\text{FPS}\rangle$. $|\,\text{LOM}\rangle_2$ phase region is located between other two phase such that they have no mutual boundary. The boundary between $|\,\text{LOM}\rangle_2$ and $|\,\text{LTM}\rangle$ phases is given by $B = 0.2501 + 0.5\Delta$, while $|\,\text{LOM}\rangle_2$ and $|\,\text{FPS}\rangle$ phases are separated by $B = -0.2501 + 0.25(\Delta + \sqrt{\Delta^2 + 1.042})$. The most stimulating result of the ground-state phase diagram within the $(B - J)$-plane is plotted in the middle panel of Fig. 4.13, revealing the topology of two different phase transitions, namely, discontinuous ground-state phase transitions (solid lines) and that of the continuous (second-order) phase transition (vertical dotted line) between $|\,\text{LOM}\rangle_1$ and $|\,\text{LOM}\rangle_2$ for which the total magnetization is in one-half of saturation value.

By inspecting right panel of Fig. 4.13, one can see that the low-temperature magnetization versus applied magnetic field exhibits zero and one-half plateaux with respect to its saturation value for the parameter set $J = 0.02$ and $\Delta = 1$. By comparing this panel with those of phase diagrams, one immediately understand that the magnetization jumps and plateaus are accompanied with the ground-state phase transition and phase region. Magnetic measurements on the model manifested ferromagnetic interactions between four Cu^{II} atoms, possessing $S_t = 2$ ground state. In order to have a comparison between our theoretical prediction for the magnetization of the model with the relevant experimental data reported in Ref. [182], we display in the inset of right panel of Fig. 4.13 the magnetization versus magnetic field by assuming the same fitting set of the other parameters, namely, at $T = 2$ K (solid green line) and fixed values of the coupling constants $J_1 = -|\Delta_1| = +5.81$ cm^{-1}, $J_2 = -|\Delta_2| = +2.36$ cm^{-1}, $J_3 = -|\Delta_3| = +1.73$ cm^{-1} and $J_4 = -|\Delta_4| = +2.37$ cm^{-1}. We observe that our analytical results are in an excellent coincidence with the experimental data (blue cycles).

4.4.3   Local quantum uncertainty

The local quantum uncertainty (LQU) was recently proposed as a discord-like measure of quantum correlations based on the principle of skew information. It is written as

$$\mathcal{U}(\rho) = \min_{K_A} \mathcal{I}(\rho, K_A \otimes I_B), \tag{4.14}$$

where K_A is some local observables on the subsystem A. I_B being the identity operator acting on the subsystem B, while $\mathcal{I}$ is the skew information associated to the density matrix ρ and defined as

$$\mathcal{I}(\rho, K_A \otimes I_B) = -\frac{1}{2}\text{Tr}([\sqrt{\rho}, K_A \otimes I_B]^2). \tag{4.15}$$

For a bipartite qubit-qudit system the closed-form of the local quantum uncertainty is given by

$$\mathcal{U}(\rho) = 1 - \lambda_{\max}(\mathcal{W}_{AB}), \tag{4.16}$$

where $\lambda_{\max}$ stands for the largest eigenvalue of the 3×3 matrix $\mathcal{W}_{AB}$ whose elements are given by

$$(\mathcal{W}_{AB})_{ij} = \text{Tr}(\sqrt{\rho}\,(\sigma_A^\alpha \otimes I_B)\,\sqrt{\rho}\,\left(\sigma_A^{\alpha'} \otimes I_B\right)). \tag{4.17}$$

In above, $\sigma_A^{\alpha(\alpha')}$ with $\alpha(\alpha') = \{x, y, z\}$ represent the Pauli operators of the subsystem A. Therefore, in terms of the Fano-Bloch components $\mathcal{R}$ associated with the matrix ρ, the eigenvalues $(\mathcal{W}_{AB})_{ij}$ can be expressed as

$$\mathcal{W}_1 = \mathcal{W}_2 = \sqrt{\left(t_1 + 2\sqrt{d_1}\right)\left(t_2 + 2\sqrt{d_2}\right)} + \frac{1}{4}\frac{\left(\mathcal{R}_{03}^2 - \mathcal{R}_{30}^2\right)}{\sqrt{(t_1 + 2\sqrt{d_1})(t_2 + 2\sqrt{d_2})}},$$

$$\mathcal{W}_3 = \frac{1}{2}\left(1 + 2\left(\sqrt{d_1} + \sqrt{d_2}\right)\right) + \frac{1}{8}\left(\frac{(\mathcal{R}_{03} + \mathcal{R}_{30})^2 - (\mathcal{R}_{11} - \mathcal{R}_{22})^2}{(t_1 + 2\sqrt{d_1})} + \frac{(\mathcal{R}_{03} - \mathcal{R}_{30})^2 - (\mathcal{R}_{11} + \mathcal{R}_{22})^2}{(t_2 + 2\sqrt{d_2})}\right),$$

with

$$t_{1,2} = \frac{1}{2}\left(\mathcal{R}_{00} \pm \mathcal{R}_{03}\right), \tag{4.18}$$

$$d_{1,2} = \frac{1}{16}\left[(\mathcal{R}_{00} \pm \mathcal{R}_{33})^2 - (\mathcal{R}_{30} \pm \mathcal{R}_{03})^2 - (\mathcal{R}_{11} \mp \mathcal{R}_{22})^2\right],$$

Hence, the LQU for the considered density operator ρ is gained from

$$\mathcal{U}(\rho) = 1 - \max(\mathcal{W}_1, \mathcal{W}_3). \tag{4.19}$$

Figure 4.14 illustrates the LQU of the model in different planes. Panels of the first row depict the temperature dependence of this function for fixed $J = 0.02$, such that left panel corresponds to the several values of the magnetic field and $\Delta = 1$, whereas right one corresponds to the case
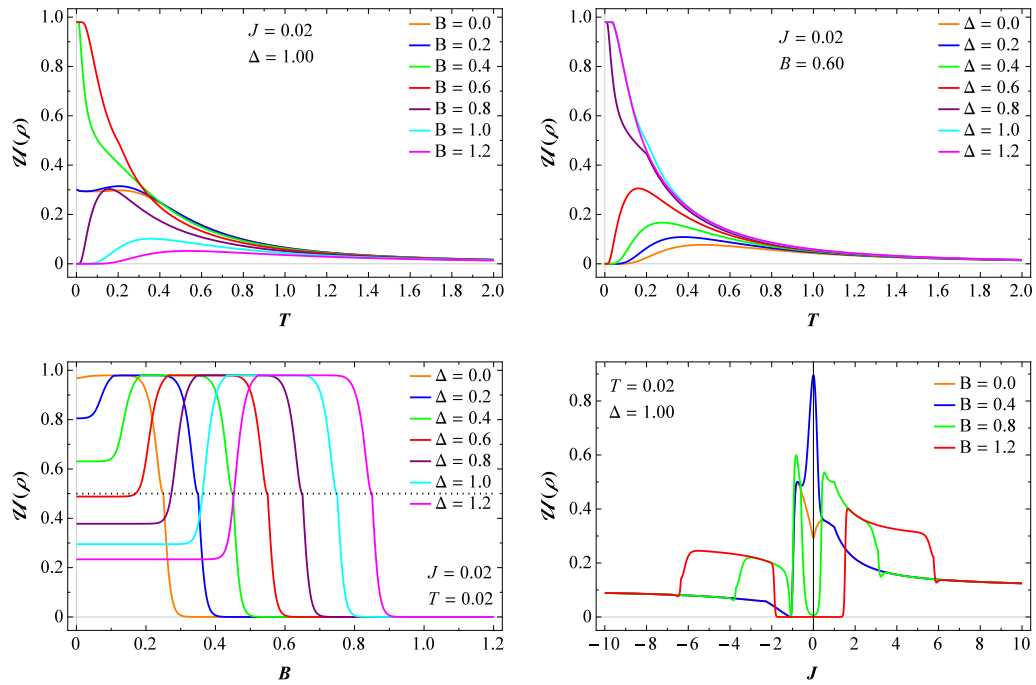
FIGURE 4.14: Local quantum uncertainty $\mathcal{U}(\rho)$ in different perspectives. Horizontal dotted line shows the critical magnetic fields where the phase boundary between $|\,\mathrm{LOM}\rangle_2$ and $|\,\mathrm{FPS}\rangle$ (black line plotted in the left panel of Fig. 4.13) exists.

when several values of the anisotropy are assumed at fixed $B = 0.6$. A vivid difference is evident between LQU and concurrence, i.g., the later reaches its maximum value 1 at finite low temperatures while the former does not. In addition, the concurrence vanishes at a critical temperature, while upon heating, LQU tends to zero but does not vanish. Lower-left panel displays the LQU as a function of the magnetic field for several values of the exchange anisotropy, supposing low temperature $T = 0.02$ and $J = 0.02$. Again, one sees that the LQU does not reaches unity, and with increase of the magnetic field it sharply decreases and ultimately vanishes nearby the same critical magnetic point to the concurrence. It is worth mentioning that another notable difference between magnetic behavior of LQU and concurrence is that, the former behaves anomalously when drops down in height to $\mathcal{U} = 1/2$. This phenomenon disclosed by horizontal dotted line is the fingerprint of the first-order phase boundary between $|\,\mathrm{LOM}\rangle_2$ and $|\,\mathrm{FPS}\rangle$ (see black line plotted in the left panel of Fig. 4.13) that was not observed in the concurrence. In result, the LQU is more robust than the concurrence to demonstrate discontinuous phase spectra.

Last but not least, let us also emphasize another important consequence of the LQU analysis with respect to the coupling constant J. Lower-right panel illustrates the LQU versus the coupling constant J at low temperature $T = 0.02$ and $\Delta = 1$, where four different values of the magnetic field have been taken. For the ferromagnetic coupling, $J > 0$, the LQU falls down close to the critical exchange coupling at which the ground-state phase transition occurs. On the other hand, for mixed ferromagnetic-antiferromagnetic case $J < 0$, we see that this function does not vanish but tends to $\mathcal{U} = 0.1$ as J decreases further than critical point $J = -1$ at which the
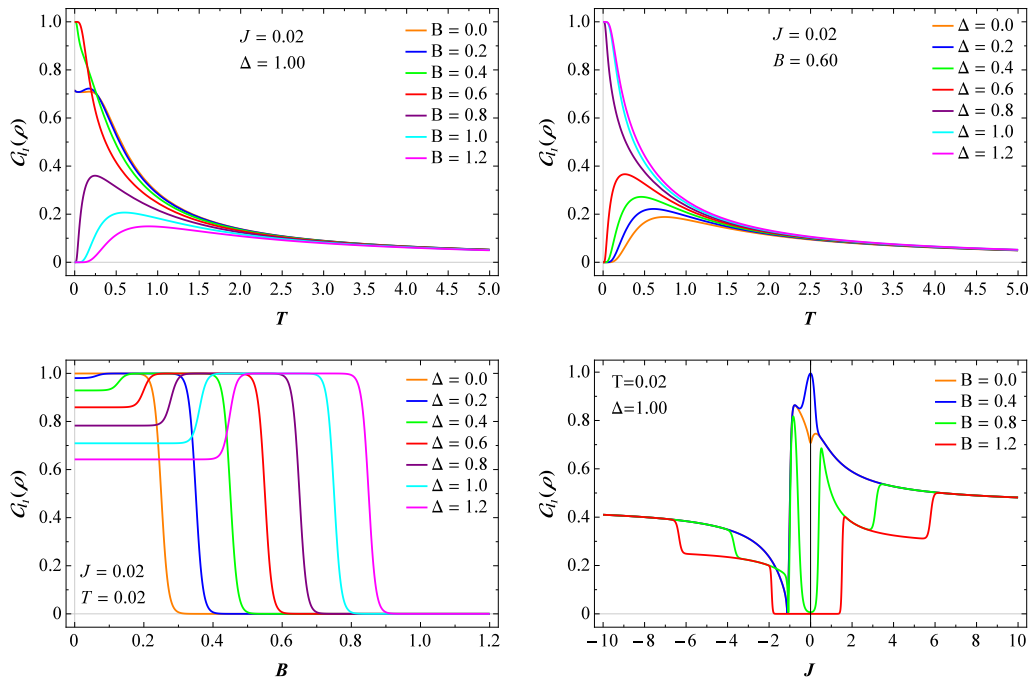
FIGURE 4.15: Quantum coherence $\mathcal{C}_{l_1}$ of the model under study with respect to the same parameter sets, as well as, with the same panel-sequence to Fig. 4.14.

second-order phase transition occurs (see vertical dotted line shown in the middle panel of Fig. 4.13). Furthermore, for region $J > 0$, at low magnetic field $B = 0.4$ (blue line), the LQU curve shows a discontinuous alteration in the vicinity of a critical point accompanied with the phase boundary between $|\,\mathrm{LOM}\rangle_2$ and $|\,\mathrm{LTM}\rangle$ (see black line plotted in the middle panel of Fig. 4.13). Hence, the LQU could be a fine witness of the discontinuous phase transition of the model that is more vigorous that the concurrence in this medium.

4.4.4 Quantum coherence

Here, we use the intuitive l_1-norm of coherence measure. We depict typical thermal variations of the l_1-norm of coherence of the tetranuclear model with successive reentrant phase transitions in Fig. 4.15. Upper left-right panels manifest the temperature dependence of the quantum coherence for the fixed $J = 0.02$ and various values of other parameters. It is evident that this quantum correlation quantifier experiences its maximum at low temperature such as the concurrence. On the other hand, when the temperature increases, at low magnetic fields and low anisotropies such a function gradually decreases and tends to zero but does not vanishes neither at higher magnetic fields nor for stronger exchange anisotropies. Returning to Fig. 4.14, it is observable that the l_1-norm of coherence and LQU have similar behavior to each other at high temperatures.

Lower-left panel displays the coherence as a function of the magnetic field at low temperature $T = 0.02$ and low exchange coupling $J = 0.02$, where several fixed values of the anisotropy Δ
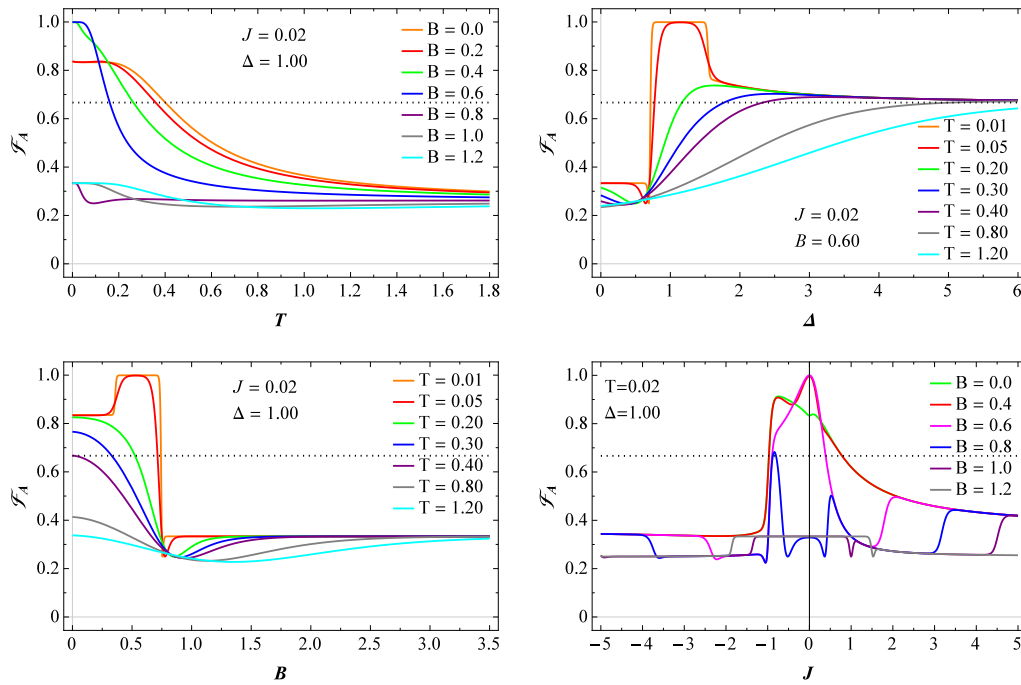
FIGURE 4.16: (Upper-left panel) $\mathcal{F}_A$ versus temperature, assuming $J = 0.02$, $\Delta = 1$ and several fixed values of the magnetic field. (Upper-right panel) The average fidelity $\mathcal{F}_A$ as a function of anisotropy Δ for fixed $J = 0.02$, $B = 0.6$ and different values of the temperature. (Lower-left panel) Field dependence of the average fidelity $\mathcal{F}_A$ for various temperatures, where other parameters have been taken as $J = 0.02$ and $\Delta = 1$. (Lower-right panel) the same function at low temperature $T = 0.02$ against the coupling constant J when different fixed values of the magnetic field are considered such that $\Delta = 1$. Horizontal dotted lines denote the limit value $2/3$ and identify the quantum teleportation becomes possible for the case when the average fidelity is greater than this value.

are assumed. The same behavior to the concurrence is evident close to the critical magnetic fields at which the ground-state phase transition occurs. The l_1-norm of coherence $\mathcal{C}_{l_1}$ versus the coupling constant J at low temperature is plotted in the lower-left panel of Fig. 4.15, where anisotropy $\Delta = 1$ and four different magnetic fields are selected. It is visible a quite different behavior of this function compared with the LQU and the concurrence. Namely, for the case when $J < 0$, by decreasing the exchange coupling J further that the critical point $J = -1$, the quantum coherence not only does not vanishes but also increases more than LQU. Jumps in the coherence curve at special critical point on the J-axis reminisce us the ground-state phase transition.

4.4.5 Quantum Teleportation

In this part, we study the quantum teleportation throughout an entangled mixed state, as a resourse; acts as a generalized depolarizing channel. Next, we investigate the effects of the anisotropy and the magnetic field on the possibility of teleportation through the model under verification.

To describe the quality of the process of teleportation, it is often quite useful to study the fidelity between ρ_{in} and ρ_{out} to characterize the teleported state. When the input state is a pure state, one can apply the concept of fidelity as a useful indicator of the teleportation performance of a quantum channel quantifier. As said earlier, the average fidelity $\mathcal{F}_A$ depends on the quantum channel parameters. In order to transmit a quantum state better than the classical communication protocols, $\mathcal{F}_A$ must be greater than $2/3$ (dotted lines plotted in Fig. 4.16) which is the best fidelity in the classical world. In upper-left panel of Fig. 4.16, is shown the average fidelity as a function of the temperature for the weak easy-axis coupling $J = 0.02$ and fixed $\Delta = 1$, where several fixed values of the magnetic field have been assumed. It is clear from this figure that $\mathcal{F}_A$ does not reaches limit of quantum fidelities for $B \gtrsim 0.8$, hence the teleportation of information happens for the magnetic field rage $B < 0.8$. By inspecting left panel of Fig. 4.13, one finds that the teleportation of information is solely possible for the region below than black line which separates the phase boundaries $\mid \text{LOM}\rangle_2$ and $\mid \text{FPS}\rangle$. Increase of the temperature leads to decease of the possibility of teleportation.

In upper-right panel we depict the average fidelity versus the anisotropy Δ for several fixed temperatures and parameter set $J = 0.02$ and $B = 0.6$. A reentrance point is evident in this figure at which a sharp change in the average fidelity behavior happens. This phenomenon is accompanied with the ground-state phase transition from $\mid \text{FPS}\rangle$ to $\mid \text{LOM}\rangle_2$. This quantity immediately reaches its maximum $\mathcal{F}_A = 1$ within the anisotropy interval $0.8 \lesssim \Delta \lesssim 1.5$, as soon as the system's ground state switches to $\mid \text{LOM}\rangle_2$ (with $M/M_s = 1/2$). So long as the system is in this ground state, the fidelity remains maximum value. Nearby the phase boundary between $\mid \text{LOM}\rangle_2$ and $\mid \text{LTM}\rangle$ the average fidelity sharply decreases. With further decrease of the anisotropy, such a function monotonically decreases and tends to limit value $2/3$. The relevant field dependence of the average fidelity at $J = 0.02$ and $\Delta = 1$ shown in the lower-left panel has also similar behavior. It can be seen from this figure a steep decrease as well as line accumulation in the average fidelity function at low temperature regime in the vicinity of critical magnetic field at which the ground-state phase transition occurs between $\mid \text{LOM}\rangle_2$ and $\mid \text{FPS}\rangle$. Under heating $\mathcal{F}_A$ decreases at low magnetic fields. Accordingly, the possibility of teleportation through this model is restricted.

The most interesting finding from the fidelity investigations is manifested in lower-right panel of Fig. 4.16 by which we illustrate the average fidelity with respect to the exchange coupling J at low temperature $T = 0.02$ and $\Delta = 1$. As one can see, $\mathcal{F}_A$ anomalously behaves nearby the critical exchange couplings at which the ground-state phase transition occurs. Surprisingly, in the antiferromagnetic region of J, close to the critical point $J = -1$ at which the second-order phase transition occurs, the average fidelity sharply drops to its minimum. Consequently, $\mathcal{F}_A$ could be an eligible candidate to trace the ground-state phase transition of the tetranuclear spin-$1/2$ square compound possessing either ferromagnetic or mixed ferromagnetic-antiferromagnetic exchange couplings.

4.5 Conclusions

In this chapter, we have rigorously examined the magnetic and thermodynamic properties of the octanuclear nickel phosphonate-based cage with the geometry of butterfly-shaped molcular structure and a set of heterometallic octanuclear $Ni_4^{II}Ln_4^{III}$ (Ln = Tb, Dy, Ho, Er) compounds. To this end, we first examined the magnetization processes of the isotropic version of the models through ED and QMC methods. We have proved that our results are in excellent agreement with the corresponding experimental data. Building on this confidence, we continued our investigations by means of the ED procedure for the magnetization process, as well as, the specific heat of these models including Heisenberg exchange anisotropy and single-ion anisotropy properties. The models show a complex magnetization landscape with a number of intermediate plateaus and magnetization jumps at low temperature accompanying with the ground-state phase transitions.

Using the reduced density matrix derived from our ED analysis, it is possible to investigate the pairwise thermal entanglement for the linked Ni atoms of $Ni_4^{II}Ln_4^{III}$ complexes. Owing to this fact, we have uncovered that there is a notable entanglement between ferromagnetically interacted Ni atoms for a range of magnetic field. Applying a relatively high magnetic field, this entanglement sharply decreases upon cooling and disappears at a critical temperature. Surprisingly, considering exchange anisotropy for Ni$\cdots$Ln interactions mostly leads to weaken the thermal pairwise entanglement in compounds **b**−**d**, and to enhance the entanglement in compound **a**.

Furthermore, we found several first-order phase transitions in the phase diagram of coupled tetranuclear Cu_4^{II} square complex. In addition, a special second-order phase transition between two localized one-magnon states with relevant magnetization in one-half of saturation magnetization has been detected when mixed ferromagnetic-antiferromagnetic exchange couplings between nearest-neighbor spins have been hypothesized. We then studied local quantum uncertainty and compared it with the concurrence for a pair of spins. We have demonstrated that the both functions behave anomalously close to the critical points at which a typical ground-state phase transition occurs. At low temperature and weak coupling constant we could observe maximum entanglement between selected pair of spins. According to our observations, we convincingly concluded that the local quantum uncertainty is generally more robust than concurrence to witness the ground-state phase transition in different Hamiltonian-parameter sets.

Concluding remarks

The main outcomes delivered from this dissertation are as follows.

i) One of our notable results reported in **chapter 1** is that the thermal pairwise entanglement of $Fe - Mn - Cu$ chain polymer can be controlled and tuned by imposing a magnetic impurity into the model. Based on our theoretical investigations, we proved that QFI can be considered as a useful quantum tool for estimating the quantum phase transition of the Ising-Heisenberg spin-1/2 chain of the heterotrimetallic coordination compound $Fe - Mn - Cu$. We have demonstrated that at low-temperature regime, the inclusion of magnetic impurity leads to remarkable enhancement in the average fidelity until reaching maximum value. Based on our findings regarding the model with magnetic impurity, we claimed that the average fidelity becomes more robust compared with the original model, enabling teleportation of information in the regions of very strong magnetic fields.

ii) The most interesting finding for the Ising-Heisenberg spin ladders discussed in **chapter 2** is that, alteration of the magnetic anisotropy and single-ion anisotropy considered for the integer spins slightly above (below) the critical points results in cooling/heating during the adiabatic demagnetization process, where the temperature rapidly falls down. So, the anisotropies play an important role to understand cooling process together with discontinuous zero-temperature phase transitions of such spin ladders. We have also realized that there are some particular points in the field-induced ground-state phase diagram of the model which makes the intersection of several different ground states. Assuming the cyclic four-spin Ising term affects on the co-ordinates of these special points. It has been demonstrated that, at low temperatures, the specific heat curve anomalously behaves nearby the critical magnetic fields at which a magnetization jump occurs. An anomalous magnetocaloric effect has been observed close to respective magnetization jumps of the Ising-Heisenberg two-leg ladder.

iii) We uncovered in **chapter 3** that the Ising-Heisenberg model on two new modeled TIT lattices exhibits a rich magnetic behavior with several unconventional quantum phases and boundaries. We witnessed that a quantum reduction of the spontaneous magnetizations of the Heisenberg and Ising spins is the result of quantum fluctuations and strongly depends on the anisotropy. Ultimately, it has been demonstrated that the specific heat of Ising-Heisenberg model on the TIT lattices exhibits a logarithmic singularity from the standard Ising universality class for the isotropic ferromagnetic Heisenberg interaction, where the model is in the ground state CFP.

iv) In **chapter 4** we observed that the Ni containing complexes show a complex magnetization landscape with a number of intermediate plateaus and magnetization jumps at low temperature accompanying with the ground-state phase transitions. Also, alteration of

the single- and two-ion anisotropies affected on the magnetization process and the thermodynamics of these models. We have realized that there is a notable entanglement between ferromagnetically interacted Ni atoms of $Ni_4^{II}Ln_4^{III}$ complexes for a special range of magnetic field. Surprisingly, considering exchange anisotropy for $Ni \cdots Ln$ interactions mostly leads to weaken the thermal pairwise entanglement in compounds $\mathbf{b-d}$, and to enhance the entanglement in compound $\mathbf{a}$.

Furthermore, we found several first-order phase transitions in the phase diagram of coupled tetranuclear Cu_4^{II} square complex. In addition, a special second-order phase transition between two localized one-magnon states with relevant magnetization in one-half of saturation magnetization has been detected when mixed ferromagnetic-antiferromagnetic exchange couplings between nearest-neighbor spins have been hypothesized. We have demonstrated that the local quantum uncertainty and concurrence as quantum correlation quantifiers behave anomalously close to the critical points at which a typical ground-state phase transition occurs. We have concluded that the local quantum uncertainty is generally more robust than concurrence to witness the ground-state phase transition and critical behavior of tetranuclear Cu_4^{II} square complex in different Hamiltonian parameter sets.

Bibliography

[1] M. Oshikawa, M. Yamanaka, I. Affleck, Magnetization Plateaus in Spin Chains: "Haldane Gap" for Half-Integer Spins, Phys. Rev. Lett. **78**, (1997) 1984-1987.

[2] J. Strečka and K. Karĺová, Magnetization curves and low-temperature thermodynamics of two spin-1/2 Heisenberg edge-shared tetrahedral, AIP Adv. **8**, (2018) 101403 (4pp).

[3] G. Vidal, J. I. Latorre, E. Rico and A. Kitaev, Entanglement in Quantum Critical Phenomena, Phys. Rev. Lett. **90**, (2003) 227902 (4pp).

[4] B. Gu and G. Su, Magnetism and thermodynamics of spin-1/2 Heisenberg diamond chains in a magnetic field, Phys. Rev. B **75**, (2007) 174437 (16pp).

[5] R. Dillenschneider, Quantum discord and quantum phase transition in spin chains, Phys. Rev. B **78**, (2008) 224413 (7pp).

[6] N. B. Ivanov, J. Richter and J. Schulenburg, Diamond chains with multiple-spin exchange interactions, Phys. Rev. B **79**, (2009) 104412 (6pp).

[7] T. Werlang, C. Trippe, G. A. P. Ribeiro and G. Rigolin, Quantum Correlations in Spin Chains at Finite Temperatures and Quantum Phase Transitions, Phys. Rev. Lett. **105**, (2010) 095702 (4pp).

[8] S. Sachdev, *Quantum Phase Transitions* (Cambridge University Press, Cambridge, (2011)).

[9] O. Rojas, M. Rojas, N. S. Ananikian and S. M. de Souza, Thermal entanglement in an exactly solvable Ising-XXZ diamond chain structure, Phys. Rev. A **86**, (2012) 042330 (8pp).

[10] H. G. Paulinelli, S. M. de Souza, and Onofre Rojas, Thermal entanglement in an orthogonal dimer-plaquette chain with alternating Ising–Heisenberg coupling, J. Phys.: Condens. Matter **25**, (2013) 306003 (8pp).

[11] J. Torrico, M. Rojas, S. M. de Souza, O. Rojas and N. S. Ananikian, Pairwise thermal entanglement in Ising-XYZ diamond chain structure in an external magnetic field, Europhys. Lett. **108**, (2014) 50007 (6pp).

[12] L. M. Veríssimo, M. S.S. Pereira, J. Strečka and M. L. Lyra, Kosterlitz-Thouless and Gaussian criticalities in a mixed spin-(1/2,5/2,1/2) Heisenberg branched chain with exchange anisotropy, Phys. Rev. B **99**, (2019) 134408 (9pp).

[13] A. Taroni, 90 years of the Ising model, Nature Physics **11**, (2015) 997.

[14] L. Turban, One-dimensional Ising model with multispin interactions, J. Phys. A: Math. Theor. **49**, (2016) 355002 (16pp).

[15] B. Lisnyi and J. Strečka, Exactly solved mixed spin-(1,1/2) Ising-Heisenberg distorted diamond chain, Phys. A **462**, (2016) 104-116.

[16] H. Arian Zad and M. Rojas, Quantum coherence, quantum Fisher information and teleportation in the Ising-Heisenberg spin chain model of a heterotrimetallic Fe-Mn-Cu coordination polymer with magnetic impurity, Physica E **126**, (2021) 114455 (12pp).

[17] V. Ohanyan, Antiferromagnetic sawtooth chain with Heisenberg and Ising bonds, Condens. Matter Phys. **12** , (2009) 343-351.

[18] S. Bellucci and V. Ohanyan, Lattice distortions in a sawtooth chain with Heisenberg and Ising bonds, Eur. Phys. J. B **75**, (2010) 531-541.

[19] V. Ohanyan and A. Honecker, Magnetothermal properties of the Heisenberg-Ising orthogonal-dimer chain with triangular X X Z clusters, Phys. Rev. B **86**, (2012) 054412 (17pp).

[20] S. Bellucci, and V. Ohanyan, Correlation functions in one-dimensional spin lattices with Ising and Heisenberg bonds, Eur. Phys. J. B **86**, (2013) 446 (12pp).

[21] F. C. Rodrigues, S. M. de Souza and O. Rojas, Geometrically frustrated Cairo pentagonal lattice stripe with Ièèsing and Heisenberg exchange interactions, Annals of Phys. **379**, (2017) 1-12.

[22] H. Arian Zad, A. Trombettoni and N. Ananikian, Spin-1/2 Ising-Heisenberg Cairo pentagonal model in the presence of an external magnetic field: effect of Landé g-factors, Eur. Phys. J. B **20** 93 (2020) 200 (10pp).

[23] H. Arian Zad, N. Ananikian and R. Kenna, The specific heat and magnetic properties of two species of spin-1/2 ladders with butterfly-shaped unit blocks, Jour.of Phys.: Condens. Matt. **31**, (2019) 445802 (11pp).

[24] O. Rojas, J. Strečka, and S. M. de Souza, Thermal entanglement and sharp specific-heat peak in an exactly solved spin-1/2 Ising-Heisenberg ladder with alternating Ising and Heisenberg inter–leg couplings, Solid State Commun. **68**, 246 (2016) 68-75.

[25] J. Strečka, R. C. Alécio, M. Lyra and O. Rojas, Spin frustration of a spin-1/2 Ising–Heisenberg three-leg tube as an indispensable ground for thermal entanglement, J. Magn. Magn. Mater. **409**, (2016) 124-133.

[26] H. Arian Zad, N. Ananikian and Michal Jaščur, Single-ion anisotropy effects on the demagnetization process of the alternating weak-rung interacting mixed spin-(1/2,1) Ising-Heisenberg double saw-tooth ladders, Phys. Scr. **95**, (2020) 095702 (8pp).

[27] H. Arian Zad and N. Ananikian, Enhanced magnetocaloric effect in a mixed spin-(1/2,1) Ising-Heisenberg two-leg honeycomb ladder with strong-rung interaction, Eur. Phys. J. Plus, **136**, (2021) 597 (22pp).

[28] S. S. Rahaman, S. Sahoo and M. Kumar, Ground state properties and exact thermodynamics of a 2-leg anisotropic spin ladder system, arXiv:2011.11901

[29] M. Freitas, C. Filgueiras, M. Rojas, The Effects of an Impurity in an Ising-XXZ Diamond Chain on Thermal Entanglement, on Quantum Coherence, and on Quantum Teleportation, Ann. Phys. (Berlin) **531**, (2019) 1900261 (10pp).

[30] I. M. Carvalho, O. Rojas, S. M. de Souza, M. Rojas, Tuning the thermal entanglement in a Ising-XXZ diamond chain with two impurities, Quantum. Inf. Process. **18**, (2019) 134 (13pp).

[31] O. Rojas, J. Strečka, O. Derzhko and S. M. de Souza, Peculiarities in pseudo-transitions of a mixed spin-(1/2,1) Ising-Heisenberg double-tetrahedral chain in an external magnetic field, J. Phys.: Condens. Matter **32**, (2020) 035804 (11pp).

[32] O. Rojas, S. M. de Souza, V. Ohanyan and M. Khurshudyan, Exactly solvable mixed-spin Ising-Heisenberg diamond chain with biquadratic interactions and single-ion anisotropy, Phys. Rev. B **83**, (2011) 094430 (9pp).

[33] R. Shrock and Y. Xu, Exact Results on Potts Model Partition Functions in a Generalized External Field and Weighted-Set Graph Colorings, J. Stat. Phys. **141**, (2010) 909-939.

[34] S. C. Chang and R. Shrock, Structure of the Partition Function and Transfer Matrices for the Potts Model in a Magnetic Field on Lattice Strips, J. Stat. Phys. **137**, (2009) 667-699.

[35] S. C. Chang and R. Shrock, Transfer matrices for the partition function of thePotts model on lattice strips with toroidal and Klein-bottle boundary conditions, Phys. A **364**, (2006) 231-262.

[36] J. Yeomans, *Statistical mechanics of phase transitions* (Clarendon, Oxford, 1992).

[37] L. Onsager, Crystal Statistics. I. A Two-Dimensional Model with an Order-Disorder Transition, Phys. Rev. **65**, (1944) 117-149.

[38] T. Horiguchi, A spin-one Ising model on a honeycomb lattice, Phys. Lett. A **113**, (1986) 425-428 .

[39] M. Kolesik and L. Samaj, Solvable Cases of the General Spin-One Ising-Model on the Honeycomb Lattice, Int. J. Mod. Phys. B **6**, (1992) 1529-1538.

[40] F. Y. Wu, Eight-vertex model on the honeycomb lattice, J. Math. Phys. **15**, (1974) 687-691; F. Y. Wu, Eight-vertex model and Ising model in a non-zero magnetic field: honeycomb lattice, J. Phys. A: Math Gen. **23**, (1990) 375-378.

[41] N. Sh. Izmailian and N. S. Ananikian, General spin-3/2 Ising model in a honeycomb lattice: Exactly solvable case, Phys. Rev. B **50**, (1994) 6829-6832.

[42] J. Kiššóva and J. Strečka, Phase Diagrams of the Spin-1/2 Ising–Heisenberg Model on a Triangle–Hexagon Lattice, Acta Phys. Polon. A 118 (2010) 730-731.

[43] J. Čisárová and J. Strečka, Unconventional quantum ordered and disordered states in the highly frustrated spin-1/2 Ising-Heisenberg model on triangles-in-triangles lattices, Phys. Rev. B **87**, (2013) 024421 (15pp).

[44] J. Strečka, L. Čanová, M. Jaščur, Exact solution of the mixed-spin Ising model on a decorated square lattice with two different kinds of decorating spins on horizontal and vertical bonds, Phys. Rev. B **76**, (2007) 014413 (9pp).

[45] L. Čanová, M. Jaščur and J. Strečka, Magnetic properties of an exactly solvable antiferromagnetic Ising-Heisenberg model on the decorated triangular lattice, J. Magn. Magn. Mater. **316**, (2007) e352-e354.

[46] S. Maťašovská and M. Jaščur, , Reentrant transitions and multicompensation phenomena of the exactly solvable mixed spin-S and spin-1/2 Ising model on decorated planar lattices, Physica A **383**, (2007) 339-350.

[47] L. Galisova, , Frustration phenomenon in the spin-1/2 Ising–Heisenberg planar model of interconnected trigonal bipyramid structures, J. Phys.: Condens. Matter **31**, (2019) 465801 (9pp).

[48] P. Azaria and H. Giacomini, An exactly solvable two-dimensional Ising model with magnetic field, J. Phys. A: Math. Gen. **21**, (1988) L935-L940.

[49] W. T. Lu and F. Y. Wu, Soluble kagome Ising model in a magnetic field, Phys. Rev. E **71**, (2005) 046120 (8pp).

[50] N. S. Ananikian, L. N. Ananikyan, L. A. Chakhmakhchyan, A. N. Kocharian, Magnetic properties and thermal entanglement on a triangulated Kagomé lattice, J. Phys. A: Math. Theor. **44**, (2011) 025001 (19pp).

[51] C. Domb, On the theory of cooperative phenomena in crystals, Adv. Phys. **9**, (1960) 149-244.

[52] G. H. Wannier, Antiferromagnetism. The Triangular Ising Net, Phys. Rev. **79**, 2 (1950) 357-364.

[53] G. F. Newell, Crystal Statistics of a Two-Dimensional Triangular Ising Lattice, Phys. Rev. **79**, (1950) 876-882;

[54] R. M. F. Houtappel, Order-disorder in hexagonal lattices, Physica (Amsterdam) **16**, (1950) 425-455.

[55] R.J. Baxter, Exactly Solved Models in Statistical Mechanics, 1989 (Academic Press: Australian Natl. U., Canberra).

[56] H. A. Kramers and G. H. Wannier: Statistics of the Two-Dimensional Ferromagnet. Part I, Phys. Rev. **60** (1941) 252-262.

[57] P. F. Godoy, M. Schmidt and F. M. Zimmer, The Ising model on the layered J1-J2 square lattice, Phys. Lett. A **384**, (2020) 126687 (6pp).

[58] R. J. Baxter, Critical Antiferromagnetic Square-Lattice Potts Model, Proc. Roy. Soc. London A: Math. and Phys.Sci. **383**, (1982) 43-54.

[59] M. I.de Berganza, E. E. Ferrero, S. A. Cannas, V. Loreto and A. Petri, Phase separation of the Potts model in the square lattice, Eur. Phys. J. Spec. Top. **143**, (2007) 273-275.

[60] J. S. Valverde, O. Rojas and S. M. de Souza, Two-dimensional XXZ-Ising model on a square-hexagon lattice, Phys. Rev. E **79**, (2009) 041101 (6pp).

[61] Strečka J and Karľova K , Magnetization curves and low-temperature thermodynamics of two spin-1/2 Heisenberg edge-shared tetrahedra, AIP Advances **8**, (2018) 101403 (4pp).

[62] H. Arian Zad, M. Sabeti, A. Zoshki and N. Ananikian, Electrocaloric effect in the two spin-1/2 XXZ Heisenberg edge-shared tetrahedra and spin-1/2 XXZ Heisenberg octahedron with Dzyaloshinskii-Moriya interaction, J. Phys.: Condens. Matter **31**, (2019) 425801 (11pp).

[63] H. Arian Zad, R. Kenna and N. Ananikian, Magnetic and thermodynamic properties of the octanuclear nickel phosphonate-based cage, Physica A **538**, (2020) 122841 (7pp).

[64] K. Karľova, J. Strečka and J. Richter, Enhanced magnetocaloric effect in the proximity of magnetization steps and jumps of spin-1/2 XXZ Heisenberg regular polyhedra, J. Phys.: Condens. Matter **29**, (2017) 125802 (13pp)

[65] G. Martinez, E. Tangarife, M. Perez and J. Mejia-Lopez, , Magnetic properties of small cobalt-copper clusters, J. Phys.: Conde. Matter **25**, (2013) 216003 (7pp).

[66] D. Die, B. X. Zheng, L. Q. Zhao, Q. W. Zhu and Z. Q. Zhao, Insights into the structural, electronic and magnetic properties of V-doped copper clusters: comparison with pure copper clusters, Phys. Rev. Lett **6**, (2016) 31978 (13pp).

[67] J. Strečka, K. Karľova and T Madaras, Giant magnetocaloric effect, magnetization plateaux and jumps of the regular Ising polyhedra, Physica B **466-467**, (2015) 76-85.

[68] H. Arian Zad, Entanglement in the Mixed-three-spin XXX Heisenberg Model with the Next-nearest-neighbour Interaction, Acta Phys. Pol. B **46**, (2015) 1911-1924.

[69] H Arian Zad, A Zoshki and M Sabeti, Magnetic Properties of an Antiferromagnetic Spin-1/2 XYZ Model in the Presence of Different Magnetic Fields: Finite-Size Effects of Inhomogeneity Property, Comm. in Theor. Phys. **71**, (2019) 1253 (8pp).

[70] K. Karľova and J. Strečka, Magnetization Process and Magnetocaloric Effect of the Spin-1/2 XXZ Heisenberg Cuboctahedron, J. Low Temp. Phys. **187**, (2017) 727-733.

[71] A. Chakraborty, J. Goura, P. Bag, and V. Chandrasekhar, Ni^{II} - Ln^{III} Heterometallic Complexes as Single-Molecule Magnets, Eur. J. Inorg. Chem., (2019) 1180-1200.

[72] Y. Z. Yu, Y. Q. Hu and Y. H. Guo *et al.*, Syntheses, crystal-solution structures and magnetic properties of a series of decanuclear heterometallic $[Ln_2^{III}Co_4^{II}Co_4^{III}]$ (Ln = Eu, Gd, Tb, Dy) clusters, Dalton Trans. **47**, (2018) 10124-10129.

[73] P. Kalita, J. Goura, J. M. Herrera, E. Colacio and V. Chandrasekhar, Heterometallic Octanuclear $Ni_4^{II}Ln_4^{III}$ (Ln = Y, Gd, Tb, Dy, Ho, Er) Complexes Containing $Ni_2^{II}Ln_2^{III}O_4$ Distorted Cubane Motifs: Synthesis, Structure, and Magnetic Properties, ACS Omega **3**, (2018) 5202-5211.

[74] M. Savva, C. Papatriantafyllopoulou, Z. Viskadourakis, J. Giapintzakis and A. J. Tasiopoulos, $Mn_2^{III}Ln_2^{III}$ (Ln = Gd, Dy, Ho) Complexes From The Initial Employment of 1,3-Propanediol In Mixed 3d/4f Metal Cluster Chemistry, Current Inorganic Chemistry **3**, (2013) 86-93.

[75] S. Mukhopadhyay , S. K . Mandal , S.Bhaduri , and W. H . Armstrong , Manganese clusters with relevance to photosystem II, Chem. Rev. **104**, (2004) 3981-4026.

[76] F. Troiania and M. Affronte, Molecular spins for quantum information technologies, Chem. Soc. Rev. **40**, (2011) 3119-3129.

[77] W. Wernsdorfer, L. Bogani, Molecular spintronics using single-molecule magnets, Nat. Mater. **7**, (2008) 179-186.

[78] A. Palii and B. Tsukerblat, Tuning of quantum entanglement in molecular quantum cellular automata based on mixed- valence tetrameric units, Dalton Trans. **45**, (2016) 16661-16672.

[79] R. Bagai, G. Christou,The Drosophila of single-molecule magnetism: $[Mn_{12}\ O_{12}\ (O_2\ CR)_{16}\ (H_2O)_4]$, Chem. Soc. Rev. **38**, (2009) 1011-1026.

[80] G. Christou, D. Gatteschi, D. N. Hendrickson, R. Sessoli, Single-molecule magnets, MRS Bulletin **25**, (2000) 66-71.

[81] S. Hill, R. S. Edwards, N. Aliaga-Alcalde, G. Christou, Quantum Coherence in an Exchange-Coupled Dimer of Single-Molecule Magnets, Sci. **302**, (2003) 1015-1018.

[82] J. M. Law, Identification and investigation of new low-dimensional quantum spin systems, Thesis, Doctor of Philosophy of Loughborough University, (2011).

[83] J.S. Miller, M. Drillon, Magnetism: Molecules to Materials I: Models and Experiments, (Wiley, Weinheim), (2002).

[84] C. J. Cairns and D. H. Busch, Intramolecular ferromagnetic interactions in polynuclear metal complexes, Coordination Chernistty Reviews **69**, (1986) 1-55.

[85] O. Kahn, Molecular Magnetism, (VCH Publishers) (1993).

[86] R. L. Carlin, Magnetochemistry, Springer (1986).

[87] S. R. White, Density Matrix Formulation for Quantum Renormalization Groups, Phys. Rev. Lett. **69**, (1992) 2863-2866.

[88] S. R. White, Density-matrix algorithms for quantum renormalization groups, Phys. Rev. B **48**, (1993) 10345 (12pp).

[89] J. C. Xavier, J. A. Hoyos, E. Miranda, Adaptive density matrix renormalization group for disordered systems, Phys. Rev. B **98**, (2018) 195115 (9pp).

[90] K. H. Marti, I. M. Ondík, G. Moritz, and M. Reiher, Density matrix renormalization group calculations on relative energies of transition metal complexes and clusters, Jour. Chem. Phys. **128**, (2008) 014104 (13pp).

[91] Q. M. Phung, A. Domingo and K. Pierloot, Dinuclear Iron(II) Spin-Crossover Compounds: A Theoretical Study, Chem. - A Euro. Jour. **20**, (2017) 5183-5190.

[92] A. Baiardi and M. Reiher, The density matrix renormalization group in chemistry and molecular physics: Recent developments and new challenges, J. Chem. Phys. **152**, (2020) 040903 (22pp).

[93] D. J. J. Farnell, R. F. Bishop, (2004) The coupled cluster method applied to quantum magnetism. In: Schollwöck U. Richter J. Farnell D.J.J. Bishop R.F. (eds) Quantum Magnetism, Lecture Notes in Physics, **645**. Springer, Berlin, Heidelberg.

[94] S. Capponi, A. Läuchli and M. Mambrini, Numerical contractor renormalization method for quantum spin models, Phys. Rev. B **70**, (2004) 104424 (14pp).

[95] J. Kolorenč and L. Mitas, Applications of quantum Monte Carlo methods in condensed systems, Rep. Prog. Phys. **74**, (2011) 026502 (28pp).

[96] Z. Yan, Y. Wu, C. Liu, O. F. Syljuåsen, J. Lou and Y. Chen, Sweeping cluster algorithm for quantum spin systems with strong geometric restrictions, Phys. Rev. B **99**, (2019) 165135 (6pp).

[97] A. Baniodeh, N. Magnani, Y. Lan, G. Buth, C. E. Anson, J. Richter, M. Affronte, J. Schnack and A. K. Powell, High spin cycles: topping the spin record for a single molecule verging on quantum criticality, npj Quant. Mater **3**, (2018) 10 (6pp).

[98] W. P. Chen, J. Singleton, L. Qin, A. Camón, L. Engelhardt, F. Luis, R. E. P. Winpenny and Y. Z. Zheng, Quantum Monte Carlo simulations of a giant $N_{21}Gd_{20}$ cage with a S=91 spin ground state, Nat. Comm. **9**, (2018) 2107 (6pp).

[99] B. Bauer, L. D. Carr, H.G. Evertz *et al.*, The ALPS project release 2.0: open source software for strongly correlated systems, J. Stat. Mech. (2011) P05001 (34pp).

[100] A.F. Albuquerque, F. Alet, P. Corboz *et al.*, The ALPS project release 1.3: Open-source software for strongly correlated systems, J. Magn. Magn. Mater. **310**, (2007) 1187-1193.

[101] J. Strečka, K. Karľová, V. Baliha and O. Derzhko, Ising versus Potts criticality in low-temperature magnetothermodynamics of a frustrated spin-1/2 Heisenberg triangular bilayer, Phys. Rev. B **98**, (2018) 174426 (14pp).

[102] H. Wang. L. F. Zhang, Z. H. Ni, W. F. Zhong, L. J. Tian, J. Jiang, Synthesis, Crystal Structures, and Magnetic Properties of One-Dimensional Mixed Cyanide- and Phenolate-Bridged Heterotrimetallic Complexes, Cryst. Growth and Des, **10**, (2010) 4231-4234.

[103] F. Souza, M. L. Lyra, J. Strečka and M. S. S. Pereira, Magnetization processes and quantum entanglement in a spin-1/2 Ising-Heisenberg chain model of a heterotrimetallic Fe-Mn-Cu coordination polymer, J. Magn. Magn. Mater. **471**, (2019) 423-431.

[104] Y. -D. Zheng, Z. Mao, B. Zhou, Entanglement teleportation via a couple of quantum channels in Ising–Heisenberg spin chain model of a heterotrimetallic Fe–Mn–Cu coordination polymer, Chi. Phys. B **28**, (2019) 120307 (12pp).

[105] K. Karľová, J. Strečka, and M. L. Lyra, Breakdown of intermediate one-half magnetization plateau of spin-1/2 Ising-Heisenberg and Heisenberg branched chains at triple and Kosterlitz-Thouless critical points, Phys. Rev. E **100**, (2019) 042127 (12pp).

[106] T. Werlang, C. Trippe, G. A. P. Ribeiro and G. Rigolin, Quantum Correlations in Spin Chains at Finite Temperatures and Quantum Phase Transitions, Phys. Rev. Lett. **105**, (2010) 095702 (4pp).

[107] W. K. Wootters, Phys. Rev. Lett, Entanglement of Formation of an Arbitrary State of Two Qubits, **80**, (1998) 2245-2248.

[108] A. S. Holevo, Probabilistic and Statistical Aspects of Quantum Theory, Math. Sci. Eng. (Edizioni della Normale, New York, NY, 1982).

[109] J. Liu, X. Jing, and X. Wang, Phase-matching condition for enhancement of phase sensitivity in quantum metrology, Phys. Rev. A **88**, (2013) 042316 (4pp).

[110] N. Li and S. Luo, Entanglement detection via quantum Fisher information, Phys. Rev. A **88**, (2013) 014301 (5pp).

[111] B. L. Ye, L. Y. Xue, Y. L. Fang, S. Liu, Q. C. Wu, Y. H. Zhou and C. P. Yang, Quantum coherence and quantum Fisher information in the XXZ system, Physica E **115**, (2020) 113690 (6pp).

[112] G. Bowen, S. Bose, Teleportation as a Depolarizing Quantum Channel, Relative Entropy, and Classical Capacity, Phys. Rev. Lett. **87**, (2001) 267901 (4pp); Y. Yeo, Teleportation via thermally entangled states of a two-qubit Heisenberg XX chain, Phys. Rev. A **66**, (2002) 062312 (3pp); Y. Zhou,

G. F. Zhang, Quantum teleportation via a two-qubit Heisenberg XXZ chain – effects of anisotropy and magnetic field, Eur. Phys. J. D **47**, (2008) 227-231.

[113] H. Arian Zad and N. Ananikian, Phase transitions and thermal entanglement of the distorted Ising–Heisenberg spin chain: topology of multiple-spin exchange interactions in spin ladders, J. Phys.: Condens. Matter **29**, (2017) 455402 (11pp).

[114] H. Arian Zad and N. Ananikian, Phase transitions and magnetization of the mixed-spin Ising–Heisenberg double sawtooth frustrated ladder, J. Phys.: Condens. Matter **30**, (2018) 165403 (9pp).

[115] H. Arian Zad and N. Ananikian, Thermal entanglement in the mixed-spin Ising-Heisenberg double sawtoothfrustrated ladder, Solid State Commun. **276**, (2018) 24-27.

[116] A. S. Oja and O. V. Lounasmaa, Nuclear magnetic ordering in simple metals at positive and negative nanokelvin temperatures, Rev. Mod. Phys. **69**, (1997) 1-136.

[117] A. M. Tishin, and Y. I. Spichkin, The Magnetocaloric Effect and its Applications, Institute of Physics (2003) (480pp).

[118] K. A. Gschneider, Jr., V. K. Pecharsky, and A. O. Tsokol, Recent developments in magnetocaloric materials, Rep. Prog. Phys. **68**, (2005) 1479-1539.

[119] D. Choudhury, T. Suzuki, Y. Tokura, and Y. Taguchi, Tuning structural instability toward enhanced magnetocaloric effect around room temperature in $MnCo_{1-x}Zn_x$ Ge, Sci. Rep. **4**, (2014) 7544 (6pp).

[120] H. Neves Bez, C. Bahl, K. K. Nielsen, and A. Smith, Magnetocaloric materials and first order phase transitions, (PhD Thesis, Department of Energy Conversion and Storage), Technical University of Denmark, (2016) (170pp).

[121] J. Y. Law, F. Franco, L. M. M. Ramírez, and *et al.*, A quantitative criterion for determining the order of magnetic phase transitions using the magnetocaloric effect, Nat. Comm. **9**, (2018) 2680 (9pp).

[122] L. Zhu, M. Garst, A. Rosch, Q. Si, Universally Diverging Grüneisen Parameter and the Magnetocaloric Effect Close to Quantum Critical Points, Phys. Rev. Lett. **91**, (2003) 066404 (4pp); M. Garst, A. Rosch, Sign change of the Grüneisen parameter and magnetocaloric effect near quantum critical point, Phys. Rev. B **72**, (2005) 205129 (10pp).

[123] M. E. Zhitomirsky, and A. Honecker, Magnetocaloric effect in one-dimensional antiferromagnets, J. Stat. Mech.: Theory Exp., (2004) P07012 (19pp).

[124] A. Honecker, and M. E. Zhitomirsky, Magneto-thermal properties of the spin-s Heisenberg antiferromagnet on the cuboctahedron, J. Phys.: Conf. Series **45**, (2009) 012982 (4pp).

[125] A. Honecker and S. Wessel, Magnetocaloric effect in quantum spin-s chains, Condens. Matter Phys. **12** , (2009) 399-410.

[126] C. Trippe, A. Honecker, A. Klümper, V. Ohanyan, Exact calculation of the magnetocaloric effect in the spin- 1/2 XXZ chain, Phys. Rev. B **81**, (2010) 054402 (10pp).

[127] M. Topilko, T. Krokhmalskii, O. Derzhko and V. Ohanyan, Magnetocaloric effect in spin-1/2 XX chains with three-spin interactions, Eur. Phys. J. B **85**, (2012) 278 (9pp).

[128] L. Gálisová, Magnetocaloric effect in the spin-1/2 Ising-Heisenberg diamond chain with the four-spin interaction, Condens. Matter Phys. **17**, (2014) 13001 (10pp).

[129] L. Gálisová and J. Strečka, Magnetic and magnetocaloric properties of the exactly solvable mixed-spin Ising model on a decorated triangular lattice in a magnetic field, Physica E **99**, (2018) 244-253.

[130] J. Strečka, J. Richter, O. Derzhko, T. Verkholyak, K. Karľová, Magnetization process and low-temperature thermodynamics of a spin-1/2 Heisenberg octahedral chain, Physica B **536** , (2018)

364-368.

[131] M. Žukovič, M. Semjan, Magnetization process and magnetocaloric effect in geometrically frustrated Ising antiferromagnet and spin ice models on a 'Star of David'nanocluster, J. Magn. Magn. Mater. **451**, (2018) 311-318.

[132] C. Beckmann, J. Ehrens and J. Schnack, Rotational magnetocaloric effect of anisotropic giant-spin molecular magnets, J. Magn. Magn. Mater. **482** , (2019) 113-119.

[133] V. Ohanyan and A. Honecker, Magnetothermal properties of the Heisenberg-Ising orthogonal-dimer chain with triangular XXZ clusters, *Phys. Rev. B* **86**, (2012) 054412 (17pp).

[134] J. Strečka, O. Rojas, T. Verkholyak, and M. L. Lyra, Magnetization process, bipartite entanglement, and enhanced magnetocaloric effect of the exactly solved spin-1/2 Ising-Heisenberg tetrahedral chain, Phys. Rev. E **89**, (2014) 022143 (10pp).

[135] L. Gálisová, Reentrant phenomenon and inverse magnetocaloric effect in a generalized spin-(1/2, s) Fisher's super-exchange antiferromagnet, J. Phys.: Condens. Matter **28** , (2016) 476005 (10pp).

[136] J. Torrico, M. Rojas, S. M. de Souza, and O. Rojas, Zero temperature non-plateau magnetization and magnetocaloric effect in an Ising-XYZ diamond chain structure, Phys. Lett. A **380**, (2016) 3655-3660.

[137] R. C. Alécio, J. Strečka, and M. L. Lyra, Thermodynamic behavior and enhanced magnetocaloric effect in a frustrated spin-1/2 Ising-Heisenberg triangular tube, J. Magn. Magn. Mater. **218**, 451 (2018) 218-225.

[138] L. Gálisová, and D. Knežo, Macroscopic ground-state degeneracy and magnetocaloric effect in the exactly solvable spin-1/2 Ising–Heisenberg double-tetrahedral chain, Phys. Lett. A **382**, (2018) 2839-2845.

[139] M. Hamedoun, R. Masrour, K. Bouslykhane, A. Hourmatallah and N. Benzakour, Magnetic phase diagram of diluted spinel $Zn_{1-x}Cu_xCr_2Se_4$ system, Jour. Mag. Mag. Mat. **320**, (2008) 1431-1435.

[140] R. Masrour, E.K. Hlil, A. Jabr, M. Hamedoun, A. Benyoussef, A. Hourmatallah, K. Bouslykhane, N. Benzakour and A. Rezzouk, , Magnetic and electronic properties of Mn2Sn thin films: First principles calculations and high temperature series expansions, Chin. Jour. Phys., **56**, (2018) 1985-1889.

[141] R. Masrour, M. Hamedoun, A. Benyoussef, Magnetic properties of $MnCr_2O_4$ nanoparticle, Jour. Mag. Mag. Mat., **322**, (2010) 301-304.

[142] R. Masrour, E.K. Hlil, M. Hamedoun, A. Benyoussef, A. Boutahar, H. Lassri, Antiferromagnetic spintronics of Mn2Au: An experiment, first principle, mean field and series expansions calculations study, Jour. Mag. Mag. Mat. , **393** (2015) 600-603.

[143] R. Masrour and M. Hamedoun, Magnetic properties of a ferromagnet spin-S, Ising, XY and Heisenberg models semi-infinites systems, Phys. Lett. A , **372**, (2008) 5203-5207.

[144] M. Roger, J. H. Hetherington, and J. M. Delrieu, Magnetism in solid ^{3}He, Rev. Mod. Phys. **55** , (1983) 1-64.

[145] M. Müller, T. Vekua and H. J. Mikeska, Perturbation theories for the S=1/2 spin ladder with a four-spin ring exchange, Phys. Rev. B **66** , (2002) 134423 (5pp).

[146] T. A. Arakelyan, V. R. Ohanyan, L. N. Ananikyan, N. S. Ananikian, and M. Roger, Multisite-interaction Ising model approach to the solid ^{3}He system on a triangular lattice, Phys. Rev. B **67**, (2003) 024424 (13pp).

[147] V. Ohanyan, and N. Ananikian, in Mathematical Physics Proceedings of the XI Regional Conference, Tehran, Iran, 2004, edited by S. Rahvar, N. Sadooghi, and F. Shojai, World Scientific, Singapore, pp. 49-51 2005.

[148] L. N. Ananikyan, The Hexagonal Recursive Approximation with Multisite-Interaction Ising Model for the Solid and Fluid ^{3}He System, Int. J. Mod. Phys. B **21**, (2007) 755-772.

[149] V. V. Hovhannisyan, R. G. Ghulghazaryan, and N. S. Ananikian, The partition function zeros of the anisotropic Ising model with multisite interactions on a zigzag ladder, Physica A **388** , (2009) 1479-1490.

[150] N. S. Ananikian, L. N. Ananikian, and H. A. Lazaryan, Magnetic Properties and Concurrence for Fluid ^{3}He on Kagome Lattice, Phys. Atom. Nucl. **75** , (2012) 1250-1255.

[151] L. Gálisová, Magnetic properties of the spin-1/2 Ising-Heisenberg diamond chain with the four-spin interaction, Phys. Status Solidi b **250** , (2013) 187-195.

[152] D. C. Cabra, A. Honecker and P Pujol, Magnetization Curves of Antiferromagnetic Heisenberg Spin- 1/2 Ladders, Phys. Rev. Lett. **79**, (1997) 5126-5129.

[153] D. C. Cabra, A. Honecker and P Pujol, Magnetization plateaux in N - leg spin ladders, Phys. Rev. B **58**, (1998) 6241-6257.

[154] A. Langari, M. Abolfath, and M. A. Martin-Delgado, Phase diagram of ferrimagnetic ladders with bond alternation, Phys. Rev. B **61**, (2000) 343-348.

[155] K. Hida, M. Shino and W. Chen, Bond Operator Mean Field Approach to the Magnetization Plateaux in Quantum Antiferromagnets –Application to the S=1/2 Coupled Dimerized Zigzag Heisenberg Chains, J. Phys. Soc. Japan **73** , (2004) 1587-1592.

[156] T. Vekua, G. I. Japaridze and H-J Mikeska, Magnetic-field-induced phase transitions in spin ladders with ferromagnetic legs, Phys. Rev. B **70**, (2004) 014425 (6pp).

[157] A. Koga, S. Kumada, N. Kawakami and T. Fukui, Mixed-Spin Ladders and Plaquette Spin Chains, Jour. Phys. Soc. Jep. **67**, (1998) 622-628.

[158] N. Avalishvili, B. Beradze, and G. I. Japaridze, Magnetic phase diagram of a spin S=1/2 antiferromagnetic two-leg ladder with modulated along legs Dzyaloshinskii-Moriya interaction, Eur. Phys. J. B **92**, (2019) 262 (7pp).

[159] G. I. Japaridze and E. Pogosyan, Magnetization plateau in the S=1/2 spin ladder with alternating rung exchange, J. Phys. Condens. Matter **18**, (2006) 9297-9306.

[160] F. Amiri, G. Sun, H.-J. Mikeska, T. Vekua, Ground-state phases of a rung alternated spin-1/2 Heisenberg ladder, Phys. Rev. B **92**, (2015) 184421 (9pp).

[161] J. Jahangiri, F. Amiri and S. Mahdavifar, Thermodynamic behavior near the quantum orders in dimerized spin S= 1/2 two-leg ladders, J. Mag. Mag. Mater. **439**, (2017) 22-29.

[162] Q. Luo, S. Hu, J. Zhao, A. Metavitsiadis, S. Eggert, X. Wang, Ground-state phase diagram of the frustrated spin- 1/2 two-leg honeycomb ladder, *Phys. Rev. B 97* , (2018) 214433 (14pp).

[163] M. T. Batchelor, X.-W. Guan, N. Oelkers and Z. Tsuboi, Integrable models and quantum spin ladders: comparison between theory and experiment for the strong coupling ladder compounds, Adv. Phys. **56**, (2007) 465-543.

[164] D. Arnaudon, A. Sedrakyan and T. Sedrakyan, Integrable N-leg Ladder Models, Int. Jour. Mod. Phys. A **19**, (2004) 16-33.

[165] K. Hida, K. Takano and H. Suzuki, Haldane Phases and Ferrimagnetic Phases with Spontaneous Translational Symmetry Breakdown in Distorted Mixed Diamond Chains with Spins 1 and 1/2, J. Phys. Soc. Jpn. **79**, (2010) 114703 (10pp).

[166] H. Lu, N. Hayashi, Y. Matsumoto, H. Takatsu and H. Kageyama , Mixed-Spin Diamond Chain $Cu_2FePO_4F_4(H_2O)_4$ with a Noncollinear Spin Order and Possible Successive Phase Transitions, Inorg. Chem. **56**, (2017) 9353-9360.

[167] Y. Mizuno, T. Tohyama and S. Maekawa, Electronic States of Doped Spin Ladders $(Sr,Ca)_{14}Cu_{24}O_4$, J. Phys. Soc. Jpn. **66**, (1997) 937-940.

[168] J. Wang, Y. Lin, H. Zou, S. Pu and J. Shi, Structural transition, electrical and magnetic properties of the B-site Co doped $Sr_{14}Cu_{24}O_{41}$ compounds, J. Phys.: Condens. Matter **21**, (2009) 075601 (10pp).

[169] I. D. Exius, Properties of undoped and doped spin-1/2 ladders at finite temperature, Thesis, Der Fakultät Physik der Technischen Universität Dortmund, (2010).

[170] J. Strečka, M. Jaščur, Disordered and ordered states of exactly solvable Ising-Heisenberg planar models with a spatial anisotropy, Acta Phys. Slov. **56**, (2006) 65-70.

[171] R. E. Norman, N. L. Rose, and R. E. Stenkmap, Crystal structure of a copper complex of 2-carboxypentonic acid; a decomposition product of dehydroascorbic acid, J. Chem. Soc. Dalton Trans., (1987) 2905-2910. ;R. E. Norman and R. E. Stenkamp, Structure of a Copper(II) Complex of 2-C-Carboxypentonic Acid (H_3cpa); Cu_9Br_2(cpa)$_6n_2$-. xH_2O, Acta Crystallogr., **46**, (1990) 6-8.

[172] R. B. Potts, Spontaneous Magnetization of a Triangular Ising Lattice, Phys. Rev. **88**, (1952) 352.

[173] S. Biswas, J. Goura, S. Das, C. V. Topping, J. Brambleby, P. A. Goddard, and V. Chandrasekhar, Octanuclear Heterobimetallic Ni_4Ln_4 Assemblies Possessing Ln_4 Square Grid [2×2] Motifs: Synthesis, Structure, and Magnetism, Inorg. Chem. **55**, (2016) 8422-8436.

[174] K. S. Cole and R. H. Cole, Dispersion and Absorption in Dielectrics, J. Chem. Phys. 9, (1941) 341-351.

[175] M. Balanda, AC Susceptibility Studies of Phase Transitions and Magnetic Relaxation: Conventional, Molecular and Low-Dimensional Magnets, Acta. Phys. Pol. A **124**, (2013) 964-976.

[176] C. V. Topping and S. J. Blundell, A.C. susceptibility as a probe of low-frequency magnetic dynamic, J. Phys.: Condens. Matter **31**, (2019) 013001 (27pp).

[177] J. A. Sheikh, A. Adhikary, H. S. Jena, S. Biswas, and S. Konar, High Nuclearity (Octa-, Dodeca-, and Pentadecanuclear) Metal (M = Co^{II}, Ni^{II}) Phosphonate Cages: Synthesis, Structure, and Magnetic Behavior, *Inorg. Chem.* **53**, (2014) 1606-1613.

[178] J. A. Sheikh, H. S. Jena, A. Clearfield, and S. Konar, Phosphonate Based High Nuclearity Magnetic Cages, *Acc. Chem. Res.* **49**, (2016) 1093-1103.

[179] B. A. Breeze, M. Shanmugam, F. Tuna, and R. E. P. Winpenny, A series of nickel phosphonate–carboxylate cages, *Chem. Commun.* (2007) 5185-5187.

[180] H. B. G. Casimir, F.K. du Pré, Note on the thermodynamic interpretation of paramagnetic relaxation phenomena, Physica **5**, (1938) 507-511.

[181] R. Kubo, T. Nagamiya, Solid State Physics, McGraw-Hill, New York, (1969).

[182] L. Salmon, P. Thuéry, E. Riviére, J. P. Costes, A. J . Motad and M. Ephritikhine, Structural, magnetic and theoretical calculations of a ferromagnetically coupled tetranuclear copper(II) square complex, New J. Chem., **38**, (2014) 1306-1314.

[183] D. Girolami, Observable Measure of Quantum Coherence in Finite Dimensional Systems, Phys. Rev. Lett. **113**, (2014) 170401 (5pp).